MONASH University

Strategies for the improvement of

Ti-6Al-4V implant osseointegration

Trina Majumdar
BE (Materials), BBiomedSci

A thesis (including published works) submitted for
the degree of *Doctor of Philosophy*
October 2018

Department of Materials Science and Engineering
Monash University
Victoria, Australia

Copyright notice

Abstract

Titanium-based alloys are used extensively in orthopaedic implants due to their low cytotoxicity and high mechanical strength. However these issues can also limit full implant functionality, particularly for patients with complex orthopaedic issues. The surfaces of Ti-based implants do not typically induce strong mechanical interlocking (especially in cement-less applications), and the elastic modulus mismatch between the implant and host bone can lead to stress shielding and bone resorption. These issues often necessitate painful and costly revision surgeries. Major strategies in solving these problems include the use of additive manufacturing (AM) processes such as selective laser melting (SLM), surface coating with bone-like minerals, and the use of hydrogels as temporary intermediaries between the implant and growing host tissue.

Ti-6Al-4V orthopaedic implants are increasingly being fabricated using SLM, which has the potential to produce complex and customised implants with both mechanical properties and bioactivity comparable to those of conventionally manufactured implants (following certain post-processing techniques). The properties of SLM-produced implants are dependent on the specific process parameters used - the interplay between process parameters such as laser scan speed and laser intensity has an enormous influence on microstructure and performance. Different combinations of process parameters, despite yielding the same overall thermal energy supplied per unit volume (VED), have different effects on SLM Ti-6Al-4V part microstructure and properties. Thus the current practice of using VED to design SLM fabrication processes may not always be appropriate.

It is difficult to measure the re-passivation of Ti-based alloys in a way which accurately represents their likely behaviour in use. A method is proposed here for the accelerated *in vitro* investigation of

re-passivation of Ti-based alloys, taking into account the inevitable surface damage during implantation, and the rapid nature of the reaction at the alloy surface.

Following fabrication, the application of bone-like minerals such as hydroxyapatite (HA) has been shown to improve implant-host bone bonding. Incorporation of HA into naturally-originating gels, including gellan and agarose, produces materials which closely mimic the viscoelastic behaviour of healthy human bone/cartilage interfaces, and to which cells (specifically mouse osteoblasts) attach readily.

Finally, this work presents another way of coating HA onto Ti-based implants. As before, HA coatings with substitutions such as strontium ions are shown to improve osteoblastic activity on the implant surfaces.

Publications

1. **T. Majumdar**, J. E. Frith, N. Birbilis, Determining the effects of SLM process parameter manipulation on Ti-6Al-4V osseointegratability, *manuscript to be submitted to ACS Biomater. Sci. Eng*. 2018

2. **T. Majumdar**, J. E. Frith, N. Birbilis, Controlling Ti-6Al-4V surface properties through selective laser melting (SLM) process parameter manipulation, *manuscript under review at PLOSOne* 2018

3. **T. Majumdar**, N. Eisenstein, J.E. Frith, S.C. Cox, N. Birbilis, Additive Manufacturing of Titanium Alloys for Orthopedic Applications : A Materials Science Viewpoint, Adv. Eng. Mater. (2018). doi:10.1002/adem.201800172.

4. **T. Majumdar,** M.E. Cooke, B.M. Lawless, F. Bellier, E.A.B.B. Hughes, L.M. Grover, S.W. Jones, S.C. Cox, Formulation and viscoelasticity of mineralised hydrogels for use in bone-cartilage interfacial reconstruction, J. Mech. Behav. Biomed. Mater. 80 (2018) 33–41. doi:10.1016/j.jmbbm.2018.01.016

5. J.L. Wang, R.L. Liu, **T. Majumdar**, S.A. Mantri, V.A. Ravi, R. Banerjee, N. Birbilis, A closer look at the in vitro electrochemical characterisation of titanium alloys for biomedical applications using in-situ methods, Acta Biomater. 54 (2017) 469–478. doi:10.1016/j.actbio.2017.03.022..

6. Y.F. Ding, R.W. Li, M. Nakai, **T. Majumdar,** D.H. Zhang, M. Niinomi, N. Birbilis, P.N. Smith, X.B. Chen, Osteoanabolic Implant Materials for Orthopedic Treatment, Adv. Healthc. Mater. 5 (2016) 1740–1752. doi:10.1002/adhm.201600074.

Conference presentations

1. **Majumdar, T.,** Bazin, T., Frith, J., Birbilis, N., "An investigation into selective laser melting (SLM) process parameters for the production of orthopaedic Ti implants", The 25th Australian Society for Biomaterials and Tissue Engineering Conference, 2017, Canberra

2. **Majumdar, T.,** Wang, J.L., Massahud, E., Banerjee, R., Birbilis, N., Frith, J., "A novel methodology for examining the re-passivation characteristics of highly noble alloys", The 5th conference of the Combined Australian Materials Societies: Incorporating Materials Australia and the Australian Ceramics Society (CAMS), 2016, Melbourne

3. **Majumdar, T.,** Birbilis, N., Chen, X.B., "An evaluation of the effects of selective laser melting process parameters on the biocompatibility of Ti-based implants", The 10th World Biomaterials Congress, 2016, Montreal

4. **Majumdar, T.,** Birbilis, N., Chen, X.B., "Developments in bioactive titanium implants: novel manufacturing and coatings", Australian Biomedical Engineering Conference (ABEC), 2015, Melbourne

Thesis including published works declaration

I hereby declare that this thesis contains no material which has been accepted for the award of any other degree or diploma at any university or equivalent institution and that, to the best of my knowledge and belief, this thesis contains no material previously published or written by another person, except where due reference is made in the text of the thesis.
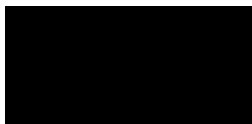
This thesis includes 4 original papers published in peer reviewed journals and 2 submitted publications. The core theme of the thesis is strategies to improve the osseointegration of titanium based implants. The ideas, development and writing up of all the papers in the thesis were the principal responsibility of myself, the student, working within the Materials Science and Engineering Department (Faculty of Engineering) under the supervision of Professor Nick Birbilis and Dr Jess Frith.

The inclusion of co-authors reflects the fact that the work came from active collaboration between researchers and acknowledges input into team-based research.

Thesis Chapter	Publication Title	Status	Nature and % of student contribution	Co-author name(s) Nature and % of Co-author's contribution*	Co-author(s), Monash student Y/N*
2	Additive manufacturing of titanium alloys for orthopaedic applications: a materials science viewpoint	Published	Concept, literature survey, writing (80%)	Neil Eisenstein; contribution to manuscript (5%) J.E. Frith; evaluation of manuscript and guiding comments (5%) Sophie C. Cox; evaluation of manuscript and guiding comments (5%) Nick Birbilis; evaluation of manuscript and guiding comments (5%)	No No No No
7	Formulation and viscoelasticity of mineralised cell-adhesive hydrogels	Published	Concept, collection of experimental data, analysis of data, writing of manuscript (50%)	Megan E Cooke; collection of experimental data, analysis of data (11%) Bernard M Lawless; collection of experimental data, analysis of data (11%) Francis Bellier; development of experimental design, collecting of data (11%) Erik A B Hughes; experimental guidance and guiding comments (2%) Liam M Grover; evaluation of manuscript and guiding comments (2%) Simon W Jones; evaluation of manuscript and guiding comments (2%) Sophie C Cox; concept, experimental guidance and evaluation of manuscript (11%)	No No No No No No No

I have not renumbered sections of submitted or published papers in order to generate a consistent presentation within the thesis.

Student signature: ████████ **Date:** 11/10/2018

The undersigned hereby certify that the above declaration correctly reflects the nature and extent of the student's and co-authors' contributions to this work. In instances where I am not the responsible author I have consulted with the responsible author to agree on the respective contributions of the authors.

Main Supervisor signature: ██████ **Date:** 11/10/2018

Acknowledgements

First, I would like to thank my supervisors, Professor Nick Birbilis and Dr Jess Frith, whose support, enthusiasm and encouragement have inspired in me a love of materials science and engineering that will guide the rest of my life.

I would like to acknowledge those who have helped me throughout my candidature;

- The members of the Corrosion group (Dr Oumaima Gharbi, Darren Feenstra, Guilherme Sander Malab, Paula de Lima Magalhaes, Dr Ruiliang Liu, Dr Chong Ke, Dr Shravan Kairy, Dr Sebastian Thomas, Ryan Donahue, Jayshri Dumbre, Qing Cao, Junlan Wang, Tiphaine Bazin, Dr Jess Lyndon) whose help with trouble-shooting, jokes and advice made lab work a breeze.

- My peers, including Yuxiang Wu, Jessie Ratcliffe, Celia Vandestadt and Luke Besley, for sharing the trials and joys of our candidature.

- Daniel Curtis, Graham Prior, Dr Jisheng Ma, Karla Kontreras, Dr Jenny Dyson and Dr Kate Nairn, without whose technical advice and experimental guidance I would be lost.

- Dr Sophie Cox (and members of the Trailab) at the University of Birmingham for hosting me as a visiting researcher for one of the most fruitful experiences of my life.

- The staff at MCAM, MCEM and MXP.

- Mio Ihashi and Dr Elizabeth Gordon, for helping me rise above.

- The Materials Science and Engineering department, particularly Kris Wirthensohn and Edna Tan.

I would like to acknowledge all of my friends and extended family, but especially;

- Emily Massahud, whose persistence and warmth helped me carry on through all the failed experiments, and celebrate the successful ones.

- Brittany Diep and Phyllix Tam, whose friendship has been constantly bright.

- Romo and Christine Herzog, for treating me like a daughter.

- Chotto Thamma, for inspiring me to push myself.

Finally, I dedicate this thesis to my family. Renan (and Bert and Ernie Grubberson), thank you for being my best friend and staying by my side through the good days, and the many bad. Ma and Baba, you taught me first how to be a good human, then how to be a good researcher. I'm beyond honoured to have followed in your footsteps.

Chapter 1: Project outline

Joint replacement surgeries are becoming increasingly prevalent globally, with 100000 surgeries recorded as having occurred in 2014 in Australia alone (1). This is due to increasing life-spans and quality of life – today's joint replacement patients are generally younger than 60 and thus require joint replacements with longer service lives (2). Successful orthopaedic implants will be biocompatible, facilitate cell attachment and differentiation, have some level of porosity and/or surface roughness and finally, similar mechanical properties to the region of replacement (1). The major aim of this project is to gain a greater understanding of various aspects of orthopaedic implant development, from the design phase through to implantation.

Titanium and its alloys are used widely in orthopaedic applications, particularly in total hip joint replacements, as they display low cytotoxicity, high mechanical strength and relative biological inertness (3–6). Ti has an oxide isoelectric point of 5-6, and so a passivating layer can be maintained at pH levels found in the body (5). However, the biological inertness of Ti reduces the effectiveness of implant-bone fixation and therefore subsequent bone formation around the implant. Additionally, the mechanical strength and density of Ti are significantly higher than those of bone — pure Ti has a modulus of ~120 GPa while bone has a modulus of 5–30 GPa (trabecular to cortical bone, respectively) (7,8). This results in elastic modulus mismatch and stress shielding — when impact forces are unevenly distributed through implant-bone interfaces, the rate of bone resorption increases. Bone resorption around implants causes interfacial weakening and the formation of wear debris, which can lead to significant inflammation and pain for patients.

Additive manufacturing (AM) methods are becoming more prevalent as ideal fabrication techniques (9), particularly with regard to personalised medicine. These new generation methods involve the building up of products, layer by layer (additively), as opposed to conventional subtractive manufacturing processes. Through AM, it is possible to create highly complex designs not currently possible through conventional manufacturing techniques. Designs such as those for standard orthopaedic implants can be customised for individual patients with the use of their personal medical data (computed tomography (CT) imaging), and fabricated immediately, without the need to wait for the commissioning of new fabrication equipment (dies, tooling etc.). Selective laser melting (SLM), a type of AM, utilises a high energy laser beam to melt and fuse pre-alloyed powders layer by layer to form three-dimensional parts.

Fabrication techniques such as SLM are still in their infancy, and much work remains to be done in the full characterisation and comprehension of the properties of SLM products. The ultimate goal is to produce orthopaedic implants through SLM that perform as well as or better than conventionally-manufactured orthopaedic implants, both in terms of bioactivity and mechanical performance. A full understanding of how best to achieve these properties requires a greater understanding of the effects of SLM process parameters on final properties. The effects of the interplay of two SLM process parameters, laser power and laser scan speed, on SLM Ti-6Al-4V are examined herein; these results are expected to contribute to the establishment of a set of guidelines for choosing SLM process parameters based on the specific requirements of an implant.

Post-processing techniques must also be investigated in relation to improving the osseointegration of orthopaedic implants. Hydroxyapatite (HA), a mineral with a similar crystal structure to that of human bone, is of particular interest, as its incorporation into either gels or coatings has been shown to

improve orthopaedic implant bioactivity. However, issues remain with the reliable and effective incorporation of HA into/onto implant surfaces, due to the low crystallinity, plasticity and flowability of HA minerals.

HA-containing hydrogel composites may be used as intermediaries between implants and host bone, or bone and cartilage to facilitate interfacial regeneration. Mineralised hydrogel composites are examined in detail in this project. A rotating simplex model was used to optimise the composition of HA-containing agarose and gellan hydrogel constructs, with the aim of obtaining composites mechanically comparable to human cartilage in terms of their ability to dissipate energy. Optimised compositions were formed and shown to successfully replicate the viscoelastic behaviour of the healthy human cartilage-bone interface, and also facilitate cell attachment, indicating potential for use in post-surgery healing processes in the human body.

HA can also be incorporated into implant coatings. Many methods have been used in the attempt to deposit uniform HA-containing coatings onto metallic implants, with varying levels of success due to issues with bonding, delamination and excessive technical requirements (high sintering temperatures, high voltages). A biomimetic HA deposition method for Ti based alloys is examined and adapted here. The responses of both osteoblasts and osteoclasts to the strontium substituted HA coating (on various Ti based alloys) is also investigated in detail. This will form the basis of a two-step protocol for the deposition of strontium-substituted HA on Ti-based alloy surfaces.

The overarching aim of this project is to improve the osseointegration of orthopaedic implants through a range of strategies addressing individual stages of orthopaedic implant design. The specific aims of this project are;

- To investigate how SLM Ti-6Al-4V microstructure, and therefore porosity, roughness, hardness and corrosion resistance change according to the combination of laser scan speed and laser power used during fabrication, and thereby create a process map for SLM Ti-6Al-4V applicable to the production of orthopaedic implants.

- To examine whether the various microstructures and surfaces achievable through the SLM production of Ti-6Al-4V exhibit different levels of bioactivity. The bioactivity of SLM Ti-6AL-4V is affected by the combination of laser scan speed and laser power used during fabrication, as evidenced by human bone cell adhesion, viability and mineralisation.

- To study how Ti surfaces re-passivate in the human body; specifically, by accurately reproducing and assessing the disruption of the passive layers of Ti-based alloys in the body, using a lab-bench model, and to determine whether re-passivation process differs between SLM and non-SLM Ti based alloys.

- To modulate the activity of osteoblasts and osteoclasts on Ti based implant surfaces through the application of HA containing coatings (and to optimise the deposition of these coatings).

- To create mineralised (HA containing) hydrogel composites which approximate the viscoelastic behaviour of the bone-cartilage interface and facilitate cell attachment.

Chapter 2: Literature review

The bulk of the work in this thesis concerns additive manufacturing (AM), a flourishing fabrication method with the potential to transform personalised medicine. The use of AM in orthopaedic applications began with the fabrication of customised orthopaedic implants for vulnerable patients, those with bone cancers or irregular bone anatomies who were unable to receive standard implants. These first adoptors, along with intrepid surgeons and clinicians, took the first steps toward the end goal of personalised medicine for all.

AM orthopaedic implants are a fertile field of enquiry for biomaterials researchers today, with studies looking at all aspects of the orthopaedic implant life cycle. This life cycle can be broken down into a few major areas: alloy design, fabrication, post-processing, implantation and service life/rate of deterioration.

To inform and situate the current research, a comprehensive literature review of the additive manufacturing of Ti-6Al-4V implants was undertaken. At present, there remain several bottlenecks in the uptake of AM for orthopaedic implant manufacture:

- Production of feed-stock – the bulk of research into AM fabrication focuses on well understood alloys such as stainless steels, nickel alloys and titanium alloys, as these pre-alloyed powders are widely available. The investigation of niche alloys with less common alloying elements such as tantalum and niobium (i.e. those with higher bioactivity) is limited by the paucity in production of these feed-stocks.

- Design specific to AM – the use of AM in fabrication requires some consideration in the design phase, both in terms of limitations and advantages. Although AM implants are

generally built using support structures, and require post-processing before implantation, AM enables the production of previously unmanufacturable features and geometries. The adaptation of standard designs to both patient anatomy and the capabilities of AM is yet to be accomplished.

- Incomplete understanding of how process parameters collectively influence final properties – generally, AM is performed using process parameters optimised for mechanical performance. The optimisation of AM processing parameters for producing orthopaedic implants is yet to be completed.

- Process-specific defects and behaviour – without careful control of processing conditions, AM products can have high residual stresses, porosity and layer-wise delamination. The relationship between processing conditions and final properties, and the application of this information to tuning the properties of orthopaedic implants is a lingering challenge.

This chapter was prepared as a paper, and published in *Advanced Engineering Materials*. The paper appears here as published.

REVIEW

XXXX

ADVANCED
ENGINEERING
MATERIALS

www.aem-journal.com

Additive Manufacturing of Titanium Alloys for Orthopedic Applications: A Materials Science Viewpoint

Trina Majumdar, Neil Eisenstein, Jess E. Frith, Sophie C. Cox, and Nick Birbilis*

Titanium-based orthopedic implants are increasingly being fabricated using additive manufacturing (AM) processes such as selective laser melting (SLM), direct laser deposition (DLD), and electron beam melting (EBM). These techniques have the potential to not only produce implants with properties comparable to conventionally manufactured implants, but also improve on standard implant models. These models can be customized for individual patients using medical data, and design features, such as latticing, hierarchical scaffolds, or features to complement patient anatomy, can be added using AM to produce highly functional patient-anatomy-specific implants. Alloying prospects made possible through AM allow for the production of Ti-based parts with compositions designed to reduce modulus and stress shielding while improving bone fixation and formation. The design-to-process lead time can be drastically shortened using AM and associated post-processing, making possible the production of tailored implants for individual patients. This review examines the process and product characteristics of the three major metallic AM techniques and assesses the potential for these in the increased global uptake of AM in orthopedic implant fabrication.

1. Introduction

Orthopedic surgeries (including joint replacements) are becoming increasingly common, with more than 1 000 000 surgeries estimated to have occurred in the United States in 2015 alone.[1] The demand for orthopedic implants has increased rapidly in the past few decades due to increases in average life spans globally, as well as increases in physical activity among the elderly. Contemporary orthopedic implants, such as those seen in **Figure 1**, must last for decades as opposed to years, as well as closely approximate and support the area of replacement in terms of mechanical properties and responses to host biology.[1–5] The requirements for implants in different areas vary, for example hip versus knee implants. Thus, a general view will be taken in this manuscript.

A cement-less orthopedic implant must bond well to bone in the first month following implantation, to ensure that complete osseointegration over the next few months occurs successfully.[3,4] Osseointegration is defined as a complete linkage between bone and the implant surface, that is, mechanical interlocking. Full host to implant contact is achieved by the development of anchorage mechanisms that can withstand natural loading. Implant and bone surface features of various sizes become important at different steps of the osseointegration process.[6]

Titanium and its alloys are used widely in orthopedic applications, as seen in Figures 1 and 2, due to low cytotoxicity, high mechanical strength, and relative biological inertness.[7–10] Pure Ti is a non-ferrous light metal, with a nominal density of $4.51 \, g \, cm^{-3}$ and elastic modulus of 115 GPa.[11] Ti undergoes an allotropic transformation at 882 °C, from a body-centered cubic (β phase) structure to a hexagonal close packed (α phase) structure (below 882 °C). The phase transformation is accompanied by slight atomic distortion due to the plane transformation, leading to a slight increase in volume when cooling through the transus temperature (882 °C).[12] Ti is spontaneously passive, reacting with air or aqueous environments to form a protective oxide layer that is typically ≈2–7 nm in thickness. This layer is well maintained at normal body pH levels, and is resistant to localized short-term changes in pH occurring due to infection, however, total corrosion resistance is known to decrease over time due to the interplay of various organic and inorganic molecules such as lipopolysaccharides and albumin.[9,13]

The elastic modulus of Ti and its common alloys are generally much higher than that of bone. Pure Ti has a modulus of ≈120 GPa while cortical bone has a modulus of 10–30 GPa.[3] When Ti-based implants are in contact with bone, this modulus mismatch results in stress shielding[3,4] — cyclic loading and impact forces are borne largely by the implant rather than the host bone, causing the resorption of this "unused" bone. Stress shielding causes interfacial weakening and the formation of wear debris, potentially leading to the requirement for revision

Prof. N. Birbilis, T. Majumdar, Dr. J. E. Frith
Department of Materials Science and Engineering
Monash University
Clayton, Victoria 3800, Australia

N. Eisenstein, Dr. S. C. Cox
School of Chemical Engineering
University of Birmingham
Edgbaston B15 2TT, UK
E-mail: nick.birbilis@monash.edu

The ORCID identification number(s) for the author(s) of this article can be found under https://doi.org/10.1002/adem.201800172.

**ADVANCED
SCIENCE NEWS**

www.advancedsciencenews.com

**ADVANCED
ENGINEERING
MATERIALS**

www.aem-journal.com

surgeries. The biological inertness of Ti-based alloys, as well as their poor wear properties and notch sensitivity compared to other commonly used stainless steels or cobalt-based alloys, remain as hurdles in successful implant osseointegration.[14,15]

Present alloy design for orthopedic applications is moving away from Ti alloys containing toxic elements such as Ti–6Al–4V, and toward lower modulus Ti-based alloys. The lower modulus Ti-alloys are usually typified by the β phase Ti alloys, with important properties summarized in **Table** 1.

Some of the most promising alloying elements under investigation are niobium (Nb), zirconium (Zr), tantalum (Ta), and strontium (Sr) These are all β-stabilizing elements (allowing alloys to retain the high temperature BCC β phase at room temperature) with similar cytocompatibility to that of Ti.[16–19] To reduce this effect, Ti is commonly alloyed with elements which act as stabilizers for the β phase, thereby reducing the Young's modulus of the material to closer to that of bone. Of such two-phase alloys, Ti–6Al–4V is the most commonly used for orthopedic implants, with aluminum (Al) serving as an α-phase stabilizer and vanadium (V) serving as a β phase stabilizer.[11] Ti–6Al–4V has an allotropic transformation temperature of 990 °C and a solidus temperature of 1605 °C.[11,20,21]

Two other strategies in reducing stress shielding and improving the osseointegration of orthopedic Ti implants[24] include: 1) the incorporation of porosity or texture into parts to reduce stiffness and density (either by design or manufacturing method), and 2) the reduction of modulus mismatch through the development of low modulus Ti-alloys; both approaches elaborated below.

Programming porosity into implant designs through scaffolding may improve the speed and efficacy of osseointegration.[25,26] The porosity of cortical bone (i.e., the femur) is approximately 5–30%, while that of cancellous bone is 30–90%.[27] Non-stochastic porous scaffolding in implants modeled on the porosity of various size scales in living bone can act as templates for the initial attachment and growth of bone-forming cells. Nano-porosity is required for molecular transport, waste removal, and cell–cell signaling, while micropores are required to allow cell migration and capillary formation. Full vascularization occurs on the macro scale (mm).[28,29] Bone cell proliferation and differentiation are thought to be positively influenced by surface roughness, with an average surface roughness or groove width below 1 μm being advocated as optimal[30,31] although other groups have suggested that larger surface grooves of up to 50 μm width[32] may be ideal. While there is no consensus on the best surface topography for osteoblastic adhesion and

Trina Majumdar received her BE and BBiomedSci in materials engineering from Monash University in 2014 and is currently a 3rd year PhD candidate in the Birbilis group at the Materials Science and Engineering Department at Monash University. Her doctoral research under the supervision of Prof. Nick Birbilis examines the additive manufacturing of titanium-based orthopedic implants, with a focus on the manipulation of additive manufacturing process parameters to produce implants with improved osseointegrative capabilities.

Dr Sophie C. Cox is a Lecturer in the School of Chemical Engineering working within the Tissue Regeneration And Interfaces Lab (TRAILab). Her research focuses on the design of biomaterials and manufacturing methods that maximize regeneration of damaged or diseased tissue. She is particularly interested in the relationship between biomaterial properties and biological response as well as the development of additive manufacturing techniques to fabricate medical implants.
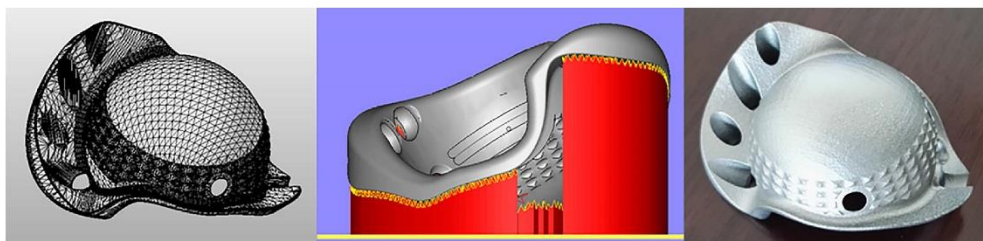
Prof. Nick Birbilis is the Head of Materials Science and Engineering at Monash University and the Woodside Innovation Chair. His research spans the broad areas of metallurgy, corrosion, and corrosion control. He is a Fellow of NACE and the Electrochemical Society.

proliferation, it is agreed that the method in which the texture is achieved is as important as the roughness parameter itself, as this affects surface chemistry[31,33] Surface roughness or texture is to date achieved through post-processing techniques upon Ti
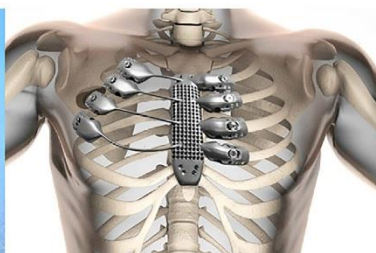
Figure 1. Examples of customized implants. These implants were designed using 3D Digital Imaging and Communications in Medicine (DICOMs) and fabricated using AM techniques.

**ADVANCED
SCIENCE NEWS**
www.advancedsciencenews.com

**ADVANCED
ENGINEERING
MATERIALS**
www.aem-journal.com

Figure 2. Patient data in the form of computed tomography (CT) scans or magnetic resonance imaging (MRI) scans can be used to create computer aided design (CAD) models, which can then be used to print custom implants. L–R this figure shows the initial design of a custom implant, the pre-print manipulation of the design including support structures in red and the final post-processed part.

and its alloys. Complex surface topographies with a wide range of differently sized features are necessary for successful implants.[34,35] These topographies support the entire process of host bone attachment and the formation of a strong bone-implant interface.

These features can be easily investigated, trialed and produced through AM processes as the page to part lead-time is relatively short. There is no need for re-tooling between design iterations, and relatively low amount of material are required to investigate different options for part design. Other global features such as porosity and surface roughness can be systematically varied through manipulation of the AM fabrication process. The final implant produced for the patient through AM can be greatly customized in a reduced time period, with reduced costs as compared to conventional processes such as casting.

Improving orthopedic implant fabrication and usage via additive manufacturing (AM) techniques offers distinct advantages. Conventional Ti fabrication techniques include near net casting, forging, and machining from wrought ingot and bars. However, as Ti has low thermal conductivity and high reactivity with and affinity for oxygen, this presents difficulties in machining,[36,37] and so these methods are often unsuitable for producing implants with patient specific geometries or features. AM processes have already demonstrated an excellent ability to serve as alternative fabrication routes in a number of industries, and as of 2014 the market was estimated to be worth \$4.1 billion,[38] with Ti and its alloys used for a significant amount of additively manufactured components. The improved geometrical freedom of AM technologies allows for increased complexity and customization. The localized metal melting possible in most AM processes permits for alloying in a manner that bypasses liquid metal (casting) issues such a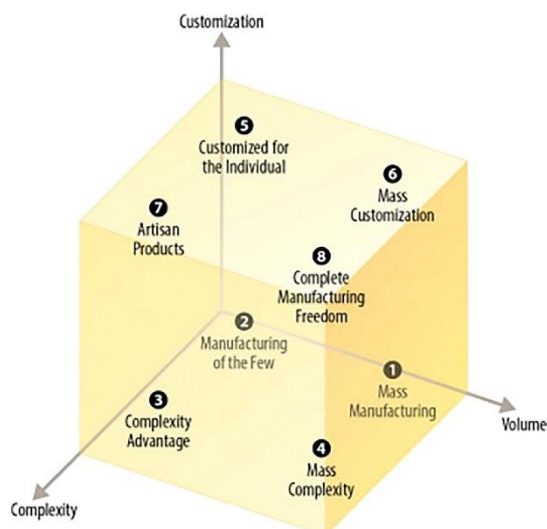s solute solubility and segregation (and dissimilar melting points, etc.). The alloying freedom of powder-based AM is metallurgically unsurpassable at present. Further benefits of AM include low material wastage and low production volumes with reduced economy of scale issues.[39] Ultimately, AM allows for the production of parts that were previously un-manufacturable or economically unviable through traditional routes, as per the three-axis model of product manufacturability seen in **Figure 3**.

In a holistic sense, AM may be carried out through seven major approaches; material extrusion, material jetting, binder jetting, vat photo-polymerization, sheet lamination, directed energy deposition, and powder bed fusion, with the latter two used for the fabrication of strong, net shape metallic bone replacements.[41] Powder bed fusion techniques, such as Electron Beam Melting (EBM) and Selective Laser Melting (SLM) utilize either a laser or electron beam to melt and fuse pre-alloyed or pure powders in specified patterns. Direct Laser Deposition (DLD) differs in terms of powder supply – the powder is gravity fed from nozzles into the laser beam and local melt pool. In this way, the powders are sintered into a melt pool on the substrate. While DLD can produce near-net shapes, these have lower tolerances and less complex internal structures than possible through SLM or EBM. DLD is largely used to produce significantly larger freeform components than either EBM or SLM. In the context of specific implant production, patient scan data, for example, computed tomography (CT), can be utilized for customized implant designs, which can then be constructed through powder bed fusion or energy deposition methods.[39] This process is visualized in **Figure 4**.

Even at this stage of AM development and the commercial availability of production units, work remains to be completed in the full characterization and understanding of AM produced part

Table 1. Nominal mechanical properties of common Ti-based alloys used for orthopedic implants.[11,22,23]

Material	Phase types	Fabrication method	Elastic modulus [GPa]	Yield strength [MPa]	Ultimate tensile strength [MPa]	β transus temp-erature [°C]
Ti–6Al–4V	α + β	Casting	110	850–900	960–970	995
Ti–13Nb–13Zr	α' + β	Casting	79	900	1030	575
Ti–6Al–7Nb	α + β	Casting	105	921	1024	1010
CP Ti (grade 4)	A	Casting	105	692	100	950
Bone	–	–	10–40	–	90–140	–

**ADVANCED
SCIENCE NEWS**
www.advancedsciencenews.com

**ADVANCED
ENGINEERING
MATERIALS**
www.aem-journal.com

Figure 3. The three-axis model of product manufacturability shows that product design must address complexity, required iterative customizability, and required volume to be readily manufacturable. Reproduced with permission[40] 2014, Elsevier.

properties. As with any technique, part fabrication is not as simple as inputting a design and fabricating with fixed settings – care must be taken with the parameters chosen for processing, as each can have a significant effect on the microstructure, build efficiency, and mechanical and implantability-related properties of the part.

The aim of this review is to assess the current research and technology in the context of AM for orthopedic implants, particularly focusing on Ti and its alloys. The first section of this manuscript examines the major AM techniques currently being used to fabricate Ti implants, as well as process-specific properties as related to Ti-based orthopedic implants, while the second and third parts examine pre- and post-fabrication considerations. The fourth section looks at current research being conducted in the area, and the final section will discuss clinical and engineering perspectives on the production of orthopedic implants through AM.

2. Additive Manufacturing Techniques Relevant to Orthopedic Implants

The three most commonly used AM processes in medical engineering (for orthopedic applications) are SLM, EBM, and DLD. Each process begins with the development of a 3D CAD model of the required implant. These models can be made using individual patient data (e.g., from MRI or CT), or from prior (known or standard) designs – this process of applying medical data to a design model can be done through commercial software such as Mimics (Materialise) and Vitrea (Vital Images).[42] Once the design is complete, it may be further modified to include support structures – these structures act as anchors to the build plate, prevent part warpage due to residual stresses, and aid in heat conduction away from the part. The design can then numerically sliced into 2D layers through the use of software (e.g., Magics (Materialise) or Netfabb (Autodesk).[42,43] The prepared file is sent
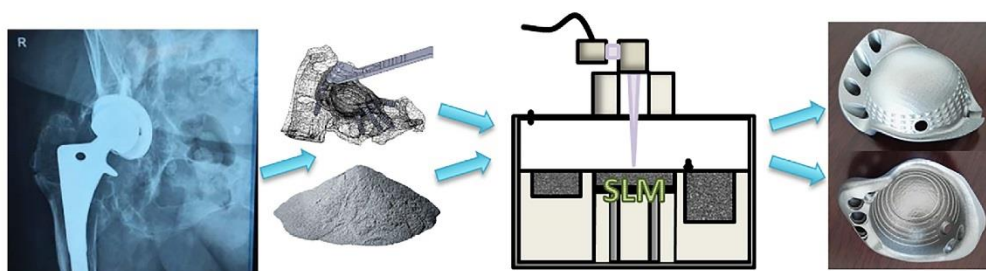
Figure 4. Patients who require custom implants can receive them through the combination of AM techniques and medical imaging. Generally, patient data (e.g., MRI or CT scans) is used to create the design of the part, this CAD file (in stereolithography format) is then sliced and otherwise manipulated such that the AM machine (SLM shown here) can fabricate the part. Following fabrication and some minor post-processing, the custom implant can be delivered to the patient, with a drastically reduced lead time.

22

to the EBM, SLM or DLD machine, where the 3D part is built up through multiple layer-wise deposition and melting stages.[39,44,45] The maximum build volume is specific for each brand of machine, but is generally no larger than 400*400*400 mm^{-3}, specifically for SLM and EBM. Following fabrication, the parts are cut away from the build plate and support structures. Post-processing procedures such as hot isostatic pressing (HIPing) and/or stress relieving are performed, followed by surface finishing or polishing as required.[46,47] The part is prepared for implantation through the application of antibacterial or osteo-inductive coatings. Following sterilization (e.g., through γ irradiation), the implant is ready for implantation.[48]

The major variables in the SLM and EBM processes are as follows; laser power, layer thickness, scan speed, and hatch spacing.[45] These parameters affect the amount of thermal energy supplied to each unit volume of material, the sum of which is termed the energy density (ED). This behavior can be quantified as in Equation 1.[49]

$$E_{\text{density}} = \frac{P_{\text{beam}}}{v_{\text{scan}} \cdot s_{\text{hatching}} \cdot t_{\text{layer}}} \tag{1}$$

where E_{density} = energy density, P_{laser} = beam power, v_{scan} = scan speed, s_{hatching} = hatch spacing, t_{layer} = layer thickness.

Each process produces parts with specific properties, which will be discussed in the following sections. It is important to note that both conventional and AM manufacturing techniques may use the same alloys – however the relationship between processing variables during AM fabrication on part properties (with respect to effects on the human body) is not yet well understood. The bulk of previous research has centered on short term, in vitro studies of AM produced parts. A historical view will be taken in the following sections.

2.1. SLM

The main components of SLM machinery, as seen in **Figure 5**, include a fiber laser (usually Ytterbium) with a beam expander and focusing lenses, a build platform, powder bunker, and powder rake.[50] Pre-alloyed metal powders with average particle diameter between 10 and 45 μm are raked over the build platform, usually pre-heated to between 100 and 200 °C, after which the CAD driven mirror system can direct and focus the laser beam (up to 1 kW) onto the build platform to melt each 2D cross-section into the powder layer. The build table drops down according to the specified layer thickness, generally between 20 and 100 μm, and another even layer of powder is raked over the work platform. The laser then melts the next layer onto the previous layer.[50] The entire process takes place in a purified nitrogen or argon gas environment to prevent oxidation of the metal powders.[24] The final part is built up by the "welding" of small overlapping regions, ending in the production of a 3D part with a complex, pulsed thermal history.[51]

2.1.1. SLM Part Properties

SLM characteristically produces parts with complex thermal histories due to the rapid heating and cooling cycles as well as the steep thermal gradients produced across layers.[52] Examples of properties produced by various groups are collected in **Table 2** and discussed in the following sections. The laser beam causes localized re-melting and re-cooling cycles adjacent to each scan track. The SLM process inherently produces a steep thermal gradient between the top and bottom surfaces of each layer due to heat transfer through multiple layers. This can lead to melt pool instability, reduction of surface energies as well as dimensional inaccuracies due to contraction on cooling.[24] Localized re-melting and re-cooling cycles lead to the formation of columnar β phase grains, which are inclined perpendicular to the laser scanning plane.[50,53] These thermal gradients will cause the part to have residual thermal stresses and non-equilibrium phases.[54] Residual stresses must be relieved prior to usage, necessitating post-processing techniques such as stress relieving and/or HIP to reduce the internal stresses and increase the fatigue resistance of parts to that comparable with conventionally fabricated equivalents.[52] Additionally, un-melted
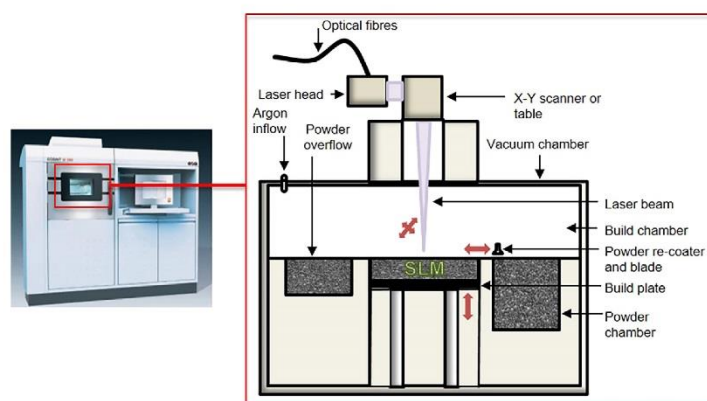
Figure 5. Schematic of SLM Equipment showing fiber laser with, build chamber, powder bunker, powder rake, and build-in-progress, and photo of a representative SLM machine.

23

**ADVANCED
SCIENCE NEWS**
www.advancedsciencenews.com

**ADVANCED
ENGINEERING
MATERIALS**
www.aem-journal.com

or partially melted powder particles may remain on each layer between scans, leading to the formation of micro-voids.[55] Specific part properties are also affected by process parameters and powder characteristics.[56]

Taking a closer view, pre-alloyed Ti–6Al–4V powders, with a liquidus temperature of 1650 °C and solidus temperature of 1605 °C, display a "mushy" zone within the melt pool, and the cooling rate of this melt pool informs the layer-wise microstructural progression.[57] Cooling rates within the melt pool can range between 12 000 and 40 000 °C s^{-1} depending on the amount of energy supplied (dictated by process parameters such as laser power and scan speed).[44,58] Ti–6Al–4V particles initially solidify into BCC β phase structures, present as both columnar and equiaxed grains. Depending on the cooling rate, the β phase can then transform into α' martensite (above 410 °C s^{-1}) or α phase. Taking a macroscopic view, part properties are also spatially dependent due to anisotropic heat removal and interaction of cooling gradients with the bulk un-melted powder surrounding the growing part. The first layer of the part will have a characteristically rough surface finish since it has a reduced thermal conductivity due to it being comprised of loose powder, although this will be further influenced by the method used to cut the part from the substrate, as well as the removal of support structures. This leads to the formation of an unstable melt pool, and stalactite patterns where the cooling melt pool sinks into the adjacent loose powder.[45] The last layer of the part will also have a rough surface finish due to a localized reduction in thermal insulation.

There is a wealth of information regarding the practical capabilities of SLM to produce Ti alloy parts with varying porosities; however, no consensus exists on the minimum or maximum possible pore sizes achievable. Minimum achievable bulk pore sizes have been variously reported as 750,[59] 500,[60] and 100 μm.[61] SLM part porosities of 31–43% and 32.2–53.4% have been achieved by Basalah et al.[27] and El-Hajje et al.[62] respectively. Guneta et al.[63] were able to achieve SLM produced porosities of between 32% and 53%, however the pore sizes produced were between 17.0 and 24.0 μm, too small for cells to penetrate into the inner pores. Apart from issues with cell penetration, smaller pore sizes are in any case more difficult to form due to the high local laser power causing the formation of larger melt pools, leading to powder sputtering and pore occlusion.[59] Additionally, issues may arise with depowdering following part completion. Depowdering refers to the process of retrieving the built part from the bulk powder surrounding it, usually through high pressure air blasting, vibratory processing or a combination thereof.[44] Solid parts can be retrieved easily, however, depowdering porous parts is complex,[60,64,65] due to instances of weak bonding between layers and loose powder, which can trap powder particles.

SLM parts typically have roughness in the micrometer range, with 2–20 μm representing an average range.[66] This is attributed to thermal gradients across layers, and the staircase effect.[45] Different roughness behavior is observed according to where in the staircase the observed region is (**Figure 6**). This is due to the presence of partially melted particles remaining on free surfaces. High hardness is also observed due to rapid cooling characteristics and low ductility, generally reported as at least 20% greater than comparable EBM parts.[67,68] Hardness

and porosity are interrelated with ED, with a higher energy input causing more complete melting and reduced porosity. The presence of non-equilibrium phases contributes to the higher yield strength of SLM parts as compared to forged parts.[45]

The major defect types in SLM produced Ti–6Al–4V parts can be classed as follows; un-melted or partially melted particles on surfaces, random porosity, and delamination between layers.[51,69,70] Random porosity is generally observed in SLM parts due to the presence of trapped gases in the melt pool, as well as a lack of fusion defects, which occur when there is insufficient ED to completely melt the powders in a small region. This results in the formation of irregularly shaped cavities with un-melted trapped powder particles and is heavily dependent on sinter neck size as well as particle size.[27] These form primarily along interlayer boundaries, and act as local stress concentrators. Micron sized pores affect fatigue strength, while residual stresses can affect fatigue crack growth.[52] SLM produced parts also generally have relatively high oxygen/nitrogen contents.[24] SLM produced coatings form irregularly shaped particles – the inherent eccentricity of these are key in the formation of porous structures.[71]

As mentioned, certain process parameters have been found to affect final product characteristics, the most important of these being scan rate, laser intensity, and layer thickness.[72,73] Changes in scan rate affect microstructural features, with increased scan rates causing the formation of finer dendritic microstructures.[74] This can be attributed to the reduced ratio of temperature gradient to solidification rate, as well as the increased turbulence of melt pools.[75] Increased laser intensity appears to increase density and therefore reduce porosity.[76,77] The increased laser intensity, while creating a larger immediate melt pool, also affects previous layers, resulting in increased heating/cooling cycles – this allows for microstructural refinement in much the same way as increased scan rates.

Key studies into the in vitro and in vivo behavior of SLM produced Ti–6Al–4V implants include the work of Hollander et al.,[78] Warnke et al.,[79] Mangano et al.,[80] Van Bael et al.,[81] and Shaoki et al.[82] Hollander et al.[78] investigated the behavior of human osteoblasts on annealed sand-blasted SLM produced Ti–6Al–4V over a time period of 14 days. Both porous (200, 400, and 7000 μm diameter pores) and non-porous samples were produced, and cell proliferation was found to occur successfully on each of these samples, with proliferation and differentiation (indicated by alkaline phosphatase (ALP) activity) occurring in a manner similar to that expected for wrought Ti–6Al–4V. Following, Warnke et al.[79] investigated the behavior of human osteoblasts (from iliac crest cancellous bone) on mesh Ti–6Al–4V scaffolds over a period of 72 days. In agreement with the work of Hollander et al. (and Van Bael et al.), this experiment showed that pore sizes smaller than 500 μm in diameter result in cell occlusion. This prevents further in-growth and bone regeneration.[79] Cell morphology on the other scaffolds was found to be star-like and well spread, with multiple filipodial extensions. SLM produced Ti–6Al–4V scaffold biocompatibility was confirmed with the use of lactate dihydrogenase (LDH), 3-(4,5-dimethylthiazol-2-yl)-2, 5-diphenyltetrazolium bromide (MTT), 5-bromo-2- deoxyuridine (BrdU), and water-soluble tetrazolium (WST) tests. The work of Van Bael et al.[81] further showed that lower scaffold permeability led to increased cell attachment.

24

**ADVANCED
SCIENCE NEWS**
www.advancedsciencenews.com

**ADVANCED
ENGINEERING
MATERIALS**
www.aem-journal.com

Their work also indicated that cell differentiation is likely to be more affected by pore size (with smaller pores providing more stimuli) than shape. The work of Hollander et al., Warnke et al. and Van Bael et al. all identified one key issue in SLM implant fabrication — actual pore size was often significantly smaller than designed pore size, with the largest diametric variance being 300 μm.

Mangano et al.[80] produced some of the first in vivo data for SLM produced implants, by implanting a Ti–6Al–4V mandibular micro-implant into a human patient without complications. This implant was acid etched with oxalic acid and maleic acid to produce a final Ra of 66.8 μm. Retrieval and analysis of this implant after 2 months of healing showed evidence of bone remodeling activity, areas of woven bone, and multiple osteocyte lacunae, with a bone-to-implant contact (BIC) percentage of 69.51%. Shaoki et al.[82] compared the in vivo performance of SLM-produced Ti–6Al–4V implants with commercially available implants in a canine model, over a period of 9 weeks. Their SLM implant had a higher roughness than the commercial implants ($R_a = 10.65 \pm 2.3 \, \mu m$ and $R_a = 0.33 \pm 0.12$) but showed no significant differences in bone-implant contact ratio or bone formation, indicating that SLM fabricated Ti–6Al–4V implants are competitive and have great potential for wide spread uptake. More long-term data is yet unavailable.

2.2. EBM

EBM is a powder bed fusion technique quite similar to SLM, with the major difference being the energy source, which is an electron beam as opposed to a laser beam.[57,83] This requires a high vacuum in the build chamber to maintain beam integrity. The powder used in EBM is pre-heated to 40–60% of its melting temperature through successive rapid scans by the electron beam.[84] This is followed by a reduced scanning rate and beam current. The chamber temperature is kept between 650 and 700 °C.

An EBM system contains a computer control/recording section and an electron beam forming and processing system (**Figure 7**). An electron gun is used to generate an electron beam (up to 3 kW), which is then accelerated through a focusing lens and magnetic scanning coil system.[50] Pre-alloyed metal powders are gravity fed from cassettes and raked evenly over the build table. The focused electron beam is directed by the CAD model slices to selectively melt patterns into the powder layer. The build table is then lowered according to the layer thickness, and the process is repeated until the part is complete. Layer thicknesses for EBM are generally kept at 50 μm, and the average particle size for powders used should be between 45 and 105 μm.[85]

EBM has several benefits, particularly for the fabrication of parts comprised of alloys that have a high chemical affinity to atmospheric gases, including Ti, this issue is bypassed in EBM, as the process occurs in a vacuum.[86] The background vacuum is maintained within 10^{-4} to 10^{-5} Torr, with a helium bleed near the build area where the vacuum is reduced to 10^{-2} Torr to aid cooling and beam scan stability.[44,87] The process is extremely energy efficient, due to the high conversion efficiency from electricity to electron beam energy.[87] Almost all of this energy

can be absorbed by the material/powder. Thus, the beam will have a large penetration depth, leading to the formation of a high temperature melt pool.[88]

2.2.1. EBM Part Properties

Parts produced through EBM undergo characteristic micro-structural progressions.[87,89] During part building, the part microstructure is initially composed of primary β phase. This then transforms to α martensite, which decomposes into α and β phases. This characteristic progression can be seen in **Figure 8**. The β phase is composed of coarse columnar grains, and therefore EBM parts are highly anisotropic.[90] This occurs as a result of the beam penetration depth being greater than the layer thickness meaning each layer is transformed several times. The uppermost layer, that is, the layer with lowest thermal insulation, is formed entirely of non-equilibrium α' phase grains. In the bulk, relatively slower cooling allows the α' phase to decompose into α and β phases, leading to closer modulus matching with bone than conventionally manufactured Ti-based alloys.

The surface features produced by EBM are often difficult to control without post processing, and are limited by the spatial resolution of the method.[35] Diffusion between build table substrates and the formed part may be observed, but this can be avoided through the use of a sacrificial support base.[87] Powder blow-away is a common undesirable process feature, which occurs due to electrostatic repulsion between beam and powder.[87] Pre-heating the powder to ≈730 °C using a defocused beam, with currents between 28 and 38 mA, and a scanning rate of 146 000 mm s^{-1},[91,92] can be done to reduce this. The small-scale sintering occurring during pre-heating can reduce the blow-away of the powder particles. However, post-process powder entrapment still presents a problem.[39,88]

Many groups have investigated the mechanical properties and surface behavior of EBM produced Ti-based alloys, and information about these is collated in Table 2. and discussed here. EBM structures have thicker oxide layers than conventionally machined surfaces,[36] with the specific thickness of these oxides being dependent on location, as seen in in Figures 8 and 9. This is thought to be due to the presence of oxidative gas species in the vacuum chamber, and the diffusion of oxygen from the bulk of the component to the outer layers, resulting in net oxide growth. Oxide thickness is also dependent on surface — different areas of the growing part will undergo different cooling patterns during manufacture.[21,36,91] Upper layers undergo rapid cooling due to the absence of surrounding material, resulting in thinner oxide layers. In contrast, side surfaces are embedded between adjacent un-melted powder particles, which act as thermal insulators. The high temperatures partially sinter these adjacent particles and vaporize residual moisture in the powder bed. This causes the formation of oxides 50% thicker than those present on the upper surfaces.[91] Oxide thickness is also affected by build height; larger builds allow for the release of trapped moisture in the chamber, leading to increased stability. The upper surface oxide layer is thus only formed after the temperature of the layer is insufficient to drive oxygen diffusion from the bulk to the surface. Therefore, the oxide formation

25

characteristics of EBM parts may be controlled to produce tunable oxide thickness gradients. This behavior is important in designing post manufacturing machining and finishing processes, as these may be affected by the oxide thickness. The cohesion and adhesive strength of these surface oxides is inversely dependent on oxide thickness.[44] The oxide layer prevents corrosion while interacting with calcium ions.[93,94]

The porosity of parts produced by EBM is thought to occur largely as a side effect of the "balling" phenomenon.[24,95,96] The formation of "balls" is likely due to the simultaneous reduction in surface energy and surface area. This leads to the generation of small cavities, which is compounded by the effect of "spattering," wherein the initial layers of the part have low resistance to electric repulsion occurring under electron beam radiation.[96] This effect is similar to that of "powder blow-away" and results in the presence of large irregular pores. Pores may also arise from the presence of trapped argon during atomization. As mentioned previously, this porosity may be beneficial for bone-forming cells, but the difficulty in removing all entrapped powder is a limiting factor, as these particles are likely to contribute to wear and inflammatory responses.

As with SLM, parts produced by EBM are heavily influenced by process conditions and powder characteristics. Initial powder particle size is related to final density and surface roughness; parts fabricated with smaller sized particles, that is, 25–45 μm (as opposed to the commonly used 45–105 μm particle size range used for EBM), tend to have higher average peak to valley ratios and more un-melted particles attached on the uppermost surface.[36,97,98] Scanning velocity and line length have significant effects on heat concentration and material deposition. Increased scanning velocities and line lengths result in less heat provided to the area. Additionally, increased beam currents affect material deposition and ultimately may decrease the numbers of internal cavities/pores as well as larger agglomerates. This can be attributed to an increased driving force for sintering particles.

It is important to note that the effects of these parameters are interrelated. The ratio between beam current (and intensity) and scanning velocity is important in considering the final properties of the part.[83,99] Ideally, a low scanning velocity should be paired
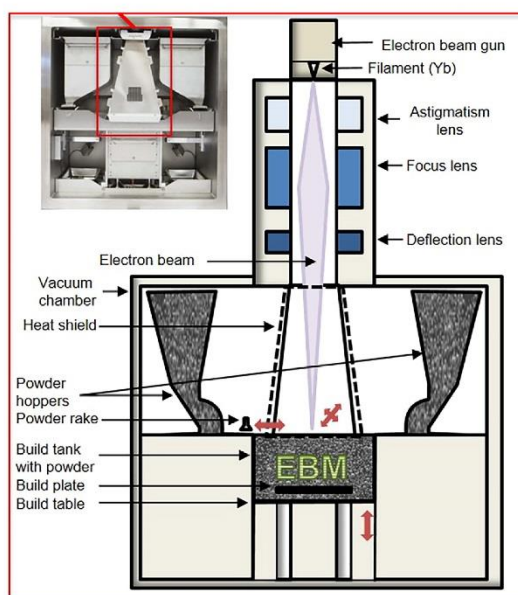
with a moderately high beam current to produce a dense and flat part with pores at the outer layers.[87] The relation between powder size and surface roughness is notable and may be exploited to achieve specific topographies. Surface roughness provides an increased surface area and micro-texture, both of which are beneficial to cell adhesion.

The effects of varying porosity and surface roughness of EBM Ti–6Al–4V parts on in vitro and in vivo properties have been investigated by a number of groups, beginning perhaps most importantly with the work of Ponader et al.[100] Their experiment examined the behavior of human osteoblasts on EBM Ti–6Al–4V discs with a variety of surfaces (smooth, unpolished, hatched, and sintered) over a period of 2 weeks. Higher cell viability and proliferation was observed on surfaces with R_a values of 0.077 μm, that is, the smooth samples. As discussed previously, conflicting reports exist on whether roughness enhances or impedes osteoblastic proliferation and development, even on EBM Ti–6Al–4V surfaces. Ponader et al. in this study hypothesized that the key factor in the interaction between surface roughness and cell behavior was the propensity of the surface to allow cell to cell interactions. Cells prefer to attach in deep lying concave areas, that is, between peaks/grooves (as this presents a low energy input configuration). Densely spread peaks (high R_q) and sharp peaks make cell-cell communication difficult, reducing the amount of cell proliferation – good cell proliferation was found in this study on surfaces with R_a values up to 24.9 μm and corresponding R_q values of up to 34.6 μm. Cell differentiation as indicated by the expression of various osteogenic genes/proteins such as ALP and osteocalcin (OC) was also examined – these markers were not significantly affected by surface roughness. It may be further hypothesized that surface roughness may affect only certain parts of the osseointegration process. In a follow-up study, Ponader et al.[86] investigated differences in the bone-regenerative ability of 60% porous vs. compact EBM Ti–6Al–4V cranial implants in a pig model over 60 days. While the porous implants displayed lower initial bone-implant contact (BIC) than the compact implants, a gradual increase in BIC from almost 0–5% in the former was seen, as compared to a gradual decrease from approximately 30–9%. Thomsen et al.[101] examined both as-produced and machined
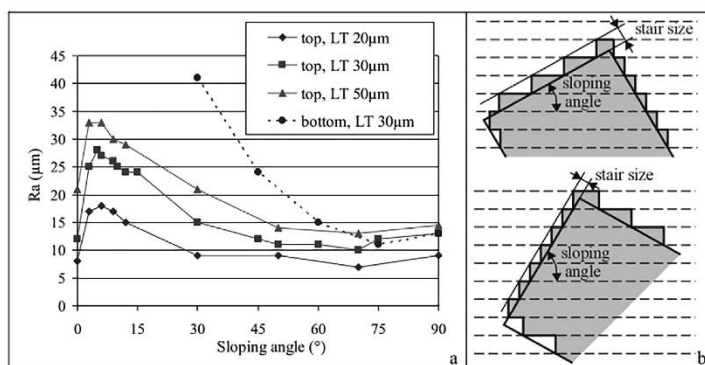
Figure 6. The surface roughness of an SLM produced part can vary significantly according to the surface location when related to a) the printing direction and b) the interaction between sloping angle and layer thickness – "down-skin" surfaces, or down-facing surfaces show higher surface roughness. This is referred to as the staircase effect. Reproduced with permission[45] 2007, Elsevier

ADVANCED
SCIENCE NEWS _____
www.advancedsciencenews.com

ADVANCED
ENGINEERING
MATERIALS
www.aem-journal.com

Figure 7. Schematic of EBM machinery showing electron gun assembly, EB focusing lens, EB deflection lens, powder hoppers, powder (layer) rake, build-in-progress, and build table, with photo of representative EBM machine.
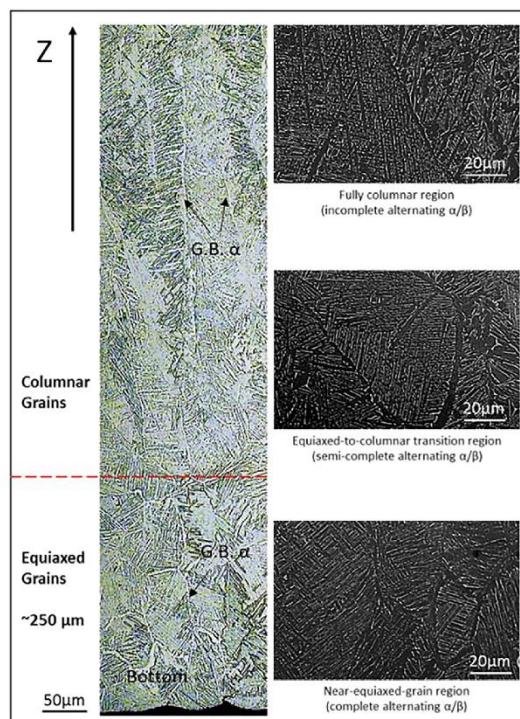
EBM Ti–6Al–4V femoral/tibial implants (compared with wrought Ti–6Al–4V implants) in a rabbit model and found between 29% and 41% BIC after 6 weeks. Further in vivo work by Palmquist et al.,[102] in a sheep model investigating the long term biocompatibility of porous femoral and dorsal EBM Ti–6Al–4V implants compared to machined compact specimens showed BIC values of 57% after 26 weeks. Puzzlingly, both compact and porous implants exhibited this level of BIC, despite the porous samples exhibiting pore sizes between 500 and 700 μm. BIC however appears to be a somewhat unreliable indicator of long term osseointegration, particularly in terms of extrapolation across models, and from animal models to human. Further work by Lv et al.[103] compared large and small pore sizes in scaffolds, and showed that the scaffold with smaller pore sizes, approximately 682 ± 27 μm, showed greater MSC viability, reduced inflammatory cytokine release and increased ALP activity. This was assumed to be due to the higher surface area allowing for increased protein adsorption, leading to increased cell proliferation and differentiation. This reinforces the high BIC observed by Palmquist et al.[102] between porous implant and the host bone. However, it is insufficient to take two studies with different cell types as incontrovertible proof for the preference of bone-forming cells for smaller pores. Different pore sizes exhibit different pore architectures, especially as perceived by cells. Thus, both pore size and roughness are somewhat simplistic variables to manipulate in order to improve cell adhesion and proliferation − issues of topography (both nano and micro) and pore interior architecture are extremely important in determining cell behavior.

More detailed work on the potential irritation caused by EBM Ti–6Al–4V parts was conducted by Haslauer et al.,[104] who cultured human adipose derived stem cells on a variety of EBM produced discs (solid polished, solid unpolished, porous) and conventionally produced discs over a period of 7 days, with a particular focus on the comparative release of pro-inflammatory cytokines. The porous EBM discs showed the highest cell viability and proliferation, as well as the lowest release of pro-inflammatory cytokines (interleukin-6 and interleukin-8). Haslauer et al. concluded that average surface roughnesses of between 30 and 40 μm (corresponding roughly to the porous and solid unpolished specimens), as tested in this study, could provide an enhanced biological response in comparison to the roughness of classical sand-blasted and acid-etched implants, of between 3 and 4 μm. Meanwhile, Koptyug et al.[35] in their in vitro examinations of MG63 cells on EBM Ti–6Al–4V samples with a surface roughness range of between 14.7 ± 4.2 μm and 22.2 ± 5.9 μm (achieved by different etching times) determined there to be no significant differences in cell spreading or ALP activity with respect to surface roughness. Conflicting reports may be attributed to the use of multiple different cell types and vastly differing time scales of analysis.

2.3. DLD

The third AM technique that shows potential for biomedical applications is DLD. It differs from EBM and SLM in that it is a blown powder technique rather than having a bed. It combines material and energy delivery through the use of gravity powder feeding, allowing the stream to meet the energy source, creating a moving melt pool.[74,105] As with SLM and EBM, the energy source is used to fuse layers together to create either full

**ADVANCED
SCIENCE NEWS**
www.advancedsciencenews.com

**ADVANCED
ENGINEERING
MATERIALS**
www.aem-journal.com

Figure 8. EBM fabrication of Ti–6Al–4V displays an equiaxed to columnar transition of β-grains through the initial 100 layers, with alternating α/β phase evolution as build height increases. Reproduced with permission,[89] 2015, Elsevier.

parts or repair existing surfaces through cladding-like techniques.[106] Another key difference of DLD is the potential for using multiple powders within the same build. This allows for the production of bespoke alloys and compositionally graded parts, along with the usual range of complex and customized parts.[107,108]

The primary components of DLD systems (**Figure 10**) include the following; a laser system, powder delivery systems (single or multiple powder hoppers), the controlled environment glove box, and the motion control system (i.e., a Computerized Numerical Control (CNC) system).[107,109,110] As with the previously discussed techniques, DLD production of parts begins with a design in STL format, which is sliced into 2D layers. This information is sent to the laser system and powder delivery nozzles, causing the assembly of each layer through the scanning of multiple tracks (in a user defined pattern). The presence of multiple powder hoppers and streams means that the composition of the deposited metal can be finely controlled;
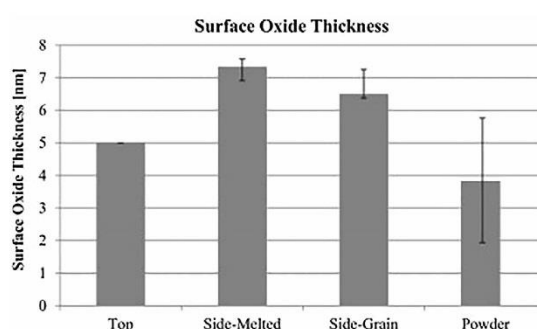
Figure 9. Surface oxide thickness relates to location (i.e., top or side) in EBM fabricated Ti–6Al–4V surfaces, and is related to variations in cooling rates. Reproduced with permission,[91] 2015, Elsevier.

**ADVANCED
SCIENCE NEWS**
www.advancedsciencenews.com

**ADVANCED
ENGINEERING
MATERIALS**
www.aem-journal.com

each hopper may be controlled individually to achieve the required composition.[111–113]

The major variables in the DLD process are; laser/substrate relative velocity or scan speed (varies between 1 and 20 mm s⁻¹), laser scanning pattern, laser power (between 100 and 5000 W), laser beam diameter (usually maintained at 1 mm), powder feed rate (1–10 g min⁻¹), powder size range (10–100 μm in diameter, spherical particles required), and inter-layer idle time.[114,115] Each of these, and combinations thereof, greatly affect the final properties of any part produced. The cooling rate/thermal gradient ratio (R), and the temperature gradient at the solid–liquid interface (G) are particularly important, as the ratio of these two parameters affects solidification and therefore microstructure,[105] as seen in **Figure 11**. Generally, equiaxed grain morphologies are produced by higher solidification rates, which are achieved by decreasing the ratio of G to R.[105] However, this is not entirely indicative of final properties, which are also highly affected by part geometry and material properties.

DLD begins with the initiation of a melt pool, which is then superheated, and solidified. This involves complex powder-specific melt pool fluid mechanics and wetting behavior, as well as inconsistent boundary and inter-layer heat transfer.[74,116] Current DLD process optimization research concentrates on the modeling of these thermal gradients and stress-forming processes as a function of the process parameters.[74,105,117] Comprehensive reviews of the possibilities and properties of DLD fabricated parts have been completed and can be read elsewhere.[115,118]

2.3.1. DLD Part Properties

Current issues with this fabrication technique can be broken down into three major categories – complex thermal history, anisotropy, and build consolidation,[119] with examples of the work done by various groups to elucidate these given in Table 2. As with the two previous processes, DLD fabrication results in parts with complex thermal histories due to the layer by layer nature of the process. As the melt pool generally penetrates multiple layers, multiple heating and cooling cycles occur, causing overlapping microstructural evolution processes and eventually non-homogeneous microstructures. Different overlapping cooling rates will form between layers, acting as another source of microstructural variation. Faster cooling causes the formation of discontinuous allotriomorphic α precipitates at existing β grain boundaries (Widmänstatten basket weave two-phase microstructures), while slower cooling rates cause the formation of continuous layers of allotriomorphic α precipitates, and coarser colony microstructures within grains.[119] Anisotropy results due to the preferential growth of columnar grains along the build direction, oriented with the 001 axis.[119,120] The width of these columnar grains are affected by scan speed (decreased width) and incident energy (increased width).[121] The size of α and β laths has been found to increase with increases in laser power, feed rate and decreases in scan speed.[121,122] Texturing arises due to continuous re-melting of β grain tips upon themselves.

Finally, DLD part consolidation is typically incomplete due to significant porosity formed during fabrication (lack of fusion and internal pores). In studies of the interplay of processing conditions on part properties, multiple groups have found that porosity decreases with increased scan speed and laser power, and a high laser power combined with a low powder flow rate is required to reduce porosity.[53,114,116,119] Post-processing is a must for any part produced by DLD, and may include annealing to alter the volume fraction, size, and aspect ratio of primary α laths, and HIPing, which closes planar pores and transforms martensite.[123]

It has been reported that as fabricated DLD Ti–6Al–4V parts display higher tensile yield stresses than cast Ti–6Al–4V but brittle failure at low strains – 0.055 in the horizontal direction and 0.012 in the vertical direction.[46] Certain groups have produced DLD Ti–6Al–4V parts exhibiting average tensile strengths from 775 to 1270 MPa, similar to or greater than wrought Ti–6Al–4V.[118,123,124] The fatigue life of Ti–6Al–4V DLD components are generally lower than those of wrought parts due to process specific porosity and distinct microstructures.

Current research into clarifying the process dependent properties of DLD is focused on the characterization of thermal gradients, localized solidification phenomena, and residual stresses, with respect to laser power and scan rate among other input parameters.[115] Very little work to date has examined the in vitro or in vivo performance of DLD produced Ti–6Al–4V parts, save for the work by Bandyopadhyay et al.[125] examining the behavior of porous implants in a rat model over 16 weeks.[125] DLD produced implants of either 25.0% or 10.7% porosity were compared to implants with 2.8% porosity. Samples with 25% porosity displayed higher intra-pore calcium ion concentrations in comparison to all other samples. This was seen to peak at 6 weeks and decrease at 16 weeks, and was postulated to be due to ongoing bone remodeling processes causing inflow/outflow of other important factors. In vitro work using human-derived bone-forming cells such as human mesenchymal stem cells or human osteoblasts remains to be completed, as well as longer term in vivo work in alternate animal models.

2.4. Comparisons and Commonalities of Major Techniques

Direct comparison of the three discussed techniques is difficult due to the range of processing conditions achievable for each. Process specific parameters such as scan rate, power supplied, and ultimate ED, as well as the interaction of these with material parameters such as powder size can lead to wildly different properties. However, some general comments can be made regarding the suitability of each technique for producing specific features.

SLM has a greater potential scan rate than comparable AM techniques such as EBM,[50] and finer control with respect to scan rate and focus. SLM can be used to create parts with tailored porosities and hierarchical structures,[71] or to deposit coatings onto ready-made parts. However, SLM has a lower energy efficiency than EBM – the laser beam can lose up to 95% of its energy due to reflection by metal particles within the build chamber.[126] Conflicting reports exist about the general surface roughness produced by EBM as opposed to SLM. The higher efficiency of EBM leads to a reduced amount of partially melted particles; however, this may depend on the build rate. In any

29

**ADVANCED
SCIENCE NEWS**
www.advancedsciencenews.com

**ADVANCED
ENGINEERING
MATERIALS**
www.aem-journal.com

case, EBM is generally reported to be the fastest technique, especially with respect to building fully dense Ti–6Al–4V parts.[85] The biocompatibility of parts produced by SLM and EBM was investigated by Wang and co-workers[127] in dog, rabbit, and guinea pig models, with cell attachment and spreading on the EBM and SLM samples shown in **Figure 12**. Multiple aspects of biocompatibility were examined, such as cytocompatibility, hemocompatibility, and dermal irritation, with no significant differences being observed between parts produced by either technique over 2 weeks.

Parts produced through EBM generally have lower tensile strength and micro-hardness as compared with SLM due to differences in cooling rates.[66] In EBM, the chamber is maintained at temperatures between 650 and 700 °C, which, along with the aid of the vacuum, causes the relative cooling rate of the molten Ti alloy to be slower — SLM is carried out just above room temperature, and so the cooling rate is much more extreme.

It is well known that Ti–6Al–4V parts produced by AM techniques such as SLM, EBM, and DLD display significantly shorter fatigue lives and fatigue strength than their wrought counterparts.[128–132] This presents a significant obstacle in the uptake of AM for use in the fabrication of orthopedic implants. This performance is particularly important given that during daily functional activities, peak bone loading occurs at relatively low frequencies (1–3 Hz), and for multiple cycles per day.[48]

Differences in fatigue behavior arise due to process specific defects, the major contributors being lack of fusion pores, general porosity and the presence of majority α phases acting as sites for crack initiation.[129] Lack of fusion pores and general porosity in AM parts arise due to incomplete particle consolidation and/or the entrapment of gases during fabrication. Defects as small as 20 µm in size can contribute to fatigue failure, and AM process related defects can range up to 200 µm in size.[128] Larger and less spherical pores are more detrimental with respect to reduced fatigue performance. The fatigue strength of AM parts is heavily affected by the presence of micro-sized pores, while the growth of fatigue cracks is affected by residual stresses.[52] Two major failure modes are observed in AM parts; surface fatigue crack initiation and internal fatigue crack initiation.[129] Surface fatigue crack initiation occurs due to porosity and lack of fusion defects while internal fatigue crack initiation begins at α grain boundaries.

More widely, EBM parts generally display lower residual stresses immediately post fabrication due to the higher temperatures maintained within the build chamber during fabrication.[129] EBM produced parts can undergo phase decomposition during cooling within the chamber, leading to the formation of bimodal microstructures with fine α and β phases[128] which generally possess longer fatigue lives than majority α phase structures. SLM parts generally display inferior fatigue performance than both EBM and LENS produced parts due to higher residual stresses.[98] Meanwhile, LENS parts have been shown to have better lower cycle fatigue performance but poorer higher cycle fatigue performance than mill annealed samples.[133] However, fatigue performance comparable with wrought and annealed Ti–6Al–4V has been achieved in AM parts, with the use of post-processing treatments such as heat and HIP treatments. Heat treatments serve to reduce the amount of residual stress within the parts, while HIPing consolidates parts and reduces the amount of internal defects. These in addition with the size reduction of α phase clusters are potent mechanisms for reducing the initiation of internal fatigue cracks.[129]

In comparison to other AM processes, DLD allows for simultaneous deposition and part forming due to the union of the material and energy source in the same region. Compared to SLM or EBM parts, DLD components display higher surface roughnesses immediately following fabrication, and require post-processing to reduce the microstructural inhomogeneities accumulated during fabrication. However, DLD has the potential to produce parts with compositional differences, due to the multi-nozzle capabilities. This is of interest for orthopedic implants, as compositions may be varied to produce functional variations across parts, corresponding to different requirements across a part, for example in fracture plates.

3. Pre-Print Considerations

3.1. Material Design

Currently, 70–80% of orthopedic implants are fabricated from Ti alloys, such as Ti–6Al–4V.[135] However, certain alloying elements have been reported to cause harmful effects when leaching out of the implant — vanadium is linked to heavy metal toxicity, while Al has been linked to the increased
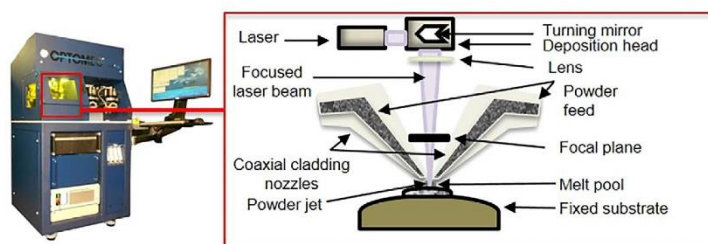
Figure 10. Schematic of DLD machinery showing powder streams converging at the point where they meet the focused laser beam, causing the formation of a melt pool on the fixed substrate, with a photo of a representative DLD machine.

30

**ADVANCED
SCIENCE NEWS**
www.advancedsciencenews.com

**ADVANCED
ENGINEERING
MATERIALS**
www.aem-journal.com
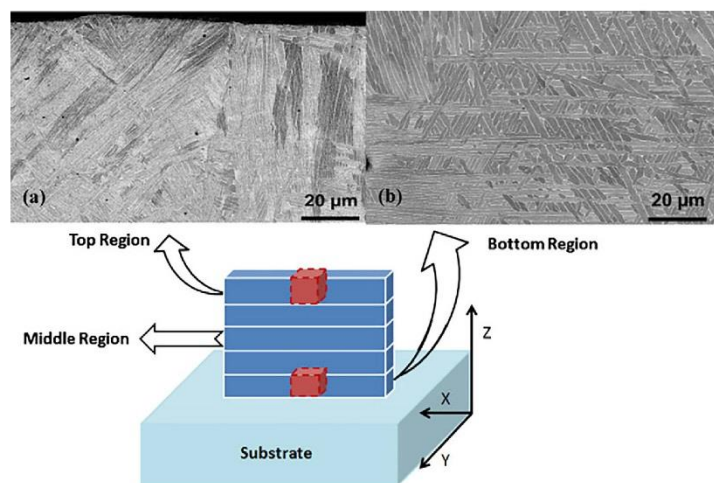
Figure 11. DLD part microstructure changes according to location within the part due to changes in thermal conductivity and repeated heating/cooling cycles, with a) showing the top region and b) showing the bottom region. While both regions display Widmänstatten structures, the top region shows colonies of fine lamellae and large laths, while the bottom region shows comparatively thicker lamellae. Reproduced with permission,[105] 2015, Elsevier.

likelihood of developing Alzheimer's disease.[136] The current focus is toward alloys with bio-active elements which have greater osteo-inductive properties, as well as mechanical properties closer to that of bone. These alloys, when used in conjunction with AM techniques, may facilitate significant improvements in initial implant fixation and bone healing. Ultimately, the role of an orthopedic implant is to work in tandem with host bone to produce a combined structure which can both withstand normal physiological loads and minimize local stress shielding. To this end, alloying elements such as Nb, Ta, Zr, and strontium (Sr) are being widely investigated. These are β stabilizing elements with low modulus, high strength, and high resistance to corrosion.[9] Additionally, Zr acts as a neutral element facilitating the formation of homogeneous solid solutions in α/β phases.[137]

Low modulus β phase Ti alloys are being developed worldwide.[138–141] The β phase of Ti has a body centered cubic structure with high symmetry (as compared to the hexagonal close packing of α Ti) – this is responsible for the reduced modulus and increased wear resistance in comparison to α-rich titanium alloys.[142,143] Investigations have been conducted into the effects of differing ratios of β-stabilizing alloying elements such as Nb, Zr, and Ta through AM fabrication[19,144] However, there is controversy over the ideal alloy composition – the amount of each element must be balanced to ensure that the AM fabrication is possible, while minimizing costs and improving performance beyond that of conventional alloy compositions and/or conventionally fabricated parts.

The current focus is toward Ti–Nb–Zr–Ta and Ti–Nb–Ta–Zr compositions, with Ti–35Nb–7Zr–5Ta and Ti–29Nb–13Ta–4.6Zr showing the most promise, with modulus values of ≈55 GPa (20% lower than comparable alloys).[22] These alloys have moduli in the range of 40–80 GPa, which, when compared with the
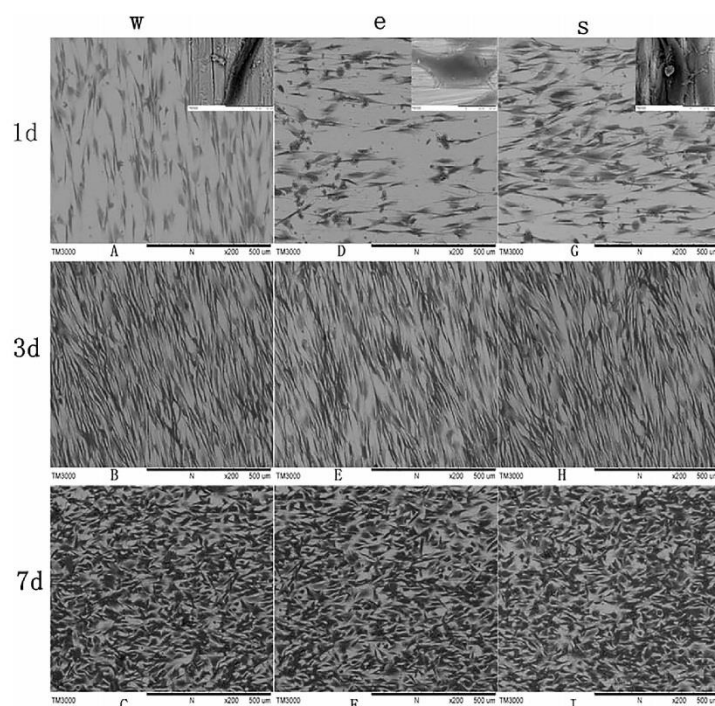
modulus range of cortical bone of 10–30 GPa, presents a significant improvement in modulus matching.[3,19,135,144,145]

While these alternate alloys have significant potential benefits, it must also be noted that their use in AM processes is currently limited due to issues with powder formation. The majority of currently available pre-alloyed powders are of structural steels and alloys with long research histories. DLD is therefore the leading technique in the investigation of new generation β phase Ti-based alloys. DLD allows for the in situ formation of multiple alloy blends through changing the powder feed rates from various hoppers containing Nb, Zr, Ta, and similar powder feedstocks. Banerjee et al. have pioneered the use of combinatorial approaches to the development of β phase Ti alloys for orthopedic implants through the use of DLD.[110]

3.2. Raw Materials

The single most important aspect of AM, particularly powder bed fusion methods such as SLM and EBM is powder morphology and size. Successful powder bed fusion requires high flowability powders composed of regular, spherical particles within a tight size range.[60,146] SLM requires particles in the diameter size range of 10–45 μm, while EBM requires slightly coarser particles in the size range of 45–105 μm.

Powder flowability is a result of the following powder properties; density, compressibility, cohesive strength, electrostatic forces, surface tension, and space filling characteristics.[44] Powders with excessively fine particle size distributions will experience high rates of electrostatic repulsion.[60] This will adversely affect flowability, as the static forces will cause rolling and recoating to occur unevenly. However, a larger average

**ADVANCED
SCIENCE NEWS**
www.advancedsciencenews.com

**ADVANCED
ENGINEERING
MATERIALS**
www.aem-journal.com

Figure 12. Mesenchymal stem cell seeding on wrought (w), EBM (e) and SLM (s) Ti–6Al–4V samples showing that cell attachment and spreading at all time points was comparable on the EBM and SLM surfaces to the wrought Ti–6Al–4V surfaces (indicating good biocompatibility). Reproduced with permission,[134] 2016, PLoS ONE.

particle size reduces the driving force for sintering.[27] It is therefore important that the particle size distribution of the powder remains within a tight threshold. Particle shape is also important, as it relates to the efficacy of particle packing. This affects the efficiency of layer forming and therefore final part properties. Flowability is linked to shape factor, that is, the shape of the particles independent of dimensions – here, the most important shape factor is sphericity.
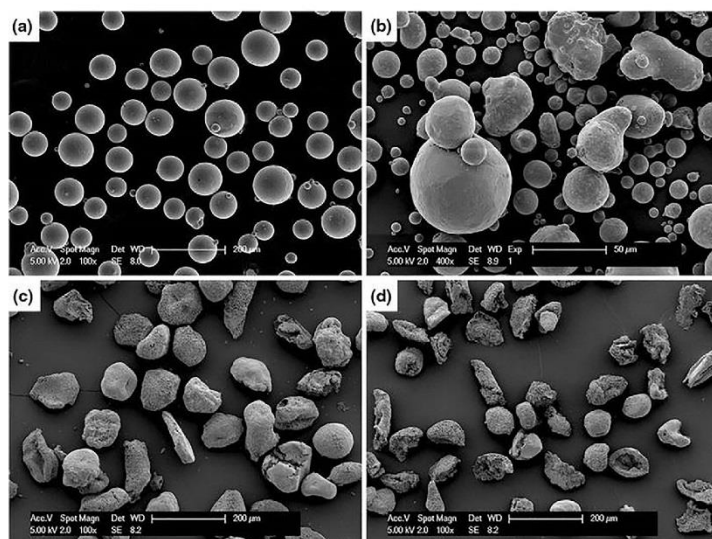
It is important to note that the size and shape of the powders used are contingent on the methods used to manufacturing. The major powder forming methods are gas atomization (GA), plasma atomization (PA), and the plasma rotating electrode process (PREP), as well as induction plasma melting. GA has been reported to produce particles with a larger mean size, while PREP produces more spherical particles.[53,147–149] Another method for forming powders with spherical morphologies is the induction plasma melting method. Smaller relative powder sizes generally lead to better surface resolution and appearance.[32] A visual comparison between fabrication types and the powder morphologies before and after printing is seen in **Figure 13**.

Though size and shape are important, the characteristics of the specific AM process must also be considered. SLM produced parts have better qualities when produced with a unimodal fine particle size distribution, while EBM produced parts have better qualities when the initial powder has a bimodal size distribution.[44] This allows better packing through improved layer filling and densification.

Notably, powders used during fabrication of parts using powder bed fusion methods may be recovered and reused. However, the characteristics of these recovered powders are often quite different to their initial properties. Powder recovery usually occurs through high pressure air blasting, vibratory processing, or a combination thereof.[44] The work of Tang et al.[150] revealed that the more times Ti–6Al–4V is used in EBM, several important properties change; average particle size decreases,and particle size distribution becomes narrower resulting in improved flowability, oxygen content increases due to air exposure and humidity (however this does not occur in the presence of helium), Al and V content decrease slightly due to vaporization in vacuum, and particle sphericity decreases. Additionally, the amount of satellite particles and agglomerates decrease due to repeated sieving between fabrication cycles. Therefore Tang et al.[150] recommend not to re-use powders more than 4 times without the addition of virgin powder, and powders should not be reused more than 16 times due to the significant amount of particle distortion and surface roughness. This detail, that is, the number of times the powder has been recovered prior to sample fabrication, is rarely reported in articles examining metallic AM processes. Going forward this is an important parameter to consider and report, especially given the effect of powder morphology on part microstructure and properties.
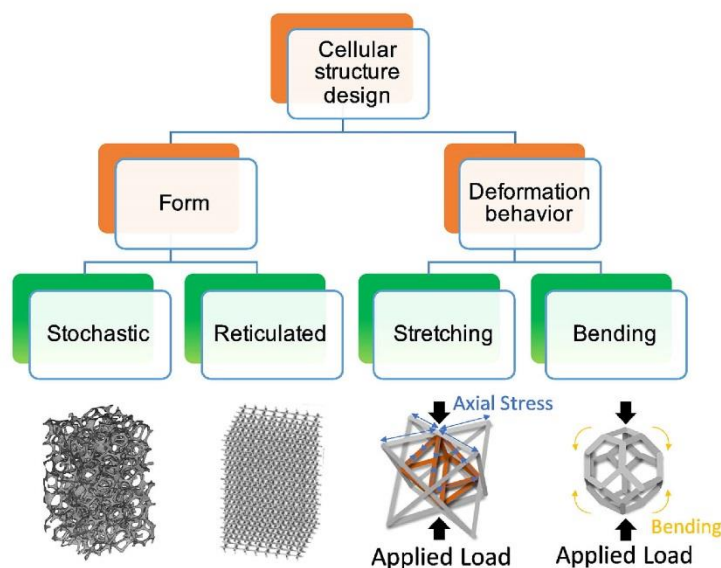
**ADVANCED
SCIENCE NEWS** _____
www.advancedsciencenews.com

**ADVANCED
ENGINEERING
MATERIALS**
www.aem-journal.com

Figure 13. SEM images of a) virgin, b) used Arcam Ti–6Al–4V 45–106 μm powder (undocumented but <30 times), c) 75–106 μm, and d) 45–75 μm as-received novel Ti precursor. Different processing and preparation techniques are thus shown to produce vastly different qualities of powder, and thus the choice of feedstock for powder-based AM techniques is of extreme importance. Reproduced with permission,[148] 2015, The Minerals, Metals and Materials Society.

3.3. Part Design and Support Structures

Part design for Ti-based orthopedic implants can be roughly split into two categories – dense implants with surface features, and cellular scaffolds or solids (open forms, unit cells, functionally graded structures).[85] Surface features such as additional holes for bone screws or the addition of small surface bumps can easily be added into CAD files through programs such as Solidworks (Dassault Systemes), Mimics (Materialise) and Rhino (Robert McNeel & Associates), or freely available and online programs such as those available from Autodesk or Sketchup (Trimble Incorporated).[42,43] Cellular scaffolds with interconnected pores (**Figure 14**) offer a range of benefits in comparison to traditional dense structures, the most important of which are; the potential to reduce stress shielding through closer property matching to bone, and the facilitation of bone cell ingrowth.[85,151] Pore shape, amount, and porosity gradients can be altered in the design stage to produce parts with specific stiffnesses and strengths (as porosity increases, stiffness, and strength generally decrease).[85] The minimum pore size for cellular scaffolds which can allow bone in-growth has been stated as 50 μm, however in terms of practical application, pore sizes of 300 μm are recommended – this ensures that cell proliferation and penetration can continue (no one pore should be occluded by a cell), and also ensures permeability and flow of nutrients/wastes.[85,152,153] Larger pore sizes are also more conducive to 3D printing processes, particularly in the depowdering stage. Graded scaffold structures are the most promising designs in terms of improving osseointegration, as these have the potential to closely mimic the complex structures found in bone.[81] The literature contains a wealth of studies examining novel hip and knee designs with superior osseointegrative abilities. Notably Melancon et al.[154] present morphological and mechanical property maps for SLM Ti–6Al–4V, emphasizing the ability to tune stiffness to native bone while accommodating for manufacturing discrepancies. Arabnejad et al.[155] present a high strength, porous implant model with a 75% reduction in modulus mismatch in comparison to solid models. The testing, success and uptake of these various alternative implant designs depends on first achieving a complete understanding of the characteristics of each AM process, and the properties of parts produced by each process.

The practical capabilities of EBM and SLM are informed by the complexity of the design. Any surface at a <45° to the previous layer will require a support structure.[156,157] These structures act as anchors to the build plate, prevent part warpage due to residual stresses, and aid in heat conduction away from the part. As mentioned previously, software such as Magics (Materialise) or Simplify3D (Simplify3D) may be used to automate or customize the design of support structures such that they are easily removed from the final part, however, the surface to which the supports were attached will generally show higher surface roughness than the rest of the part, in the micrometer range.[158–160] Support structures are typically built to resemble trusses, but can take many other forms, for example blocks, points, or lines (**Figure 15**).[157,158] The incorporation of teeth into the part of the support contacting the part can aid in removal – the spacing between teeth, the height of the teeth, and tooth contact area can all be altered according to the specific requirements. However, often even the presence of support structures may be insufficient to prevent warping or to prevent the part from peeling off the plate due to excessively high

33

**ADVANCED
SCIENCE NEWS**
www.advancedsciencenews.com

**ADVANCED
ENGINEERING
MATERIALS**
www.aem-journal.com

Figure 14. Map of possible cellular scaffold types in terms of form and deformation behavior. Reproduced with permission,[85] 2017, Elsevier.

residual stresses, particularly in Ti-based alloys. In such extreme cases, a part redesign may be necessary. Other strategies to reduce the amount of support structures required include rotating the build orientation, as well as using algorithmic methods in the design phase. Various researchers have proposed algorithms for optimizing the amount and location of support structures, for example the methods suggested by Frank[161] and more recently Strano,[159] however the use of Taguchi methods show the most promise.[156] There is currently a gap in the literature regarding the proper design and application of support structures specifically for Ti-based orthopedic implants with respect to the extremely high amounts of residual stresses formed. Going forward, this will be extremely important in the manufacture of delicate parts such as customized fracture plates and screws.

4. Post-Processing Considerations

4.1. Heat Treatments

SLM and EBM parts are both notable for the formation of non-equilibrium phases due to the rapid heating/cooling cycles produced during fabrication. This causes a build-up of thermal stresses and segregation phenomena. Heat treatments may be applied to partially alleviate the presence of these stresses.[162] Vrancken et al. studied the effects of heat treatments on SLM produced Ti–6Al–4V parts, and reported the conversion of α' phase to a lamellar mixture of α and β phases.[110] The samples were heated to above 995 °C, where large β grains formed. These decomposed into lamellar α and β phases on cooling. A post-treatment at 850 °C for 2 hours followed by furnace cooling increased ductility to ≈12% compared to 7%.[162] Transformation
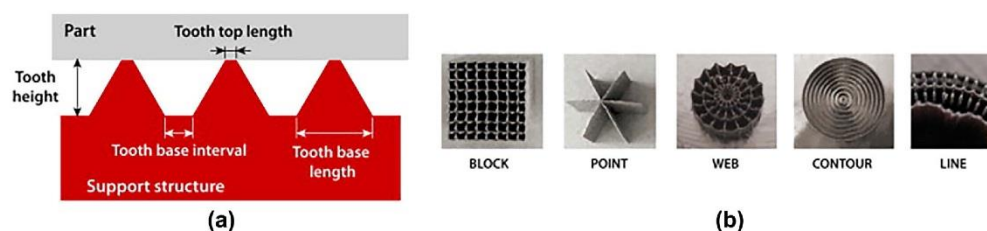
from columnar to spherical β grains has also been observed through the application of heat treatments above 1000 °C.[163] The presence of β grains has been observed at treatment temperatures as low as 700 °C, however, overall martensitic morphology appears to be dominant until larger α plates form at higher temperatures.[75] An instructive comparison between the various microstructures produced by heat treatments can be seen in **Figure 16**.

4.2. Surface Patterning

The ultimate goal for the surface modification of permanent Ti implant surfaces (i.e., those required to osseointegrate) is to improve osteoblast adhesion and differentiation, leading to increased bone deposition. *In vivo*, osteoblasts work within nano-scale topographies, with collagen fibrils and HA having lengths of 50 to 300 nm and widths of ≈0.5 nm respectively.[15] Thus, osseointegration is known to be affected by surface roughness and porosity,[15] although little agreement exists in the literature on the specifics, be it the 'optimum' pore size range, porosity percentage, or the average roughness.

Osteoblast or osteoblast-like cells grown on roughened Ti surfaces (ideal pore sizes of between 100 and 500 μm, with ideal porosity of ≈60%) have been shown by some groups to present reduced proliferation, enhanced differentiation and the up-regulation of genes related to bone deposition.[15,164,165] Conversely, other groups indicate that osteoblast proliferation is improved on smooth surfaces with Ra values of less than 0.5 μm.[166–168] Numerous mechanisms are thought to be in play, with surface roughness dictating protein absorption and subsequent intracellular signaling cascades, particularly those related to integrins and fibronectin.[169] Higher pore volume has

34

**ADVANCED
SCIENCE NEWS** _____

www.advancedsciencenews.com

**ADVANCED
ENGINEERING
MATERIALS**

www.aem-journal.com

Figure 15. Examples of different types of support structures used for SLM and EBM parts with a) showing tooth characteristics and b) showing alternative support structure designs. Reproduced with permission,[155] 2014, Elsevier.

been shown to be roughly correlated with higher Ca+ concentration within pores,[125] facilitating osteoblast adhesion and osteogenic cell ingrowth. Further into the osseointegration process, micro-rough surfaces have been shown to reduce osteoclast activity, thereby decreasing the resorption of bone. Thus, the role of roughness in osseointegration can be thought of as important to the remodeling process, or rather the balance of activity between bone forming and bone resorbing cells, with surface roughness affecting multiple processes at different time scales.

Current methods used for surface texturing of Ti-based implants can generate features on the micrometric or nano scales, through physical, chemical, electrochemical deposition and biochemical methods,[170] however a major consideration in the application of surface texturing is the effect on the fatigue and other mechanical properties of the part. Line of sight methods such as plasma spray coating are falling out of favor due to their inability to treat complex geometries. Biomimetic methods such as anodization and acid etching are most commonly used to roughen AM produced Ti–6Al–4V implant surfaces.[171]

4.3. Coatings

4.3.1. Calcium Phosphate-Based Coatings

Coatings are also of great use in facilitating osteoblast interactions with (cement-less) implant surfaces, and are an important post-processing modification to consider in the development of AM implants. Calcium phosphate or hydroxy-apatite (HA) containing coatings have long been shown to improve future bone deposition and osseointegration through ion-exchange facilitated protein deposition.[172,173] Multiple methods for hydroxyapatite coating deposition have been investigated including plasma spraying and chemical vapor deposition, and newer biomimetic solution-based precipitation methods. As far back as 1993, Søballe et al.[174] were able to show that plasma sprayed hydroxyapatite coatings on Ti-based implants improved bone ingrowth into implant surfaces, even in cases of osteopenic host bone stock (shown in a canine model). Eckardt et al.[175] were also able to show an improvement in bone contact (65% HA-coated implant vs. 14.7% uncoated implant) with the use of HA-coatings on implants in dog models, over a longer observation period of 2 years. The application of these coatings to AM implants is a potent strategy for improving fixation.

4.3.2. Refractory Ion Containing Coatings

Coatings containing bio-active molecules or elements can also be used to act as stimulation for bone forming processes. Chief among the bio-active elements currently under investigation for their abilities to improve bone bonding are the refractory elements Ta, Nb, Zr, and Sr.

Tantalum bonds well to bone and forms an apatite-like layer in simulated bodily fluid, and is noted for having high fatigue and corrosion resistance.[176,177] The 3D geometry of porous Ta is similar to that of trabecular bone.[178] It also has a high surface energy and wettability, increasing the likelihood of effective cell attachment and distribution.[179] Numerous studies have shown increased bone-forming behavior on Ta containing surfaces as
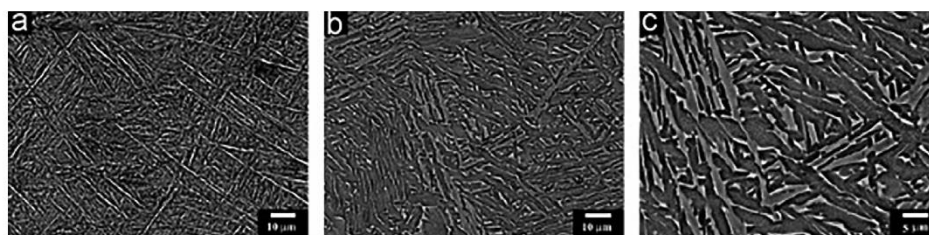
Figure 16. Microstructural changes can be observed according to the different post-processing heat treatment conditions of SLM Ti–6Al–4V, a) shows an SLM sample annealed at 600 °C, b) shows an SLM sample annealed at 700 °C, with α plate formation, and c) shows a HIPed SLM sample. Reproduced with permission,[75] 2013, Elsevier.

35

**ADVANCED
SCIENCE NEWS**
www.advancedsciencenews.com

**ADVANCED
ENGINEERING
MATERIALS**
www.aem-journal.com

opposed to plain Ti surfaces.[178–181] Balla et al. demonstrated the use of DLD to deposit a Ta coating on Ti, with significantly higher cell density on Ta coated Ti at all time points. After 14 days of culture, a sixfold increase was observed on Ta coated Ti as opposed to uncoated Ti, accompanied by increased filipodial extension by cells.[179] Tantalum however has a high cost of manufacture, making it suitable only as a minor alloying element. It has a low laser absorption coefficient due to low electrical resistivity. This has a large effect in SLM, where the shallow thermal gradient within layers will affect the melt pool characteristics and therefore the microstructure of the part.

Niobium has also has seen use in bioactive coatings and alloys.[8,71,135,182] Elemental Nb also displays good wear resistance and biocompatibility. The presence of Nb has been seen to improve cell attachment and growth, and has a beneficial effect on cell morphology, with adhering cells displaying multiple extensions and spreading.[71] Zhang et al.[71] fabricated porous Nb coating on Ti substrates using SLM. This coating, composed of Nb_2O_5 and NbO_2, displayed a pore size of 15–50 μm, with an average hardness of ≈392 HV. This relatively short-term study showed that Nb coated Ti showed significantly higher numbers of cells after 11 days, indicating a potential enhancement of proliferation. Zhang et al. also noted the lower melting temperature of Nb as opposed to Ta (2468 °C vs. 3017 °C). However, it is also quite expensive and has a low laser absorption coefficient. It has not either, to date, seen wide uptake in coating applications, being used more frequently as an alloying element.

Perhaps the most promising element for use in orthopedic implants is Sr. The presence of Sr ions as substitutions in HA layers has been shown to enhance bone formation and inhibit bone resorption.[15] Sr is an alkaline earth metal with properties like that of calcium. For this reason, it functions similarly to Ca in the body. Strontium acts on bone cells to control bone resorption and regulate genes involved in osteoblastic cell replication, differentiation, and survival. More specifically, it inhibits osteoclasts and therefore bone resorption, and improves the differentiation and activity of osteoblasts.[183–189] Li et al.[190] investigated the effects of 10% Sr substituted HA coatings on implant fixation in a rat model, and found that after 12 weeks, bone to implant contact increased by 49.9% as compared to implants coated with non-substituted HA. Subsequently Yang et al. investigated the effect on bone marrow mesenchymal stem cell osteogenesis of coating Ti with Sr substituted nano-hydroxyapatite deposited via electrochemical techniques. Sr substitution significantly enhanced ALP activity in bone marrow stromal cells (BMSCs) in comparison to non-substituted HA coatings.[191]

4.4. Surface Finishing and Sterilization

All AM processes produce parts with relatively high surface roughnesses (>Ra 15 μm), which relates to the presence of semi-melted particles left on outer surfaces following fabrication. As discussed previously, these areas experience different cooling rates due to heat transfer from the melted part directly to the powder bed, and do not undergo re-melting cycles from subsequent layer laser penetration. This roughness has important consequences with respect to both material performance

and biological responses (e.g., inflammation, osseointegration), and combined with the high notch sensitivity of Ti–6Al–4V mean that as-fabricated AM parts will generally exhibit shorter fatigue lives. Without surface finishing, semi-melted particles on AM Ti–6Al–4V surfaces have the potential to detach following implantation, and cause localized osteolysis.[192] Semi-melted particles have been shown to affect cell migration and reduce the effective surface area for integration.[192,193] However, there is little data in the literature at present to quantify this with regards to specific processes and parameters used. Of the few studies currently published, Vaithilingam et al and Matsoukova et al performed in vitro studies to investigate the potential cytotoxicity of particles detaching from the surface of AM Ti–6Al–4V implants and found no evidence of particles detaching even without post-processing.[192,194]

In any case, the surface finish of AM parts is of paramount importance in post-implantation osseointegration. Common methods for improving the surface finish of AM parts include mechanical blasting, chemical etching, laser ablation, micro-machining, vibratory grinding, and polishing.[195] These processes are generally line-of-sight dependent, and so difficulties arise in the appropriate finishing of intricate internal structures such as pores and lattices. Relatively few studies have compared processes but initial evidence suggests that sand blasting and electropolishing are inappropriate as the finishing media can be difficult to remove. Specifically, sand blasted parts display surfaces with impregnated blast media in the form of AlO_x elements – Al ions in the outer oxide layer of Ti–6Al–4V have been shown to reduce the oxide stability and increase the likelihood of Al ion dissolution.[192,193] Electropolishing and chemical etching can lead to the formation of micropits, increasing oxygen infiltration, as well as destabilize the native oxide layer, reducing corrosion resistance.[192,196] Conversely, Longhitano et al investigated the combination of various finishing processes on SLM Ti–6Al–4V, and found that blasting followed by chemical etching produced parts with and R_a of approximately 4 μm – this can be explained by the stepwise action of blasting removing material from the surface, and subsequent etching removing blast media from the surface.

Surface finishing techniques such as laser ablation and milling show more promise. Mohammad et al.[197] investigated the use of laser ablation in reducing the surface roughness of EBM Ti–6Al–4V and were able to achieve a surface finish of 13 μm (R_a) with a laser fluence of 150 J cm^{-2}. Bagehorn et al.,[130] compared various finishing techniques on SLM Ti–6Al–4V and found milling to produce the smoothest surface compared to blasting, vibratory grinding and micro-machining. Additionally, milling improved the fatigue performance of the SLM Ti–6Al–4V to replicate that of forged Ti–6Al–4V.

It is important to note that surface finishing processes are "line of sight" limited, and so intricate internal structures like pores or lattices are difficult to finish, much less inspect. In the same manner as finishing processes are "line of sight" limited, so too are sterilization methods. Commonly used sterilization processes for orthopedic implants, including AM, extend to ethylene oxide gas sterilization (exposure to ethylene oxide under vacuum), steam sterilization (exposure to high temperature steam) and γ radiation. Of these, γ radiation is the most favorable, as it has the potential to sterilize both intricate internal

36

structures, internal voids (defects), and complex geometries without leaving behind sterilization products.[198] To our knowledge, no studies have examined the effects of sterilization on the mechanical properties of AM parts, and this remains a significant gap in the literature.

At present, the assessment of the efficacy of finishing and sterilization processes occurs on a case by case basis. As the technology develops, so too do regulatory concerns and guidelines, and at present the Food and Drug Administration of the United States of America requires premarket submissions for medical devices in 3D printing to provide validation of any cleaning and sterilization process used.[199] The relevant regulations and guidelines are discussed further in Section 6.

5. Case Studies

6. A Clinical Perspective

The bulk of research into the properties of AM fabricated Ti-based parts has been from a metallurgical or biological perspective, using part geometries far removed from actual implant designs. With this research in its infancy, relatively little long-term clinical data is available, and so actual bench-to-bedside feasibility is poorly understood. With the advent of AM, and the increasing practicalities of producing tailored structures, it is important to consider how this new technique will be received by clinicians and their patients, particularly with regards to such aspects as financial viability and quality control/regulation. From the perspective of an orthopedic clinician, AM technologies offer three major advantages in comparison to conventional manufacturing; the ability to create Patient Specific Implants (PSIs) by combining 3D Digital Imaging and Communications in Medicine (DICOMs) with standard implant designs, utilize these in surgical planning, and to produce aids for surgical education.[42,45,60,204–206]

PSIs in orthopedics have historically been created only for patients with rare diseases or complex reconstructive needs, that is, approximately 1% of all implanted devices.[39] However, computational power and technology has improved significantly in the past 10 years, allowing more widespread uptake of AM for PSIs, particularly for patients with bone deficits as follows[207,208];

1) Trauma in the form of extreme fractures arising from long term osteoporosis – implants can be designed to include "fixation features" such as extra holes for bone screws.
2) Bone cancers, which accounted for 0.2% of new cancers in the U.S. in 2014, 26.9% of which arose in patients younger than 20 years old – standard designs can be adapted to both include "fixation features," as above, or to compensate for areas of bone loss local to the implant.
3) Congenital or developmental deformities such as spondyloses or scoliosis – implants can be made with reference to DICOMS to directly complement the non-standard structure of the patients' bone in establishing optimal performance.
4) Osteoarthritis and other degenerative joint diseases which are expected to affect 25% of adults in the U.S. by 2030– custom shaping allows for optimized bone preservation.

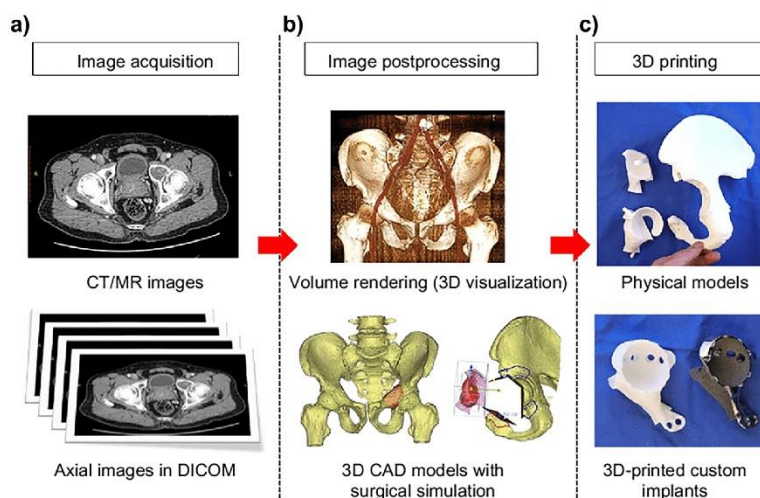**Table 2.** Selected AM processing parameters and properties of Ti–6Al–4V parts.

Process	Particle size [μm]	Layer thickness [μm]	Scan rate [mm s⁻¹]	Laser power [W]	Spot size [μm]	Hatch spacing [μm]	Young's modulus [GPa]	Yield strength [MPa]	Ultimate tensile strength [MPa]	Elongation [%]	Vickers hardness	Density/porosity	Surface roughness	Other	Ref.
SLM	15–70 (PA¹)	50	225	157	70	100	xz: 115 ⊥ 6 zx: 119 ⊥ 7 xy: 113 ±5	xz: 978 ⊥ 5 zx: 967 ⊥ 10 xy: 1075 ± 25	xz: 1143 6 zx: 2228 3 xy: 1199 ± 49	xz: 118 ⊥ 0.5 zx: 8.9 ⊥ 0.4 xy: 7.6 ± 0.5	–	–	upskin – 6.834 sideskin – 28.587 (Ra in μm)		[199]
	15–75 (PA³)	50	58	42	30	30	119 ±7	–	–	–	500	99.4 ±0.2%	–		[200]
	5–50 (PA¹)	30	1600	250	52	60	109 ±7	967 ± 10	1117 ±3	8.9 ±0.4	–	–	–		[161]
	30 (GA²)	50	200	200	130	50	–	910 = 9.9	1035 ±29.0	3.3 ±0.76	–	–	–		[98]
	15–25 (CA³)	30	686	175	–	12	–	1100	–	–	–	–	–		[201]
		60	710	375		18									
		90	102												
	20–50 (GA²)	20	800–1500	150–200	150	75	–	>1 (0.2% proof stress)	1200	<10	–	0.1%	–		[51]
	43 (GA²)	30	710	175	–	150	–	–	–	–	–	–	–	Mean fatigue life of 27 000 cycles	[52]
	40	30	450	100	–	–	–	1008 ±30	1080 ±30	1.6 ±2%	–	–	–	For EBM1 (top	
EBM	30 (GA²)	build						1150 1100	1200 1150 1230	25% 16%	3.6 3.8 3.6 4.1	–	–		

(Continued)

Table 2. (Continued)

Process	Particle size [μm]	Layer thickness [μm]	Scan rate [mm s⁻¹]	Laser power [W]	Spot size [μm]	Hatch spacing [μm]	Young's modulus [GPa]	Yield strength [MPa]	Ultimate tensile strength [MPa]	Elongation [%]	Vickers hardness	Density/porosity	Surface roughness	Other	Ref.
	d45–100 (GA²)	parameters absent		60 kV	Arcam standard	Arcam standard	180 + 15	1170		12%	380			end) For EBM2 (top end) For wrought Ti64	[36]
		70	Arcam standard		Arcam standard						425 + 50				
	45–100 (GA²)	100	Energy input per unit				Parallel loading = 12.9 ± 0.9 perpendicular loading = 3.9 ± 2.1 complete infiltration of Osseous tissue	Parallel				Mean pore size = 0.45 mm porosity = 61.3%		Designed porosity	[66]
	45–105	50	Arcam standard	Arcam standard	Arcam standard	Arcam standard		Top	Top	Top	Top	–	–		[89]
	45–105	50						10 mm 1; 851.8 ± 5.8; 10 mm 2; 836.6 ± 8.7; 10 mm 3; 827.9 ± 0.9; 10 mm 4; 823.4 ± 0.1	10 mm 1; 964.5 ± 0.3; 10 mm 2; 953.7 ± 4.3; 10 mm 3; 944.5 ± 5.8; 10 mm 4; 940.5 ± 6.5	10 mm 1; 16.3 ± 0.8; 10 mm 2; 15.2 ± 1.2; 10 mm 3; 14.0 ± 0.5; 10 mm 4; 13.2 ± 0.7					
DLD	50–150	–	22.5 mm s⁻¹	200 W	–	–						30%			[108]
	150 mesh	–	635 mm min⁻¹	350 W	–	Hatch distance of 0.38 mm, with layer spacing of 0.25 mm								Single β phase formed, average grain size of 50 μm	[202]
	45	30	1250	170	100	–	–	1185	1293	6.23	402.81 ± 11.31	–	35 ± 5	–	[119]
	15–45	50	EOS default	EOS default	100	–	114.9	1093	1130	–	–	95–99% dense	11–13	–	[46]
	(GA²)	30	0.6 m min⁻¹, powder feed	330	–	50	–	1005	1073	4	–	–	–		[133]
	89 (PREP³)		10.6	2 kW	–	–	111 ± 3	938 ± 22	1048 ± 23	23 ± 3					

¹⁾Plasma atomized particles; ²⁾Gas atomized particles; ³⁾Plasma rotating electrode process used to prepare particles.

**ADVANCED
SCIENCE NEWS**
www.advancedsciencenews.com

**ADVANCED
ENGINEERING
MATERIALS**
www.aem-journal.com

Figure 17. Schematic showing the sequential process of custom implant design and printing showing a) image acquisition, b) image post-processing and CAD modeling, and c) 3D printing of models and custom implants. Reproduced with permission[213] 2016, Dove Press.

5) Bone infection or decay, for example, through osteomyelitis or dental caries — DICOMS and "fixation features" can be combined to produce implants that support natural function.

Atypical bone anatomy, poor bone stock, and extreme iatrogenic bone loss are cases where AM can provide great value. Many patients requiring orthopedic implants will present with poor bone stock due to conditions such as osteoporosis, as well as long term steroid treatment.[174] These patients will have significantly lower bone turnover and remodeling activity, and thus there is a significant need in this sector for "smarter" implant behavior.[2] These pre-existing conditions contraindicate the use of standard implants, as these are likely to both fit poorly and create additional problems in the months and years following implantation due to poor fixation (loosening, wear debris formation).[10,169,209]

In this regard, AM has the potential to improve on classical orthopedic implant designs, which have to date been limited by conventional manufacturing techniques. Direct patient data (DICOMs) can be used to make exact copies of removed bone sections or to guide the design process in terms of inserting additional features likely to improve fixation.[210] Potential features to reduce stress shielding include; unique internal structures, latticing to maintain strength but not stiffness, surface texture, and graded porosity.[211] The design of reservoirs with pharmaceutical payloads (slow or fast release therapeutics, for example, chemotherapeutic agents, bone growth promoters or antibiotics) is a popular new area.[207,212] Thirdly, AM fabrication lends itself well to producing low volumes of highly complex parts — this means that pediatric implants can be sized specifically and iteratively for growing pre-pubescent patients, and take into account the complexities of young and incompletely ossified bone structures.[213] However, it must also be noted that there will be a compromise between added design complexity and AM fabrication feasibility — for example,

pore diameters must exceed a critical threshold to allow for the full removal of residual particles present during the build process. Furthermore, a more complete understanding of the differences between conventional and AM fabrication in terms of safety is required before many of these advances can be widely applied in the clinic.

On the other side of the operating table, AM proves invaluable for surgical planning. Surgeons plan for implantation by using multiple sources of 2D patient data (e.g., X-rays and CT images), and compile them to create a surgery strategy.[214] With the advent of AM, exact replicas of custom implants can be made (in medical grade polymers if not metals) and used to optimize the surgical planning process by providing a visual and tactile aid,[205,206] as seen in **Figure 17**, or even used as a reference to guide the clinician during surgery. This is particularly useful in cases where fracture patterns are complex, or where intra-operation difficulties are expected. Further to this, patient specific instrumentation, for example, small jigs with holes to guide surgical equipment during sectioning or screw insertion (osteotomy guides), can be made using the same process.[205,206] Despite the invaluable assistance provided by these aids, uptake will be significantly affected by cost. For example, in Australia, while AM surgery guides are widely used, the patient must pay the entire amount of up to AUD$2000, without any rebates from Medicare (publicly funded health care in Australia).[205] Whether the significant costs incurred by relatively small populations of vulnerable patients for complicated surgeries, custom implants, and patient specific instrumentation will be accounted for in health care systems is as yet uncertain.

While the uptake of AM in medicine has been growing exponentially, particularly for vulnerable patients, certain questions and confusions persist regarding the regulation, quality assurance, and intellectual property of customized AM implants. Medical devices in the U.S.A. are classified by the Food and Drug Administration (FDA) based on the risk of the device

39

**ADVANCED
SCIENCE NEWS**
www.advancedsciencenews.com

**ADVANCED
ENGINEERING
MATERIALS**
www.aem-journal.com

and/or the levels of control necessary to ensure safety and efficacy; Class I (exempt), Class II (pre-market notification, 510 k pathway), or Class III (high risk, premarket approval pathway).[210,215] Most orthopedic implants belong to Class III, indicating that these devices may be used in FDA-regulated clinical trials to collect safety and efficacy data prior to receiving approval to market.[215,216] AM techniques pose an interesting dilemma in terms of safety and liability, being that the fabrication technique is the only point of departure from approved devices, many AM implants are treated similarly to conventionally manufactured implants and require only the application for and reception of patents with finite duration (as well as patient waivers).[217] This simplistic consideration ignores some of the more pressing issues with AM, particularly in terms of the quality of the customized design, the effects of the build process on part properties and inter-machine variability, even discounting issues that could arise with design features that may impact safety and efficacy. Many simple AM medical devices have reached the American market through the class II pathway, which allows limited use of the device but no commercial marketing without subsequent rigorous testing, and limited numbers have been approved for emergency use.[211,217] However, data on wide-scale testing and comparisons between the properties of conventionally manufactured implants and AM equivalents is not yet available. Long-term data is required to give clinicians and patients a good basis for determining whether AM is likely to provide any benefits over conventional implants with regards to improved functionality and service life. Beyond this, further issues arise with privacy and patents. Is the dissemination of patient-specific designs/models for surgical training or education an assault on said patient's right to privacy? Should the design produced for a specific patient be treated as the intellectual property of the patient or the designer, or even that of the machine technician? This current lack of clarity is likely to deter the involvement of manufacturing companies, and may prove a challenge too burdensome for individual hospitals.[218]

The present excitement around focus on custom implants is perhaps overly optimistic, and obscures some of the more pertinent issues regarding 3D printing. While multiple miracle cases have been reported in the media (see[219–221]), the reality of patient-specific implants is altogether murkier. At present, the literature contains less than five systematic in vivo comparisons between AM fabricated implants and conventionally fabricated implants. Apart from the significant regulatory issues discussed previously, there will likely be significant pushback from clinicians – at present, the quality of conventionally manufactured implants is near perfect, and plenty of long term data is available. No such easily comparable data is available for AM implants as yet. Little data is available on how quality is controlled, particularly outside the jurisdiction of the FDA in the U.S.A. Consequently, from a clinician's perspective, certain questions must be answered prior to wider uptake;

1) Is it worthwhile to produce implants through AM, given that very little long-term usage data exists? Is the current data indicative of actual performance based on the specifics of the surgery, or of long-term performance?
2) How will AM change the practices of individual doctors/ surgeons – will it be cheaper and/or comparable to
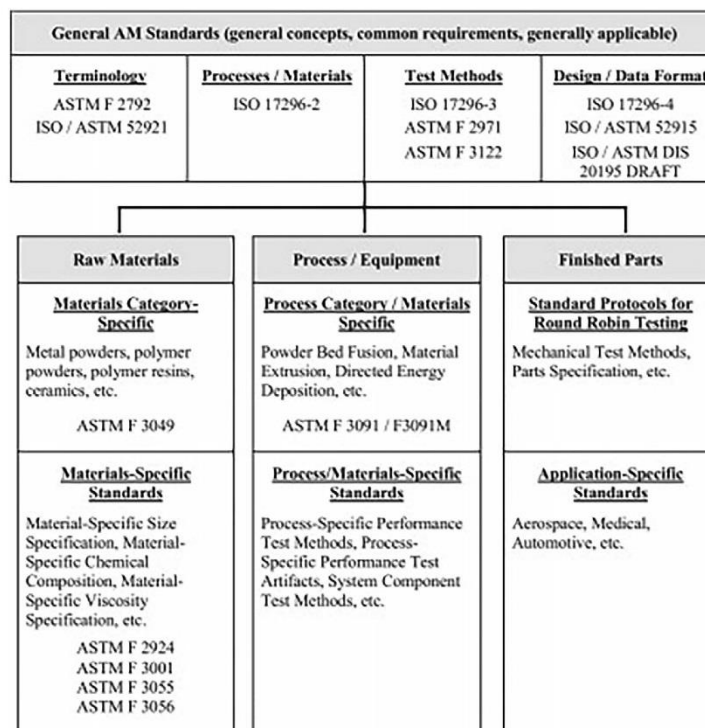
conventionally-produced implants? Is it worthwhile to try new technologies, when the risks associated with the implementation of new technologies may be significant? Will willing surgeons be matched with willing patients given that current medical insurance policies are unlikely to cover many of the significant associated costs?
3) What quality regulation and legislation is in place, or is possible? How are reproducibility, quality, and properties assured? Is the technology scalable to large numbers of patients?
4) Can AM implants provide added functionality, for example, through longer service lives, increased osteogenic activity, or contain reservoirs with controlled release biologics or therapeutics? What design features to improve implant function are being developed?
5) What breakdown products may be produced as compared to conventionally manufactured implants? How will these be excreted? Is the implant likely to cause any inflammatory reactions?
6) What are the specific properties (wear, tensile strength, corrosion resistance), and how will these change over time?
7) What sterilization methods can be used?

7. An Engineering Perspective

The International Organization for Standardization and ASTM International define additive manufacturing to be the process of joining materials to make parts or objects from 3D model data, usually layer upon layer, as opposed to subtractive manufacturing methodologies (ISO 17296 and ASTM F2792).[147] A workflow for the fabrication and implantation of customized orthopedic implants occurs generally as follows,[147,213] noting that some aspects of the workflow below are under present revision;

1) Patient data is obtained via X-Ray and CT imaging, and converted into DICOMS.
2) CAD software is used to join and modify the DICOMs with standard implant designs, as well as design any required patient specific instrumentation (with input from surgeons). Triangulation converts this geometry to an external closed surface, and this is converted into an STL file that describes to designed component to distinguish between inside/outside surfaces. Depending on the complexity of the implant, and the requirement for internal detail or free space, conversion may introduce errors such as surface non-unions or facet degeneration, and these can generally be repaired using CAD.
3) The file is processed prior to printing to allow for the specification of build orientation, the generation of support structures, and the slicing of the 3D design into layers.
4) Net shape production via SLM or EBM occurs, notably process parameters such as laser power and scan speed must be carefully chosen to ensure that the build is successful. Alternatively, near net shape production may occur via DLD production.
5) Following printing, the parts may be post-processed to relieve residual stress or heat treatment, and if applicable may be

**ADVANCED
SCIENCE NEWS**
www.advancedsciencenews.com

**ADVANCED
ENGINEERING
MATERIALS**
www.aem-journal.com

General AM Standards (general concepts, common requirements, generally applicable)			
Terminology	**Processes / Materials**	**Test Methods**	**Design / Data Format**
ASTM F 2792 ISO / ASTM 52921	ISO 17296-2	ISO 17296-3 ASTM F 2971 ASTM F 3122	ISO 17296-4 ISO / ASTM 52915 ISO / ASTM DIS 20195 DRAFT

Raw Materials	**Process / Equipment**	**Finished Parts**
Materials Category- Specific Metal powders, polymer powders, polymer resins, ceramics, etc. ASTM F 3049	**Process Category / Materials Specific** Powder Bed Fusion, Material Extrusion, Directed Energy Deposition, etc. ASTM F 3091 / F3091M	**Standard Protocols for Round Robin Testing** Mechanical Test Methods, Parts Specification, etc.
Materials-Specific Standards Material-Specific Size Specification, Material-Specific Chemical Composition, Material-Specific Viscosity Specification, etc. ASTM F 2924 ASTM F 3001 ASTM F 3055 ASTM F 3056	**Process/Materials-Specific Standards** Process-Specific Performance Test Methods, Process-Specific Performance Test Artifacts, System Component Test Methods, etc.	**Application-Specific Standards** Aerospace, Medical, Automotive, etc.

Figure 18. Summary of the ASTM and ISO standards relevant to each stage of producing a customized implant through additive manufacturing. Reproduced with permission,[210] 2016, Elsevier.

subjected to hot isostatic pressing for densification. Furthermore, surface machining may be carried out to smooth, roughen or otherwise modify implant surfaces, which may include the application of coatings (e.g., antimicrobial). Following sterilization, the implant may be inserted. Numerous copies of each implant can be produced to allow for sizing trials or surgical planning – these copies may be made using alternate AM techniques (e.g., polymer jetting) to reduce costs.

The progression from design to implantation requires the consideration of multiple factors, including but not limited to patient-specific issues (atypical bone anatomy, quality of bone stock, age and life expectancy) and process-specific issues (intra-machine variation, dimensional tolerances, complexity of design features requiring significant post-processing). As discussed in the previous section, the regulatory legislation for this process must take into account six major aspects affecting implant quality; equipment, material, production, batch, part, and finishing.[147] Current regulations are summarized in **Figure 18**. These can be linked successfully by good thermal management – sensor concepts can be used to monitor intra-process signals such as reflected laser light and melt pool temperature.

The most important issue in successful AM implant fabrication is satisfactory design. With new design freedoms come unique design restrictions, discussed briefly here.[147,213] To ensure the even distribution of thermal energy, part cross-sections should be larger at the bottom than at the top, if not constant – this can be achieved through intrinsic design, or through altering build orientation. Sharp edges should be avoided to reduce form defects, as should enclosed pores, as post-process powder removal would not be possible. Finally, overhangs of more than 45° from the vertical should be minimized or supported, as the build-up of thermal stresses can cause the part to warp.

Much research has been conducted into the optimization of AM techniques to produce highly effective orthopedic implants. However, significant gaps remain in the literature with respect to the interplay of various process parameters in the final properties of parts – scan speed, laser power, and layer thickness are the most commonly investigated process parameters. Multiple adjacent factors must also be fully understood for effective implant design, fabrication, and usage, including but not limited to; the influence of powder feed rate in DLD, oxygen pick-up in EBM, and the replication of bone features of multiple length scales (osteons, lamellae, and collage fibers).[60,70,129] The development of strategies to reduce residual stresses during fabrication is of paramount importance, as is the quantification of processing strategies to produce tailored porosity, surface roughness, and bulk properties. Of particular interest is the

41

development of weight reducing lattice structures within orthopedic implants, which can both reduce modulus mismatch and improve host responses.

8. Summary

Titanium and its alloys have proven to be a model material for orthopedic implants, aided by evident bio-inertness and low cytotoxicity; while readily produced by numerous AM production routes. Techniques such as SLM, EBM, and DLD have been used widely in the research and development of customized orthopedic implants, with parts produced behaving comparably to implants produced from wrought material. The properties of parts produced by each technique are variable based on the specific process parameters used, but certain generalizations can be made as follows – SLM has greater possible scan rates and thus cooling rates than EBM, and so SLM parts generally have greater fractions of α'phases as compared to EBM parts which have α lamellae and β phases in their microstructures. This affects their mechanical properties – parts produced by SLM generally have higher surface roughness, porosity, and residual stress, but also higher tensile strength. Porosity is observed between layers in SLM parts, while at the laser turning point in EBM parts. The amount of porosity produced in SLM and EBM parts generally requires the application of hot isostatic processing post-build to closer the pores and increase the fatigue strength. SLM parts will have higher fracture strengths but correspondingly lower ductility than EBM parts. The energy efficiency and build time minimization of EBM is better than that of SLM. DLD parts have the highest surface roughness and structural inhomogeneity of all three techniques, and generally require post-processing to reduce microstructural inhomogeneity. However, compositional gradients may be formed with this technique leading to the possibility of functional variation. Research into the optimization of process parameters (all three techniques) for orthopedic applications is as yet in its early stages, as the bulk of research into mechanical properties and surfaces has been from the perspective of aerospace and industrial applications.

Further to the new possibilities offered by AM fabrication, new alloy compositions are also of great interest in improving orthopedic implant functionality. The continued development of lower modulus β-Ti alloys shows great promise in matching bone tissue. Compositions such as Ti–35Nb–7Zr–5Ta and Ti–29Nb–13Ta–4.6Zr with moduli between 40 and 80 GPa are suited to production by additive manufacturing. The rate-limiting aspect of utilizing these new alloys in the AM of orthopedic implants is the difficulty in producing feed-stock suitable for SLM, EBM, or DLD. Powder production is still limited to a handful of companies worldwide. Similarly, improvements in computing power and software capabilities will further improve the translation of DICOMs to patient-specific implants and instrumentation.

Many post-processing techniques have been widely investigated for the further functionalization of AM Ti-based orthopedic implants, including the use of heat treatment, surface patterning, and the application of coatings. Surface modifications such as roughening through physical, chemical, or biochemical methods, as well as coatings incorporating

calcium phosphate-based ceramics or bio-active elements such as Sr will further improve the effectiveness of Ti-based orthopedic implants.

Presently, AM has the potential to improve upon conventional fabrication techniques, particularly in the production of low volumes of highly complex parts. This is already invaluable for vulnerable patients, and going forward, the increased uptake of AM orthopedic implants and PSI has the potential to improve patient outcomes. Considerable research has been conducted into the efficacy of SLM, EBM, and DLD as fabrication techniques for orthopedic implants. Properties comparable to conventional Ti implants have been produced, however, currently all evidence as to efficacy is in its infancy – long-term performance has not yet been studied extensively. As the understanding of these techniques develops, further tailoring and customization for specific types of implants can be implemented. This is the current state of the field, and significant advances are expected in the next 10 years.

[1] A. J. R. Registry, *Third AJRR Annual Report on Hip and Knee Arthroplasty Data*, American Joint Replacement Registry, Rosemont **2016**.
[2] B. M. Holzapfel, J. C. Reichert, J. T. Schantz, U. Gbureck, L. Rackwitz, U. Nöth, F. Jakob, M. Rudert, J. Groll, D. W. Hutmacher, *Adv. Drug Deliv. Rev.* **2013**, *65*, 581.
[3] M. Long, H. Rack, *Biomaterials* **1998**, *19*, 1621.
[4] L. Linder, A. Carlsson, L. Marsal, L. M. Bjursten, P. I. Brånemark, *J. Bone Joint Surg. Br.* **1988**, *70*, 550.
[5] M. Geetha, A. K. Singh, R. Asokamani, A. K. Gogia, *Prog. Mater. Sci.* **2009**, *54*, 397.
[6] L. Feller, Y. Jadwat, R. A. G. Khammissa, R. Meyerov, I. Schechter, J. Lemmer, *Biomed. Res. Int.* **2015**, *2015*, 1.
[7] M. Browne, P. J. Gregson, *Biomaterials* **1994**, *15*, 894.
[8] H. Matsuno, A. Yokoyama, F. Watari, M. Uo, T. Kawasaki, *Biomaterials* **2001**, *22*, 1253.
[9] A. Sidambe, *Materials (Basel)* **2014**, *7*, 8168.
[10] V. S. de Viteri, E. Fuentes, in *Tribology: Fundamentals and Advancements* (Ed.: J. Gegner), InTech Open, London **2013**.
[11] M. Peters, J. Hemptenmacher, J. Kumpfert, C. Leyens, in *Titanium and Titanium Alloys: Fundamentals and Applications* (Eds.: C. Leyens, M. Peters), John Wiley & Sons, Inc., New York **2003**, pp. 1–36.

**ADVANCED
SCIENCE NEWS**
www.advancedsciencenews.com

**ADVANCED
ENGINEERING
MATERIALS**
www.aem-journal.com

[12] M. Peters, C. Leyens, D. L. R. German, in *Titanium and Titanium Alloys: Fundamentals and Applications* (Ed.: C. Leyens, M. Peters), John Wiley & Sons, Inc., New York **2003**, pp. 245–261.

[13] F. Yu, O. Addison, A. J. Davenport, *Acta Biomater.* **2015**, *26*, 355.

[14] P. Fox, S. Pogson, C. J. Sutcliffe, E. Jones, *Surf. Coat. Technol.* **2008**, *202*, 5001.

[15] A. Nouri, P. D. Hodgson, C. Wen, *Biomimetics: Learn from Nature* (Ed.: A. Mukherjee), InTech Open, London **2010**, pp. 415–450.

[16] S. Nag, R. Banerjee, H. L. Fraser, *Acta Biomater.* **2007**, *3*, 369.

[17] V. Brailovski, S. Prokoshkin, M. Gauthier, K. Inaekyan, S. Dubinskiy, *J. Alloys Compd.* **2013**, *577*, S413.

[18] F. Y. Zhou, B. L. Wang, K. J. Qiu, W. J. Lin, L. Li, Y. B. Wang, F. L. Nie, Y. F. Zheng, *Mater. Sci. Eng. C* **2012**, *32*, 851.

[19] S. Ozan, J. Lin, Y. Li, R. Ipek, C. Wen, *Acta Biomater.* **2015**, *20*, 176.

[20] C. Oldani, A. Dominguez, *Recent Advances in Arthroplasty* (Ed.: S. Fokter), InTech Open, London **2012**, pp. 149–162.

[21] L. De Nardo, G. Raffaini, E. Ebramzadeh, F. Ganazzoli, *Int. J. Artif. Organs* **2012**, *35*, 629.

[22] S. Nag, R. Banerjee, in *ASM Handbook* (Ed.: R. Narayan), ASM International, Ohio **2012**, pp. 6–16.

[23] J. Breme, E. Eisenbarth, V. Biehl, in *Titanium and Titanium Alloys. Fundamentals and Applications* (Eds.: C. Leyens, M. Peters), Wiley-VCH Verlag GmbH & Co. KGaA, Weinheim **2003**, pp. 423–451.

[24] E. Sallica-Leva, A. L. Jardini, J. B. Fogagnolo, *J. Mech. Behav. Biomed. Mater.* **2013**, *26*, 98.

[25] P. Heinl, C. Körner, R. F. Singer, *Adv. Eng. Mater.* **2008**, *10*, 882.

[26] G. E. Ryan, A. S. Pandit, D. P. Apatsidis, *Biomaterials* **2008**, *29*, 3625.

[27] A. Basalah, Y. Shanjani, S. Esmaeili, E. Toyserkani, *J. Biomed. Mater. Res. Part B Appl. Biomater.* **2012**, *100 B*, 1970.

[28] M. Tamaddon, J. T. Czernuszka, *Hard Tissue* **2013**, *2*, 1.

[29] S. Sobieszczyk, *Adv. Mater. Sci.* **2010**, *10*, 20.

[30] L. Ponsonnet, K. Reybier, N. Jaffrezic, V. Comte, C. Lagneau, M. Lissac, C. Martelet, *Mater. Sci. Eng. C* **2003**, *23*, 551.

[31] M. Bigerelle, K. Anselme, B. Noel, I. Ruderman, P. Hardouin, A. Iost, *Biomaterials* **2002**, *23*, 1563.

[32] J. Fu, Y. Hu, Z. Guo, Y. Zhang, Y. Hao, S. Li, *Appl. Surf. Sci.* **2008**, *255*, 286.

[33] T. P. Kunzler, T. Drobek, M. Schuler, N. D. Spencer, *Biomaterials* **2007**, *28*, 2175.

[34] F. C. Fierz, F. Beckmann, M. Huser, S. H. Irsen, B. Leukers, F. Witte, Ö. Degistirici, A. Andronache, M. Thie, B. Müller, *Biomaterials* **2008**, *29*, 3799.

[35] A. Koptyug, C. Bergemann, R. Lange, V. E. Jaggi, L. E. Rännar, J. B. Nebe, in *Materials Science Forum*, Trans Tech Publications, Switzerland **2014**, pp. 1292–1297.

[36] J. Karlsson, A. Snis, H. Engqvist, J. Lausmaa, *J. Mater. Process. Technol.* **2013**, *213*, 2109.

[37] B. Baufeld, O. Van Der Biest, R. Gault, *Mater. Des.* **2010**, *31*, S106.

[38] T. T. Wohlers, W. Associates, *Wohlers Report 2015: Additive Manufacturing and 3D Printing State of the Industry: Annual Worldwide Progress Report*, Wohlers Associates, Colorado **2015**.

[39] P. Unwin, *SPIE Photonics West 2014-LASE Lasers Sources* **2014**, *8970*, 897005.

[40] B. P. Conner, G. P. Manogharan, A. N. Martof, L. M. Rodomsky, C. M. Rodomsky, D. C. Jordan, J. W. Limperos, *Addit. Manuf.* **2014**, *1-4*, 64.

[41] H. Miura, *KONA Powder Part. J.* **2015**, *32*, 253.

[42] J. U. Pucci, B. R. Christophe, J. A. Sisti, E. S. Connolly, *Biotechnol. Adv.* **2017**, *35*, 521.

[43] D. Beski, T. Dufour, F. Gelaude, A. Ilankovan, M. Kvasnytsia, M. Lawrenchuk, I. Lukyanenko, M. Mir, L. Neumann, A. Nguyen, A. Soares, E. Sauvage, K. Vanderperren, D. Vangeneugden, in *Essentials of 3D Biofabrication and Translation* (Ed.: J. J. Yoo, A. Atala), Academic Press, Boston **2015**, pp. 19–41.

[44] L. E. Murr, S. M. Gaytan, F. Medina, H. Lopez, E. Martinez, B. I. Machado, D. H. Hernandez, L. Martinez, M. I. Lopez, R. B. Wicker, J. Bracke, *Philos. Trans. A. Math. Phys. Eng. Sci.* **2010**, *368*, 1999.

[45] B. Vandenbroucke, J.-P. Kruth, *Rapid Prototyp. J.* **2007**, *13*, 196.

[46] T. M. Mower, M. J. Long, *Mater. Sci. Eng. A* **2016**, *651*, 198.

[47] V. Cain, L. Thijs, J. Van Humbeeck, B. Van Hooreweder, R. Knutsen, *Addit. Manuf.* **2014**, *5*, 68.

[48] M. A. Fernandez-Yague, S. A. Abbah, L. McNamara, D. I. Zeugolis, A. Pandit, M. J. Biggs, *Adv. Drug Deliv. Rev.* **2015**, *84*, 1.

[49] X. Wu, J. Liang, J. Mei, C. Mitchell, P. S. Goodwin, W. Voice, *Mater. Des.* **2004**, *25*, 137.

[50] L. E. Murr, E. Martinez, K. N. Amato, S. M. Gaytan, J. Hernandez, D. A. Ramirez, P. W. Shindo, F. Medina, R. B. Wicker, *J. Mater. Res. Technol.* **2012**, *1*, 42.

[51] Q. C. Liu, J. Elambasseril, S. J. Sun, M. Leary, M. Brandt, P. K. Sharp, *Adv. Mater. Res.* **2014**, *891-892*, 1519.

[52] S. Leuders, M. Thöne, A. Riemer, T. Niendorf, T. Tröster, H. A. A. Richard, H. J. J. Maier, *Int. J. Fatigue* **2013**, *48*, 300.

[53] M. N. Ahsan, A. J. Pinkerton, R. J. Moat, J. Shackleton, *Mater. Sci. Eng. A*, **2011**, p. 7648.

[54] T. Marcu, C. Menapace, L. Girardini, D. Leordean, C. Popa, *Rapid Prototyp. J.* **2014**, *20*, 301.

[55] D. K. Pattanayak, A. Fukuda, T. Matsushita, M. Takemoto, S. Fujibayashi, K. Sasaki, N. Nishida, T. Nakamura, T. Kokubo, *Acta Biomater.* **2011**, *7*, 1398.

[56] I. Yadroitsev, P. Krakhmalev, I. Yadroitsava, *J. Alloys Compd.* **2014**, *583*, 404.

[57] J. Romano, L. Ladani, J. Razmi, M. Sadowski, *Addit. Manuf.* **2015**, *8*, 1.

[58] M. Simonelli, Y. Y. Tse, C. Tuck, *J. Phys. Conf. Ser.* **2012**, *371*, 012084.

[59] M. Speirs, J. Van Humbeeck, J. Schrooten, J. Luyten, J. P. Kruth, *Procedia CIRP* **2013**, *5*, 79.

[60] A. Butscher, M. Bohner, S. Hofmann, L. Gauckler, R. Müller, *Acta Biomater.* **2011**, *7*, 907.

[61] W. Xue, B. V. Krishna, A. Bandyopadhyay, S. Bose, *Acta Biomater.* **2007**, *3*, 1007.

[62] A. El-Hajje, E. C. Kolos, J. K. Wang, S. Maleksaeedi, Z. He, F. E. Wiria, C. Choong, A. J. Ruys, *J. Mater. Sci. Mater. Med.* **2014**, *25*, 2471.

[63] V. Guneta, J. K. Wang, S. Maleksaeedi, Z. M. He, M. T. C. Wong, C. Choong, *J. Biomimetics, Biomater. Biomed. Eng.* **2014**, *21*, 101.

[64] S. C. Cox, J. A. Thornby, G. J. Gibbons, M. A. Williams, K. K. Mallick, *Mater. Sci. Eng. C Mater. Biol. Appl.* **2015**, *47*, 237.

[65] A. Butscher, M. Bohner, N. Doebelin, S. Hofmann, R. Müller, *Acta Biomater.* **2013**, *9*, 9149.

[66] S. L. Sing, J. An, W. Y. Yeong, F. E. Wiria, *J. Orthop. Res.* **2016**, *34*, 369.

[67] L. E. Murr, *Addit. Manuf.* **2014**, *5*, 40.

[68] L. E. Murr, S. A. Quinones, S. M. Gaytan, M. I. Lopez, A. Rodela, E. Y. Martinez, D. H. Hernandez, E. Martinez, F. Medina, R. B. Wicker, *J. Mech. Behav. Biomed. Mater.* **2009**, *2*, 20.

[69] H. Gong, K. Rafi, H. Gu, T. Starr, B. Stucker, *Addit. Manuf.* **2014**, *1-4*, 87.

[70] K. S. Munir, Y. Li, C. Wen, *Metallic Foam Bone: Processing, Modification and Characterization and Properties* (Ed.: C. Wen), Woodhead Publishing Limited, **2016**, pp. 1–23.

[71] S. Zhang, X. Cheng, Y. Yao, Y. Wei, C. Han, Y. Shi, Q. Wei, Z. Zhang, *Mater. Sci. Eng. C* **2015**, *53*, 50.

[72] P. Hanzl, M. Zetek, T. Bakša, T. Kroupa, *Procedia Eng.* **2015**, *100*, 1405.

[73] A. M. Khorasani, I. Gibson, M. Goldberg, G. Littlefair, *Mater. Des.* **2016**, *103*, 348.

[74] T. Amine, J. W. Newkirk, F. Liou, *Case Stud. Therm. Eng.* **2014**, *3*, 21.

[75] C. Qiu, N. J. E. Adkins, M. M. Attallah, *Mater. Sci. Eng. A* **2013**, *578*, 230.

[76] D. Leordean, S. A. Radu, D. Frățilă, P. Berce, *Int. J. Adv. Manuf. Technol.* **2015**, *79*, 905.

[77] T. Marcu, M. Todea, L. Maines, D. Leordean, P. Berce, C. Popa, *Powder Metall.* **2012**, *55*, 309.

[78] D. A. Hollander, M. von Walter, T. Wirtz, R. Sellei, B. Schmidt-Rohlfing, O. Paar, H.-J. Erli, *Biomaterials* **2006**, *27*, 955.

[79] P. H. Warnke, T. Douglas, P. Wollny, E. Sherry, M. Steiner, S. Galonska, S. T. Becker, I. N. Springer, J. Wiltfang, S. Sivananthan, *Tissue Eng. Part C Methods* **2009**, *15*, 115.

[80] C. Mangano, A. Piattelli, S. D'Avila, G. Iezzi, F. Mangano, T. Onuma, J. A. Shibli, *J. Oral Implantol.* **2010**, *36*, 91.

[81] S. Van Bael, Y. C. Chai, S. Truscello, M. Moesen, G. Kerckhofs, H. Van Oosterwyck, J. P. Kruth, J. Schrooten, *Acta Biomater.* **2012**, *8*, 2824.

[82] A. Shaoki, J. Xu, H. Sun, X. Chen, J. Ouyang, X. Zhuang, F. Deng, *Biofabrication* **2016**, *8*, 045014.

[83] N. Hrabe, T. Quinn, *Mater. Sci. Eng. A* **2013**, *573*, 271.

[84] D. Herzog, V. Seyda, E. Wycisk, C. Emmelmann, *Acta Mater.* **2016**, *117*, 371.

[85] X. P. Tan, Y. J. Tan, C. S. L. Chow, S. B. Tor, W. Y. Yeong, *Mater. Sci. Eng. C* **2017**, *76*, 1328.

[86] S. Ponader, C. Von Wilmowsky, M. Widenmayer, R. Lutz, P. Heinl, C. Körner, R. F. Singer, E. Nkenke, F. W. Neukam, K. A. Schlegel, *J. Biomed. Mater. Res. Part A* **2010**, *92*, 56.

[87] C. Guo, W. Ge, F. Lin, *J. Mater. Process. Technol.* **2015**, *217*, 148.

[88] M. Seifi, M. Dahar, R. Aman, O. Harrysson, J. Beuth, J. J. Lewandowski, *Jom* **2015**, *67*, 597.

[89] X. Tan, Y. Kok, Y. J. Tan, M. Descoins, D. Mangelinck, S. B. Tor, K. F. Leong, C. K. Chua, *Acta Mater.* **2015**, *97*, 1.

[90] A. A. Antonysamy, J. Meyer, P. B. Prangnell, *Mater. Charact.* **2013**, *84*, 153.

[91] J. Karlsson, M. Norell, U. Ackelid, H. Engqvist, J. Lausmaa, *J. Manuf. Process.* **2015**, *17*, 120.

[92] G. Chahine, M. Koike, T. Okabe, P. Smith, R. Kovacevic, *Jom* **2008**, *60*, 50.

[93] W. Xia, C. Lindahl, J. Lausmaa, H. Engqvist, *Acta Biomater.* **2010**, *6*, 1591.

[94] L. T. Duarte, S. R. Biaggio, R. C. Rocha-Filho, N. Bocchi, *Corros. Sci.* **2013**, *72*, 35.

[95] X. Bin Su, Y. Q. Yang, P. Yu, J. F. Sun, *Trans. Nonferrous Met. Soc. China (English Ed.)* **2012**, *22*, s181.

[96] B. Song, S. Dong, B. Zhang, H. Liao, C. Coddet, *Mater. Des.* **2012**, *35*, 120.

[97] J. W. Park, Y. J. Kim, J. H. Jang, *Clin. Oral Implants Res.* **2010**, *21*, 398.

[98] P. Edwards, M. Ramulu, *Mater. Sci. Eng. A* **2014**, *598*, 327.

[99] D. H. Abdeen, B. R. Palmer, *Rapid Prototyp. J.* **2016**, *22*, 609.

[100] S. Ponader, E. Vairaktaris, P. Heinl, C. V. Wilmowsky, A. Rottmair, C. Körner, R. F. Singer, S. Holst, K. A. Schlegel, F. W. Neukam, E. Nkenke, *J. Biomed. Mater. Res. Part A* **2008**, *84*, 1111.

[101] P. Thomsen, J. Malmstrom, L. Emanuelsson, M. Rene, A. Snis, J. Malmstro, L. Emanuelsson, M. Rene, A. Snis, J. Malmström, L. Emanuelsson, M. René, A. Snis, *J. Biomed. Mater. Res. B. Appl. Biomater.* **2009**, *90 B*, 35.

[102] A. Palmquist, A. Snis, L. Emanuelsson, M. Browne, P. Thomsen, *J. Biomater. Appl.* **2013**, *27*, 1003.

[103] J. Lv, Z. Jia, J. Li, Y. Wang, J. Yang, P. Xiu, K. Zhang, H. Cai, Z. Liu, *Adv. Eng. Mater.* **2015**, *17*, 1391.

[104] C. M. Haslauer, J. C. Springer, O. L. A. Harrysson, E. G. Loboa, N. A. Monteiro-Riviere, D. J. Marcellin-Little, *Med. Eng. Phys.* **2010**, *32*, 645.

[105] N. Shamsaei, A. Yadollahi, L. Bian, S. M. Thompson, *Addit. Manuf.* **2015**, *8*, 12.

[106] R. Vilar, in *Comprehensive Materials Processing* (Ed.: S. Hashmi), Elsevier, Amsterdam **2014**, pp. 163–216.

[107] M. Polanski, M. Kwiatkowska, I. Kunce, J. Bystrzycki, *Int. J. Hydrogen Energy* **2013**, *38*, 12159.

[108] V. K. Balla, P. D. DeVasConCellos, W. Xue, S. Bose, A. Bandyopadhyay, *Acta Biomater.* **2009**, *5*, 1831.

[109] R. Banerjee, P. C. Collins, D. Bhattacharyya, S. Banerjee, H. L. Fraser, *Acta Mater.* **2003**, *51*, 3277.

[110] R. Banerjee, S. Nag, H. L. Fraser, *Mater. Sci. Eng. C* **2005**, *25*, 282.

[111] M. A. Larosa, A. L. Jardini, L. F. Bernardes, M. R. Wolf Maciel, R. Maciel Filho, C. A. C. Zaváglia, F. Zaváglia, D. R. Calderoni, P. Kharmandayan, in *High Value Manufacturing: Advanced Research in Virtual and Rapid Prototyping: Proceedings of the 6th International Conference on Advanced Research and Rapid Prototyping*, Elsevier, Amsterdam **2014**, pp. 297–301.

[112] E. C. Santos, M. Shiomi, K. Osakada, T. Laoui, *Int. J. Mach. Tools Manuf.* **2006**, *46*, 1459.

[113] K. Zhang, W. Liu, X. Shang, *Opt. Laser Technol.* **2007**, *39*, 549.

[114] A. Suárez, M. J. Tobar, A. Yáñez, I. Pérez, J. Sampedro, V. Amigó, J. J. Candel, *Phys. Procedia* **2011**, *12*, 666.

[115] S. M. Thompson, L. Bian, N. Shamsaei, A. Yadollahi, *Addit. Manuf.* **2015**, *8*, 36.

[116] A. J. Sterling, B. Torries, N. Shamsaei, S. M. Thompson, D. W. Seely, *Mater. Sci. Eng. A* **2016**, *655*, 100.

[117] M. Gharbi, P. Peyre, C. Gorny, M. Carin, S. Morville, P. Le Masson, D. Carron, R. Fabbro, *J. Mater. Process. Technol.* **2013**, *213*, 791.

[118] A. Sterling, N. Shamsaei, B. Torries, S. M. Thompson, *Procedia Eng.* **2015**, *133*, 576.

[119] S. Palanivel, A. K. Dutt, E. J. Faierson, R. S. Mishra, *Mater. Sci. Eng. A* **2016**, *654*, 39.

[120] R. P. Mulay, J. A. Moore, J. N. Florando, N. R. Barton, M. Kumar, *Mater. Sci. Eng. A* **2016**, *666*, 43.

[121] P. A. Kobryn, S. L. Semiatin, *J. Mater. Process. Technol.* **2003**, *135*, 330.

[122] X. Wu, J. Liang, J. Mei, C. Mitchell, P. S. S. Goodwin, W. Voice, *Mater. Des.* **2004**, *25*, 137.

[123] C. Qiu, G. A. Ravi, C. Dance, A. Ranson, S. Dilworth, M. M. Attallah, *J. Alloys Compd.* **2015**, *629*, 351.

[124] J. S. Keist, T. A. Palmer, *Mater. Des.* **2016**, *106*, 482.

[125] A. Bandyopadhyay, F. Espana, V. K. Balla, S. Bose, Y. Ohgami, N. M. Davies, *Acta Biomater.* **2010**, *6*, 1640.

[126] X. Li, Y. F. Feng, C. T. Wang, G. C. Li, W. Lei, Z. Y. Zhang, L. Wang, *PLoS ONE* **2012**, *7*, 1.

[127] X. Zhao, S. Li, M. Zhang, Y. Liu, T. B. Sercombe, S. Wang, Y. Hao, R. Yang, L. E. Murr, *Mater. Des.* **2016**, *95*, 21.

[128] P. Li, D. H. Warner, A. Fatemi, N. Phan, *Int. J. Fatigue* **2016**, *85*, 130.

[129] J. Günther, D. Krewerth, T. Lippmann, S. Leuders, T. Tröster, A. Weidner, H. Biermann, T. Niendorf, *Int. J. Fatigue* **2017**, *94*, 236.

[130] S. Bagehorn, J. Wehr, H. J. Maier, *Int. J. Fatigue* **2017**, *102*, 135.

[131] Y. Zhai, D. A. Lados, E. J. Brown, G. N. Vigilante, *Int. J. Fatigue* **2016**, *93*, 51.

[132] K. F. Walker, Q. Liu, M. Brandt, *Int. J. Fatigue* **2017**, *104*, 302.

[133] Y. Zhai, H. Galarraga, D. A. Lados, in *Procedia Engineering*, Elsevier, Amsterdam **2015**, pp. 658–666.

[134] H. Wang, B. Zhao, C. Liu, C. Wang, X. Tan, M. Hu, *PLoS ONE* **2016**, *11*, 1.

[135] M. Niinomi, M. Nakai, J. Hieda, *Acta Biomater.* **2012**, *8*, 3888.

[136] M. Niinomi, *Mater. Sci. Eng. A* **1998**, *243*, 231.

[137] L. M. Elias, S. G. Schneider, S. Schneider, H. M. Silva, F. Malvisi, *Mater. Sci. Eng. A* **2006**, *432*, 108.

[138] B. Vrancken, L. Thijs, J.-P. Kruth, J. Van Humbeeck, *Acta Mater.* **2014**, *68*, 150.

[139] Y. Zhou, S. F. Wen, B. Song, X. Zhou, Q. Teng, Q. S. Wei, Y. S. Shi, *Mater. Des.* **2016**, *89*, 1199.

44

**ADVANCED
SCIENCE NEWS**

www.advancedsciencenews.com

**ADVANCED
ENGINEERING
MATERIALS**

www.aem-journal.com

[140] J. M. Calderon-Moreno, C. Vasilescu, S. I. Drob, S. Ivanescu, P. Osiceanu, P. Drob, M. Popa, S. Preda, E. Vasilescu, *J. Alloys Compd.* **2014**, *612*, 398.

[141] S. Samuel, S. Nag, S. Nasrazadani, V. Ukirde, M. El Bouanani, A. Mohandas, K. Nguyen, R. Banerjee, *J. Biomed. Mater. Res. Part A* **2010**, *94*, 1251.

[142] E. Eisenbarth, D. Velten, M. Müller, R. Thull, J. Breme, *Biomaterials* **2004**, *25*, 5705.

[143] M. T. Mohammed, Z. A. Khan, M. Geetha, A. N. Siddiquee, *J. Alloys Compd.* **2015**, *634*, 272.

[144] Q. Meng, S. Guo, Q. Liu, L. Hu, X. Zhao, *Prog. Nat. Sci. Mater. Int.* **2014**, *24*, 157.

[145] L. Nie, Y. Zhan, T. Hu, X. Chen, C. Wang, *J. Mech. Behav. Biomed. Mater.* **2014**, *29*, 1.

[146] M. Schmidt, M. Merklein, D. Bourell, D. Dimitrov, T. Hausotte, K. Wegener, L. Overmeyer, F. Vollertsen, G. N. Levy, *CIRP Ann. Manuf. Technol.* **2017**, *66*, 561.

[147] B. Engel, D. L. Bourell, *Rapid Prototyp. J.* **2000**, *6*, 97.

[148] Y. Y. Sun, S. Gulizia, C. H. Oh, C. Doblin, Y. F. Yang, M. Qian, *Jom* **2015**, *67*, 564.

[149] H. P. Tang, J. Wang, M. Qian, *Titan. Powder Metall.*, Elsevier, Oxford **2015**, pp. 601–608.

[150] H. P. Tang, M. Qian, N. Liu, X. Z. Zhang, G. Y. Yang, J. Wang, *Jom* **2015**, *67*, 555.

[151] Z. Zhang, L. Yuan, P. D. Lee, E. Jones, J. R. Jones, *J. Biomed. Mater. Res. Part B Appl. Biomater.* **2014**, *102*, 1689.

[152] S. Maleksaeedi, J. K. Wang, A. El-Hajje, L. Harb, V. Guneta, Z. He, F. E. Wiria, C. Choong, A. J. Ruys, in *Procedia CIRP* (Ed.: M. Mitsubishi, P. Bartolo), Elsevier, Amsterdam **2013**, pp. 158–163.

[153] T. B. Kim, S. Yue, Z. Zhang, E. Jones, J. R. Jones, P. D. Lee, *J. Mater. Process. Technol.* **2014**, *214*, 2706.

[154] D. Melancon, Z. S. Bagheri, R. B. Johnston, L. Liu, M. Tanzer, D. Pasini, *Acta Biomater.* **2017**, *63*, 350.

[155] S. Arabnejad, B. Johnston, M. Tanzer, D. Pasini, *J. Orthop. Res.* **2017**, *35*, 1774.

[156] F. Calignano, *Mater. Des.* **2014**, *64*, 203.

[157] M. X. Gan, C. H. Wong, *J. Mater. Process. Technol.* **2016**, *238*, 474.

[158] A. Hussein, L. Hao, C. Yan, R. Everson, P. Young, *J. Mater. Process. Technol.* **2013**, *213*, 1019.

[159] G. Strano, L. Hao, R. M. Everson, K. E. Evans, *Int. J. Adv. Manuf. Technol.* **2013**, *66*, 1247.

[160] K. Zeng, D. Pal, C. Teng, B. E. Stucker, *Addit. Manuf.* **2015**, *6*, 67.

[161] D. Frank, G. Fadel, *J. Intell. Manuf.* **1995**, *6*, 339.

[162] B. Vrancken, L. Thijs, J.-P. Kruth, J. Van Humbeeck, *J. Alloys Compd.* **2012**, *541*, 177.

[163] E. Brandl, D. Greitemeier, *Mater. Lett.* **2012**, *81*, 84.

[164] J. I. Rosales-Leal, M. A. Rodríguez-Valverde, G. Mazzaglia, P. J. Ramón-Torregrosa, L. Díaz-Rodríguez, O. García-Martínez, M. Vallecillo-Capilla, C. Ruiz, M. A. Cabrerizo-Vílchez, *Colloids Surf. A Physicochem. Eng. Asp.* **2010**, *365*, 222.

[165] D. Deligianni, N. Katsala, S. Ladas, D. Sotiropoulou, J. Amedee, Y. Missirlis, *Biomaterials* **2001**, *22*, 1241.

[166] B. D. Boyan, T. W. Hummert, D. D. Dean, Z. Schwartz, *Biomaterials* **1996**, *17*, 137.

[167] J. Lincks, B. D. Boyan, C. R. Blanchard, C. H. Lohmann, Y. Liu, D. L. Cochran, D. D. Dean, Z. Schwartz, *Biomater. Silver Jubil. Compend.* **2006**, *19*, 147.

[168] P. Linez-Bataillon, F. Monchau, M. Bigerelle, H. F. Hildebrand, *Biomol. Eng.* **2002**, *19*, 133.

[169] A. Wennerberg, T. Albrektsson, R. Jimbo, *Implant Surfaces and Their Biological and Clinical Impact*, Springer, Berlin **2015**.

[170] E. Sachs, A. Curodeau, D. Gossard, H. Jee, M. Cima, S. Caldarise, *Solid Free. Fabr. Symp.*, University of Texas, Austin **1994**, pp. 56–64.

[171] H. Shahali, A. Jaggessar, P. K. Yarlagadda, *Procedia Eng.* **2017**, *174*, 1067.

[172] B. G. X. Zhang, D. E. Myers, G. G. Wallace, M. Brandt, P. F. M. Choong, *Int. J. Mol. Sci.* **2014**, *15*, 11878.

[173] W. Xia, C. Lindahl, J. Lausmaa, P. Borchardt, A. Ballo, P. Thomsen, H. Engqvist, *Acta Biomater.* **2010**, *6*, 1591.

[174] K. Søballe, *Acta Orthop. Scand. Suppl.* **1993**, *255*, 1.

[175] A. Eckardt, H. M. Aberman, H. D. Cantwell, J. Heine, *Arch. Orthop. Trauma Surg.* **2003**, *123*, 28.

[176] B. R. Levine, S. Sporer, R. A. Poggie, C. J. Della Valle, J. J. Jacobs, *Biomaterials* **2006**, *27*, 4671.

[177] D. M. Findlay, K. Welldon, G. J. Atkins, D. W. Howie, A. C. W. Zannettino, D. Bobyn, *Biomaterials* **2004**, *25*, 2215.

[178] Y. Liu, C. Bao, D. Wismeijer, G. Wu, *Mater. Sci. Eng. C* **2015**, *49*, 323.

[179] V. K. Balla, S. Banerjee, S. Bose, A. Bandyopadhyay, *Acta Biomater.* **2010**, *6*, 2329.

[180] N. Harrison, P. E. McHugh, W. Curtin, P. Mc Donnell, *J. Mech. Behav. Biomed. Mater.* **2013**, *21*, 37.

[181] P. Stenlund, O. Omar, U. Brohede, S. Norgren, B. Norlindh, A. Johansson, J. Lausmaa, P. Thomsen, A. Palmquist, *Acta Biomater.* **2015**, *20*, 165.

[182] J. B. Tong, X. Lu, C. C. Liu, L. N. Wang, X. H. Qu, *Jom* **2015**, *67*, 573.

[183] M. T. Vestermark, E.-M. Hauge, K. Soballe, J. E. Bechtold, T. Jakobsen, J. Baas, *Acta Orthop.* **2011**, *82*, 614.

[184] M. Schnabelrauch, A. R. Kautz, J. Weisser, J. Schmidt, A. Henning, C. Schrader, U. Bayer, F. Schlottig, *Eur. Cells Mater.* **2007**, *14*, 91.

[185] J. Yan, Y. Zhang, Y. Han, Y. Zhao, J. Sun, H. Yan, *Zhonghua Kou Qiang Yi Xue Za Zhi* **2010**, *45*, 89.

[186] J. Terra, E. R. Dourado, J.-G. Eon, D. E. Ellis, G. Gonzalez, A. M. Rossi, *Phys. Chem. Chem. Phys.* **2009**, *11*, 568.

[187] M. T. Vestermark, *Dan. Med. Bull.* **2011**, *58*, B4286.

[188] S. Tan, B. Zhang, X. Zhu, P. Ao, H. Guo, W. Yi, G.-Q. Zhou, *Biomed Res. Int.* **2014**, *2014*, 814057.

[189] Z. Saidak, P. J. Marie, *Pharmacol. Ther.* **2012**, *136*, 216.

[190] Y. Li, Q. Li, S. Zhu, E. Luo, J. Li, G. Feng, Y. Liao, J. Hu, *Biomaterials* **2010**, *31*, 9006.

[191] H. Yang, M. Lin, Y. Xu, G. Shang, R. Wang, K. Chen, *Int. J. Clin. Exp. Med.* **2015**, *8*, 257.

[192] J. Vaithilingam, E. Prina, R. D. Goodridge, R. J. M. Hague, S. Edmondson, F. R. A. J. Rose, S. D. R. Christie, *Mater. Sci. Eng. C* **2016**, *67*, 294.

[193] S. C. Cox, P. Jamshidi, N. M. Eisenstein, M. A. Webber, H. Burton, R. J. A. Moakes, O. Addison, M. Attallah, D. E. T. Shepherd, L. M. Grover, *ACS Biomater. Sci. Eng.* **2017**, *3*, 1616.

[194] L. Matouskova, M. Ackermann, J. Horakova, L. Capek, P. Henys, J. Safka, *Expert Rev. Med. Devices* **2018**, *15*, 313.

[195] L. E. J. Thomas-Seale, J. C. Kirkman-Brown, M. M. Attallah, D. M. Espino, D. E. T. Shepherd, *Int. J. Prod. Econ.* **2018**, *198*, 104.

[196] F. L. O'Malley, H. Millward, D. Eggbeer, R. Williams, R. Cooper, *Addit. Manuf.* **2016**, *9*, 25.

[197] A. Mohammad, M. K. Mohammed, A. M. Alahmari, *Int. J. Adv. Manuf. Technol.* **2016**, *87*, 1033.

[198] W. Wangsgard, M. Winters, *Radiat. Phys. Chem.* **2018**, *143*, 38.

[199] J. M. Beck, M. D. Jacobson, *Minnesota J. Law, Sci. Technol.* **2017**, *18*, 143.

[200] M. Simonelli, Y. Y. Tse, C. Tuck, *Mater. Sci. Eng. A* **2014**, *616*, 1.

[201] M. Simonelli, Y. Y. Tse, C. Tuck, *J. Mater. Res.* **2014**, *29*, 1.

[202] W. Xu, M. Brandt, S. Sun, J. Elambasseril, Q. Liu, K. Latham, K. Xia, M. Qian, *Acta Mater.* **2015**, *85*, 74.

[203] R. Banerjee, S. Nag, S. Samuel, H. L. Fraser, *J. Biomed. Mater. Res. A* **2007**, *81*, 771.

[204] G. Ryan, A. Pandit, D. P. Apatsidis, *Biomaterials* **2006**, *27*, 2651.

[205] J. S. Mulford, S. Babazadeh, N. Mackay, *ANZ J. Surg.* **2016**, *86*, 648.

[206] Y. E. Choonara, L. C. du Toit, P. Kumar, P. P. D. Kondiah, V. Pillay, *Expert Rev. Pharmacoecon. Outcomes Res.* **2016**, *16*, 23.

[207] M. Larsen, R. Mishra, M. Miller, D. Dean, *Bioprinting of Bone*, Elsevier Inc., Boston **2015**.

[208] Y. Oshida, in *Bioscience and Bioengineering of Titanium Materials* (Ed.: Y. Oshida), Elsevier, Amsterdam **2013**, pp. 225–268.

[209] M. Puthiya Veettil, J. M. Latham, *Orthop. Trauma* **2015**, *29*, 105.

[210] S. J. Hollister, C. L. Flanagan, D. A. Zopf, R. J. Morrison, H. Nasser, J. J. Patel, E. Ebramzadeh, S. N. Sangiorgio, M. B. Wheeler, G. E. Green, *Ann. Biomed. Eng.* **2015**, *43*, 774.

[211] M. K. Thompson, G. Moroni, T. Vaneker, G. Fadel, R. I. Campbell, I. Gibson, A. Bernard, J. Schulz, P. Graf, B. Ahuja, F. Martina, *CIRP Ann. Manuf. Technol.* **2016**, *65*, 737.

[212] S. C. Cox, P. Jamshidi, N. M. Eisenstein, M. A. Webber, H. Hassanin, M. M. Attallah, D. E. T. Shepherd, O. Addison, L. M. Grover, *Mater. Sci. Eng. C* **2016**, *64*, 407.

[213] P. S. Unwin, A. Eshraghi, in *Computer-Assisted Musculoskeletal Surgery. Thinking and Executing in 3D* (Eds.: L. E. Ritacco, F. E. Milano, E. Chao), Springer International Publishing, Switzerland **2016**, p. 181.

[214] K. C. Wong, *Orthop. Res. Rev.* **2016**, *8*, 57.

[215] R. J. Morrison, K. N. Kashlan, C. L. Flanangan, J. K. Wright, G. E. Green, S. J. Hollister, K. J. Weatherwax, *Clin. Transl. Sci.* **2015**, *8*, 594.

[216] M. Maruthappu, B. Keogh, *Bmj* **2014**, *349*, g7709.

[217] M. Di Prima, J. Coburn, D. Hwang, J. Kelly, A. Khairuzzaman, L. Ricles, *3D Print. Med.* **2015**, *2*, 1.

[218] C. L. Ventola, *Pharmacy and Therapeutics* **2014**, *39*, 704.

[219] B. Marshall, *Skeletal Wonder From Down Under* https://www.meddeviceonline.com/doc/skeletal-wonder-from-down-under-0001, **2017**.

[220] T. Economist, *A Printed Smile*, **2016**.

[221] A. Hodgekiss, M. Davies, *Dly. Mail Aust.* **2017**.

Chapter 3: The joint replacement/bone interface; understanding the metallurgy of SLM Ti-6Al-4V

Conventional Ti-6Al-4V orthopaedic implants are produced via subtractive manufacturing processes – blocks of Ti-6Al-4V are milled and machined into final geometries as specified in the design phase. Because milling and machining processes are often automated and highly specialized with respect to manufacturing capabilities, the range of orthopaedic implants available is limited. The leading companies in the orthopaedic implant space offer a range of sizings and fitting solutions; for example, Stryker produces total hip replacement components including the Anato femoral component which comes in 8 sizes, as well as the Trident Acetabular Shell systems. However, these components are often not suitable for revision surgeries, for patients with diverse orthopaedic issues, or for patients requiring atypically-shaped implants.

New generation fabrication techniques such as Selective Laser Melting (SLM) are gaining in popularity for the production of Ti-6Al-4V implants, as their unique process characteristics enable the rapid production of highly customised and complex implants, i.e. personalised solutions. However, for the widespread uptake of AM fabrication for orthopaedic implants, the processes must be fully characterised and understood with respect to achievable properties. Currently, most research into the SLM production of Ti-6Al-4V focuses on the optimisation of mechanical properties, as opposed to optimisation for properties conducive to osseointegration or biocompatibility. 3D printing in medical applications is set to mature into a $1.9 billion industry by 2024 [11], and thus a detailed investigation into SLM in relation to biomedical applications is timely.

The properties of SLM Ti-6Al-4V can be manipulated through SLM process parameters such as laser scan speed and laser power. The interplay of these process parameters is not yet fully understood; thus there may be unexplored combinations of process parameters for SLM Ti-6Al-4V that could produce improved orthopaedic implants. Examples of desirable implant properties include elastic modulus closer to that of bone, and surfaces that facilitate osteoblast attachment and activity. Current analyses of interactions between parameters have been completed for other processes and materials, but relatively little data exists for SLM Ti-6Al-4V.

This study presents the results of iterative analyses of the effects of SLM scan speed and laser intensity on part properties such as hardness, porosity and cytotoxicity, as well as electrochemical behaviour. Key findings demonstrate that though different combinations of scan speeds and laser intensities may result in the same energy density supplied to the material, energy density is a poor predictor for part properties. Matching scan speed and laser intensity (e.g. slow scan speed and lower laser intensity) produces more stable melting and better properties. Low stochastic porosity (0–5%) is produced using intermediate laser powers and scan speeds (120–180 W and 400–600 mm/s respectively).

A clear understanding of the individual contributions of laser intensity and scan speed to SLM part properties will allow optimisation of the process for the production of Ti-based orthopaedic implants. This will improve not only implant performance but also patient quality of life.

This chapter was prepared as a paper which has been accepted to **PLOSOne,** with the final manuscript presented here.

Understanding the effects of SLM process parameter interplay on Ti-6Al-4V surface properties

Trina Majumdar[1, 2]*, Tiphaine Bazin[1,3]¶, Emily Massahud Carvalho Ribeiro[1,4]¶, Jess Frith[1,2] and N. Birbilis[1,2]

[1] Department of Materials Science and Engineering, Monash University, Clayton, Victoria 3800, Australia

[2] Monash Institute of Medical Engineering (MIME), Monash University, Clayton, Victoria 3800, Australia

[3] Ecole Nationale Supérieure de Chimie de Rennes, Rennes, France

[4] Centro Federal de Educação Tecnológica de Minas Gerais, Belo Horizonte, Brazil

* Corresponding author

Email: trina.majumdar@monash.edu (TM)

¶ These authors contributed equally to this work.

Abstract

Ti-6Al-4V is commonly used in orthopaedic implants, and fabrication techniques such as Selective Laser Melting (SLM) are becoming increasingly popular for the net-shape production of such implants, as SLM allows for complex customisation and minimal material wastage. Present research into SLM fabricated Ti-6Al-4V focuses on new design strategies (e.g. designing pores, struts or lattices) or mechanical property optimisation through process parameter control – however, it is pertinent to examine the effects of altering SLM process parameters on properties relating to bioactivity. Herein, changes in Ti-6Al-4V microstructure, mechanical properties and surface characteristics were examined as a result of varying SLM process parameters, with a view to understanding how to tune Ti-6Al-4V bio-activity during the fabrication stage itself. The interplay between various SLM laser scan speeds and laser powers influenced Ti-6Al-4V hardness, porosity, roughness and corrosion resistance, in a manner not clearly described by the commonly used volumetric energy density (VED) design variable. Key findings indicate that the relationships between SLM process parameters and ultimate Ti-6Al-4V properties are not straightforward as expected, and that wide ranges of porosity (0.03 ± 0.01 % to 32.59 ± 2.72 %) and corrosion resistance can be achieved through relatively minor changes in process parameters used – indicating volumetric energy density is a poor predictor of SLM Ti-6Al-4V properties. While variations in electrochemical behaviour with respect to the process parameters used in the SLM fabrication of Ti-6Al-4V have previously been reported, this study presents data regarding important surface characteristics over a large process window, reflecting the full capabilities of current SLM machinery.

Highlights

- Selective laser melted Ti-6Al-4V properties can be controlled by the choice, and balance of, laser scan speed and power.
- Combining high laser scan speed with low laser power (or vice versa) adversely affects consolidation, resulting in high porosity and roughness as well as drastic differences in corrosion resistance and current density.
- The relationship between laser power and scan speed was presented as a property map and discussed in the context of porosity, corrosion resistance and hardness.

Striking Image
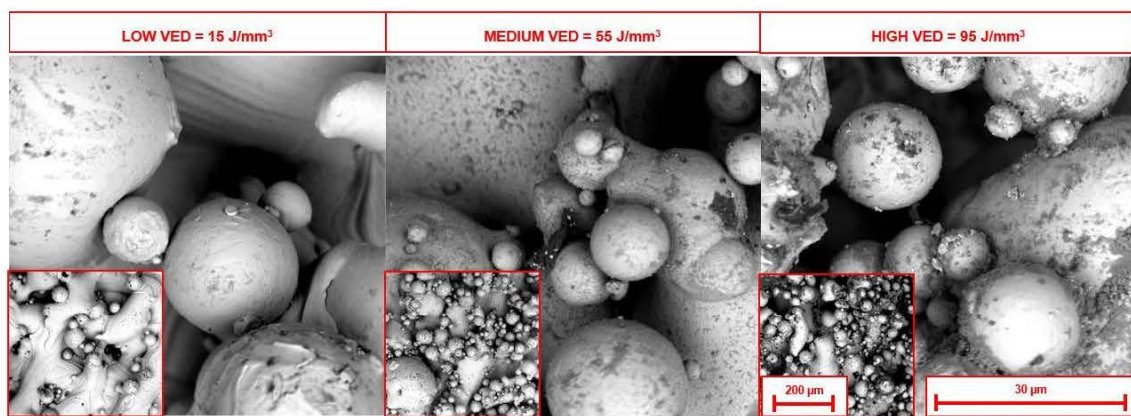
Introduction

Titanium-based alloys, particularly Ti-6Al-4V, are the most commonly used materials for orthopaedic implants, due to properties such as low cytotoxicity and high mechanical strength (1–4). However, in spite of widespread clinical use, challenges remain in the use of Ti-6Al-4V for orthopaedic implants, particularly with respect to implant-bone fixation. Successful orthopaedic implant fixation requires good osseointegration, with osseointegration being defined as the formation of a direct structural and functional connection between living bone and the surface of a load-bearing implant (5–7). Thus, for permanent fixation, the host bone must be active enough to form a stable chemical bond with the orthopaedic implant surface. Ti-6Al-4V surfaces exhibit low cytotoxicity, but unfortunately are also bio-inert, and so do not interact well with host bone cells; only weak interfacial bonds are formed following implantation, leading to inferior long term fixation (8–11). Patients with so-called poor bone stock (bone with low bio-activity) due to pre-existing conditions (e.g. osteoporosis or atypical bone anatomy) often require implants with extra osseo-inductive features such as bone screws or surface patterning to enhance bone formation processes at the implant-bone interface (12–14). Conventional implant manufacturing processes cannot accommodate the need for supplementary features or patient-specific implants, however, advances in additive manufacturing now allow for the production of previously un-manufacturable complex shapes, structures and features.

Additive manufacturing (AM) methods such as selective laser melting (SLM) are becoming increasingly attractive for the fabrication of customised implants. SLM can produce highly complex components, the designs of which can be directly modelled from patient data (e.g. Magnetic Resonance Imaging or Computed Tomography scans). SLM fabrication occurs as follows; first the 3D CAD (Computer Aided Design) model is prepared and sliced into 2D layers of specified layer thickness. Within the SLM build chamber, thin layers of pre-alloyed powders are spread onto a build platform, and a high energy laser beam scans over the powder bed following the pattern of the sliced CAD model, at a set speed. The high energy laser beam melts the powder particles, forming a melt pool (also referred to as a scan track, similar to a weld track) which solidifies rapidly (<<0.1s). Once the layer is complete, the build platform is moved down by one layer and recoated with powder. The process is repeated, resulting in the layer-wise production of the component. Commonly used process parameter ranges are tabulated in Table 1.

3

Table 1. Process parameter ranges commonly used for SLM Ti-6Al-4V (15–21)

Process parameter	Common usage range
Layer thickness	20 - 50 μm
Particle size range	15 - 45 μm
Laser power	80 - 280 W
Laser scan speed	200 - 1200 mm/s
Atmosphere	Nitrogen or Argon

SLM Ti-6Al-4V implant functionality can be modified at various stages, for example; 1) during the design stage, when features can be added into the 3D models, 2) during fabrication, by manipulating the SLM processing parameters, or 3) through various post-processing treatments. At this stage, it is clear that the choice of parameters in the SLM fabrication stage has an enormous influence on final Ti-6Al-4V properties (15,22–29), due to their effect on phase formation. Ti-6Al-4V has an allotropic temperature of approximately 995°C (30–34), with its phase diagram shown in Fig 1.
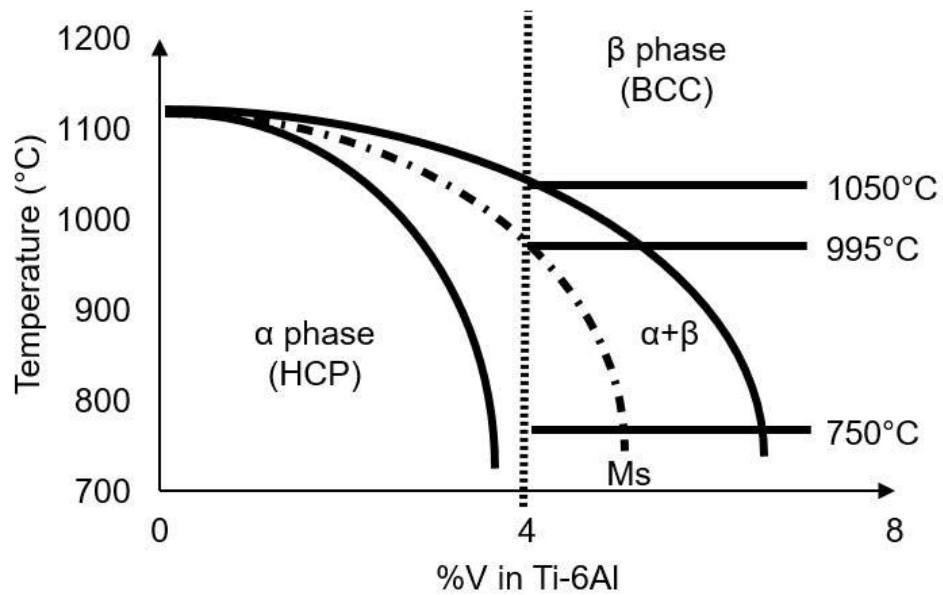
Fig 1. Equilibrium Ti-6Al-4V phase diagram

4

'As-built' SLM Ti-6Al-4V components characteristically have complex thermal histories due to the extreme heating, melting and cooling rates intrinsic to the process – which also locally vary based on component geometry. Cooling rates within the SLM melt pool can range between 12000 and 40000°C/s depending on the amount of energy supplied (35,36), and these extreme cooling rates through the transus temperature produce microstructures composed mainly of fine grained acicular α' Ti-6Al-4V (4,36–40). Additionally, the transfer of heat from the molten zone into the surrounding powder causes dendrite formation. The high energy laser beam, while scanning over each layer, generally penetrates through to previous layers, resulting in each layer undergoing multiple heating and cooling cycles. Therefore, fine microstructural evolution occurs during building due to the transfer of heat from the molten zone into the surrounding powder, with dendrites forming perpendicular to the applied layer, allowing vertical crystal growth through several layers (28). These columnar β grain structures aligned along the print height can lead to anisotropy particularly with respect to tensile strength (41). The martensitic α' phase present in as-built SLM Ti-6Al-4V is associated with increased susceptibility to corrosion in comparison to the stable β phase partly due to a less stable TiO_2 oxide layer (4,42), however, passive corrosion current density has been shown to increase with α' to β phase ratio, due to the formation of a micro-galvanic cell between the two phases – which is important to consider in the choice of post heat treatments aimed at decomposition of the α' phase into the stable α or β phases (43). The martensitic phases and build-up of residual stresses from the layer-wise variations in cooling rates necessitate post-processing stress relieving heat treatments below the transus temperature (generally at 800°C).

Within the SLM process, many parameters can be altered, the most important of which are laser power, laser scan speed, layer thickness and hatch spacing (distance between scan lines). These first order factors affect the volumetric energy density (VED) or thermal energy supplied per unit volume, as described in Equation 1 (44–47).

$$\textbf{Volumetric energy density } = \frac{\textbf{Laser power (W)}}{\textbf{laser scan speed } \left(\frac{\textbf{mm}}{\textbf{s}}\right) \textbf{ x hatch spacing (mm) x layer thickness (mm)}} \frac{\textbf{J}}{\textbf{mm}^3} \qquad (1)$$

Certain microstructural and mechanical properties of SLM Ti-6Al-4V can be produced/tuned with careful control of the process parameters per Equation 1, and it may be possible to fabricate SLM Ti-6Al-4V implants that better support the functions and properties of natural bone than conventionally produced implants. To better utilise the potential of SLM, we must first come an understanding of how properties change with respect to process parameters chosen.

Previous work in the field includes that of Pattanayak et al (48), and Sallica-Leva et al (49) examining the SLM fabrication of Ti-6Al-4V using EOS M270 machines. Pattanayak et al examined the interplay of laser scan speed, and hatching pattern, and showed that fully dense thin plates could be obtained when maintaining

5

a laser power to laser scan speed ratio of above 0.5, with a hatch spacing smaller than the laser diameter (48), while Sallica-Leva et al examined the relationship between energy input and porosity and determined that three main porosity levels can be produced, which are produced with changes in energy input (49). This is in agreement with the work of Qiu et al (Concept Laser M2 Cusing), Song et al and Thijs et al. (47,50,51). However, it should be noted that the work of Song et al and Thijs et al examine SLM Ti-6Al-4V produced with in-house constructed SLM machinery. Porosity in SLM Ti-6Al-4V has been shown to negatively affect fatigue strength (specifically micron sized pores) (36,38,52), while residual stresses have been shown to affect fatigue crack growth (34). Shunmugavel et al further showed that the fracture mode of SLM (SLM 125^{HL}) Ti-6Al-4V is transgranular due to low ductility (53). The work of Chen et al (EOS M280, the same machinery as used in this work) indicates that apart from the process parameters, build location/direction also affect SLM Ti-6Al-4V properties (54). Their investigations showed that while Young's moduli did not vary across the planes, the hardness of the x-plane (perpendicular to the build plate as well as the scanning directions) was approximately 20% lower than that of the other planes, and showed reduced corrosion resistance due to high porosity, supporting the work of Murr et al (2).

In this study, Ti-6Al-4V samples were produced using 20 different combinations of laser scan speed and laser power. The properties of these samples were compared to those of samples produced using the process parameters recommended by EOS, i.e. 280 W and 1200 mm/s (referred to as EOS DEF), and wrought Ti-6Al-4V samples (referred to as WROUGHT). The range of laser scan speeds and laser powers was chosen with reference to key works in the field, as seen in Table 2. The wide range of laser powers (100 – 400 W) and laser scan speeds (200 – 1550 mm/s) used was used here to set the outer limits for process window investigations. The surfaces of the samples (parallel to the build plate) were examined with respect to their surface morphology, porosity, hardness and roughness, as well as their electrochemical behaviour in simulated body conditions. While the optimal surface parameters for osseointegration, and therefore the target properties for orthopaedic implants, are yet undefined (55–58), the testing of Ti-6Al-4V surfaces produced by each SLM parameter combination will allow for the establishment of a process/property map for SLM. Current analyses of interactions between parameters have been completed for other processes and materials but little exists for Ti-6Al-4V and SLM, and not to the extent examined in this study. This data bank is necessary to inform future experiments and printing guidelines, and the future usage of SLM for orthopaedic implants and personalised medicine.

6

Table 2. Selective laser melting process parameters used in previous studies of Ti-6Al-4V (30,34,36,50,52,59,60). GA indicates that the powders were gas atomised, while PA indicates that the powders were plasma atomised.

Study	Machine	Laser scan speed (mm/s)	Laser power (W)	Layer thickness (µm)	Average particle size/ range (µm)
Simonelli et al., 2012 (36)	Renishaw AM250	225	157	50	15 - 70 (PA)
Song et al., 2012 (51)	Realiser 250	200 - 1600	110	30	-
Leuders et al., 2013 (34)	SLM 250HL	450	100	30	40
Qiu et al., 2013 (50)	Concept Laser M2 Cusing	800 - 1500	150 - 200	20	20-50 (GA)
Edwards and Ramulu, 2014 (52)	MTT 250	200	200	50	30 (GA)
Liu et al., 2014 (59)	SLM 250HL	710	175	30	43 (GA)
Gong et al, 2014 (61)	EOS M270	120 - 1560	40 - 160	30	25-45
Xu et al., 2015 (60)	SLM 250HL	686	375	30	15 - 25 (GA)
Mower and Long, 2016 (62)	EOS M280	-	-	30	15 - 45
Li et al, 2017 (63)	EOS M280	950 - 1550	150 - 190	30	33.77
Shang et al, 2017 (64)	EOS M280	800 - 1200	195	20	24 - 59
Ran et al, 2018 (65)	EOS M280	700	400	20	15 - 45

Materials and methods

Sample fabrication

Ti-6Al-4V samples were produced using an EOS M280 system (EOS GmbH, Germany) and pre-alloyed spherical Ti-6Al-4V powder (size range 1-53 µm (Falcontech, China)) produced through gas atomisation. A sand-blasted Ti-6Al-4V build plate was used as a substrate and pre-heated to 100°C during printing. The fabrication process took place in an argon gas atmosphere with an oxygen content of 1300 ppm, as measured prior to printing. Fixed processing parameters were as follows; hatch spacing of 0.14 mm, recoat

7

layer thickness of 30 µm, beam offset at 0.015 mm, and stripe width at 5 mm. All samples were produced using the continuous island scan strategy. Samples were fabricated using the laser power and laser scan speed recommended by the manufacturer (EOS GmbH), and are referred to here as the EOS DEF samples. Other samples were fabricated using a range of laser scan speeds and laser powers, resulting in samples built with VED ranging from 15 J/mm^3 to 240 J/mm^3 (Table 3.) – each parameter combination is named MOD (for modification) followed by a number.

Table 3. Process parameters used to produce SLM Ti-6Al-4V specimens in this study (VED: Volumetric energy density in J/mm^3, MOD is the naming convention given for modification).

Laser scan speed (mm/s)	Laser power (W)				
	80	100	120	200	280
200	MOD 11 VED = 95	MOD 6 VED = 120	MOD 8 VED = 145	MOD 5 VED = 240	MOD 13 VED = 330
500	MOD 12 VED = 40	MOD 15 VED = 50	MOD 9 VED = 55	MOD 16 VED = 95	MOD 14 VED = 135
1000	MOD 18 VED = 20	MOD 19 VED = 25	MOD 20 VED = 30	MOD 21 VED = 50	MOD 1 VED = 65
1200	MOD 10 VED = 15	MOD 17 VED = 20	MOD 7 VED = 25	MOD 3 VED = 40	EOS DEF VED = 55

Sample characterisation and testing

Following fabrication, samples were prepared as though for implantation. The samples were stress relieved by heating at 800°C for 2 hours in a vacuum furnace (cooled to room temperature in furnace), and cut from the build plate using electrical discharge machining (EDM). SLM Ti-6Al-4V is rarely used without stress relieving procedures, as the temperature gradients produced during fabrication cause significant amounts of residual stress to build up in the bulk – this necessarily causes some amount of α' martensite phase decomposition. Wrought Ti-6Al-4V control samples were also treated at 800°C for 2 hours (referred to as WROUGHT). All samples were then ground with ethanol and water using successively finer grit silicon carbide paper (180 to 2400), and polished using Struers OP-S® and Struers MD-CHEM® cloth. All tests were conducted on sample surfaces parallel to the build plate, or the XY plane in ASTM terminology. The preparation strategy and test surfaces were chosen to approximate pre-implantation implant surfaces, however,

it is important to note that as orthopaedic implants involve curvature in the x, y and z axes, it is unproductive to complete testing in all axes at this initial stage of data collection. Samples were labelled according to the parameter combination used to produce them (per Table 3.), e.g. SLM Ti-6Al-4V samples produced using a laser scan speed of 200 mm/s and a laser power of 90 W were labelled as MOD 11 samples.

Imaging of all samples was carried out using an FEI Phenom scanning electron microscope (SEM) operating at 5k V. A Bruker D8 Advance X-ray diffractometer was used to perform x-ray diffraction (XRD) on samples. A Cu Kα radiation source was used, with analysis performed at 40 kV and 40 mA. The diffraction angle range used was between 30° and 100°, with a step increment of 0.5° and a time step of 0.25 seconds. The obtained spectra were compared to reference data from the International Centre for Diffraction Data using DIFFRACplus EVA software (AXS, Bruker, Karlsruhe, Germany).

Average surface roughness (Ra) was analysed using a Veeco Wyko NT1100 optical profilometer. The samples were imaged using vertical shift interference (VSI) mode, 1.0x magnification, 1.0x laser scan speed and a threshold of 0.1%. The back scan and the length were set at 200 μm and 500 μm. 5 measurements were taken for each sample group, with re-grinding and polishing steps following each measurement (i.e. multiple layers were examined).

Porosity was determined using optical microscopy, rather than porosimetry techniques, due to the nature of the porosity expected; the non-connected (and stochastic) pores are likely to contain unmelted or partially melted particles, as there is no scope for particle removal during or following the formation of these pores. The agglomeration of particles within these pores affects the measurement of density and porosity through displacement techniques or porosimetry respectively, and thus porosity was determined through optical analyses. All samples were sonicated for 3 minutes in ethanol, dried with compressed air, and imaged using an Olympus GX51 optical microscope at 5x magnification. Image analysis (to determine % porosity and average pore area) was carried out using ImageJ (v1.50b) (66), an image analysis software created by Wayne Rasband of the National Institutes of Health (Bethesda, MD, USA) – this software is commonly used in biomaterials research. Each image was opened in ImageJ, split according to colour channel, then manually thresholded. The 'Analyse Particles' feature of ImageJ was then used to count and size the pores (in terms of 2D area), with a minimum pore area set as 10 μm^2, and a minimum circularity set as 0.5 (i.e. more than 50% circular). Three images (and measurements) were taken for each category, with re-grinding and polishing steps following each measurement. Sample hardness was measured using a Wilson Rockwell hardness tester. A 120° diamond spheroconical indenter (C Rockwell scale) was used with a load of 150 kg. 10 measurements were made for each category.

9

Electrochemical testing was carried out in a double-chambered three-electrode electrochemical cell connected to a Biologic VMP-3Z potentiostat. All samples were mounted in epoxy, with the exposed surface acting as the working electrode, with copper tape or wires extending from the rear to allow voltage measurement. A platinum mesh was used as the counter electrode, and a saturated calomel reference electrode was placed in a Haber-Luggin capillary extending to within 5 mm of the sample surface. A biologically relevant media was used as the electrolyte to approximate in vivo conditions - minimum essential media (MEM) was made up from powder (Gibco® GlutaMAX™) (1 packet added to 1L of water with 2.2 g of sodium bicarbonate), and the pH of this solution was adjusted with 5% HCl/1M NaOH to pH 7.2 ± 0.2. The composition and ion concentrations present in this solution can be seen in Supplementary Table 1. The electrolyte was maintained at 37°C using a circulating water bath. All samples were left to rest for 10 minutes minimum at open circuit potential (OCP), following which potentiodynamic polarisation was carried out from − 150 mV / Eoc to 1.0 V / Eref (reference electrode potential) with a scan rate of 1 mV/s.

Results

Morphology and porosity of as-produced and polished SLM Ti-6Al-4V surfaces

XRD analysis of samples as compared to references from the International Centre for Diffraction Data (PDF Refs. 01-072-5007, 00-044-1294, 00-022-1058 and 00-044-1288) indicated that all samples displayed evidence of α phase Ti peaks and minimal evidence of β phase Ti peaks (Fig S1.). Each process parameter combination produced samples with majority HCP α phase Ti-6Al-4V. Immediately following building, SLM Ti-6Al-4V is composed predominantly of acicular α' phase (50,67–69), but following stress relieving procedures, a significant portion of this metastable α' phase decomposes into the stable α phase.

The uppermost layers of all of the stress relieved, unpolished surfaces were covered in partially melted particles, as seen in Fig 2. As previously mentioned, the outer layers of SLM Ti-6Al-4V experience different cooling rates to the bulk, due to fewer re-melting/re-cooling cycles caused by laser penetration. Heat energy dissipates readily into the surrounding powder, leaving partly melted/fused particles across the layers. Notably, more partly fused particles were observed along the z-plane edges of SLM Ti-6Al-4V, as compared to the XY topmost layer (parallel to the build plate). The amount of partially fused particles on the outer layers are also influenced by powder splash caused by the laser beam diameter (spot size) and hatch spacing used. The samples produced with low VED (< 50 J/mm^3) had comparatively fewer partially melted particles across their x/y surfaces than those produced with higher VED (> 55 J/mm^3), likely due to comparatively exaggerated cooling rates/heat transfer between the final layer and the surrounding powder caused by the higher thermal energy supplied per unit volume. The production of rough outer surfaces is near unavoidable with SLM, and

10

59

thus these outermost layers are generally removed prior to usage. As-built surface roughness, however, is important to consider with respect to the future reduction of post-processing treatments.
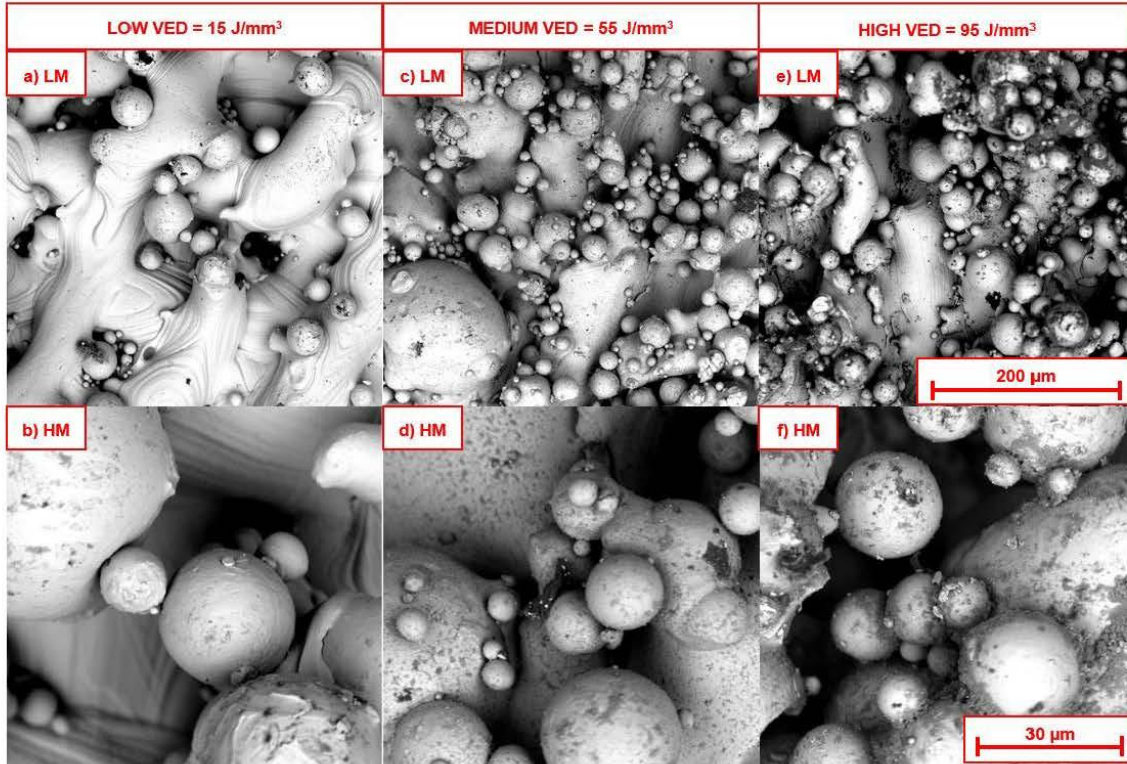

Fig 2. Scanning electron micrographs of the as-produced (as selective laser melted) surfaces, showing: a, b) Specimen prepared with low energy density (MOD 10: 80 W, 1200 mm/s, VED = 15 J/mm^3) at low and high magnification, c, d) Specimen prepared with intermediate energy density (EOS DEF: 280 W, 1200 mm/s, VED = 55 J/mm^3) at low and high magnification, e, f) Specimen prepared with high energy density (MOD 16: 200 W, 500 mm/s, VED = 95 J/mm^3) at low and high magnification

Following the grinding back and polishing of the uppermost XY layer of the samples, distinct variations in surface appearances could be observed even without etching. Black dots were seen on the majority of sample surfaces produced by each process parameter combination, as seen in Fig 3, indicating the presence of pores formed through either gas entrapment or accumulated layer-wise defects produced during fabrication.

The sample surfaces in the top left quadrant of Fig 3., i.e. those produced with low laser power/low laser scan speed exhibited irregular distributions of pores and defects. The combination of high laser scan speed and low laser power have the layer-wise effect of providing insufficient energy to fully melt all particles, leaving partially melted particles across each layer, affecting the deposition of subsequent layers. Insufficient powder consolidation may be partly fixed through the use of multiple laser passes per layer (increases costs), or

11

60

avoided through the careful balancing of process parameters in the first instance.
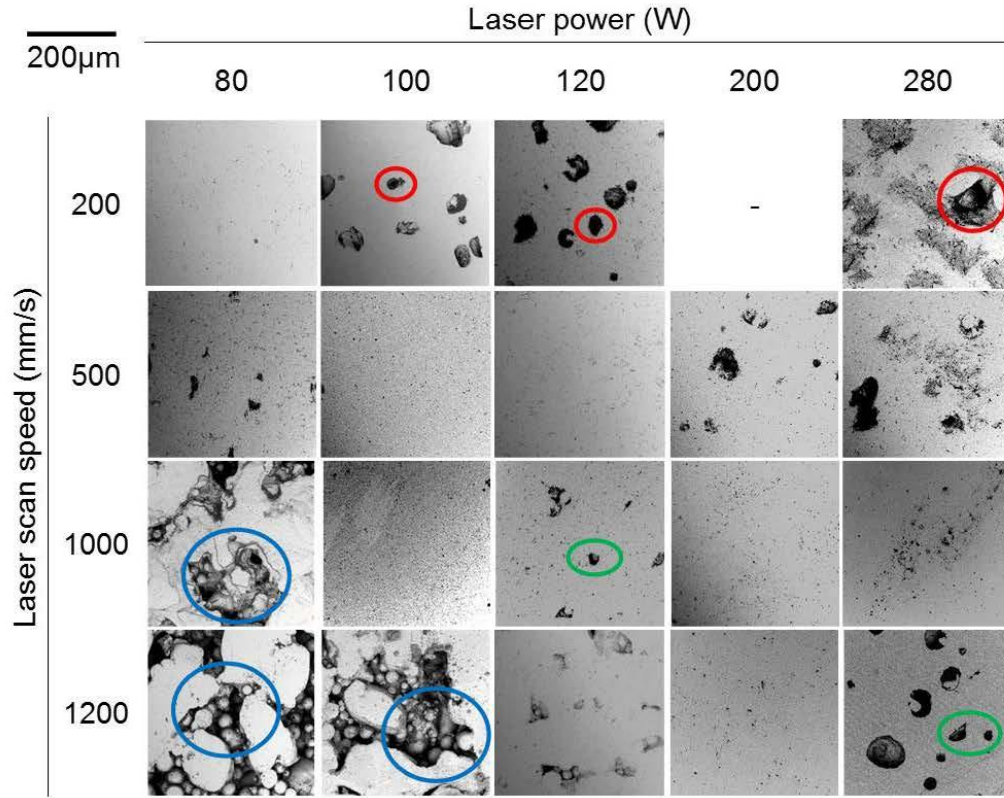
Fig 3. Secondary electron micrographs of polished surfaces corresponding to various laser parameter combinations. Burn-through pores circled in red, lack of fusion pores (with partially melted particles) circled in blue, and ideal pores circled in green.

Increasing laser scan speed from 200 mm/s to 1200 mm/s while keeping laser power constant (i.e. top to bottom on Fig 3.) affected powder consolidation. At low laser power (80W), increasing laser scan speed was accompanied by larger proportions of incompletely melted particles scattered throughout build height, as well as large gaps where completely fused layers were not able to form. At intermediate and high laser powers (100-280W), increases in laser scan speed had a roughly parabolic effect on the quantity of manufacturing defects. At low laser scan speeds (200 - 500 mm/s), laser powers of 100-200 W resulted in the supply of excessive local thermal energy, causing the formation of keyhole pores within the samples. At higher laser scan speeds (> 500 mm/s), the energy supplied was more evenly spread, reducing the number of keyhole pores, however the number of lack of fusion (LoF) and metallurgical pores increased. LoF and metallurgical pores form due to fast cooling, preventing gas escape from the melt pool. At the upper limits of laser scan speed (1200 mm/s), porosity again increased – the combination of intermediate laser power with high laser

scan speed resulted in large sections of incompletely melted particles. At high laser power (280 W), high laser scan speeds produced samples with large quantities of keyhole pores as opposed to metallurgical pores. This is visualised graphically in Fig 4.
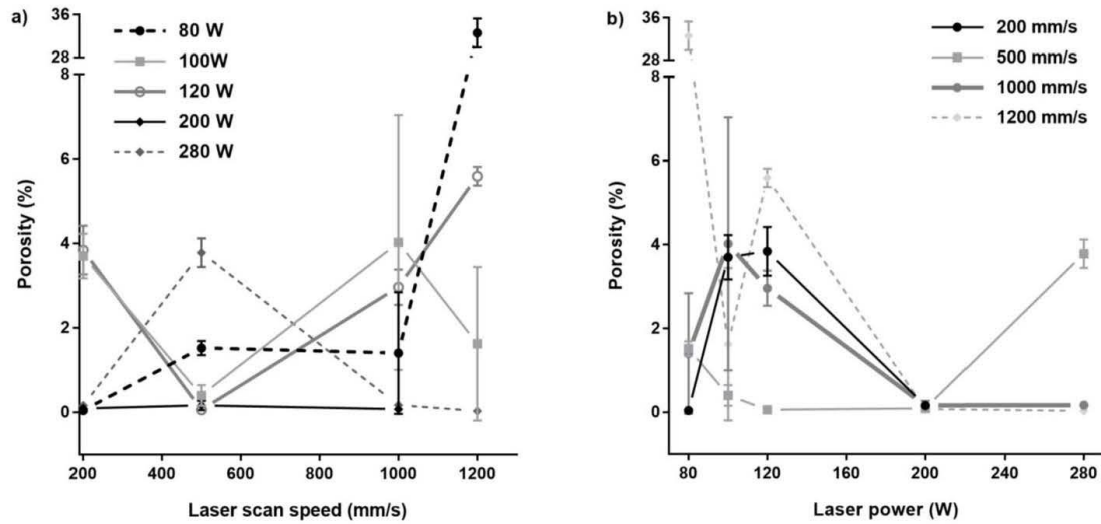
Fig 4. Average porosity (in %) produced as a function of selective laser melting parameter combinations, a) showing porosity as a function of laser scan speed, b) showing porosity as a function of laser power.

The EOS DEF settings (80 W, 1200 mm/s, VED = 55 J/mm^3) produced samples with both the lowest percent porosity and the smallest average pore areas, of 0.03 $\pm$ 0.01 % and 43.8 $\pm$ 4.1 μm^2 respectively. The largest average pore areas and percent porosity of 3383.6 $\pm$ 246.6 μm^2 and 32.59 $\pm$ 2.72 % were produced with the MOD 10 settings (80 W, 1200 mm/s, VED – 15 J/mm^3). Interestingly, both EOS DEF and MOD 10 samples were produced using a laser scan speed of 1200 mm/s but with the highest and lowest laser power respectively (80 and 280 W). Though pore shape irregularity impedes the precise quantitative comparison of pore area, a qualitative comparison can be made between the pores produced using each combination. Porosity obtained in samples formed with different VEDs can be seen in Fig 5.

13
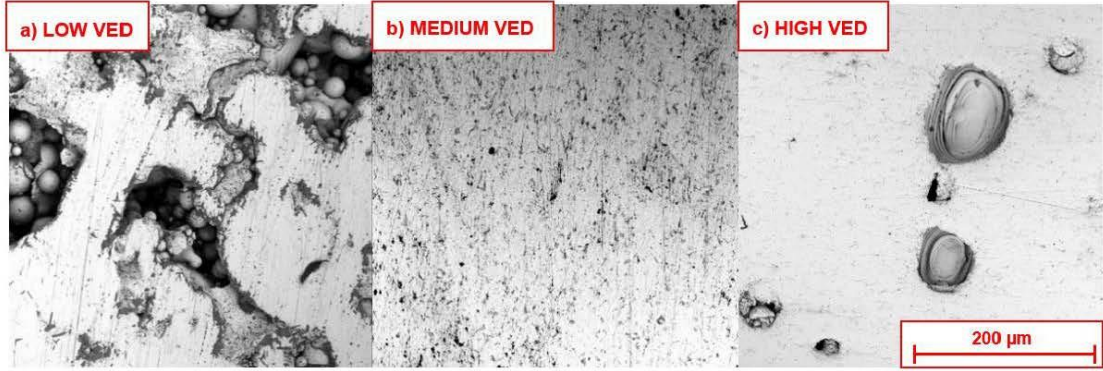
Fig 5. Secondary electron images of pore type with respect to energy density range. a) representative pores produced at low energy density (80 W, 1200 mm/s, VED = 15 J/mm^3), b) representative pores produced at intermediate energy density (280 W, 1200 mm/s, VED = 55 J/mm^3) and c) pores produced at high energy density (200 W, 500 mm/s, VED = 95 J/mm^3).

As expected, the % porosity produced using each parameter combination was somewhat linked to calculated VED. Samples produced using low VEDs, 15 to 40 J/mm^3, exhibited large and irregular pores, as well as incompletely melted particles. The highest VEDs, 70 to 140 J/mm^3, formed samples with small, regular pores with very few unmelted particles. The lowest porosity was obtained using intermediate VEDs, between 40 and 60 J/mm^3. This is in direct opposition to previous work by Bertoli et al (44), El Sayed et al (15) and Song et al (27), who state that ideal porosity is produced when the VED is maintained at above 100 J/mm^3, between 90-130 J/mm^3 and between 120-140 J/mm^3 respectively. A contour map of porosity arising from the combination of various laser scan speeds and laser powers can be seen in Fig 6, alongside data from Gong et al (61) and Song et al (51).
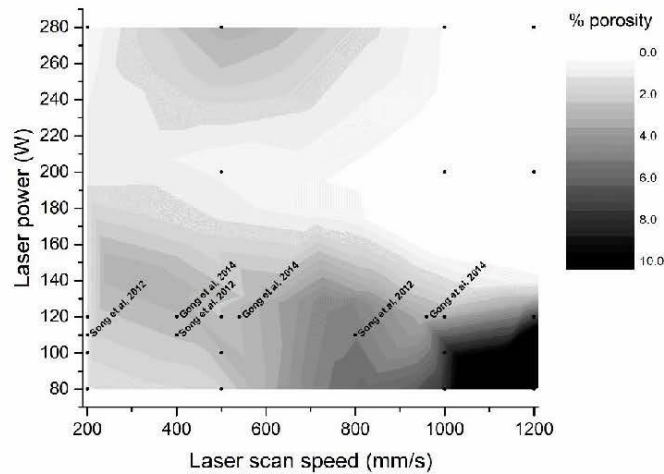
Fig 6. Porosity contour map for SLM Ti-6Al-4V with respect to laser power and laser scan speed

While a general relationship was observed between calculated VED and porosity percentage, it is important to note that the individual parameters contributing to VED i.e. laser power and laser scan speed, may have a larger influence on final porosity. Samples built using the same VED but with differing parameters (i.e. different laser scan speed and laser power resulting in the same VED) displayed different porosity levels, indicating that the interplay of the process parameters had a larger influence on porosity than the calculated VED value itself. Specifically, the parameter combinations used to build MOD 12 (80 W, 500 mm/s) and MOD 3 (200 W, 1200 mm/s) supplied the same VED of 40 J/mm^3, but these samples displayed differing porosity percentages of 1.52 ± 0.17 % and 0.07 ± 0.01 % respectively.

Variations in roughness and hardness of SLM Ti-6Al-4V according to process parameter interplay

This study examined the SLM fabrication of Ti-6Al-4V with a view to ultimately producing customised orthopaedic implants for patients. Thus, all samples were polished as per guidelines for implant materials (ASTM F1108b). However, significant differences in roughness were observed even following polishing. Layer-wise balling can affect subsequent layer re-coating and thus affect the bulk and final surface topography.

A large range of surface roughness was produced within the experimental process window, with average roughness, R_a, ranging from 0.40 ± 0.01 μm (MOD 3: 200 W, 1200 mm/s, VED = 40 J/mm^3) to 17.97 ± 4.10 μm (MOD 10: 80 W, 1200 mm/s, VED = 15 J/mm^3). Layer wise roughness arises in SLM Ti-6Al-4V due to both balling and incomplete particle fusion. Neither roughness nor hardness showed a significant relationship to VED as per Fig 6, in agreement with the work of Song et al [51] and Kruth et al [70] who reported balling at both high and low VED respectively. Rather, the combination of laser scan speed and laser power had a greater influence on roughness and hardness. The EOS DEF settings (280 W, 1200 mm/s, VED = 55 J/mm^3) produced surfaces with an R_a of 4.62 ± 0.9 μm.

15
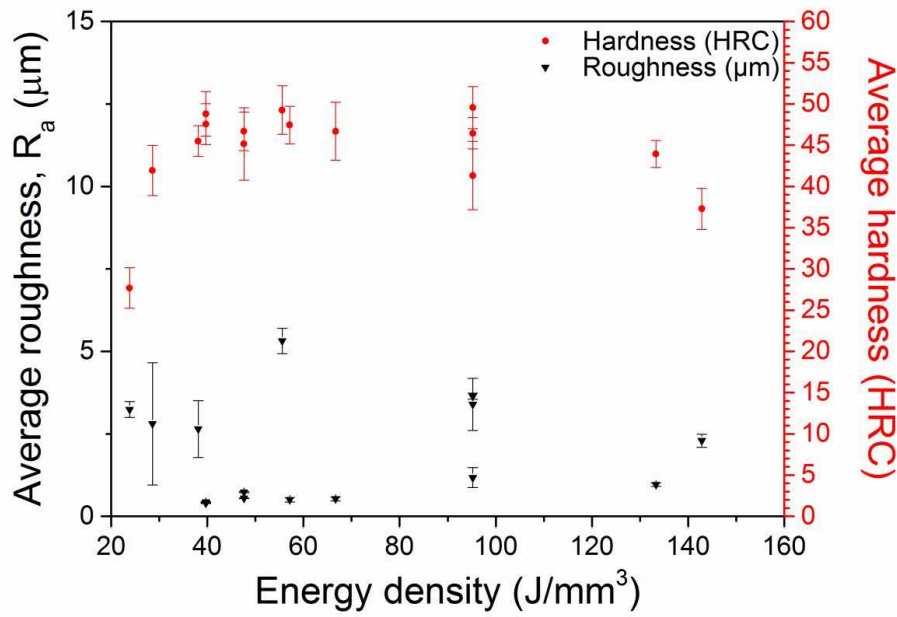
Fig 7. Average Rockwell Hardness (HRC) and roughness (Rₐ) as a function of VED used to prepare specimens

The experimental process window produced samples with average hardness ranging from 35.6 ± 2.0 HRC (MOD 7: 120 W, 1200 mm/s, VED = 25 J/mm^3) to 49.0 ± 2.9 HRC (MOD 6: 100 W, 200 mm/s, VED = 96 J/mm^3), with the EOS DEF settings (280 W, 1200 mm/s, VED = 55 J/mm^3) producing samples with a hardness of 48.7 ± 3.2 HRC, as compared to WROUGHT with a hardness of 36 HRC (28,69,71), as seen in Fig 6 (note that porosity above 10% prevents the accurate determination of hardness values and thus certain data sets were omitted). The high hardness of SLM Ti-6Al-4V arises due to the rapid cooling rate of the process. High hardness α' martensite nucleates at prior β grain boundaries and grows within parent β grains (67,71,72). Post-process stress relieving heat treatments have been shown to facilitate the decomposition of the α' phase into lamellar α+β microstructures through α precipitation at the α' boundaries (30,73). According to the XRD data (Supplementary Fig A), low intensity β peaks could be observed in all samples, indicating that while α' phase decomposition occurred during the stress relief treatment, the proportion of β phase is likely to be low. Certain parameter combinations produced samples with similar hardness to that of wrought Ti-6Al-4V; MODs 7 and 8 (MOD 7: 120 W, 1200 mm/s, VED = 25 J/mm^3, MOD 8: 120 W, 200 mm/s, VED = 145 J/mm^3) exhibited hardness values of 35.6 ± 2.0 and 36.6 ± 2.9 HRC respectively, despite having been fabricated with the highest and lowest laser scan speeds in the process window.

The relationship between surface roughness and hardness has not been extensively investigated with regards to SLM Ti-6Al-4V and bears further inquiry.

16

65

The effects of SLM process parameter interplay on corrosion resistance and repassivation characteristics

The corrosion behaviour of SLM Ti-6Al-4V has not received much attention in comparison to properties such as fatigue resistance or elastic modulus, however, understanding the corrosion characteristics of materials used in orthopaedic implants is of paramount importance. To date, relatively few groups have systematically examined the corrosion behaviour of stress relieved SLM Ti-6Al-4V under simulated physiological conditions. Dai et al report that as-built SLM Ti-6Al-4V exhibits reduced corrosion resistance as compared to wrought Ti-6Al-4V due to the majority α' microstructure (74).

The experimental process window produced samples with average hardness ranging from 35.6 ± 2.0 HRC (MOD 7: 120 W, 1200 mm/s, VED = 25 J/mm^3) to 49.0 ± 2.9 HRC (MOD 6: 100 W, 200 mm/s, VED = 96 J/mm^3), with the EOS DEF settings (280 W, 1200 mm/s, VED = 55 J/mm^3) producing samples with a hardness of 48.7 ± 3.2 HRC, as compared to WROUGHT with a hardness of 36 HRC (28,69,71), as seen in Fig 6 (note that porosity above 10% prevents the accurate determination of hardness values and thus certain data sets were omitted). The high hardness of SLM Ti-6Al-4V arises due to the rapid cooling rate of the process. High hardness α' martensite nucleates at prior β grain boundaries and grows within parent β grains (67,71,72). Post-process stress relieving heat treatments have been shown to facilitate the decomposition of the α' phase into lamellar α+β microstructures through α precipitation at the α' boundaries (30,73). According to the XRD data (Supplementary Fig A), low intensity β peaks could be observed in all samples, indicating that while α' phase decomposition occurred during the stress relief treatment, the proportion of β phase is likely to be low. Certain parameter combinations produced samples with similar hardness to that of wrought Ti-6Al-4V; MODs 7 and 8 (MOD 7: 120 W, 1200 mm/s, VED = 25 J/mm^3, MOD 8: 120 W, 200 mm/s, VED = 145 J/mm^3) exhibited hardness values of 35.6 ± 2.0 and 36.6 ± 2.9 HRC respectively, despite having been fabricated with the highest and lowest laser scan speeds in the process window.

The relationship between surface roughness and hardness has not been extensively investigated with regards to SLM Ti-6Al-4V and bears further inquiry.

The effects of SLM process parameter interplay on corrosion resistance and repassivation characteristics

The corrosion behaviour of SLM Ti-6Al-4V has not received much attention in comparison to properties such as fatigue resistance or elastic modulus, however, understanding the corrosion characteristics of materials used in orthopaedic implants is of paramount importance. To date, relatively few groups have systematically examined the corrosion behaviour of stress relieved SLM Ti-6Al-4V under simulated

physiological conditions. Dai et al report that as-built SLM Ti-6Al-4V exhibits reduced corrosion resistance as compared to wrought Ti-6Al-4V due to the majority α' microstructure (74), while Yang et al report that the inferior corrosion resistance of as-built SLM Ti-6Al-4V can be corrected through an appropriate heat treatment, i.e. holding at a sub-transus temperature for 2 hours (75). The electrochemical behaviour of the samples examined in this study, having undergone an appropriate heat treatment as recommended by Yang et al (i.e. held at 800°C for 2 hours), are thereby appropriate for use in predicting behaviour in the human body. More recently, Chiu et al studied the electrochemical behaviour of SLM Ti-6Al-4V formed with laser powers between 42 and 50 W and laser scan speeds between 100 and 400 mm/s, and indicate that the surface titanium oxide layer acts as an n-type semiconductor (76). However, all of these studies were conducted in simple solutions such as NaCl or Ringer's solution, and thus fail to incorporate the effects of other compounds found in human body fluids such as amino acids and vitamins.

In this study, changing the laser scan speed and/or laser power used in sample fabrication had a pronounced effect on electrochemical behaviour, even considering that specimens tested underwent stress relief heat treatment (Table 4.). Electrochemical testing was completed on multiple samples in simulated physiological conditions, i.e. at 37°C in MEM. The scatter in the current densities observed between samples of the same category indicate that factors apart from the laser scan speed and laser power affect electrochemical behaviour. It has been reported that SLM component properties such as porosity and roughness can vary spatially across the build plate (77), and thus the scatter in data is important to consider in any recommendations as to ranking parameter combinations.

18

Table 4. Corrosion properties of SLM Ti-6Al-4V produced with varied process parameters, as determined from potentiodynamic polarisation curves

| Specimen ID	Laser scan speed (mm/s)	Laser power (W)	VED (J/mm^3)	E_{corr} (mV$_{SCE}$)	i_{corr} (μA/cm^2)	Porosity (%)
WROUGHT	n/a	n/a	n/a	-451 ± 70	0.07 ± 0.03	n/a
EOS DEF	1200	280	56	-412 ± 23	0.10 ± 0.05	0.03 ± 0.01
MOD 1	1000	280	67	-348 ± 39	0.07 ± 0.06	0.17 ± 0.08
MOD 3	1200	200	40	-398 ± 76	0.13 ± 0.07	0.07 ± 0.01
MOD 6	200	100	95	-450 ± 64	0.13 ± 0.06	3.70 ± 0.53
MOD 7	1200	120	24	-158 ± 29	1.06 ± 0.14	5.59 ± 0.22
MOD 8	200	120	143	-473 ± 41	0.15 ± 0.07	3.84 ± 0.58
MOD 9	500	120	57	-615 ± 60	0.12 ± 0.08	0.06 ± 0.01
MOD 10	1200	80	16	-387 ± 30	2.32 ± 1.79	32.59 ± 2.72
MOD 11	200	80	95	-603 ± 42	0.09 ± 0.02	0.04 ± 0.01
MOD 12	500	80	38	-497 ± 102	0.07 ± 0.02	1.52 ± 0.17
MOD 13	200	280	333	-567 ± 57	0.08 ± 0.05	0.16 ± 0.04
MOD 14	500	280	133	-572 ± 16	0.10 ± 0.06	3.78 ± 0.34
MOD 15	500	100	48	-578 ± 31	0.04 ± 0.01	0.40 ± 0.25
MOD 16	500	200	95	-532 ± 40	0.08 ± 0.06	0.09 ± 0.04
MOD 17	1200	100	20	-430 ± 28	1.37 ± 0.35	1.62 ± 1.82
MOD 18	1000	80	19	-355 ± 26	2.71 ± 0.41	1.40 ± 1.44
MOD 19	1000	100	24	-296 ± 32	0.54 ± 0.09	4.02 ± 3.02
MOD 20	1000	120	29	-466 ± 24	0.15 ± 0.04	2.96 ± 0.42
MOD 21	1000	200	48	-503 ± 43	0.10 ± 0.05	0.16 ± 0.11

As Ti-6Al-4V is a relatively inert alloy in terms of corrosion, the large variation in E_{corr} according to process parameters used is unusual and bears detailed examination. The samples with the lowest corrosion resistance of -615 ± 60 mV$_{SCE}$ (MOD 9: 120 W, 500 mm/s, VED = 60 J/mm^3) were fabricated using a well-balanced combination of laser power and laser scan speed, and the calculated VED equalled that of the EOS DEF settings. The current density for these samples was three times that of the samples with the lowest current densities of 0.04 ± 0.01 μA/cm^2 (MOD 15: 100 W, 500 mm/s, VED = 50 J/mm^3). Interestingly, the MOD 9 samples, while showing the highest corrosion rate, were found to have among the lowest % porosity (0.06 ± 0.01 %) and R$_a$ (0.53 ± 0.15 μm). This is visualised in Fig 8.

19
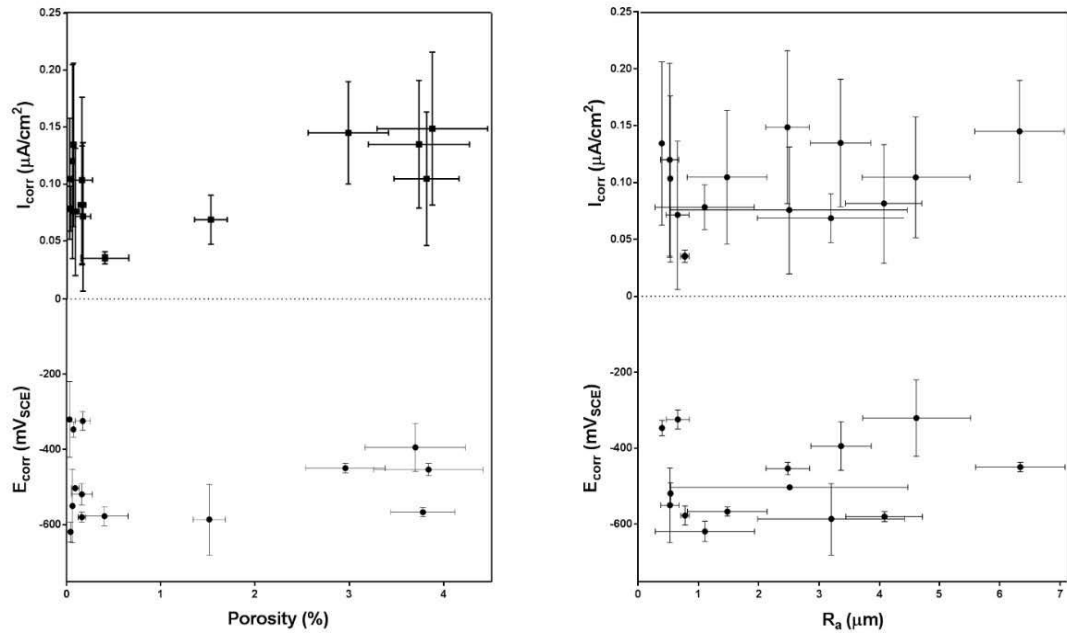
Fig 8. Porosity and E$_{corr}$ did not display a straightforward relationship, due to the presence of both partially melted particles within pores and alterations in surface chemistry through keyholing.

Of the SLM Ti-6Al-4V samples, 5 sample groups were notable for displaying drastically different electrochemical behaviour, with regard to the shape of the re-passivation window; these were produced with parameter combinations in the bottom left quadrant of the parameter combination matrix, indicating a combination of low laser scan speed and laser power, and energy densities below 30 J/mm^3. It can be inferred that the heterogeneity in surface morphology (particularly porosity) caused by incomplete particle melting due to low energy input leads to poor corrosion resistance and re-passivation, and may affect the formation of the surface oxide. Each group had similar I$_{corr}$ values, but significantly different E$_{corr}$ values – these are visualised in Fig 8. MOD 10 (80 W, 1200 mm/s), with the lowest VED of 15 J/mm^3, displayed the highest corrosion current density of 2.32 ± 1.79 µA/cm^2. MOD 7 (120 W, 1200 mm/s, VED = 25 J/mm^3) showed the least active E$_{corr}$ of -158 ± 29 mV$_{SCE}$. Comparatively, MOD 12 (80 W, 500 mm/s) with a slightly higher VED of 40 J/mm^3, showed a 'normal' re-passivation window, with an E$_{corr}$ of -497 ± 102 mV$_{SCE}$, in the range of wrought Ti-6Al-4V.

20

69
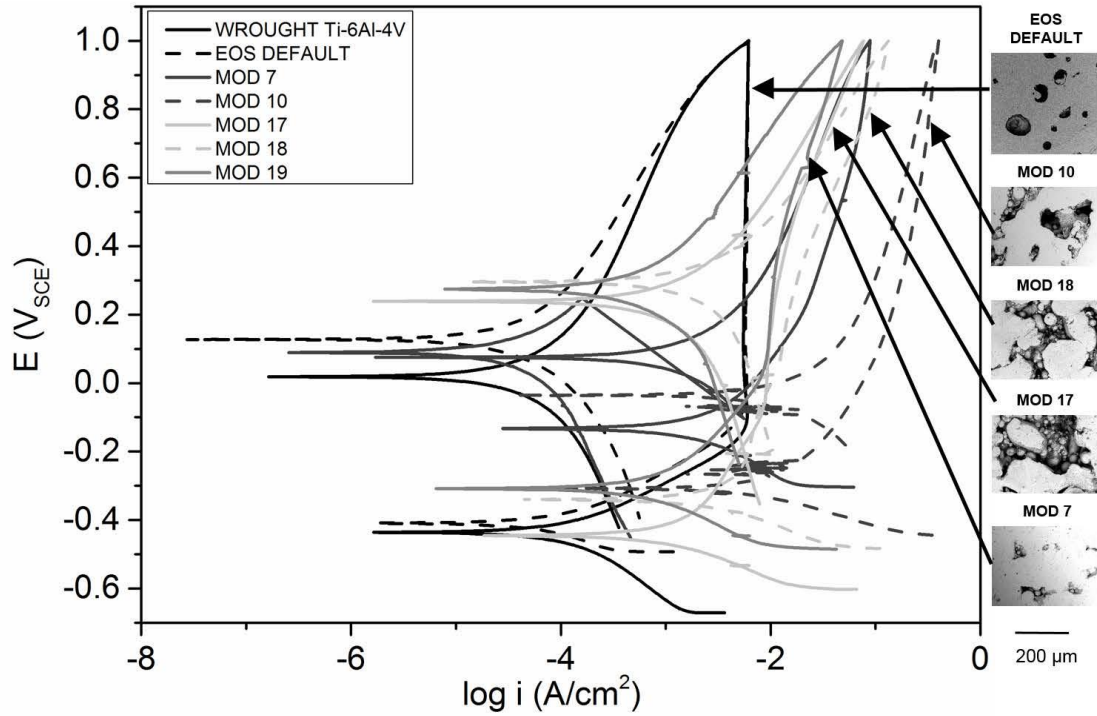
Fig 9. Representative cyclic potentiodynamic polarisation curves for specimens produced using various SLM parameter combinations, showing extremely altered repassivation behaviour.

This analysis however assumes that the active area of all the samples is the same – realistically the surface area due to pores may be much larger, and so the actual current density (as opposed to calculated current density) may be lower. The samples with the highest porosity (MODs 7, 10, 17, 18, 19) did display the highest current densities, as well as reduced ability to re-passivate, but appeared to have higher corrosion resistance than most of the other samples. The measurement of active surface area was out of the scope of this study, but it is clear that apparent current density (and apparent surface area) is more relevant when it comes to predicting Ti-6Al-4V implant behaviour in the body. Non-stochastic corrosion initiation is likely to have occurred, with pores acting as pre-existing pits, leading to crevice corrosion-like processes and random spikes in current density according to the pores 'activated'. However, no severe pitting was observed, even up to 2 mV$_{SCE}$, and so the actual likelihood of pitting corrosion in the body is low, even for the most active samples examined.

Discussion

To explain the generation of layer-wise roughness and porosity in SLM, it is necessary to understand the behaviour of the moving melt pool (17,26,44,70,78,79). As the laser beam interacts with the powder bed, a pool of molten Ti-6Al-4V is formed, and as the laser beam scans across the bed, the melt pool cools to form

21

70

a weld track. The cooling melt pool/weld track is subject to Plateau-Rayleigh instability due to perturbations arising from the extreme cooling rates of the melt pool – as the track cools, the melt pool is driven to break up into smaller droplets to reduce its surface energy and area. Should the level of this instability be too high, distinct 'balls' of Ti-6Al-4V will appear along the weld tracks (17,27,79). Within the moving melt pool, both surface tension and temperature gradients form, resulting in thermo-capillary convection flow (the Marangoni effect). Balling and partially melted particles can affect subsequent layer deposition and adherence. When subsequent layers are melted onto previous layers, there is potential for partially melted particles to be re-melted due to the multiple layer penetration of the laser, however, as the bulk forms, a random distribution of partially melted particles and pores will form throughout the build height. Once the track has solidified, small wavelike ripples are apparent on the weld tracks (79), as well as partially melted particles. Therefore, surface topographies and indeed porosity are unavoidable without the careful choice of processing parameters to maintain the dynamic equilibrium of the melt pool. This is shown schematically in Fig 10. Laser power and laser scan speed have the greatest effect on the melt pool, with increases in scan speed causing the size of the melt pool to increase, while increasing scan speed elongates/narrows and lowers the temperature of the melt pool (23). Increasing the overall VED is linked to comparatively more gradual cooling rates.
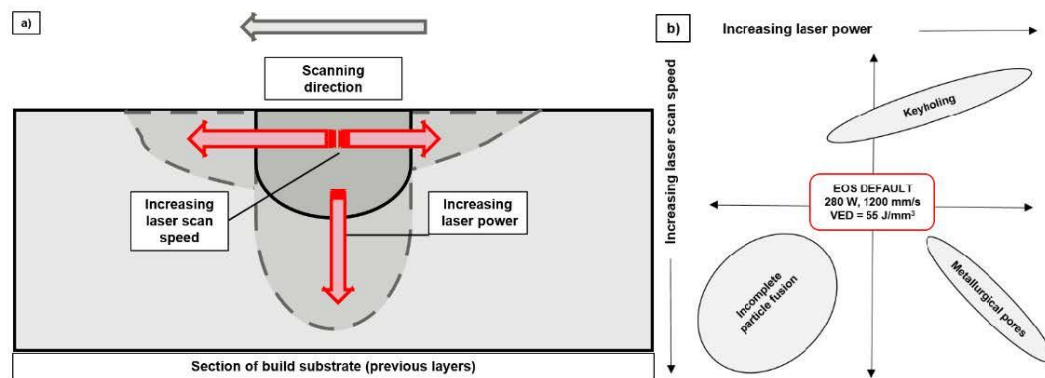
Fig 10. Changing laser scan speed or laser power affects melt pool depth during the selective laser melting build process, with a phenomenological diagram shown in a) and a graphical schematic of the specific defects formed shown in b).

Currently, there is little consensus in the biomedical community on the optimal porosity/roughness for osseointegration (80–82). The optimal roughness values for osseointegration have variously been reported as $R_a > 1$ μm, $R_a = 3$ to 5 μm and even $R_a > 5$ μm (6,83–85). With respect to the results of this study, it is clear that any of these roughness values can be achieved. With this understanding of how surface roughness, porosity, hardness and electrochemical behaviour changes with changes in laser scan speed and laser power, it is possible to choose the most appropriate laser scan speed and laser power to produce an SLM Ti-6Al-4V component with the required properties. However it should be noted that porosity and roughness have a

significant effect on wear and fatigue performance and thus future work should explore the changes in fatigue behaviour between Ti-6Al-4V built with various process parameter combinations. In the current study, each of the non-standard process parameter combinations used produced samples with one or more improved properties when compared to wrought Ti-6Al-4V, and so it is clear that sample properties can be tuned through careful manipulation of the SLM process parameters, leading to potential reductions in fabrication costs (energy) and lead time, as seen in Table 5.

Table 5. Summary of Ti-6Al-4V properties achieved using a variety of SLM process parameter combinations

Specimen ID	WROUGHT	EOS DEF	MOD 1	MOD 3	MOD 7	MOD 9	MOD 11
Laser scan speed (mm/s)	n/a	1200	1000	1200	1200	500	200
Laser power (W)	n/a	280	280	200	120	120	80
VED (J/mm^3)	n/a	56	67	40	24	57	95
Avg. E_{corr} (mV$_{SCE}$)	-451 ± 70	-412 ± 23	-348 ± 39	-398 ± 76	*-158 ± 29*	-615 ± 60	-603 ± 42
Avg. I_{corr} (µA/cm^2)	0.07 ± 0.03	0.10 ± 0.05	*0.07 ± 0.06*	0.13 ± 0.07	1.06 ± 0.14	*0.12 ± 0.08*	0.08 ± 0.02
Avg. R_a (µm)	n/a	4.62 ± 0.90	0.66 ± 0.19	*0.40 ± 0.01*	6.67 ± 1.26	*0.53 ± 0.15*	1.11 ± 0.82
Avg. HRC	36	48.7 ± 3.2	46.7 ± 3.5	46.7 ± 2.8	*35.6 ± 2.0*	46.9 ± 2.6	46.4 ± 1.9
Avg. porosity (%)	n/a	0.03 ± 0.01	0.17 ± 0.08	0.07 ± 0.01	2.48 ± 0.31	0.06 ± 0.01	*0.04 ± 0.01*
Avg. pore area (µm^2)	n/a	41.6 ± 3.3	*43.8 ± 4.1*	467.2 ± 35.5	2035.0 ± 133.2	286.5 ± 56.4	271.0 ± 45.3
Comment	Wrought Ti-6Al-4V	Manufacturers settings	Lowest I_{corr}, small pores	Lowest R_a	Least active E_{corr}, lowest hardness	Low I_{corr} and Ra	Low % porosity

Corrosion resistance must also be considered if choosing to increase surface roughness or porosity. Ti-6Al-4V normally exhibits high corrosion resistance due to its spontaneously formed passive oxides able to withstand the local bodily environment (i.e. joint fluid). SLM Ti-6Al-4V will necessarily behave differently to wrought Ti-6Al-4V, due to but not limited to the peculiarities of the melt pool and rapid solidification related solute segregation. As-built SLM Ti-6Al-4V is composed of majority α' phase, which is reported by some groups to be less resistant to corrosion (74). Following stress relieving procedures, the decomposition

of the metastable α' phase into lower energy α + β phases, the corrosion behaviour of SLM Ti-6Al-4V has been reported to more closely match that of wrought Ti-6Al-4V (86). Ti-6Al-4V is generally reported to have a predominantly TiO_2 passive layer and TiO/Ti_2O_3 sub-oxides, with small amounts of aluminium and vanadium oxides (87–89). However, bulk microstructure affects surface oxide formation. Some groups have reported that the solute partitioning between α and β phases in Ti-6Al-4V (Al segregates to the α phase while V segregates to the β phase) affects surface oxide formation, with vanadium oxide dissolution in the biphasic oxide film leading to cation vacancy generation and thus weakening of the film (87,90). The interfacial regions between the phases (both bulk and surface) are also reported to be more susceptible to corrosion (91). Thus, it is not clear which of the α' or mixed α+β phases are more desirable in terms of corrosion resistance. Changing the laser scan speed and/or laser power appear to have an effect on corrosion resistance and current density, not only through the characteristic changes in porosity and roughness, but also likely through changes in surface chemistry arising from keyholing or partial melting. SLM Ti-6Al-4V samples produced using laser power < 120W and laser scan speed < 1200 contained porosity > 1%, and displayed significantly narrowed repassivation windows (likely due to changes in the formation of the surface oxide), with increased corrosion current densities (>1 μA/cm2). Thicker oxide layers are accepted to be more protective against corrosion (88).

Following analysis of porosity, roughness and hardness, it was determined that there was little relationship between VED and final SLM Ti-6Al-4V properties. Despite this, VED is often used in the pre-fabrication stage to predict and differentiate the final properties of SLM Ti-6Al-4V produced with differing process parameters. It is more pertinent to choose individual SLM process parameters with an understanding of how these process parameters work together to produce the final Ti-6Al-4V product. Moreover, VED as it stands describes the immediate environment of the moving laser, and so is a layer-wise descriptor at best. It is important to reduce the dependence on VED as a design variable for SLM Ti-6Al-4V. This study was not without limitations, in large part due to the examination of top, or x-y, surfaces only. Future work should focus on curved surfaces and cross-sections for improved microstructural analysis.

The properties investigated in this study relate to the ultimate bio-activity of SLM Ti-6Al-4V. It is important to note that although the choice of parameters may require the sacrifice of certain features (i.e. lower porosity but higher corrosion resistance), implants may well be fabricated through SLM in two parts – the bulk vs. the shell. The properties of the shell, or outer layers, of the implant are the most important as they directly impact osseointegration and thus the achievement of successful long-term implant fixation.

24

Conclusions

Selective laser melting has the potential to produce effective and long-lasting customised Ti-6Al-4V orthopaedic implants, with the careful control of process parameters used during fabrication. Key findings regarding the effect of varying laser scan speed and laser power on SLM Ti-6Al-4V were as follows;

- The EOS DEF settings for Ti-6Al-4V (280 W, 1200 mm/s, VED = 55 J/mm^3) produced ± 23 mV and hardness of 48.7 ± 3.2 HRC.

- Each of the other process parameter combinations produced samples with one or more improved properties when compared to wrought Ti-6Al-4V, and so it is clear that sample properties can be tuned through careful manipulation of the SLM process parameters, leading to potential reductions in fabrication costs (energy) and lead time, as seen in Table 5.

- Changes in laser scan speed and laser power affect melt pool formation; the dynamic equilibrium of the melt pool is affected by surface tension and thermo-capillary convection flow. Increasing laser scan speed produces elongated melt pools with increased Plateau-Rayleigh instabilities, and higher likelihood of balling. Increasing laser power deepens the melt pool and increases the number of remelting/recooling cycles experienced by each layer. Laser scan speed and laser power must be balanced to ensure full powder consolidation.

- The combination of high laser scan speed (> 1000 mm/s) with low laser power (< 120 W) in the SLM fabrication of Ti-6Al-4V leads to poor powder consolidation due to the insufficient supply of thermal energy per unit volume. This results in porosity levels of above 15%, high roughness, low hardness and increased susceptibility to corrosion.

- The SLM fabrication of Ti-6Al-4V with low laser scan speed (< 200 mm/s) and high laser power (> 100W) results in the supply of excessive thermal energy per unit volume, and more specifically, increases in layer wise laser penetration depth and keyholing.

- The combination of intermediate laser power and laser scan speed produces the most homogeneous SLM Ti-6Al-4V surfaces, with low amounts of evenly distributed pores, low roughness and hardness/corrosion resistance similar to conventionally produced Ti-6Al-4V.

Presently, there is little consensus in the biomedical community on the optimal porosity/roughness for osseointegration (80–82); however once osseointegration is better understood, the results of this study can be used to choose SLM process parameters to produce Ti-6Al-4V implants with the required properties. For example, if osseointegration with Ti-6Al-4V implants is definitively found to be enhanced when surfaces have a minimum R_a of 0.5 μm and maximum porosity of 0.7%, then it is clear that a laser scan speed of 200 mm/s and laser power of 280 W could be used.

25

The present study examined the effects of altering laser scan speed and laser power on SLM Ti-6Al-4V, and provides a map of the SLM process with respect to achievable properties relevant to biomedical applications. The most consistent properties are observed in samples built with 'balanced' laser scan speed and laser power, i.e. MODS 9 (120 W, 500 mm/s), 11 (80 W, 120 mm/s), 16 (200 W, 500 mm/s), 20 (120 W, 1000 mm/s) and EOS DEF (280 W, 1200 mm/s). These parameters however are not the only ones which affect final component properties – other important SLM process parameters include spot size, scan strategy, particle characteristics, and temperature uniformity, as well as second order factors include defocussing distance, gas shielding and time between passes (92). Studies investigating the interplay of these additional SLM process parameters are required to build on the relationships observed in the current study.

Acknowledgements

26

References

1. Butscher A, Bohner M, Hofmann S, Gauckler L, Müller R. Structural and material approaches to bone tissue engineering in powder-based three-dimensional printing. Acta Biomater. 2011 Mar;7(3):907–20.

2. Murr LE, Martinez E, Amato KN, Gaytan SM, Hernandez J, Ramirez D a., et al. Fabrication of metal and alloy components by additive manufacturing: examples of 3D materials science. J Mater Res Technol. 2012 Apr;1(1):42–54.

3. Tan XP, Tan YJ, Chow CSL, Tor SB, Yeong WY. Metallic powder-bed based 3D printing of cellular scaffolds for orthopaedic implants: A state-of-the-art review on manufacturing, topological design, mechanical properties and biocompatibility. Mater Sci Eng C. 2017;76:1328–43.

4. Zhang LC, Attar H. Selective Laser Melting of Titanium Alloys and Titanium Matrix Composites for Biomedical Applications: A Review. Adv Eng Mater. 2016;18(4):463–75.

5. Branemark P-II. Osseointegration and its experimental background. J Prosthet Dent. 1983 Sep;50(3):399–410.

6. Shaoki A, Xu J, Sun H, Chen X, Ouyang J, Zhuang X, et al. Osseointegration of three-dimensional designed titanium implants manufactured by selective laser melting. Biofabrication. 2016;8(4):045014.

7. Karazisis D, Petronis S, Agheli H, Emanuelsson L, Norlindh B, Johansson A, et al. The influence of controlled surface nanotopography on the early biological events of osseointegration. Acta Biomater. 2016;53:559–71.

8. Cox SC, Jamshidi P, Eisenstein NM, Webber MA, Burton H, Moakes RJA, et al. Surface Finish has a Critical Influence on Biofilm Formation and Mammalian Cell Attachment to Additively Manufactured Prosthetics. ACS Biomater Sci Eng. 2017;3(8):1616–26.

9. Pucci JU, Christophe BR, Sisti JA, Connolly ES. Three-dimensional printing: technologies, applications, and limitations in neurosurgery. Biotechnol Adv. 2017;35(5):521–9.

10. Wang Z, Wang C, Li C, Qin Y, Zhong L, Chen B, et al. Analysis of factors influencing bone ingrowth into three-dimensional printed porous metal scaffolds: A review. J Alloys Compd. 2017;717:271–85.

11. Markhoff J, Krogull M, Schulze C, Rotsch C, Hunger S, Bader R. Biocompatibility and inflammatory potential of titanium alloys cultivated with human osteoblasts, fibroblasts and

macrophages. Materials (Basel). 2017;10(1):9–12.

12.   Shah FA, Snis A, Matic A, Thomsen P, Palmquist A. 3D printed Ti6Al4V implant surface promotes bone maturation and retains a higher density of less aged osteocytes at the bone-implant interface. Acta Biomater. 2016;30:357–67.

13.   Murr LE, Gaytan SM, Medina F, Lopez H, Martinez E, Machado BI, et al. Next-generation biomedical implants using additive manufacturing of complex, cellular and functional mesh arrays. Philos Trans A Math Phys Eng Sci. 2010 Apr;368(1917):1999–2032.

14.   Li Y, Yang W, Li X, Zhang X, Wang C, Meng X, et al. Improving Osteointegration and Osteogenesis of Three-Dimensional Porous Ti6Al4V Scaffolds by Polydopamine-Assisted Biomimetic Hydroxyapatite Coating. ACS Appl Mater Interfaces. 2015 Mar 18;7(10):150303141938004.

15.   El-Sayed M, Ghazy M, Yehia Y, Essa K. Optimization of SLM Process Parameters for Ti6Al4V Medical Implants. Rapid Prototyp J. 2018;

16.   Kao WH, Su YL, Horng JH, Chang CY. Tribological, electrochemical and biocompatibility properties of Ti6Al4V alloy produced by selective laser melting method and then processed using gas nitriding, CN or Ti-C:H coating treatments. Surf Coatings Technol. 2018;350(July):172–87.

17.   Chen Z, Wu X, Tomus D, Davies CHJ. Surface roughness in Selective Laser Melted Ti-6Al-4V alloy components. Addit Manuf. 2018;21(17):30273–7.

18.   FalconTech Co Ltd. Ti-6Al-4V powder - technical data sheet. Wuxi: FalconTech Co Ltd; p. 1671459.

19.   Heraeus Additive Manufacturing GmbH. Ti-6Al-4V powder - technical data sheet. Heraeus Additive Manufacturing GmbH; 2017.

20.   EOS GmbH. Ti-6Al-4V powder - technical data sheet. Munchen: EOS GmbH; 2011. p. 5.

21.   Arcam AB. Ti-6Al-4V powder - technical data sheet. Molndal: Arcam AB; 2014. p. 4–6.

22.   Liverani E, Toschi S, Ceschini L, Fortunato A. Effect of selective laser melting (SLM) process parameters on microstructure and mechanical properties of 316L austenitic stainless steel. J Mater Process Technol. 2017;249(November 2016):255–63.

23.   Shipley H, McDonnell D, Culleton M, Coull R, Lupoi R, O'Donnell G, et al. Optimisation of process parameters to address fundamental challenges during selective laser melting of Ti-6Al-4V: A review. Int J Mach Tools Manuf. 2018;128(January):1–20.

24.   Hanzl P, Zetek M, Bakša T, Kroupa T. The Influence of Processing Parameters on the

Mechanical Properties of SLM Parts. Procedia Eng. 2015;100:1405–13.

25. Mezzetta J. Process-Property Relationships of Ti6Al4V Fabricated through Selective Laser Melting. McGill University; 2016.

26. Masmoudi A, Bolot R, Coddet C. Investigation of the laser–powder–atmosphere interaction zone during the selective laser melting process. J Mater Process Technol. 2015 Nov;225:122–32.

27. Song B, Dong S, Liao H, Coddet C. Process parameter selection for selective laser melting of Ti6Al4V based on temperature distribution simulation and experimental sintering. Int J Adv Manuf Technol. 2012;61(9–12):967–74.

28. Khorasani AM, Gibson I, Goldberg M, Littlefair G. A survey on mechanisms and critical parameters on solidification of selective laser melting during fabrication of Ti-6Al-4V prosthetic acetabular cup. Mater Des. 2016 Aug;103:348–55.

29. Kurzynowski T, Chlebus E, Kuźnicka B, Reiner J. Parameters in selective laser melting for processing metallic powders. 2012;(February):823914.

30. Vrancken B, Thijs L, Kruth J-P, Van Humbeeck J. Heat treatment of Ti6Al4V produced by Selective Laser Melting: Microstructure and mechanical properties. J Alloys Compd. 2012 Nov;541:177–85.

31. Vrancken B, Thijs L, Kruth J-P, Van Humbeeck J. Microstructure and mechanical properties of a novel β titanium metallic composite by selective laser melting. Acta Mater. 2014 Apr;68:150–8.

32. Campanelli SL, Contuzzi N, Ludovico AD, Caiazzo F, Cardaropoli F, Sergi V. Manufacturing and characterization of Ti6Al4V lattice components manufactured by selective laser melting. Materials (Basel). 2014;7(6):4803–22.

33. Yadroitsev I, Krakhmalev P, Yadroitsava I. Selective laser melting of Ti6Al4V alloy for biomedical applications: Temperature monitoring and microstructural evolution. J Alloys Compd. 2014 Jan;583:404–9.

34. Leuders S, Thöne M, Riemer A, Niendorf T, Tröster T, Richard HA a., et al. On the mechanical behaviour of titanium alloy TiAl6V4 manufactured by selective laser melting: Fatigue resistance and crack growth performance. Int J Fatigue. 2013 Mar;48:300–7.

35. Murr LE, Gaytan SM, Ramirez DA, Martinez E, Hernandez J, Amato KN, et al. Metal Fabrication by Additive Manufacturing Using Laser and Electron Beam Melting Technologies. J Mater Sci Technol. 2012 Jan;28(1):1–14.

29

36. Simonelli M, Tse YY, Tuck C. Microstructure of Ti-6Al-4V produced by selective laser melting. J Phys Conf Ser. 2012 Jul;371:012084.

37. Gilbert JL, Piehler HR. On the nature and crystallographic orientation of subsurface cracks in high cycle fatigue of Ti-6Al-4V. Metall Trans A. 1993;24(3):669–80.

38. Gong H, Rafi K, Gu H, Janaki Ram GD, Starr T, Stucker B. Influence of defects on mechanical properties of Ti–6Al–4V components produced by selective laser melting and electron beam melting. Mater Des. 2015 Dec;86:545–54.

39. Hrabe N, Quinn T. Effects of processing on microstructure and mechanical properties of a titanium alloy (Ti–6Al–4V) fabricated using electron beam melting (EBM), part 1: Distance from build plate and part size. Mater Sci Eng A. 2013 Jun;573:264–70.

40. Suárez A, Tobar MJ, Yáñez A, Pérez I, Sampedro J, Amigó V, et al. Modeling of phase transformations of Ti6Al4V during laser metal deposition. Phys Procedia. 2011;12(PART 1):666–73.

41. Ahsan MN, Pinkerton AJ, Moat RJ, Shackleton J. A comparative study of laser direct metal deposition characteristics using gas and plasma-atomized Ti-6Al-4V powders. Mater Sci Eng A. 2011 Sep;528(25–26):7648–57.

42. Dai N, Zhang L-C, Zhang J, Chen Q, Wu M. Corrosion behavior of selective laser melted Ti-6Al-4V alloy in NaCl solution. Corros Sci. 2016;102:484–9.

43. Geetha M, Kamachi Mudali U, Gogia a. K, Asokamani R, Raj B. Influence of microstructure and alloying elements on corrosion behavior of Ti-13Nb-13Zr alloy. Corros Sci. 2004 Apr;46(4):877–92.

44. Scipioni Bertoli U, Wolfer AJ, Matthews MJ, Delplanque JPR, Schoenung JM. On the limitations of Volumetric Energy Density as a design parameter for Selective Laser Melting. Mater Des. 2017;113:331–40.

45. Wu X, Liang J, Mei J, Mitchell C, Goodwin PSS, Voice W. Microstructures of laser-deposited Ti-6Al-4V. Mater Des. 2004 Apr;25(2):137–44.

46. Vandenbroucke B, Kruth J-P. Selective laser melting of biocompatible metals for rapid manufacturing of medical parts. Rapid Prototyp J. 2007;13(4):196–203.

47. Thijs L, Verhaeghe F, Craeghs T, Humbeeck J Van, Kruth J-P. A study of the microstructural evolution during selective laser melting of Ti–6Al–4V. Acta Mater. 2010 May;58(9):3303–12.

48. Pattanayak DK, Fukuda A, Matsushita T, Takemoto M, Fujibayashi S, Sasaki K, et al. Bioactive Ti metal analogous to human cancellous bone: Fabrication by selective laser melting and

30

chemical treatments. Acta Biomater. 2011 Mar;7(3):1398–405.

49. Sallica-Leva E, Jardini AL, Fogagnolo JB. Microstructure and mechanical behavior of porous Ti-6Al-4V parts obtained by selective laser melting. J Mech Behav Biomed Mater. 2013 Oct;26:98–108.

50. Qiu C, Adkins NJE, Attallah MM. Microstructure and tensile properties of selectively laser-melted and of HIPed laser-melted Ti-6Al-4V. Mater Sci Eng A. 2013 Aug;578:230–9.

51. Song B, Dong S, Zhang B, Liao H, Coddet C. Effects of processing parameters on microstructure and mechanical property of selective laser melted Ti6Al4V. Mater Des. 2012 Mar;35:120–5.

52. Edwards P, Ramulu M. Fatigue performance evaluation of selective laser melted Ti-6Al-4V. Mater Sci Eng A. 2014 Mar;598:327–37.

53. Shunmugavel M, Polishetty A, Littlefair G. Microstructure and Mechanical Properties of Wrought and Additive Manufactured Ti-6Al-4V Cylindrical Bars. Procedia Technol. 2015;20:231–6.

54. Chen LYY, Huang JCC, Lin CHH, Pan CTT, Chen SYY, Yang TLL, et al. Anisotropic response of Ti-6Al-4V alloy fabricated by 3D printing selective laser melting. Mater Sci Eng A. 2017;682(October 2016):389–95.

55. Damiati L, Eales MG, Nobbs AH, Su B, Tsimbouri PM, Salmeron-Sanchez M, et al. Impact of surface topography and coating on osteogenesis and bacterial attachment on titanium implants. J Tissue Eng. 2018;9:2041731418790694.

56. Habibovic P, Barralet JE. Bioinorganics and biomaterials: Bone repair. Acta Biomater. 2011 Aug;7(8):3013–26.

57. Oshida Y. Implant Application. In: Oshida Y, editor. Bioscience and Bioengineering of Titanium Materials. 2nd ed. Elsevier; 2013. p. 225–68.

58. Oldani C, Dominguez A. Titanium as a Biomaterial for Implants. In: Fokter S, editor. Recent Advances in Arthroplasty. InTech Open; 2012. p. 149–62.

59. Liu QC, Elambasseril J, Sun SJ, Leary M, Brandt M, Sharp PK. The Effect of Manufacturing Defects on the Fatigue Behaviour of Ti-6Al-4V Specimens Fabricated Using Selective Laser Melting. Adv Mater Res. 2014 Mar;891–892:1519–24.

60. Xu W, Brandt M, Sun S, Elambasseril J, Liu Q, Latham K, et al. Additive manufacturing of strong and ductile Ti–6Al–4V by selective laser melting via in situ martensite decomposition. Acta Mater. 2015 Feb;85:74–84.

31

61. Gong H, Rafi K, Gu H, Starr T, Stucker B. Analysis of defect generation in Ti–6Al–4V parts made using powder bed fusion additive manufacturing processes. Addit Manuf. 2014 Oct;1–4:87–98.

62. Mower TM, Long MJ. Mechanical behavior of additive manufactured, powder-bed laser-fused materials. Mater Sci Eng A. 2016;651:198–213.

63. Li Z, Kucukkoc I, Liu F. Optimising the process parameters of selective laser melting for the fabrication of Ti6Al4V alloy. Rapid Prototyp J. 2017;24(1):150–9.

64. Shang Y, Yuan Y, Zhang Y, Li D, Li Y. Investigation into Effects of Scanning Speed on in Vitro Biocompatibility of Selective Laser Melted 316L Stainless Steel Parts. MATEC Web Conf. 2017;95:01009.

65. Ran Q, Yang W, Hu Y, Shen X, Yu Y, Xiang Y, et al. Osteogenesis of 3D printed porous Ti6Al4V implants with different pore sizes. J Mech Behav Biomed Mater. 2018;84(April):1–11.

66. Rasband WS. ImageJ. Bethesda, Maryland, USA: U.S. National Institutes of Health; 2018.

67. Yang J, Yu H, Yin J, Gao M, Wang Z, Zeng X. Formation and control of martensite in Ti-6Al-4V alloy produced by selective laser melting. Mater Des. 2016;108:308–18.

68. Ali H, Ghadbeigi H, Mumtaz K. Effect of scanning strategies on residual stress and mechanical properties of Selective Laser Melted Ti6Al4V. Mater Sci Eng A. 2018;712(October 2017):175–87.

69. Simonelli M, Tse YY, Tuck C. The formation of α + β microstructure in as-fabricated selective laser melting of Ti–6Al–4V. J Mater Res. 2014 Jul 25;29(17):1–8.

70. Kruth J-P, Levy G, Klocke F, Childs THC. Consolidation phenomena in laser and powder-bed based layered manufacturing. CIRP Ann - Manuf Technol. 2007;56(2):730–59.

71. Murr LE, Quinones SA, Gaytan SM, Lopez MI, Rodela A, Martinez EY, et al. Microstructure and mechanical behavior of Ti-6Al-4V produced by rapid-layer manufacturing, for biomedical applications. J Mech Behav Biomed Mater. 2009;2(1):20–32.

72. Sallica-Leva E, Caram R, Jardini ALL, Fogagnolo JBB. Ductility improvement due to martensite α' decomposition in porous Ti-6Al-4V parts produced by selective laser melting for orthopedic implants. J Mech Behav Biomed Mater. 2016 Feb;54:149–58.

73. Zhang XY, Fang G, Leeflang S, Böttger AJ, A. Zadpoor A, Zhou J. Effect of subtransus heat treatment on the microstructure and mechanical properties of additively manufactured Ti-6Al-4V alloy. J Alloys Compd. 2018;735:1562–75.

32

74. Dai N, Zhang LC, Zhang J, Zhang X, Ni Q, Chen Y, et al. Distinction in corrosion resistance of selective laser melted Ti-6Al-4V alloy on different planes. Corros Sci. 2016;111:703–10.

75. Yang J, Yang H, Yu H, Wang Z, Zeng X. Corrosion Behavior of Additive Manufactured Ti-6Al-4V Alloy in NaCl Solution. Metall Mater Trans A. 2017;48(7):3583–93.

76. Chiu TM, Mahmoudi M, Dai W, Elwany A, Liang H, Castaneda H. Corrosion assessment of Ti-6Al-4V fabricated using laser powder-bed fusion additive manufacturing. Electrochim Acta. 2018;279:143–51.

77. Palanivel S, Dutt AK, Faierson EJ, Mishra RS. Spatially dependent properties in a laser additive manufactured Ti–6Al–4V component. Mater Sci Eng A. 2016;654:39–52.

78. Vrancken B. Study of Residual Stresses in Selective Laser Melting. 2016.

79. Cabanettes F, Joubert A, Chardon G, Dumas V, Rech J, Grosjean C, et al. Topography of as built surfaces generated in metal additive manufacturing: a multi scale analysis from form to roughness. Precis Eng. 2018;(October 2017):0–1.

80. Wang X, Xu S, Zhou S, Xu W, Leary M, Choong P, et al. Topological design and additive manufacturing of porous metals for bone scaffolds and orthopaedic implants: A review. Biomaterials. 2016;83:127–41.

81. Karageorgiou V, Kaplan D. Porosity of 3D biomaterial scaffolds and osteogenesis. Biomaterials. 2005 Sep;26(27):5474–91.

82. Le Guehennec L, Lopez-Heredia M-A, Enkel B, Weiss P, Amouriq Y, Layrolle P. Osteoblastic cell behaviour on different titanium implant surfaces. Acta Biomater. 2008;4(3):535–43.

83. Lincks J, Boyan BD, Blanchard CR, Lohmann CH, Liu Y, Cochran DL, et al. Response of MG63 osteoblast-like cells to titanium and titanium alloy is dependent on surface roughness and composition. Biomater Silver Jubil Compend. 2006;19:147–60.

84. Koptyug A, Bergemann C, Lange R, Jaggi VE, Rännar LE, Nebe JB. Osteoblast ingrowth into titanium scaffolds made by electron beam melting. In: Materials Science Forum. Switzerland: Trans Tech Publications; 2014. p. 1292–7.

85. Zhu X, Chen J, Scheideler L, Reichl R, Geis-Gerstorfer J. Effects of topography and composition of titanium surface oxides on osteoblast responses. Biomaterials. 2004;25(18):4087–103.

86. Longhitano GA, Arenas MA, Conde A, Larosa MA, Jardini AL, Zavaglia CA de C, et al. Heat treatments effects on functionalization and corrosion behavior of Ti-6Al-4V ELI alloy made by additive manufacturing. J Alloys Compd. 2018;765:961–8.

33

87.   Metikoš-Huković M, Kwokal A, Piljac J. The influence of niobium and vanadium on passivity of titanium-based implants in physiological solution. Biomaterials. 2003;24(21):3765–75.

88.   Vaithilingam J, Prina E, Goodridge RD, Hague RJM, Edmondson S, Rose FRAJ, et al. Surface chemistry of Ti6Al4V components fabricated using selective laser melting for biomedical applications. Mater Sci Eng C. 2016;67:294–303.

89.   Niemeyer TC, Grandini CR, Pinto LMC, Angelo ACD, Schneider SG. Corrosion behavior of Ti-13Nb-13Zr alloy used as a biomaterial. J Alloys Compd. 2009 May;476(1–2):172–5.

90.   Milošev I, Metikoš-Huković M, Strehblow HH. Passive film on orthopaedic TiAlV alloy formed in physiological solution investigated by X-ray photoelectron spectroscopy. Biomaterials. 2000;21(20):2103–13.

91.   Atapour M, Pilchak A, Frankel GS, Williams JC, Fathi MH, Shamanian M. Corrosion Behavior of Ti-6Al-4V with Different Thermomechanical Treatments and Microstructures. CORROSION. 2010 Jun 1;66(6):65004–9.

92.   Gharbi M, Peyre P, Gorny C, Carin M, Morville S, Le Masson P, et al. Influence of various process conditions on surface finishes induced by the direct metal deposition laser technique on a Ti-6Al-4V alloy. J Mater Process Technol. 2013 May;213(5):791–800.

93.   Thermofisher Scientific. Technical Resources: 61100, MEM Powder. 2015.
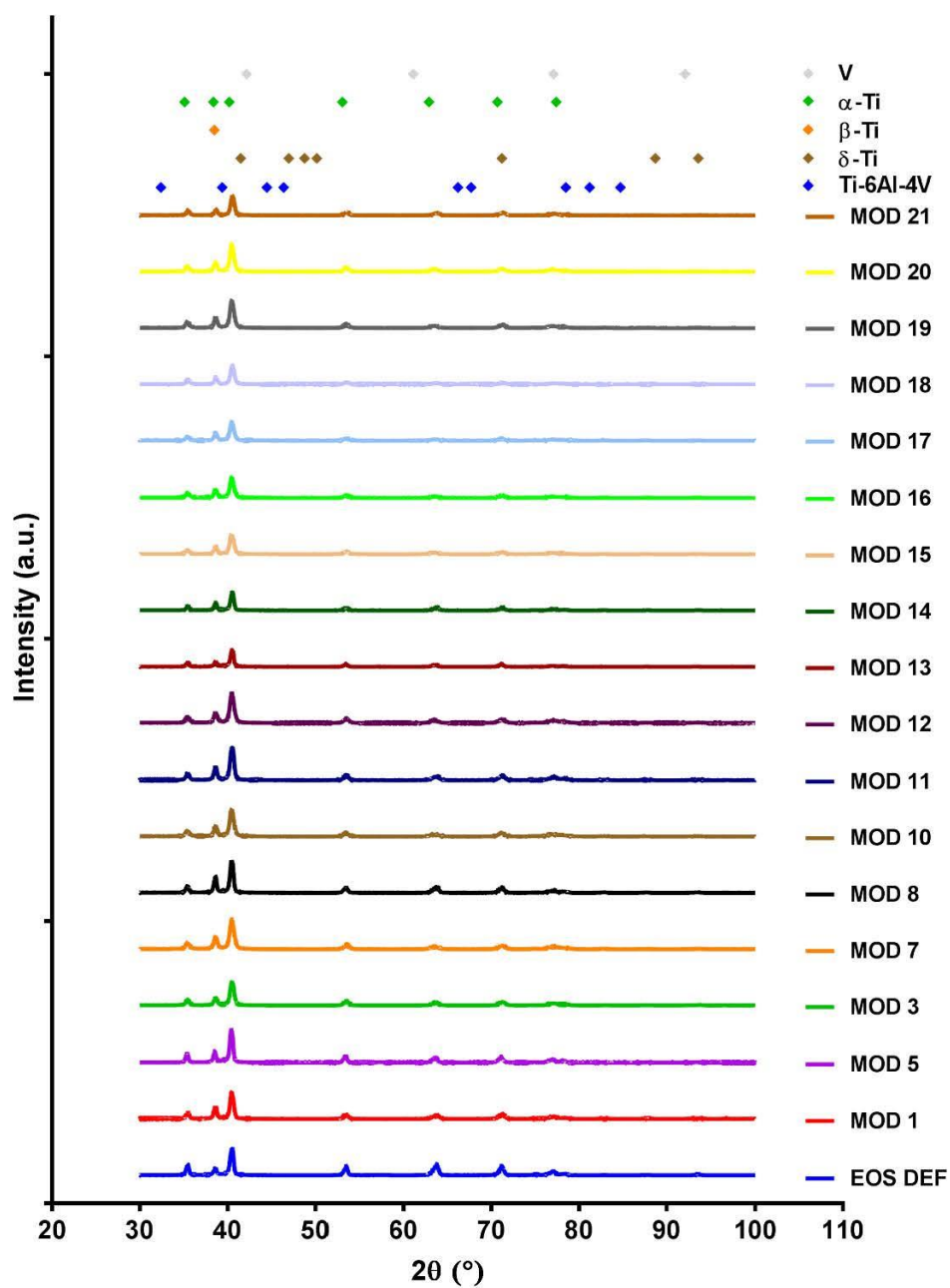
S1 Fig. X-ray diffraction data for SLM Ti-6Al-4V produced with various process parameter combinations, with all specimens displaying peaks corresponding to tetragonal Ti-6Al-4V (PDF Ref. 01-072-5007), hexagonal close packed α' phase Ti (PDF ref. 00-044-1294), and cubic V (PDF Ref. 00-022-1058) and none corresponding to body centred cubic β-Ti (PDF Ref. 00-044-1288).

35

84

S1 Table. Summary of data collected/determined for SLM Ti-6Al-4V specimens fabricated using varying combinations of laser power and laser scan speed.

Specimen ID	Laser scan speed (mm/s)	Laser power (W)	VED (J/mm^3)	E_{corr} (mV$_{SCE}$)		i_{corr} (μA/cm^2)		R_a (μm)		Rockwell Hardness (HRC)		Porosity (%)		Pore Area (μm^2)	
				Avg.	SD	Avg.	SD	Avg.	SD	Avg.	SD	Avg.	SD	Avg.	SD
EOS DEF	1200	280	56	-412	23	0.10	0.05	4.62	4.62	48.7	3.2	0.03	0.01	41.6	3.3
MOD 1	1000	280	67	-348	39	0.07	0.06	0.66	0.66	46.7	3.5	0.17	0.08	0.17	0.08
MOD 3	1200	200	40	-398	76	0.13	0.07	0.53	0.40	46.7	2.8	3.70	0.53	3.70	0.53
MOD 6	200	100	95	-450	64	0.13	0.06	3.74	3.36	49.0	2.9	5.59	0.22	5.59	0.22
MOD 7	1200	120	24	-158	29	1.06	0.14	5.75	6.67	35.6	2.0	3.84	0.58	3.84	0.58
MOD 8	200	120	143	-473	41	0.15	0.07	3.23	2.48	36.6	2.9	0.06	0.01	0.06	0.01
MOD 9	500	120	57	-615	60	0.12	0.08	0.53	0.53	46.9	2.6	32.59	2.72	32.59	2.72
MOD 10	1200	80	16	-387	30	2.32	1.79	16.26	17.97	47.1	3.3	0.04	0.01	0.04	0.01
MOD 11	200	80	95	-603	42	0.08	0.02	2.25	1.11	46.4	1.9	1.52	0.17	1.52	0.17
MOD 12	500	80	38	-497	102	0.07	0.02	3.97	3.20	44.7	2.3	0.16	0.04	0.16	0.04
MOD 13	200	280	333	-567	57	0.08	0.05	3.56	4.08	43.1	3.5	3.78	0.34	3.78	0.34
MOD 14	500	280	133	-572	16	0.10	0.06	1.48	1.48	44.7	1.5	0.40	0.25	0.40	0.25
MOD 15	500	100	48	-578	31	0.04	0.00	0.78	0.78	46.7	2.9	0.09	0.04	0.09	0.04
MOD 16	500	200	95	-532	40	0.08	0.06	2.51	2.51	40.5	4.5	1.62	1.82	1.62	1.82
MOD 17	1200	100	20	-430	28	1.37	0.35	15.72	15.72	25.4	1.3	1.40	1.44	1.40	1.44
MOD 18	1000	80	19	-355	26	2.71	0.41	4.61	4.61	20.8	2.8	4.02	3.02	4.02	3.02
MOD 19	1000	100	24	-296	32	0.54	0.09	5.13	3.94	27.7	2.5	2.96	0.42	2.96	0.42
MOD 20	1000	120	29	-466	24	0.15	0.04	4.26	6.34	41.2	3.5	0.16	0.11	0.16	0.11
MOD 21	1000	200	48	-503	43	0.10	0.07	0.61	0.54	47.0	4.1	0.17	0.08	0.17	0.08
WROUGHT (Ti-6Al-4V)	n/a	n/a	n/a	-451	70	0.07	0.03	n/a	n/a	36	n/a	n/a	n/a	n/a	n/a

36

S2 Table. Composition and ionic concentration of Minimum Essential Media formulation (Thermofisher #61100) used as electrolyte in electrochemical testing. Adapted from Technical Resource (93)

	Components	Molecular Weight	Concentration	
			(mg/L)	**mM**
Amino Acids	L-Arginine hydrochloride	211.0	126.64	0.60018957
	L-Cystine 2HCl	313.0	31.0	0.09904154
	L-Glutamine	146.0	292.0	2.0
	L-Histidine hydrochlorideH2O	210.0	42.0	0.2
	L-Isoleucine	131.0	52.0	0.39694658
	L-Leucine	131.0	52.0	0.39694658
	L-Lysine hydrochloride	183.0	72.5	0.39617488
	L-Methionine	149.0	15.0	0.10067114
	L-Phenylalanine	165.0	32.0	0.19393939
	L-Threonine	119.0	48.0	0.40336135
	L-Tryptophan	204.0	10.0	0.04901961
	L-Tyrosine disodium salt	225.0	52.0	0.23111111
	L-Valine	117.0	46.0	0.3931624
Vitamins	Choline chloride	140.0	1.0	0.007142857
	D-Calcium pantothenate	477.0	1.0	0.002096436
	Folic Acid	441.0	1.0	0.0022675737
	Niacinamide	122.0	1.0	0.008196721
	Pyridoxal hydrochloride	204.0	1.0	0.004901961
	Riboflavin	376.0	0.1	2.6595744E4
	Thiamine hydrochloride	337.0	1.0	0.002967359
	i-Inositol	180.0	2.0	0.011111111
Inorganic Salts	Calcium Chloride (CaCl2) (anhyd.)	111.0	200.0	1.8018018
	Magnesium Sulfate (MgSO4) (anhyd.)	120.0	97.67	0.8139166
	Potassium Chloride (KCl)	75.0	400.0	5.3333335
	Sodium Chloride (NaCl)	58.0	6800.0	117.24138
	Sodium Phosphate monobasic (NaH2PO4-H2O)	138.0	140.0	1.0144928
Other	D-Glucose (Dextrose)	180.0	1000.0	5.5555553
	Phenol Red	376.4	10.0	0.026567481

Chapter 4: The joint replacement/bone interface; investigating the biocompatibility of SLM Ti-6Al-4V

The production of Ti-6Al-4V orthopaedic implants through additive manufacturing techniques like SLM present a leap forward in the field of patient-specific medicine. However, Ti-6Al-4V implants are generally quite bio-inert. By manipulating the SLM process parameters, it is possible to change Ti-6Al-4V surface properties, and therefore tune biological interactions upon implantation. The effects of changing SLM process parameters, such as laser scan speed or laser power, on mechanical properties are well documented, however, the effects of changing these parameters on surface biological interactions are as yet poorly understood.

This study examined the interplay of SLM laser power and laser scan speed in relation to acute biological interactions, using the MG63 cell line to model osteoblastic responses to the various Ti-6Al-4V surfaces produced. Key findings demonstrate that while the most commonly used process parameters, i.e. those supplied by the companies producing the SLM machines, produce Ti-6Al-4V with adequate mechanical performance and cytocompatibility, using a reduced laser power and laser scan speed, i.e. 120 W and 500 mm/s, can produce Ti-6Al-4V with higher surface osteogenic potential. Improving biological interactions from the fabrication stage presents a significant reduction in the need for post-processing treatments used to promote osteogenesis.

This chapter was prepared as a paper for submission to *Materials Science and Engineering C*, and is present here in the unrevised form.

Understanding the influence of selective laser melting (SLM) process parameters on Ti-6Al-4V surface interactions with osteoblasts

Trina Majumdar[a, b]*, Jennifer Dyson[a,b], Jess Frith[a,b] and Nick Birbilis[a,b]

[a] Department of Materials Science and Engineering, Monash University, Clayton, Victoria 3800, Australia

[b] Monash Institute of Medical Engineering (MIME), Monash University, Clayton, Victoria 3800, Australia

* Corresponding author

Email: trina.majumdar@monash.edu (TM)

Abstract

Selective laser melting (SLM) is becoming increasingly popular for the fabrication of patient specific Ti-6Al-4V orthopaedic implants. The ability of SLM to both produce design features previously unmanufacturable through conventional techniques, and to produce designs modelled directly from patient data make it a particularly potent technique for providing patient specific solutions. The properties of SLM Ti-6Al-4V depend heavily on processing conditions, i.e. the choice of laser power and laser scan speed among others. At present, the majority of work in the field has examined the effects of altering SLM process parameters on component mechanical properties, but to date little has examined the effects on surface bioactivity. It is hypothesised that surface bioactivity can be tuned, along with mechanical properties such as porosity and roughness, to produce SLM Ti-6Al-4V that requires minimal post-processing modifications to interact favourably with osteoblasts following implantation. SLM Ti-6Al-4V fabricated with a laser power of 120 W and laser scan speed of 500 mm/s was successful in supporting MG63 cell growth, proliferation and differentiation as well as, if not better than, both conventionally produced Ti-6Al-4V and SLM Ti-6Al-4V produced using the most commonly applied settings. This study investigates how the interplay between SLM laser scan speed and laser power on Ti-6Al-4V affects initial osteoblast adhesion, proliferation and differentiation, as well as short term mineralisation.

Graphical abstract
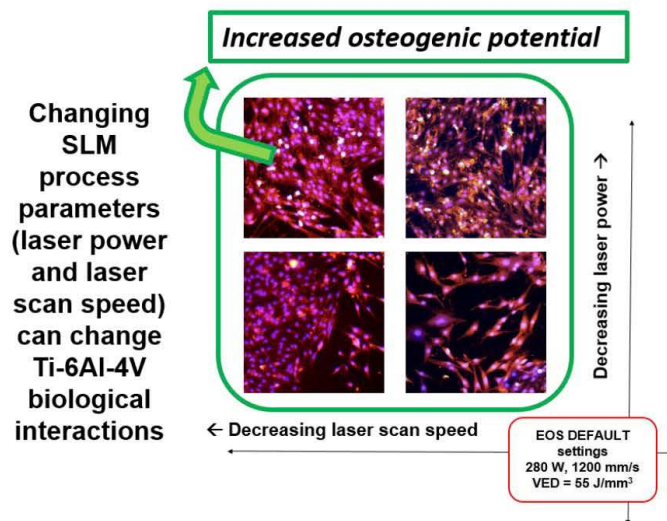
Highlights

- Changing laser power and/or laser scan speed during SLM changes surface properties such as porosity and roughness
- Various SLM Ti-6Al-4V surfaces were produced by varying laser power and laser scan speed
- SLM Ti-6Al-4V with improved osteogenic potential was produced with a laser power of 120 W and laser scan speed of 500 mm/s

1. Introduction

The fabrication of customised orthopaedic implants through selective laser melting (SLM) is becoming both more popular, and more importantly, more feasible. Standard orthopaedic implant designs can be modified according to patient data, printed, post-processed and implanted in a relatively short time frame – weeks to months, as opposed to years. Various groups have reported the fabrication of Ti-6Al-4V via SLM with mechanical properties and bioactivity comparable to that of conventionally produced Ti-6Al-4V [1–8]. However, as with any new fabrication method, the process itself requires further investigation to maximise its potential. There is scope to manipulate the properties of SLM components, i.e. mechanical performance and bioactivity, through the manipulation of processing parameters such as laser scan speed or laser power [9–18]. The combined effects of individual SLM process parameters (e.g. laser scan speed and laser power) are often quantified per Equation 1 as volumetric energy density (VED) [11,19,20].

$$\textbf{Volumetric energy density } = \frac{\textbf{Laser power (W)}}{\textbf{Laser scan speed }\left(\frac{\textbf{mm}}{\textbf{s}}\right) \textbf{x hatch spacing (mm) x layer thickness (mm)}} \frac{\textbf{J}}{\textbf{mm}^3} \qquad (1)$$

The most commonly used parameters for SLM are often those supplied by the manufacturers of the machines, for example, the settings recommended by EOS which are proprietary and optimised for mechanical performance. The ways in which the interplay of various process parameters affect Ti-6Al-4V bioactivity is not yet fully understood, and it is possible that there are specific SLM process parameter combinations which can produce Ti-6Al-4V surfaces with higher bio-activity and propensity to support bone healing than conventionally fabricated implants.

SLM Ti-6Al-4V typically exhibits slightly different properties to wrought Ti-6Al-4V due to the characteristics of the fabrication process [21–23]. Specifically, the bottom up or layer-wise mode of fabrication causes SLM Ti-6Al-4V microstructure to vary in 3 dimensions – across each layer in the x and y directions, and through the build direction (i.e. the z axis) [12,24,25] . SLM involves the application of a high energy laser to a powder bed in order to rapidly melt and fuse pre-alloyed powder particles according to CAD models [12,24,26,27]. The power of the laser and the speed at which the laser traverses each layer (laser scan speed), can both be manipulated, thereby changing how heat energy is supplied to the powder bed. The interaction of laser power and laser scan speed affects the formation and stability of the melt pool, and the characteristics of the moving melt pool are the main contributor to final microstructure and surface properties [9–15,20,28,29]. The stability, or instability, of the melt pool arises from the peculiar hydrodynamics of the moving melt pool – upon laser interaction with the powder bed, a melt pool or weld track is created, which rapidly cools as the laser moves across the rest of the layer. On cooling, the melt pool is thermodynamically driven to reduce its surface energy, and thus breaks up into smaller 'droplets' – this is termed Plateau-Rayleigh instability [30–34]. The less stable the melt pool is, the more droplets appear, and this trail of droplets is often termed balling [9,28,35]. The surface tension of the melt pool also attracts adjacent particles from the powder bed into the melt pool, which

then partly adhere behind the moving melt pool [9,18,30,36]. Therefore, changes in either the laser scan speed and/or the laser power used during SLM affect final microstructure and surface properties. Layer-wise defects such as pores, gaps or clumps of partly adhered particles affect subsequent layer deposition, and this accumulation of defects through the layer has a significant effect on SLM Ti-6Al-4V wear and fatigue resistance, as well as other bulk properties [17,37–40]. Therefore, the careful choice of SLM processing parameters is critical in ultimate Ti-6Al-4V component performance. Beyond choosing parameters carefully to avoid defect accumulation, the interplay of various processing parameters may be manipulated to tune the surface properties of implants to improve interactions with cells involved in bone healing and growth. The surface properties (e.g. surface energy, roughness, porosity and surface oxides) of orthopaedic implants have a significant influence on the post-implantation healing processes within the body, specifically in relation to protein adsorption, initial osteoblast adhesion, proliferation and differentiation [41–50]. Various groups have examined osteoblast-like cell responses to various engineered SLM Ti-6Al-4V surfaces (Table 1.) but relatively little work has examined the effects of altering both laser power and laser scan speed, the two largest contributors to melt pool behaviour, on osteoblast-like cell behaviour on surfaces prepared as per current orthopaedic implant specifications (ASTM F1108b).

Table 1. Summary of work examining the effects of varying SLM Ti-6Al-4V surfaces on in vitro osteoblast-like cell behaviour

Relevant SLM process parameters		In vitro test conditions		Cell-surface interactions	Ref
Laser power (W)	Laser scan speed (mm/s)	Cell type	Test duration (days)		
95	900	hBMSC	7	• All SLM Ti-6Al-4V surfaces supported cell growth and proliferation within the 7 day test period. • Cells on SLM Ti-6Al-4V exhibited elongated/polygonal morphology, expansive networks of actin filaments, with increased amounts of hBMSCs on heat-treated Ti-6Al-4V indicating that heat treatment of SLM Ti-6Al-4V (annealing at 820°C for 4 hours) improved cytocompatibility.	Wang et al, 2016 [8]
100	275	MC3T3-E1	14	• Improved cell adhesion (qualitative) compared to Nobel- Speedy® Replace RP implants from Nobel Biocare, Germany	Shaoki et al, 2016 [1]
200	-	NIH- 3T3	7	• All SLM Ti-6Al-4V surfaces supported cell viability within the time period, with no dissolution of metal ions to cell media within 7 days.	Vaithiling am et al, 2016 [51]
150	1750	MC3T3-E1	7	• All SLM Ti-6Al-4V surfaces supported cell proliferation to confluence across all sample surfaces except where partially melted particles present.	Cox et al, 2017 [52]
200	1250	U-2 OS	5	• No significant cytotoxic effect (qualitative assessment) observed for SLM Ti-6Al-4V surfaces, with cells exhibiting healthy well-spread cell morphology on all.	Fousová et al, 2017 [53]
200	1250	U-2 OS	5	• SLM Ti-6Al-4V supported comparable cell adhesion but increased corrosion resistance to EBM Ti-6Al-4V.	Fojt et al, 2017 [54]

25, 35, 45	500	hBMSC	7	• SLM Ti-6Al-4V exhibits increased surface energy and material density, but decreased cell adhesion and cell proliferation with increases in laser power and total VED.	Wysocki et al, 2018 [13]
275	1100	MG63	8	• As built and sand blasted SLM Ti-6Al-4V both support cell growth • Higher cell proliferation on glass blasted (smooth, R_a= 3.4 µm) surfaces compared to as-built (rough, R_a = 13.3 µm).	Matouskova et al, 2018 [43]

The effects of various Ti-6Al-4V surface features on bone healing processes are commonly examined through the use of either MG63 or MC3T3-E1 immortalised cell lines in *in vitro* models. Immortalised cell lines display phenotypic stability, however, these phenotypes do not necessarily reflect the complete range of phenotypic features characteristic of maturing osteoblasts in the human body. MG63 cells are osteoblast-like cells derived from human osteosarcomas, which remain in an arrested pre-osteoblast form and are sensitive to vitamin D metabolites in the same way as human osteoblasts [55–57] MC3T3-E1 cells are osteoblast precursors derived from rat osteocalvaria, which undergo differentiation into mature osteoblasts, however, at high passage numbers, reduced proliferation (>36) and signs of inconsistent cell cycling (>60) appear [57,58]. Both cell lines behave similarly to mature human osteoblasts, however, it is important to note that both have drawbacks which should be taken into consideration in the choice of cell line used, and in the interpretation of data arising from the experiments. Well-designed experiments must also take into account the effects of various media supplements and their effects on the cell behaviour observed, as well as the timelines of various sub-processes involved in the initial stages of osseointegration.

In this study, differences in interactions between osteoblasts and the various Ti-6Al-4V surfaces produced through SLM were modelled through the use of MG63 cells, as the behaviour of these cells is similar to that of immature *in vivo* osteoblasts in the early stages of differentiation. The cells were cultured on samples with basal media supplemented with 50 µg/mL ascorbic acid and 5 mM glycerol-2-phosphate, to examine the acute effects of the various surfaces on MG63 cell growth, proliferation, differentiation and mineralisation, variously at 1, 7, 14 and 21 days following seeding. A prospecting approach is taken in this study, where the various properties achievable by varying either laser power and/or laser scan speed are examined in terms of osteoblast response, as opposed to designing surfaces for osteoblasts.

2. Methods

2.1 Sample fabrication and preparation

Ti-6Al-4V samples were produced using an EOS M280 instrument and pre-alloyed spherical Ti-6Al-4V powder (size range 1-53 µm) produced through gas atomisation. A sand-blasted Ti-6Al-4V build plate was used as a substrate and pre-heated to 100°C during printing. The fabrication process took place in an argon gas atmosphere with an oxygen content of 1300 ppm. Fixed processing parameters were as follows; hatch

spacing of 0.14 mm, recoat layer thickness of 30 μm, beam offset at 0.015 mm, and stripe width at 5 mm. All samples were produced using the continuous island scan strategy. The most commonly used laser scan speed and laser power for EOS machines, 280W and 1200 mm/s, are hereafter referred to as the EOS DEFAULT settings.

All samples were examined with respect to surface imaging, porosity, hardness, roughness and electrochemical behaviour, the results of which are reported elsewhere (Chapter 3 of this thesis). A subset of parameters, as highlighted in Table 1., was chosen for further *in vitro* testing. Samples were labelled according to the parameter combination used to produce them (per Table 1.) – for example, SLM Ti-6Al-4V samples produced using a laser scan speed of 500 mm/s and a laser power of 120 W are referred to as 120W-500S samples.

Table 1: Varied process parameters used to build Ti-6Al-4V samples, with highlighted cells indicating samples chosen for in vitro testing

Laser scan speed (mm/s) \ Laser power (W)	80	100	120	200	280
200	80W-200S VED = 95	100W-200S VED = 120	120W-200S VED = 145	200W-200S VED = 240	280W-200S VED = 330
500	80W-500S VED = 40	100W-500S VED = 50	120W-500S VED = 55	200W-500S VED = 95	280W-500S VED = 135
1000	80W-1000S VED = 20	100W-1000S VED = 25	120W-1000S VED = 30	200W-1000S VED = 50	280W-1000S VED = 65
1200	80W-1200S VED = 15	100W-1200S VED = 20	120W-1200S VED = 25	200W-1200S VED = 40	280W-1200S (EOS DEFAULT settings) VED = 55

Following production, all samples were stress relieved by heating at 800°C for 2 hours in a vacuum furnace, then cut from the build plate using electrical discharge machining (EDM). SLM Ti-6Al-4V is rarely used without stress relieving procedures, as the temperature gradients produced during fabrication cause significant amounts of residual stress to build up in the bulk – this necessarily causes some amount of α' martensite phase decomposition. Wrought Ti-6Al-4V (Grade V) samples were also treated at 800°C for 2 hours. All samples were cut to 3 mm in height, and ground with ethanol and water using successively finer grit silicon carbide paper (180 to 2400 μm), then polished using Struers OP-S® and Struers MD-CHEM® cloth. All tests were conducted on sample surfaces parallel to the build plate. The preparation strategy and test surfaces were chosen to approximate pre-implantation implant surfaces, however, it is important to note that as orthopaedic implants involve curvature in the x, y and z axes, it is unproductive to complete testing in all axes at this initial stage of data collection.

2.2 Metallurgical sample characterisation and electrochemical behaviour assessment

Samples were imaged using a FEI Phenom scanning electron microsope (SEM) operating at 5 kV,

with additional imaging carried out on an FEI Quanta 3D FED operating at 20 kV. A Bruker D8 Advance X-ray diffractometer was used to perform x-ray diffraction (XRD) on samples. A Cu Kα radiation source was used, with analysis performed at 40 kV and 40 mA. The diffraction angle range used was between 30° and 100°, with a step increment of 0.5° and a time step of 0.25 seconds. The obtained spectra were compared to reference data from the International Centre for Diffraction Data using DIFFRACplus EVA software (AXS, Bruker, Karlsruhe, Germany).

Sample porosity along the XY planes was examined using optical microscopy. All samples were polished, sonicated for 3 minutes in ethanol, dried with compressed air, and imaged using an Olympus GX51 optical microscope at 5x magnification. Image analysis (to determine % porosity and average pore area) was carried out using ImageJ (v1.50b, Bethesda, MD, USA) – this software is commonly used in biomaterials research. Each image was opened in ImageJ, split according to colour channel, then manually thresholded. The 'Analyse Particles' feature of ImageJ was then used to count and size the pores (in terms of 2D area), with a minimum pore area set as 10 μm^2, and a minimum circularity set as 0.5 (i.e. more than 50% circular). Three images (and measurements) were taken for each category, with re-grinding and polishing steps following each measurement.

The average surface roughness (Ra) of polished samples fabricated using each set of process parameters was analysed using a Veeco Wyko NT1100 optical profilometer. The samples were imaged using vertical shift interference (VSI) mode, 1.0x magnification, 1.0x laser scan speed and a threshold of 0.1%. The back scan and the length were set at 200 μm and 500 μm. 5 measurements were taken for each category, with re-grinding and polishing steps following each measurement (i.e. multiple layers were examined). Sample hardness (polished) was measured using a Wilson Rockwell hardness tester. A 120° diamond spheroconical indenter (C Rockwell scale) was used with a load of 150 kg. 10 measurements were made for each category.

Electrochemical testing was carried out in a double-chambered three-electrode electrochemical cell connected to a Biologic VMP-3Z potentiostat. All samples were mounted in epoxy, with the exposed surface acting as the working electrode, with copper tape or wires extending from the rear to allow voltage measurement. A platinum mesh was used as the counter electrode, and a saturated calomel reference electrode was placed in a Haber-Luggin capillary extending to within 5 mm of the sample surface. A biologically relevant medium was used as the electrolyte to approximate in vivo conditions - minimum essential media (MEM) was made up from powder (Gibco® GlutaMAX™) (1 packet added to 1L of water with 2.2 g of sodium bicarbonate), and the pH of this solution was adjusted with 5% HCl/1M NaOH to pH 7.2 ± 0.2. The electrolyte was maintained at 37°C using a circulating water bath. All samples were left to rest for 10 minutes minimum at open circuit potential (OCP), following which potentiodynamic polarisation was carried out from – 150 mV / E_{oc} to 1.0 V / E_{ref} (reference electrode potential) with a scan rate of 1 mV/s.

Polished sample hydrophilicity was measured using a contact angle meter (OCA 20, DataPhysics instruments, GmbH, Germany). Drops of deionised water were delivered onto the sample surfaces with a set drop volume of 2 µl and a dosing rate of 0.5 µl/s. An average of 10 readings was taken per category, from multiple samples.

2.3 In vitro characterisation

2.3.1. Cell culture

Samples were sterilised as follows; samples were sonicated in 99% ethanol for 20 minutes, exposed to ultraviolet light for 20 minutes (submerged in fresh ethanol), flipped, and then the opposite sides were exposed to ultraviolet light for a further 20 minutes. The samples were transferred to PBS for 20 minutes prior to cell seeding. Following testing, the samples were submerged in 0.1% Triton-X in PBS (Sigma Aldrich, Australia) to facilitate cell detachment, then reground, re-polished and re-sterilised.

The MG63 (ATCC® CRL-1427™) human osteosarcoma cell line was used as a model for osteoblastic response to the SLM Ti-6Al-4V samples. Low glucose (1g/L) DMEM (Gibco, ThermoFisher Scientific Australia) supplemented with 10% foetal bovine serum (FBS, Gibco, ThermoFisher Scientific Australia) and 100 units/ml antibiotic solution (Gibco, ThermoFisher Scientific Australia) was used as MG63 basal media (BM). The MG63 basal media was supplemented with ascorbic acid 2-phosphate (50 µM) and β-glycerophosphate/glycerol-2-phosphate (10 mM) to promote osteogenic differentiation (termed osteogenic media, OM). All experiments utilised MG63 cells of passage numbers between 5 and 25, with media changed every 3 days.

Cells were cultured to confluence and subcultured via trypsinisation (TrypLE; Invitrogen, Sydney, Australia). Test samples (280W-1200S, 120W-1200S, 120W-500S, 280W-500S, WROUGHT) were placed into 24-multiwell plates (tissue culture plastic, TCP) and seeded at a density of either 1000 or 5000 cells/cm^2. Cell seeding was completed in two steps to prevent cells being flushed off the upper surface of the 3 mm tall samples during seeding. In the first step, 100 µl of cell suspension was pipetted in a dropwise manner onto sample surfaces, with the remaining required media pipetted in after 10 minutes.

Prior to assays being performed as described below, the seeded samples were transferred to new 24-multiwell plates to separate the sample-adhered cells from the TCP adhered cells. Each experiment was performed at least twice, with functional triplicates for each group (n=3 per experiment and n≥6 total). Media was changed every 3 days.

2.3.2 Cell attachment and viability

Cell viability was examined with a LIVE/DEAD™ Viability/Cytotoxicity kit (Invitrogen, UK). Cultured samples were rinsed with PBS and stained with 5µM calcein AM and 10 µM ethidium homodimer-1 in PBS,

then imaged with an upright microscope (Nikon Eclipse Ti, Tokyo, Japan). 5 representative images were captured for each sample and analysed with ImageJ. Images were split according to colour channel and thresholded, then analysed using the 'Analyse particles' function of ImageJ to determine the percentage of live cells in each area.

2.3.3 Cell attachment and spreading

Cell attachment and spreading were examined by visualising F-actin (cytoskeleton) with phalloidin-TRITC and by visualising nuclei with DAPI. After culturing cells on samples for 1 or 7 days, the samples were rinsed with PBS, fixed with 4% paraformaldehyde (PFA) for 1 hour, permeablised with 0.1% Triton-X in PBS for 20 minutes then stained with ActinRed™ 555 ReadyProbes® Reagent (Invitrogen, ThermoFisher Scientific, Australia) and Hoechst 33342 (10 µg/mL, Invitrogen, ThermoFisher Scientific, Australia) in 3% bovine calf serum (in PBS) for 1 hour (dilutions as directed by manufacturers). The samples were rinsed with PBS and imaged using fluorescence microscopy (Nikon Eclipse Ti, Tokyo, Japan). 5 representative images were captured for each sample at both low and high magnification (5x and 20x). Day 1 images were analysed with ImageJ. Images were split according to colour channel and thresholded, then analysed using the 'Analyse particles' function of ImageJ to determine cell aspect ratio and circularity. Following, total cell area (orange) was divided by number of nuclei (blue) to give average cell area (μm^2).

2.3.4 Cell proliferation

An MTS assay (Cell Titre 96 Aqueous One Solution Cell Proliferation Assay, ThermoFisher Scientific, Australia) was used to determine the proportion of proliferating cells at days 1 and 7. After transferring the seeded samples to new plates, 800 µL OM with 317 µg/ml MTS reagent was added to each test well and incubated for 6 hours at 37°C with 5% CO_2. Following incubation, samples were removed from the test plates, and the optical absorbance (OD) of each test well was measured at 490 nm with a microplate reader (ThermoScientific™ Multiskan Spectrophotometer, Vantaa, Finland). Analysis was completed after subtracting averaged background values (800 µL OM with 317 µg/ml MTS on TCP, no cells) from each replicate.

2.3.5 Cell differentiation and mineralisation

To examine osteogenic behaviour at day 7, a colourimetric p-nitrophenol phosphate assay (pNPP, Sigma Aldrich, UK) was used to measure alkaline phosphatase (ALP) expression (a strong marker for osteogenesis), which was then normalised to DNA concentration for each sample using a PicoGreen assay (Invitrogen). Samples were washed twice with 0.2 M carbonate buffer and lysed with 0.1% Triton-X-100 (Sigma Aldrich, Australia) in 0.2 M carbonate buffer. The samples were then subjected to 3 freeze/thaw cycles between -80°C and 25°C. 50 µl from each well was transferred to a new 96 well plate for the pNPP assay, and 50 µl from each well was transferred to a white 96 well plate for the picogreen assay. pNPP standards were made up

through serial dilutions as per manufacturer instructions, incubated for 1 hour, then read using a microplate reader (ThermoScientific™ Multiskan Spectrophotometer, Vantaa, Finland). DNA standards were made up through serial dilutions as per manufacturer instructions. The PicoGreen reagent was made up at a 1:50 dilution in a buffer composed of 200 mM Tris-HCl and 20 mM EDTA (pH 7.5) buffer. The PicoGreen solution was added to each standard and sample well. Following shaking, the test plates were read at 485 nm excitation and 538nm emission using a Tecan microplate reader (Infinite 200 PRO, Tecan, Switzerland).

Average cell mineralisation and calcium deposition were examined through the chelation of calcium with xylenol orange (calcium deposits appear orange) and by visualising nuclei with DAPI. After culturing cells on samples for 21 days, the samples were rinsed with PBS, and fixed with 4% paraformaldehyde (PFA) for 15 minutes. The samples were stained with Hoechst 33342 (10 µg/mL PBS, Invitrogen, ThermoFisher Scientific, Australia), rinsed thrice with PBS and once with DI H_2O, and counterstained with xylenol orange (1 µM in DI H_2O). The samples imaged using fluorescence microscopy (Nikon Eclipse Ti, Tokyo, Japan). 5 representative images were captured for each sample at both low and high magnification (5x and 20x). Day 1 images were analysed with ImageJ. Images were split according to colour channel and thresholded, then analysed using the 'Analyse particles' function of ImageJ to determine cell aspect ratio and circularity. Following, total calcium deposit area (orange) was divided by number of nuclei (blue) to give average calcium amount per cell area (μm^2).

2.4 Statistical analysis

The significance of differences in cell behaviour on the various samples at various time points was performed using GraphPad Prism 7 (GraphPad Software, Inc., La Jolla, CA). Data are presented here as mean ± standard deviation (SD). One-way analyses of variation (ANOVA) together with Dunnett's post hoc analyses were used to identify significant differences (significance threshold: $p < 0.05$).

3. Results

3.1 Microstructural characterisation of Ti-6Al-4V surfaces produced using various SLM process parameter combinations

Each of the process parameter combinations examined produced Ti-6Al-4V with significantly different porosity percentages than the 280W-1200S (EOS DEFAULT settings), as seen in Figure 1. The highest porosity percentages were observed for the 120W-1200S samples (VED = 25 J/mm^3). 120W-1200S samples were built with a relatively low laser power combined with a relatively high laser scan speed – the combination of 'mismatched' parameters leads to the formation of instable and elongated melt pools, causing balling and the formation of lack of fusion defects. The high porosity, low hardness and high surface roughness are all due to the insufficient dwell time of the laser at each layer.
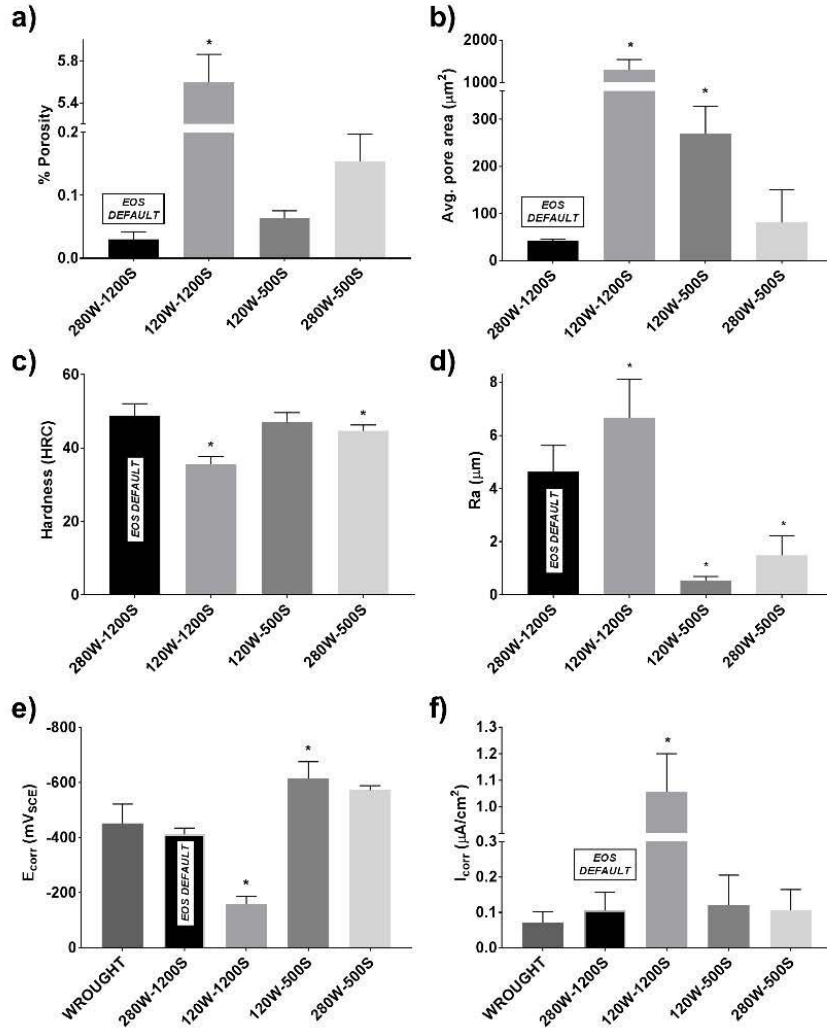
Figure 1: The properties of SLM Ti-6Al-4V vary according to the laser scan speed and laser power used during fabrication. Variations in % porosity and pore area, hardness, roughness, corrosion resistance (E_{corr}) and current density (I_{corr}) are shown in Figures 1a), b), c), d), e) and f) respectively. All data shown as mean ± standard deviation, with significant differences between samples and 280W-1200S (EOS DEFAULT settings) indicated with * ($p < 0.05$).

The 120W-500S samples (VED = 55 J/mm^3) displayed the lowest porosity percentage and surface roughness, even lower than that of the 280W-1200S (EOS DEFAULT settings) samples. The 120W-500S samples were built with lower laser power and laser scan speed than the 280W-1200S (EOS DEFAULT settings) samples, however, the VED for both categories is the same. Differences in VED affect the formation and solidification of the melt pool, specifically how well melting and solidification occurs across each layer and the bulk. Pores are formed when there is insufficient energy to allow for full particle melting and fusion, or when there is excessive energy leading to the key-holing effect. Therefore, while the supplied thermal energy per unit volume was the same for both the 280W-1200S (EOS DEFAULT settings) and 120W-500S samples, the interactions between the laser power and laser scan speed used produced melt pools with different

characteristics and thus differing porosity percentage and surface roughness as seen in Figure 2.
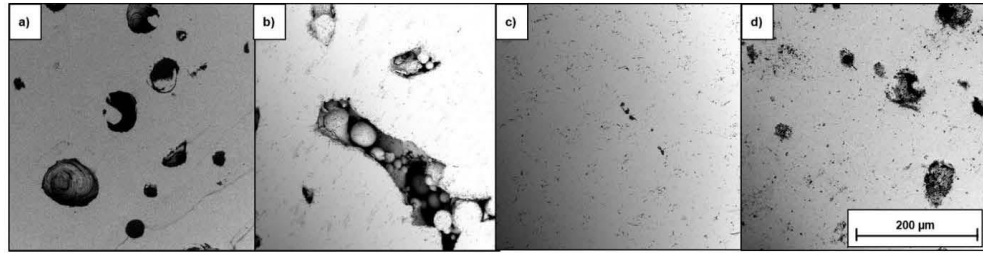
Figure 2: SEM images of a) 280W-1200S (EOS DEFAULT settings), b) 120W-1200S, c) 120W-500S and d) 280W-500S

3.2 Cell viability and proliferation

Numerous groups have reported that SLM Ti-6Al-4V supports osteoblast-like cell growth [4,23,26]. To investigate whether changes in process parameters produced surfaces that could also support cell growth, live/dead staining and MTS assays were performed on the cultures after 24 hours and after 168 hours (7 days). All samples supported cell attachment within 24 hours of seeding, as determined qualitatively and from quantitative analyses of live/dead stained cells, seen in Figure 3. At day 1, only the 280W-1200S (EOS DEFAULT settings) and 120W-500S samples supported cell viability to the same extent as the TCP control - the WROUGHT, 120W-1200S and 280W-500S samples supported approximately 10% fewer cells compared to TCP, indicating slightly lower cell viability (Figure 3b). Cell viability above 70% (i.e. less than 30% cytotoxicity) indicates biocompatibility, according to the International Organization for Standardization [59].
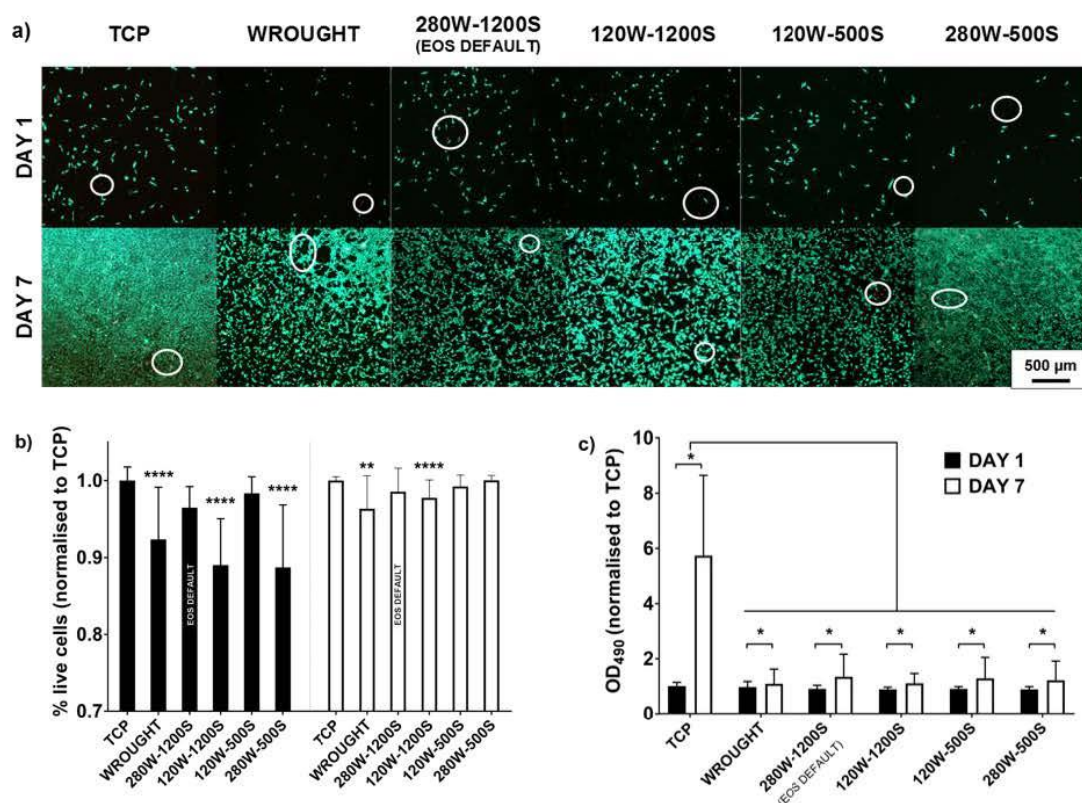
Figure 3: Cell viability and proliferation, with a) showing live/dead staining of cells after 24 and 168 hours with live cells in green and dead cells in red (circled in white)), b) showing quantitative analysis of live/dead staining, normalised to TCP and c) showing quantitative analysis of MTS reduction, normalised to TCP. Graphical data shown as mean ± standard deviation, with significant differences from TCP denoted with * ($p < 0.05$), ** ($p < 0.01$), * ($p < 0.001$) or **** ($p < 0.0001$), n=9.**

Supporting the results of the live/dead staining, the MTS assays indicated that all samples supported cell growth as determined by the significantly increased metabolic activity of the cultures between days 1 and 7 (Figure 3c). However, after 7 days, all Ti-6Al-4V samples displayed significantly less cell proliferation than the TCP controls – assuming equal metabolic rate, it can be said that while the tested Ti-6Al-4V surfaces supported cell proliferation, the rate of division is lower than on TCP.

3.3 Cell attachment and spreading

To examine whether the different sample surfaces affected the osteoblast-like cell interaction and spreading, culture cell morphology after 24 hours was imaged and analysed quantitatively to determine differences in average cell area, aspect ratio and circularity. Representative images can be seen in Figure 4.

Significant differences in average cell area between cells on TCP and cells on all Ti-6Al-4V samples were seen, with average cell area on the Ti-6Al-4V samples approximately half that of the cells on the TCP control. Generally, larger cell area, i.e. higher coverage of cytoplasm over the material, predicates better cell spreading.

100

Cell circularity and aspect ratio indicate changes in cell shape, i.e. round vs. spindle morphology - higher circularity and aspect ratios (i.e. higher values) indicating a higher degree of cell spreading, or a tendency towards the spindle vs. round morphology. Comparing the SLM Ti-6Al-4V samples to the wrought Ti-6Al-4V samples (secondary control), cells on the 120W-500S samples had slightly higher average cell areas and aspect ratios (i.e. were more elongated), indicating a preference of the MG63 cells for this surface. Two types of cell morphology were observed on the SLM Ti-6Al-4V samples – polygonal morphology with thin filopodia on the 120W-500S samples, and fusiform morphology with bundled stress fibres on the 120W-1200S, 280W-500S and 280W-1200S (EOS DEFAULT settings) samples.
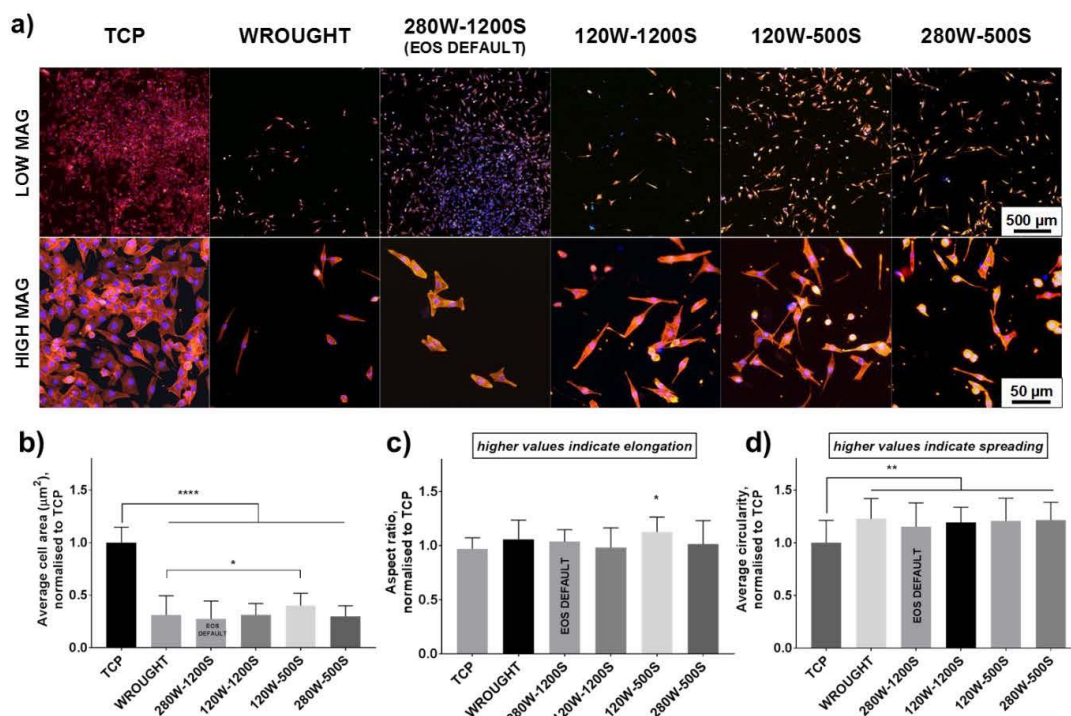
Figure 4: Differences in cell morphology were observed on each Ti-6Al-4V surface (compared to TCP) after 1 day as determined by DAPI and actin staining, with a) showing representative micrographs of orange-stained intracellular F-actin blue-stained nuclei. Average cell area, aspect ratio and circularity on each sample, normalised to TCP are shown in a), b) and c) respectively. Data shown as mean ± standard deviation, with significant differences from TCP denoted with * (p < 0.05), ** (p < 0.01), or *** (p < 0.001), n=9.

3.4 Cell differentiation and mineralisation

To determine whether there were differences in osteogenic potential between the Ti-6Al-4V sample surfaces, two measures of osteogenic activity were examined – ALP activity and calcium deposition. The MG63 cells were cultured in basal media supplemented with ascorbic acid 2-phosphate and β-glycerophosphate/glycerol-2-phosphate to induce mineralisation as recommended by Czekanska et al [57].

The activity of ALP is a marker of the early stages of osteoblast differentiation, and has been shown to peak

between 7 and 14 days for osteoblast-like cells on titanium-based alloys [47,56]. Evidence of cell osteogenic differentiation at day 7 was observed on all samples, indicating that the osteogenic supplements did facilitate osteogenic differentiation, as seen both qualitatively and quantitatively in Figure 5. Cells displayed approximately 5-fold higher ALP activity on all of the Ti-6Al-4V surfaces compared to the TCP, and within the Ti-6Al-4V samples, it was clear that the SLM Ti-6Al-4V samples yielded more than 5-fold higher ALP activity than the wrought Ti-6Al-4V samples. Notably, the cells on the 120W-500S samples exhibited the highest ALP activity, approximately 15 times that of the cells on the wrought Ti-6Al-4V samples.
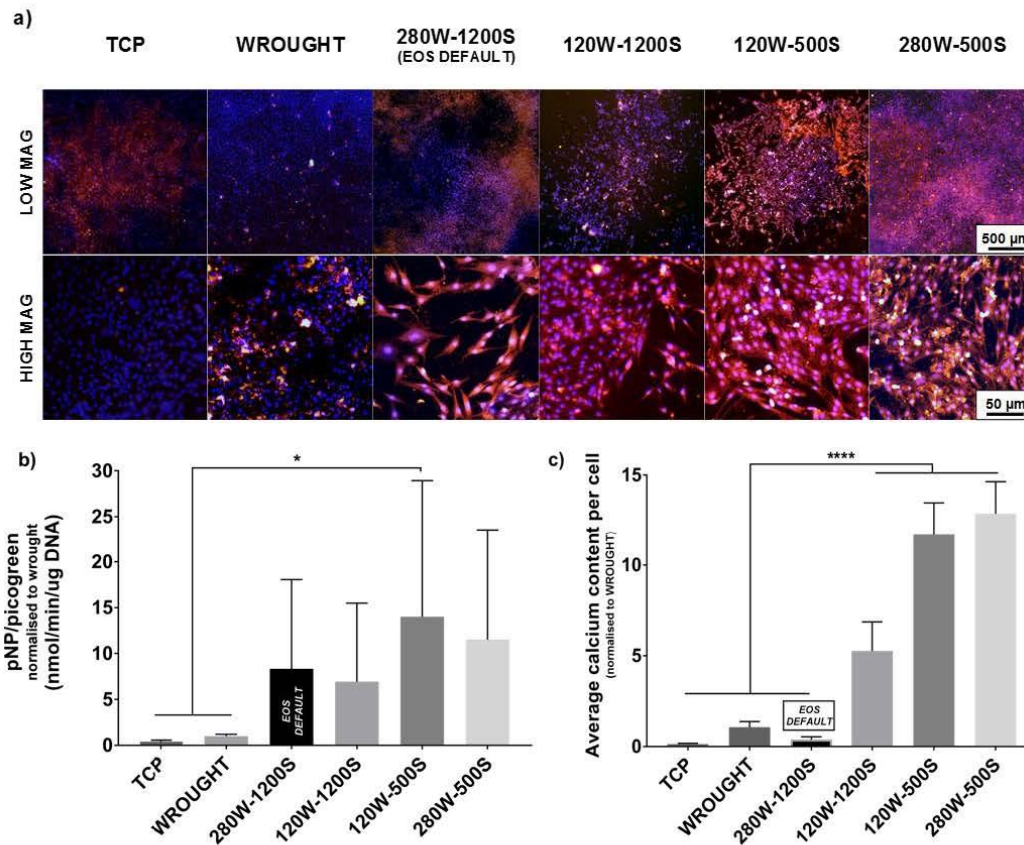
Figure 5: Both ALP activity and average calcium content per cell differed according to sample surface as determined through pNP/picogreen kit analyses and xylenol orange staining, with a) showing stained calcium deposits (orange) and nuclei (blue) after 21 days, b) showing quantitative analysis of ALP activity after 7 days, normalised to TCP and c) showing quantitative analysis of the amount of calcium deposited per cell, normalised to TCP. Data shown as mean ± standard deviation, with significant differences from WROUGHT denoted with * (p < 0.05), ** (p < 0.01), *** (p < 0.001) or **** (p < 0.0001), n=9.

Calcium deposition indicates the beginning of successful *in vitro* bone formation, and was examined after 21 days through the use of the calcium-chelating agent, xylenol orange, as seen in Figure 5a). Quantitative analysis showed that calcium deposition was similar on the wrought and 280W-1200S (EOS DEFAULT) samples, while calcium deposition on the other SLM Ti-6Al-4V samples was at least 5 fold higher. The 280W-500S samples supported similar amounts of calcium deposition to the 280W-1200S (EOS DEFAULT)

samples, likely due to similar surface roughness ($R_a = 1.48 \pm 0.66$ and $R_a = 4.62 \pm 0.9$ respectively) and porosity (porosity percentage = 0.16 ± 0.04 and 0.03 ± 0.01 respectively). Overall, the 120W-500S samples exhibited both the highest ALP activity and among the highest amount of deposited calcium suggesting that they have the highest potential for osteogenic induction.

4. Discussion

This study examined biological interactions between osteoblast like cells and various Ti-6Al-4V surfaces produced by either SLM or conventional methods. Varying SLM process parameters such as laser power and/or scan speed was hypothesised to affect the surface characteristics of the SLM Ti-6Al-4V and thus have effects on bioactivity. Results showed that osteoblast-like MG63 cells successfully attached to and proliferated on each of the samples examined, with little evidence of cytotoxicity (<5%) as compared to wrought Ti-6Al-4V (conventionally produced Ti-6Al-4V), in agreement with multiple other works in the field [1,8,13,43,60,61].

The choice of SLM process parameters was found to significantly affect Ti-6Al-4V surface properties such as roughness, porosity, hardness and corrosion resistance, as well as the biological response of osteoblast-like MG63 cells, with substantial differences in cell viability, morphology and osteogenic behaviour observed between cells cultured on each surface and cells cultured on wrought Ti-6Al-4V.

The samples produced using the most commonly used settings (280W-1200S, EOS DEFAULT settings) exhibited low porosity and roughness (0.03 ± 0.02 % and $R_a = 4.62 \pm 0.9$ µm), as well as high hardness and corrosion resistance (48.7 ± 3.3 HRC and $E_{corr} = -411.7 \pm 20.3$ mV$_{SCE}$). Osteoblast-like MG63 cells were able to interact well with 280W-1200S surfaces, with cell viability above 95% at days 1 and 7 following seeding, and evidence of proliferation between days 1 and 7. Thus, the 'default settings', optimised for mechanical performance, display adequate bioactivity as well. It should be noted while all Ti-6Al-4V surfaces supported reduced cell activity in comparison to TCP, this is as expected, likely due to the specific hydrophilicity of TCP being ideal for cell adhesion (~70°) [62,63].

The Ti-6Al-4V samples produced with a laser power of 120 W and laser scan speed of 1200 mm/s (VED = 25 J/mm^3) exhibited both the highest roughness and porosity, as well as the lowest corrosion resistance and highest current density. Cell viability on the 120W-1200S samples was significantly lower at both days 1 and 7. The process parameters used to make the 120W-1200S samples were not well matched, as the low laser power and high laser scan speed cause the formation of a highly unstable moving melt pool, leading to poor particle melting and fusion. The resulting porosity, roughness and improper surface oxide formation can be assumed to adversely affect initial protein adsorption, and thus subsequent cell attachment and activity. The *in vitro* data confirms that laser scan speed must be carefully chosen with respect to laser power, to prevent

103

poor bioactivity, and indicates a lower threshold for VED, i.e. 25 J/mm^3.

Notably, the 120W-500S samples supported the highest cell viability (at both days 1 and 7), the development of polygonal morphology as well as high rates of ALP activity and calcium deposition. The 120W-500S samples were built using lower laser power and slower laser scan speed than the EOS DEFAULT samples (280W-1200S), however, the VED was the same, i.e. 55 J/mm^3. This indicates that reducing the laser scan speed and/or laser power during SLM can still produce microstructures and bulk properties conducive to bone cell adhesion and proliferation. Cells on the 120W-500S samples displayed the cell morphology closest to that of the prototypical thriving osteoblast *in vivo*, i.e. well spread and polygonal with long filopodial extensions. The tensegrity model of cytoskeletal organisation states that actin microfilaments act as tension bearing elements, and thus the cytoskeleton provides both shape stability and acts as a mechanotransducer (primarily through the Rho pathways) [64]. Together with the plasma membrane, the actin microfilaments maintain cellular tension. Cells on the 120W-500S samples displayed polygonal morphology and long filopodial extensions with aligned stress fibres at the ends, indicating high cellular tension, which has been shown to be osteogenic [65].

Cell adhesion to implant surfaces is mediated by cellular receptor/ligand interactions between cells and proteins adsorbed onto implant surfaces. Implant surface properties strongly affect the initial layer of adsorbed proteins (both in terms of composition and folding), and thus surface properties directly influence the attachment rate, spreading, proliferation (and differentiation) of osteoblast-like cells on implant surfaces. Specific surface properties such as roughness, porosity and hydrophilicity are known to affect osteoblast adhesion and growth. Hydrophilic surfaces have been shown to enhance surface reactivity with surface ions, amino acids and proteins in tissue fluid [61]. There is little consensus on the effects of surface roughness on initial cell adhesion leading to subsequent bone formation, however, it is thought that rougher surfaces, up to a critical level, encourage the entrapment of fibrin, and thus the increased adhesion of osteogenic cells [66]. Roughness and isolated pits can also trap ionic species – with the restricted access of oxygen into these crevices, the passive oxide layer that normally forms on Ti-6Al-4V can be impeded, leading to the increased likelihood of pitting corrosion in these areas [67]. The trapping of calcium ions, while very aggressive in corrosion terms, has been shown to increase the rate of tissue generation [68]. Wysocki et al report that increasing VED improves SLM Ti-6Al-4V densification and reduces roughness due to changes in melt pool viscosity, with associated increases in proliferation [13], leading to increases in cell proliferation on these surfaces. This agrees with the work of Linez-Bataillon et al, who reported changes in cellular morphology according to surface roughness, with smoother surfaces causing cell morphology to become elongated with large lamellipodes and fine pseudopodia [58]. However, this effect has a threshold value, with Linez-Bataillon et al reporting that mirror polished Ti-6Al-4V samples exhibited reduced osteoblast adhesion and cell activity. Thus it is clear that a somewhat backwards approach must be taken in determining optimal SLM process parameters for Ti-6Al-4V implant fabrication, with analysis of the surfaces achievable by SLM warranting

further investigation.

In all, the 280W-1200S (EOS DEFAULT settings) settings, optimised for mechanical performance, produce Ti-6Al-4V which supports the early stages of osseointegration. However, the 120W-500S settings, while supplying the same energy density, produced Ti-6Al-4V surfaces with improved interactions with osteoblast adhesion, proliferation and differentiation. Thus it is clear that there is great potential in tuning cellular activity through the SLM process itself. This could facilitate a significant reduction in processing steps. At present, a multitude of post-processing surface modifications are utilised to increase the bioactivity of AM Ti-6Al-4V implant surfaces, including topographical modifications through surface roughening. The topographical changes possibly through manipulation of the process parameters, as shown in this study, present an alternate route to improving Ti-6Al-4V implant bioactivity [63,69,70].

5. Conclusion

Ti-6Al-4V orthopaedic implants are generally produced through casting processes and subsequent heat treatments, however, new generation fabrication methods such as SLM have great potential, particularly in the field of personalised medicine. The improvement of orthopaedic implant functionality and performance is being investigated through multiple strategies, from altering material composition, to design features such as scaffolding, and post-processing surface modifications. This study shows that the SLM process itself can be manipulated to improve osteoblast interaction with SLM Ti-6Al-4V implant surfaces. Further work remains to be completed in characterising initial osteoblast interactions with SLM Ti-6Al-4V produced with a larger process window, and combinations of process parameters including but not limited to laser scan speed and laser power. This indicates that further work should be completed to determine the best process parameter combinations in terms of bioactivity.

Funding

6. References

[1]   A. Shaoki, J. Xu, H. Sun, X. Chen, J. Ouyang, X. Zhuang, F. Deng, Osseointegration of three-dimensional designed titanium implants manufactured by selective laser melting, Biofabrication. 8 (2016) 045014. doi:10.1088/1758-5090/8/4/045014.

[2]   J.D. Avila, S. Bose, A. Bandyopadhyay, Additive manufacturing of titanium and titanium alloys for biomedical applications, Elsevier Inc., 2018. doi:10.1016/B978-0-12-812456-7.00015-9.

[3]   S. Bose, S.F. Robertson, A. Bandyopadhyay, Surface modification of biomaterials and biomedical devices using additive manufacturing, Acta Biomater. 66 (2018) 6–22. doi:10.1016/j.actbio.2017.11.003.

[4]   X.P. Tan, Y.J. Tan, C.S.L. Chow, S.B. Tor, W.Y. Yeong, Metallic powder-bed based 3D printing of cellular scaffolds for orthopaedic implants: A state-of-the-art review on manufacturing, topological design, mechanical properties and biocompatibility, Mater. Sci. Eng. C. 76 (2017) 1328–1343. doi:10.1016/j.msec.2017.02.094.

[5]   B. Wysocki, J. Idaszek, K. Szlazak, K. Strzelczyk, T. Brynk, K.J. Kurzydłowski, W. Święszkowski, S. Eszkowski, Post processing and biological evaluation of the titanium scaffolds for bone tissue engineering, Materials (Basel). 9 (2016). doi:10.3390/ma9030197.

[6]   K.S. Munir, Y. Li, C. Wen, Metallic scaffolds manufactured by selective laser melting for biomedical applications, in: C. Wen (Ed.), Met. Foam Bone Process. Modif. Charact. Prop., Woodhead Publishing Limited, 2016: pp. 1–23. doi:10.1016/B978-0-08-101289-5.00001-9.

[7]   J. Liu, G. Han, S. Pan, Y. Ge, H. Feng, Z. Shen, Biomineralization stimulated peri-titanium implants prepared by selective laser melting, J. Mater. 1 (2015) 253–261. doi:10.1016/j.jmat.2015.07.008.

[8]   M. Wang, Y. Wu, S. Lu, T. Chen, Y. Zhao, H. Chen, Z. Tang, Fabrication and characterization of selective laser melting printed Ti–6Al–4V alloys subjected to heat treatment for customized implants design, Prog. Nat. Sci. Mater. Int. 26 (2016) 671–677. doi:10.1016/j.pnsc.2016.12.006.

[9]   H. Shipley, D. McDonnell, M. Culleton, R. Coull, R. Lupoi, G. O'Donnell, D. Trimble, Optimisation of process parameters to address fundamental challenges during selective laser melting of Ti-6Al-4V: A review, Int. J. Mach. Tools Manuf. 128 (2018) 1–20. doi:10.1016/j.ijmachtools.2018.01.003.

[10]   M. El-Sayed, M. Ghazy, Y. Yehia, K. Essa, Optimization of SLM Process Parameters for Ti6Al4V Medical Implants, Rapid Prototyp. J. (2018).

[11]   T. Kurzynowski, E. Chlebus, B. Kuźnicka, J. Reiner, Parameters in selective laser melting for processing metallic powders, (2012) 823914. doi:10.1117/12.907292.

[12]   A.M. Khorasani, I. Gibson, U.S. Awan, A. Ghaderi, The Effect of SLM Process Parameters on Density, Hardness, Tensile Strength and Surface Quality of Ti-6Al-4V, Addit. Manuf. (2018). doi:10.1016/J.ADDMA.2018.09.002.

[13]   B. Wysocki, J. Idaszek, J. Zdunek, K. Rożniatowski, M. Pisarek, A. Yamamoto, W. Święszkowski, The influence of selective laser melting (SLM) process parameters on in-vitro cell response, Int. J. Mol. Sci. 19 (2018). doi:10.3390/ijms19061619.

[14]   Z. Li, I. Kucukkoc, F. Liu, Optimising the process parameters of selective laser melting for the fabrication of Ti6Al4V alloy, Rapid Prototyp. J. 24 (2017) 150–159.

[15]   J. Mezzetta, Process-Property Relationships of Ti6Al4V Fabricated through Selective Laser Melting, McGill University, 2016.

[16]   T.M. Chiu, M. Mahmoudi, W. Dai, A. Elwany, H. Liang, H. Castaneda, Corrosion assessment of Ti-6Al-4V fabricated using laser powder-bed fusion additive manufacturing, Electrochim. Acta. 279 (2018) 143–151. doi:10.1016/j.electacta.2018.04.189.

[17]   H. Gong, K. Rafi, H. Gu, G.D. Janaki Ram, T. Starr, B. Stucker, Influence of defects on mechanical properties of Ti–6Al–4V components produced by selective laser melting and electron beam melting, Mater. Des. 86 (2015) 545–554. doi:10.1016/j.matdes.2015.07.147.

[18]   I. Yadroitsev, P. Krakhmalev, I. Yadroitsava, Hierarchical design principles of selective laser melting for high quality metallic objects, Addit. Manuf. 7 (2015) 45–56. doi:10.1016/j.addma.2014.12.007.

[19]   S. Pal, G. Lojen, V. Kokol, I. Drstvensek, Evolution of metallurgical properties of Ti-6Al-4V alloy fabricated in different energy densities in the Selective Laser Melting technique, J. Manuf. Process. 35 (2018) 538–546. doi:https://doi.org/10.1016/j.jmapro.2018.09.012.

[20]   A.M. Khorasani, I. Gibson, M. Goldberg, G. Littlefair, A survey on mechanisms and critical parameters on solidification of selective laser melting during fabrication of Ti-6Al-4V prosthetic

acetabular cup, Mater. Des. 103 (2016) 348–355. doi:10.1016/j.matdes.2016.04.074.

[21] M. Shunmugavel, A. Polishetty, G. Littlefair, Microstructure and Mechanical Properties of Wrought and Additive Manufactured Ti-6Al-4V Cylindrical Bars, Procedia Technol. 20 (2015) 231–236. doi:10.1016/j.protcy.2015.07.037.

[22] M. Simonelli, Microstructure evolution and mechanical properties of selective laser melted Ti-6Al-4V, Loughborough University, 2014. doi:10.1016/j.phpro.2011.03.033.

[23] W.S.W. Harun, N.S. Manam, M.S.I.N. Kamariah, S. Sharif, A.H. Zulkifly, I. Ahmad, H. Miura, A review of powdered additive manufacturing techniques for Ti-6al-4v biomedical applications, Powder Technol. 331 (2018) 74–97. doi:10.1016/j.powtec.2018.03.010.

[24] E. Liverani, S. Toschi, L. Ceschini, A. Fortunato, Effect of selective laser melting (SLM) process parameters on microstructure and mechanical properties of 316L austenitic stainless steel, J. Mater. Process. Technol. 249 (2017) 255–263. doi:10.1016/j.jmatprotec.2017.05.042.

[25] C. Kusuma, The Effect of Laser Power and Scan Speed on Melt Pool Characteristics of Pure Titanium and Ti-6Al-4V Alloy for Selective Laser Melting The Effect of Laser Power and Scan Speed on Melt Pool Characteristics of Pure Titanium and Ti-6Al-4V alloy for Selective, (2016).

[26] T. Majumdar, N. Eisenstein, J.E. Frith, S.C. Cox, N. Birbilis, Additive Manufacturing of Titanium Alloys for Orthopedic Applications : A Materials Science Viewpoint, Adv. Eng. Mater. (2018). doi:10.1002/adem.201800172.

[27] S. Bose, D. Ke, H. Sahasrabudhe, A. Bandyopadhyay, Additive Manufacturing of Biomaterials, Prog. Mater. Sci. 93 (2017) 45–111. doi:10.1016/j.pmatsci.2017.08.003.

[28] B. Song, S. Dong, H. Liao, C. Coddet, Process parameter selection for selective laser melting of Ti6Al4V based on temperature distribution simulation and experimental sintering, Int. J. Adv. Manuf. Technol. 61 (2012) 967–974. doi:10.1007/s00170-011-3776-6.

[29] P. Hanzl, M. Zetek, T. Bakša, T. Kroupa, The Influence of Processing Parameters on the Mechanical Properties of SLM Parts, Procedia Eng. 100 (2015) 1405–1413. doi:10.1016/j.proeng.2015.01.510.

[30] B. Vrancken, Study of Residual Stresses in Selective Laser Melting, 2016.

[31] Z. Chen, X. Wu, D. Tomus, C.H.J. Davies, Surface roughness in Selective Laser Melted Ti-6Al-4V alloy components, Addit. Manuf. 21 (2018) 30273–7. doi:10.1016/j.addma.2018.02.009.

[32] U. Scipioni Bertoli, A.J. Wolfer, M.J. Matthews, J.P.R. Delplanque, J.M. Schoenung, On the limitations of Volumetric Energy Density as a design parameter for Selective Laser Melting, Mater. Des. 113 (2017) 331–340. doi:10.1016/j.matdes.2016.10.037.

[33] F. Cabanettes, A. Joubert, G. Chardon, V. Dumas, J. Rech, C. Grosjean, Z. Dimkovski, Topography of as built surfaces generated in metal additive manufacturing: a multi scale analysis from form to roughness, Precis. Eng. (2018) 0–1. doi:10.1016/j.precisioneng.2018.01.002.

[34] A. Masmoudi, R. Bolot, C. Coddet, Investigation of the laser–powder–atmosphere interaction zone during the selective laser melting process, J. Mater. Process. Technol. 225 (2015) 122–132. doi:10.1016/j.jmatprotec.2015.05.008.

[35] J.-P. Kruth, G. Levy, F. Klocke, T.H.C. Childs, Consolidation phenomena in laser and powder-bed based layered manufacturing, CIRP Ann. - Manuf. Technol. 56 (2007) 730–759. doi:10.1016/j.cirp.2007.10.004.

[36] S.H. Riza, S.H. Masood, C. Wen, Laser-Assisted Additive Manufacturing for Metallic Biomedical Scaffolds, Elsevier, 2014. doi:10.1016/B978-0-08-096532-1.01017-7.

[37] Q.C. Liu, J. Elambasseril, S.J. Sun, M. Leary, M. Brandt, P.K. Sharp, The Effect of Manufacturing Defects on the Fatigue Behaviour of Ti-6Al-4V Specimens Fabricated Using Selective Laser Melting, Adv. Mater. Res. 891–892 (2014) 1519–1524. doi:10.4028/www.scientific.net/AMR.891-892.1519.

[38] H. Gong, K. Rafi, N. V. Karthik, T. Starr, B. Stucker, Defect morphology in Ti-6Al-4V parts fabricated by Selective Laser Melting and Electron Beam Melting, 24th Int. SFF Symp. - An Addit. Manuf. Conf. SFF 2013. (2013) 440–453. doi:10.1007/s11665-013-0658-0.

[39] D. Agius, K. Kourousis, C. Wallbrink, A Review of the As-Built SLM Ti-6Al-4V Mechanical Properties towards Achieving Fatigue Resistant Designs, Metals (Basel). 8 (2018) 75. doi:10.3390/met8010075.

[40] H. Gong, K. Rafi, H. Gu, T. Starr, B. Stucker, Analysis of defect generation in Ti–6Al–4V parts made using powder bed fusion additive manufacturing processes, Addit. Manuf. 1–4 (2014) 87–98. doi:10.1016/j.addma.2014.08.002.

[41] M. Bigerelle, K. Anselme, B. Noel, I. Ruderman, P. Hardouin, A. Iost, Improvement in the

morphology of Ti-based surfaces: A new process to increase in vitro human osteoblast response, Biomaterials. 23 (2002) 1563–1577. doi:10.1016/S0142-9612(01)00271-X.

[42]   K. Anselme, Osteoblast adhesion on biomaterials, Biomaterials. 21 (2000) 667–681. doi:10.1016/S0142-9612(99)00242-2.

[43]   L. Matouskova, M. Ackermann, J. Horakova, L. Capek, P. Henys, J. Safka, How does the surface treatment change the cytocompatibility of implants made by selective laser melting?, Expert Rev. Med. Devices. 15 (2018) 313–321. doi:10.1080/17434440.2018.1456335.

[44]   J.I. Rosales-Leal, M.A. Rodríguez-Valverde, G. Mazzaglia, P.J. Ramón-Torregrosa, L. Díaz-Rodríguez, O. García-Martínez, M. Vallecillo-Capilla, C. Ruiz, M.A. Cabrerizo-Vílchez, Effect of roughness, wettability and morphology of engineered titanium surfaces on osteoblast-like cell adhesion, Colloids Surfaces A Physicochem. Eng. Asp. 365 (2010) 222–229. doi:10.1016/j.colsurfa.2009.12.017.

[45]   K. Anselme, P. Linez, M. Bigerelle, D. Le Maguer, A. Le Maguer, P. Hardouin, H.F. Hildebrand, A. Iost, J.M. Leroy, The relative relative influence of the topography and chemistry of TiAl6V4 surfaces on osteoblastic cell behaviour, 21 (2000) 1567–1577.

[46]   T.P. Kunzler, T. Drobek, M. Schuler, N.D. Spencer, Systematic study of osteoblast and fibroblast response to roughness by means of surface-morphology gradients, Biomaterials. 28 (2007) 2175–2182. doi:10.1016/j.biomaterials.2007.01.019.

[47]   C.H. Ku, D.P. Pioletti, M. Browne, P.J. Gregson, Effect of different Ti-6Al-4V surface treatments on osteoblasts behaviour, Biomaterials. 23 (2002) 1447–1454. doi:10.1016/S0142-9612(01)00266-6.

[48]   H.H. Huang, C.T. Ho, T.H. Lee, T.L. Lee, K.K. Liao, F.L. Chen, Effect of surface roughness of ground titanium on initial cell adhesion, Biomol. Eng. 21 (2004) 93–97. doi:10.1016/j.bioeng.2004.05.001.

[49]   J. Lincks, B.D. Boyan, C.R. Blanchard, C.H. Lohmann, Y. Liu, D.L. Cochran, D.D. Dean, Z. Schwartz, Response of MG63 osteoblast-like cells to titanium and titanium alloy is dependent on surface roughness and composition, Biomater. Silver Jubil. Compend. 19 (2006) 147–160. doi:10.1016/B978-008045154-1.50019-8.

[50]   K. Cai, J. Bossert, K.D. Jandt, Does the nanometre scale topography of titanium influence protein adsorption and cell proliferation?, Colloids Surfaces B Biointerfaces. 49 (2006) 136–144. doi:10.1016/j.colsurfb.2006.02.016.

[51]   J. Vaithilingam, E. Prina, R.D. Goodridge, R.J.M. Hague, S. Edmondson, F.R.A.J. Rose, S.D.R. Christie, Surface chemistry of Ti6Al4V components fabricated using selective laser melting for biomedical applications, Mater. Sci. Eng. C. 67 (2016) 294–303. doi:10.1016/j.msec.2016.05.054.

[52]   S.C. Cox, P. Jamshidi, N.M. Eisenstein, M.A. Webber, H. Burton, R.J.A. Moakes, O. Addison, M. Attallah, D.E.T. Shepherd, L.M. Grover, Surface Finish has a Critical Influence on Biofilm Formation and Mammalian Cell Attachment to Additively Manufactured Prosthetics, ACS Biomater. Sci. Eng. 3 (2017) 1616–1626. doi:10.1021/acsbiomaterials.7b00336.

[53]   M. Fousová, D. Vojtěch, J. Kubásek, E. Jablonská, J. Fojt, Promising characteristics of gradient porosity Ti-6Al-4V alloy prepared by SLM process, J. Mech. Behav. Biomed. Mater. 69 (2017) 368–376. doi:10.1016/j.jmbbm.2017.01.043.

[54]   J. Fojt, M. Fousova, E. Jablonska, L. Joska, V. Hybasek, E. Pruchova, D. Vojtech, T. Ruml, Corrosion behaviour and cell interaction of Ti-6Al-4V alloy prepared by two techniques of 3D printing, Mater. Sci. Eng. C. 93 (2018) 911–920. doi:10.1016/j.msec.2018.08.066.

[55]   L. Lo Muzio, A. Santarelli, G. Orsini, L. Memé, M. M, R. Gatto, G. Gallusi, P.F. Nocini, D. Bertossi, M. Emanuelli, A. Putignano, F. Bambini, MG63 and MC3T3-El osteoblastic cell lines response to raloxifene, Eur. J. Inflamm. 11 (2013) 797–804. doi:10.1177/1721727X1301100322.

[56]   E.M. Czekanska, M.J. Stoddart, J.R. Ralphs, R.G. Richards, J.S. Hayes, A phenotypic comparison of osteoblast cell lines versus human primary osteoblasts for biomaterials testing, J. Biomed. Mater. Res. - Part A. 102 (2014) 2636–2643. doi:10.1002/jbm.a.34937.

[57]   E.M. Czekanska, M.J. Stoddart, R.G. Richards, J.S. Hayes, In search of an osteoblast cell model for in vitro research, Eur Cell Mater. 24 (2012) 1–17. doi:vol024a01 [pii].

[58]   P. Linez-Bataillon, F. Monchau, M. Bigerelle, H.F. Hildebrand, In vitro MC3T3 osteoblast adhesion with respect to surface roughness of Ti6Al4V substrates, Biomol. Eng. 19 (2002) 133–141. doi:10.1016/S1389-0344(02)00024-2.

[59]   International Organisation for Standardization, Biological evaluation of medical devices -- Part 5:

Tests for in vitro cytotoxicity (ISO 10993-5:2009), (2009).

[60] E. Onal, J.E. Frith, M. Jurg, X. Wu, a Molotnikov, Mechanical properties and in vitro behavior of additively manufactured and functionally graded Ti6Al4V porous scaffolds, Metals (Basel). 8 (2018). doi:10.3390/met8040200.

[61] H. Wang, B. Zhao, C. Liu, C. Wang, X. Tan, M. Hu, A comparison of biocompatibility of a titanium alloy fabricated by electron beam melting and selective laser melting, PLoS One. 11 (2016) 1–19. doi:10.1371/journal.pone.0158513.

[62] A. Cimpean, V. Mitran, C.M. Ciofrangeanu, B. Galateanu, E. Bertrand, D.M. Gordin, D. Iordachescu, T. Gloriant, Osteoblast cell behavior on the new beta-type Ti-25Ta-25Nb alloy, Mater. Sci. Eng. C. 32 (2012) 1554–1563. doi:10.1016/j.msec.2012.04.042.

[63] Y. Luo, S. Ge, Z. Jin, J. Fisher, Effect of surface modification on surface properties and tribological behaviours of titanium alloys, Proc. Inst. Mech. Eng. Part J J. Eng. Tribol. 223 (2009) 311–316. doi:10.1243/13506501JET488.

[64] I. Titushkin, M. Cho, Modulation of cellular mechanics during osteogenic differentiation of human mesenchymal stem cells, Biophys. J. 93 (2007) 3693–3702. doi:10.1529/biophysj.107.107797.

[65] R. McBeath, D.M. Pirone, C.M. Nelson, K. Bhadriraju, C.S. Chen, Cell shape, cytoskeletal tension, and RhoA regulate stemm cell lineage commitment, Dev. Cell. 6 (2004) 483–495. doi:10.1016/S1534-5807(04)00075-9.

[66] L. Le Guehennec, M.-A. Lopez-Heredia, B. Enkel, P. Weiss, Y. Amouriq, P. Layrolle, Osteoblastic cell behaviour on different titanium implant surfaces, Acta Biomater. 4 (2008) 535–543. doi:10.1016/j.actbio.2007.12.002.

[67] G. Ryan, A. Pandit, D.P. Apatsidis, Fabrication methods of porous metals for use in orthopaedic applications, Biomaterials. 27 (2006) 2651–2670. doi:10.1016/j.biomaterials.2005.12.002.

[68] A. Bandyopadhyay, F. Espana, V.K. Balla, S. Bose, Y. Ohgami, N.M. Davies, Influence of porosity on mechanical properties and in vivo response of Ti6Al4V implants, Acta Biomater. 6 (2010) 1640–1648. doi:10.1016/j.actbio.2009.11.011.

[69] M. Geetha, A.K. Singh, R. Asokamani, A.K. Gogia, Ti based biomaterials, the ultimate choice for orthopaedic implants - A review, Prog. Mater. Sci. 54 (2009) 397–425. doi:10.1016/j.pmatsci.2008.06.004.

[70] X. Liu, P.K. Chu, C. Ding, Surface modification of titanium, titanium alloys, and related materials for biomedical applications, Mater. Sci. Eng. R Reports. 47 (2004) 49–121. doi:10.1016/j.mser.2004.11.001.

Supplementary information
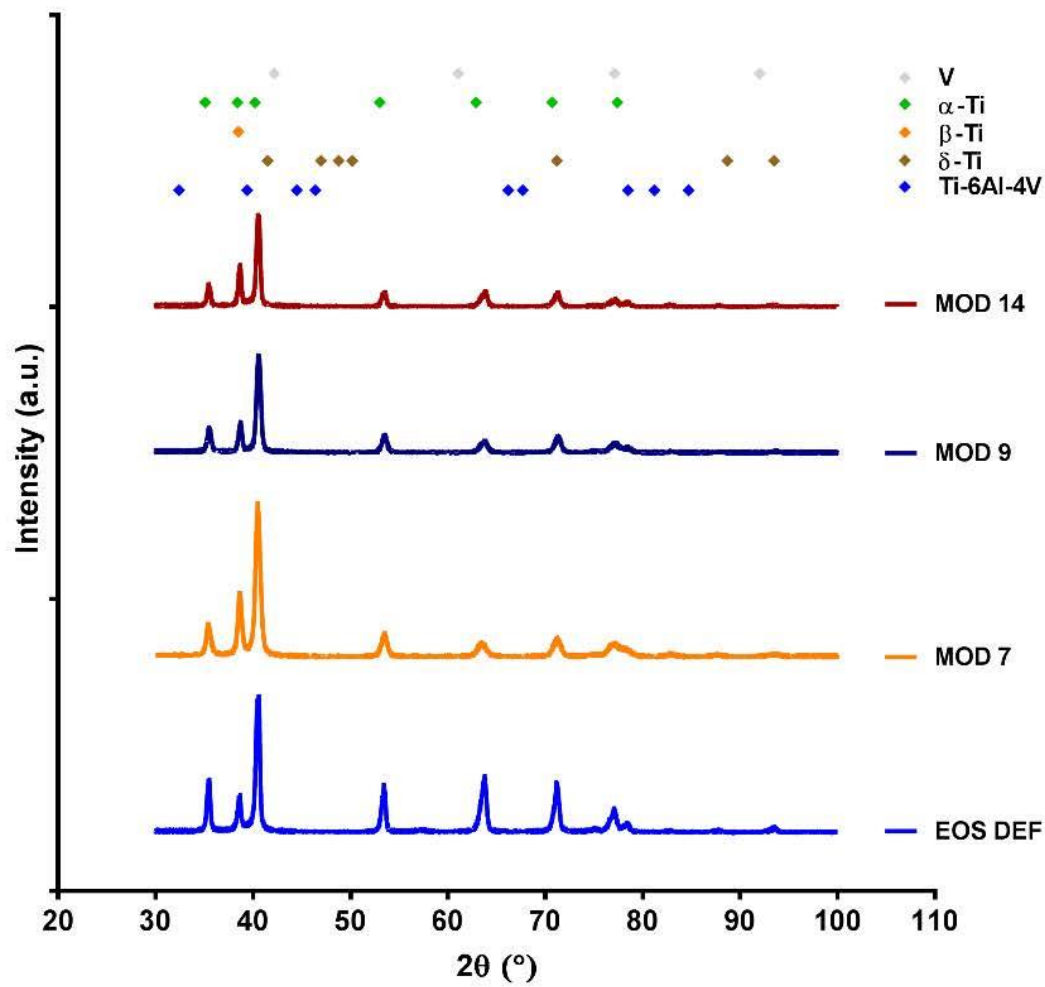
Supplementary Figure A. XRD data for SLM Ti-6Al-4V

Supplementary Table A. Summary of surface data collected

Sample ID	280W-1200S	120W-1200S	120W-500S	280W-500S
Laser scan speed (mm/s)	1200	1200	500	500
Laser power (W)	280	120	120	280
VED (J/mm^3)	55	25	55	135
Ra (µm)	4.62 ± 0.9	35.6 ± 2.0	0.53 ± 0.15	1.48 ± 0.66
Porosity (%)	0.03 ± 0.01	5.59 ± 0.22	0.06 ± 0.01	0.16 ± 0.04
Rockwell hardness (HRC)	41.6 ± 3.3	35.6 ± 2.0	46.9 ± 2.6	44.7 ± 1.5
E_{corr} (mV$_{SCE}$)	4.62 ± 0.9	35.6 ± 2.0	0.53 ± 0.15	1.48 ± 0.66
I_{corr} (µA/cm^2)	0.11 ± 0.05	1.06 ± 0.12	0.12 ± 0.07	0.11 ± 0.05
Contact angle (º)	72.4 ± 6	70.4 ± 4	74.8 ± 6	74.1 ± 5

Chapter 5: The joint replacement/bone interface; measuring the re-passivation of Ti-6Al-4V implant surfaces

For metallic implants to function successfully in the human body, certain criteria must be met, not least in terms of corrosion resistance, ionic dissolution and propensity to provoke adverse physiological responses. The corrosion resistance of Ti-based alloys is well understood and attributed to the passive surface layer which forms in physiological conditions. The disruption of this passive surface layer (breakdown event) through scratching during implantation or during service can lead to corrosion of the underlying surface, mimicking crevice corrosion. Despite this, the re-passivation characteristics of Ti-based alloys are poorly understood due to difficulties in replicating passive layer disruption experimentally. Results from the polarisation testing of Ti and its alloys are limited in that most polarisation curves for these alloys in simulated body fluids do not present classical 'breakdown' or pitting potentials – to examine passive layer disruption and the resulting re-passivation processes, the passive layer must be disrupted manually.

This study presents both a novel experimental technique for the investigation of Ti-based alloy re-passivation, and previously unreported details regarding Ti alloy responses to breakdown events and actual rates of Ti dissolution in physiological conditions. In this study, multiple Ti alloys were investigated; commercially pure Ti (cp-Ti), Ti-6Al-4V, Ti-29Nb-13Ta-4.5Zr (TNTZ), selective laser melted Ti-6Al-4V, direct laser deposited cp-Ti, Ti-35Nb-15Zr, and Ti-25Nb-8Zr. This allowed for the analysis of multiple fabrication methods and compositions, and comparisons thereof. Results revealed that both fabrication method and alloying elements influence 're-passivation' behaviour. Furthermore, atomic emission spectroelectrochemistry as applied to cp-Ti indicated actual dissolution currents of ~2-3 $\mu A/cm^{-2}$ (i.e. ~9 $\mu m/yr$) in the range of the corrosion potential, also revealing such

dissolution is persistent, even with cathodic polarisation, and definitively revealing that the presence of hydrogen peroxide and albumin activate anodic dissolution of Ti.

This chapter was prepared as a paper, and published in *Acta Biomaterialia*. The paper appears here as published.

Full length article

A closer look at the *in vitro* electrochemical characterisation of titanium alloys for biomedical applications using in-situ methods

J.-L. Wang [a,b], R.L. Liu [a], T. Majumdar [a,b], S.A. Mantri [c], V.A. Ravi [d], R. Banerjee [c], N. Birbilis [a,b,*]

[a] Department of Materials Science and Engineering, Monash University, Clayton, Victoria 3800, Australia
[b] Monash Institute of Medical Engineering (MIME), Monash University, Clayton, Victoria 3800, Australia
[c] Department of Materials Science and Engineering, University of North Texas, Denton, TX 76207, USA
[d] Department of Chemical and Materials Engineering, Cal Poly Pomona, Pomona, CA 91768, USA

ARTICLE INFO

ABSTRACT

Titanium (Ti) and its alloys are widely used in several biomedical applications, particularly as permanent orthopaedic implants. Electrochemical testing provides a means to perform accelerated corrosion testing, however whilst results from polarisation testing for Ti and its alloys to date have been generally useful, they are also rather limited on the basis of several reasons. One reason is that the polarisation curves for Ti and its alloys in simulated body fluids all appear rather similar, and they do not present a classical 'breakdown' or pitting potential, making discrimination between alloys difficult. Of practical relevance however, are two key issues; (1) how do Ti alloys respond to a breakdown event? (i.e. do they readily 'repassivate'?), and, (2) what is that *actual* rate of Ti ion loss from exposure to physiological conditions? The answers to these questions are probed herein. Several Ti alloys of either unique composition or different fabrication method were studied, including commercially pure Ti (cp-Ti), Ti-6Al-4V, Ti-29Nb-13Ta-4.5Zr (TNTZ), selective laser melted Ti-6Al-4V, direct laser deposited cp-Ti, Ti-35Nb-15Zr, and Ti-25Nb-8Zr. Results reveal that both fabrication method and alloying influence 'repassivation' behaviour. Furthermore, atomic emission spectroelectrochemistry as applied to cp-Ti indicated actual dissolution currents of $\sim$2–3 $\mu A/cm^2$ (i.e. $\sim$9 $\mu m/yr$) in the range of the corrosion potential, also revealing such dissolution is persistent, even with cathodic polarisation, and definitively revealing that the presence of hydrogen peroxide and albumin activate anodic dissolution of Ti.

Statement of Significance

We believe the paper makes a significant and important contribution to the field of permanent implant biomaterials. Whilst we concede that the paper does not include any *in vivo* work, the timeliness of the work, and the completely new nature of the findings, we believe carries the impact required for *Acta Biomaterialia*.

Statement of Significance: Key highlights include:

- A means of assessment of 'repassivation' of Ti-alloys used as biomaterials (for the first time).
- Reportage of the performance of various Ti-alloys fabricated by 3D printing (for the first time).
- The first unambiguous reporting of the TRUE corrosion rate of Ti in biological environments, employing the advanced AESEC method (for the first time).
- Demonstration of the real, and important, effect of the combination of albumin and H_2O_2 upon dissolution kinetics of Ti (recently revealed to be critically important in this journal: F. Yu, O. Addison, A.J. Davenport, A synergistic effect of albumin and H_2O_2 accelerates corrosion of Ti6Al4V, *Acta Biomater*, 26 (2015) 355–365)

All of the above combine to produce a manuscript that we believe has wide appeal, and can be used as both a port of reference to those working with Ti biomaterials, and also those wishing to apply useful characterisation techniques to their own work (with two very novel methods demonstrated herein, along with the unique information they provide).

* Corresponding author at: Department of Materials Science and Engineering, Monash University, Clayton, Victoria 3800, Australia.
 E-mail address: nick.birbilis@monash.edu (N. Birbilis).

1. Introduction

Titanium and its alloys are the present material of choice as permanent metallic biomaterials, particularly for orthopaedic applications [1,2]. Ti alloys have demonstrated improved biocompatibility, suitable mechanical properties and enhanced corrosion resistance relative to conventional stainless steels and cobalt-based alloys for use as permanent implants [3–5]. Corrosion resistance is a property of key importance for permanent implants as the dissolution of Ti may impact the structural integrity of the implant (although that would require appreciable degradation), whilst even the case of low corrosion rates poses a risk of ion and particle release that can cause inflammatory reactions in the host. Generally, Ti alloys are immune to physiological fluids due to the presence of a nominally protective surface oxide film, however, several corrosion-related failure cases of Ti implants have been previously reported [6,7]. This is due to the fact that this protective film can be damaged by wear processes following implantation. If such films cannot promptly self-heal, localised corrosion may occur on the newly exposed implant surfaces. The combined effect of electrochemical, chemical and mechanical processes may result in premature surface cracks and/or accelerated release of corrosion products, eventually leading to implant failure [7]. As such the ultimate surgical success of implanted Ti will in part, rely on the healing of surface films (repassivation) in response to scratches.

Extensive research has focused on the corrosion behaviour of Ti alloys in physiological fluids, with comparatively little research in Ti repassivation [8–12]. Works to date have also focused on the structure and corrosion resistance of oxide films formed upon alloy surfaces during passivation. For instance, Karthega et al. found that Ti-29Nb-13Ta-4.6Zr (TNTZ) alloys exhibited different surface film structures at various potentials using electrochemical impedance spectroscopy (EIS) [8]. Ti-6Al-4V and Ti-6Al-7Nb alloys were reported to form a bilayer oxide film upon their surface, depending on the electrochemical potential [9]. It merits comment that no passive film breakdown was observed or reported in the above-mentioned experiments. Ti alloys have been reported to show negligible damage of surfaces/surface films even at potentials as high as +5 V in simulated body fluids [13]. In other words, the anodic currents recorded for Ti and its alloys do not reach considerable current densities, in spite of excessive polarisation. As such, electrochemical polarisation does not reveal what would be considered a classical "breakdown" event, instead revealing that Ti is highly polarisable. Electrochemical testing up to high potentials (i.e. ≥+1 V vs. SHE) is not considered relevant, as excessive anodic potentials result in oxygen evolution and do not permit the unambiguous analysis of a dissolution current, and most importantly, conditions *in vivo* will be confined to the vicinity of the open circuit potential. Nevertheless, characterisation of the repassivation behaviour of Ti alloys necessarily requires the local breakdown of the surface oxide layer. To this end, conventional electrochemical testing under physiological conditions cannot be readily employed to characterise the repassivation behaviour of Ti alloys. To date, the repassivation characteristics of Ti alloys in the broader corrosion field have been studied through electrochemical measurements in electrolytes of varying pH or the addition of corrosive species (i.e. fluorides), however such electrolytes do not mimic body fluids [14], nor the physiological conditions arising as a result of inflammation. Local inflammation causes an increase in the production of reactive oxygen species, particularly hydrogen peroxide [15], which has been shown to be a potent bacteriostatic antiobiotic [16] – and of relevance to the peri-implant environment. As recently highlighted by Yu and co-workers, the interaction of reactive oxygen species with proteins such as albumin, is highly relevant to the context of Ti as a biomaterial [17].

The use of mechanical abrasion to examine the repassivation behaviour of commercially pure Ti (cp-Ti) and Ti-6Al-4V in physiological fluids has been documented [18,19]. Contu et al. found that cp-Ti repassivated faster than Ti-6Al-4V in inorganic buffer solutions by monitoring potential changes before, during and after mechanical disruption of the passive film using a tribo-electrochemical micro-cell [18]. Gilbert et al. investigated the repassivation behaviour of Ti-6Al-4V through scratch test methods at varying pH levels, loads and potentials, and demonstrated that all three factors can influence repassivation behaviour [19]. Sakairi et al. studied the repassivation kinetics of cp-Ti using a photon rupture methodology, revealing that oxidation of Ti occurs through a combination of electrochemical and chemical reactions [20]. Such studies as relevant to the repassivation of Ti alloys have been very illuminating, revealing that the repassivation of Ti alloys is indeed critical to study, and a complex parameter to accurately determine. In fact, the abovementioned works have studied potential changes and other means to indirectly predict repassivation rate. In this work, we continue the study of Ti repassivation, however with a focus on instantaneous changes in current density and empirically determined time constants for repassivation.

Herein, seven Ti alloys are explored in regards to their *in vitro* repassivation characteristics – with a prime focus on the role of alloy composition and fabrication method, using *in situ* scratching while concurrently monitoring current density. This is of importance in the context of permanent Ti implants. Surfaces were manually scratched using a sapphire lancet to examine the ability to return to a baseline current density along with the relevant re-establishment rates as determined via chronoamperometry. Furthermore, in order to definitively compare the currents observed from polarisation testing and real Ti ion loss, potentiodynamic polarisation was coupled with measurement of actual dissolution currents for pure Ti using atomic emission spectroelectrochemistry (AESEC). Finally, the effect of inflammation on electrochemistry and corrosion was also examined through the use of hydrogen peroxide and albumin additions to simulated body fluid.

2. Materials and methods

2.1. Materials preparation

A total of seven Ti alloys were tested in this study. The alloys include two commercially available alloys; cp-Ti (commercially pure Ti, ASTM Grade 4) and Ti-6Al-4V (ASTM Grade 5). A custom Ti-29Nb-13Ta-4.5Zr (TNTZ) alloy was also studied. This alloy was produced from round bar initially forged at 1273 K under argon, followed by hot rolling with a reduction ratio of 80% and solution heat treatment at 1013 K for 3.6 ks (as described in [21]). Selective laser melted Ti-6Al-4V (SLM Ti-6Al-4V) was produced using an EOS M280 system (EOS GmbH) and a layer thickness of 30 μm, scan speed of 1200 mm.s⁻¹ and laser power of 280 W. Ti-6Al-4V powder was sourced from Falcontech (Wuxi, PRC). Three alloys were also produced by direct laser deposition (DLD), including 50Ti-35Nb-15Zr (DLD-A), 67Ti-25Nb-8Zr (DLD-B) and cp-Ti (DLD-C). DLD produced alloys were fabricated using the Laser Engineering Net Shaping technique (LENS, Optomec, USA) using a laser power of 500 W, travel speed of 125 mm/min, hatch width of 0.38 mm and layer spacing of 0.25 mm [22,23]. Each specimen was connected to a copper wire on the rear side and cold mounted in an epoxy resin, leaving an exposed surface area varying from 0.16 cm^2 to 1.2 cm^2. Mounted specimens were successively ground to a 4000 grit finish using silicon carbide papers and ethanol as lubricant. Prior to electrochemical testing, specimens were ultrasonically cleaned in ethanol for 5 min and dried in air.
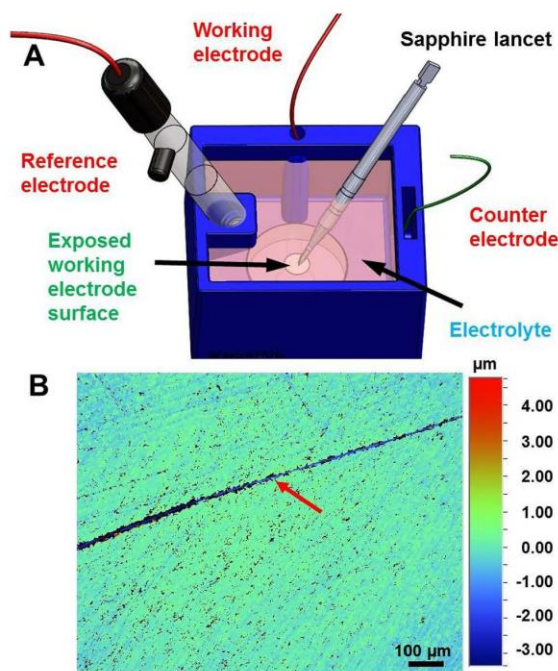
114

2.2. Electrochemical set-up and electrolyte

Electrochemical testing was performed using a custom designed electrochemical cell (fabricated by fused deposition modelling using a Flashforge® Creator Pro), designed to contain 150 mL of Minimum Essential Media, MEM (Gibco® GlutaMAX™), and seen in Fig. 1A.

The chemical composition of MEM is given in Table 1.

In some cases, as described in the relevant section, hydrogen peroxide (Sigma-Aldrich, Australia) and albumin (Sigma-Aldrich, Australia), were also added to the MEM. The concentration of albumin studied herein was one of the concentrations studied in [17]. The concentration utilised (0.1%) is lower than the concentration in blood serum (4.2–5.3% w/v), however a lower concentration

Fig. 1. (A) Electrochemical test set-up employed for in-situ scratch testing: working electrode, reference electrode, counter electrode, electrolyte and sapphire lancet; (B) Typical interferometry image (collected using optical profilometry) of Ti alloy surface following scratching (denoted by red arrow).

Table 1
Major components of MEM used (unit: mmol l^{-1}). The MEM used was Gibco® GlutaMAX™. Full composition is available at (http://www.thermofisher.com/au/en/home/technical-resources/media-formulation.109.html).

Compositions	MEM
Na^+	117.4
Cl^-	123.5
K^+	5.4
Ca^{2+}	1.8
Mg^{2+}	0.4
HPO_4^{2-}	1.0
SO_4^{2-}	0.4
D-Glucose	5.5
Bicarbonate (HCO^{3-})	26.2
Phenol red	0.03

was justified on the basis that an electrochemical effect was anticipated, and to also permit atomic emission spectroelectrochemistry, described below. All tests were carried out in an incubator at 37 °C in a humidified atmosphere of 5% CO_2. The Ti alloys studied were mounted in epoxy and had an insulated copper wire connected to their rear (using adhesive copper tape), whilst the exposed surface served as the working electrode. A platinised mixed-metal oxide Ti-mesh was used as the counter electrode, and a saturated calomel electrode (SCE) as reference electrode. Leakage of Cl^- from the reference electrode was considered negligible. The working electrode wire was insulated and exited the electrochemical cell via a tube to permit connection to the potentiostat (BioLogic SP-150, USA). The alloy surface was boldly exposed during testing, and therefore capable of being manually scratched using a non-conductive sapphire lancet (ProSciTech, Australia). An image of the alloy surface following in-situ scratching was taken using an optical profilometer (Veeco NT-1100, USA), as shown in Fig. 1B.

2.3. Potentiodynamic polarisation and chronoamperometry

Potentiodynamic polarisation tests were carried out using a scan rate of 1 mV/s^{-1} after 10 min exposure to the electrolyte at the respective open circuit potential (OCP). The polarisation curves were collected from −150 mV vs. OCP to +1000 mV vs. SCE. In addition to revealing the electrochemical characteristics of the tested specimens, polarisation curves were also used to estimate the corrosion current density, i_{corr}, via a Tafel-type fit using EC-Lab software (version 10.39, BioLogic). As a general rule, fits were executed by selecting a portion of the curve that commenced >50 mV from corrosion potential, E_{corr}, and i_{corr} was subsequently estimated from the value where the fit intercepted the potential value of the true E_{corr}. A minimum of three separate scans were carried out for each specimen type.

To more closely interrogate the electrochemical response of the alloys tested, given the persistence of a 'passive-like' region in the potentiodynamic polarisation response, the specimens were potentiostatically polarised at +0.1V_{SCE}, and their current density prior to and following scratching monitored. The scratching was performed after 10 min of potentiostatic polarisation, and the current prior to scratching defined as the baseline current density, i_{base}. Following scratching with a sapphire lancet, the time taken to re-establish i_{base} was carefully measured as a means to assess the time required to repair any physical surface damaged and to simulate a classical 'breakdown' event. At least three replicates were taken for each specimen to ensure reproducibility.

2.4. Atomic emission spectroelectrochemistry

The atomic emission spectroelectrochemistry method as developed by Ogle [24–29], has been described in detail elsewhere. The method involves the utility of a flow cell, whereby the electrolyte flows past the working electrode surface and onto an ICP-OES (inductively coupled plasma optical emission spectrometer) for elemental analysis of the electrolyte. This method has been demonstrated to have ultra high sensitivity to the detection of metal ions released into solution as a result of corrosion and/or electrochemical polarisation. Herein, the electrolytes used are as described above, whilst a flow cell (012799, ALS Co., Ltd, Tokyo, Japan) was used, with an exposed working electrode area of 0.6 cm^2 and electrolyte flow rate of 1.5 ml/min. The sketches and descriptions of this cell are provided in [30]. The ICP-OES instrument used in this study was a Perkin Elmer Optima 8000 ICP-OES Spectrometer using Syngistix software.

3. Results

3.1. Potentiodynamic polarisation measurements

The typical potentiodynamic polarisation curves collected for the Ti specimens tested in MEM at 37 °C are presented in Fig. 2.

What is evident from Fig. 2 is that all the Ti alloys displayed what is nominally described as a 'passive window' for a wide range of potentials as anodic polarisation proceeds approximately 100–200 mV more positive than the corrosion potential. As described in the introduction, the apparent passive window only alters slightly until the maximum polarisation studied herein was reached (+1 V vs. SCE). However, most importantly, what is noted from Fig. 2, is that the current density associated with the passive-like region – whilst different for different specimen types – was in most cases in the range of 5–10μA/cm². This is not an exceptionally high current, but considered to be greater than what may be anticipated for passive metals (i.e.<1 μA/cm²) As discussed below however, the current may be signalling the conversion of Ti to an oxide/surface film. In the subsequent section, the response of the Ti surface process to manual film disruption (depassivation) is probed.

Inspection of the typical potentiodynamic polarisation results indicates nearly identical behaviour for cp-Ti and TNTZ alloys, with these alloy types exhibiting well-defined passive-like regions with steady current densities of $\sim$5 μA/cm^{-2}. No alloy breakdown was observed over the range of applied potentials (up to 1 V$_{SCE}$), indicating the formation of a stable surface oxide film. Ti-6Al-4V and SLM Ti-6Al-4V presented comparable passive regions with current densities between 5 and 10 μA/cm², respectively. In the case of SLM
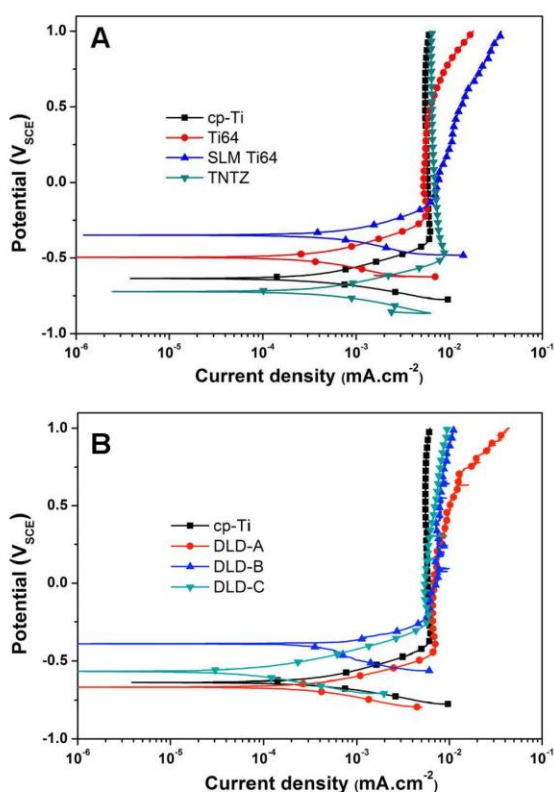
Ti-6Al-4V a gradual increase in current density was observed with increased anodic polarisation, however there was no evidence of a classical breakdown event, and current densities remained below those indicative of active dissolution.

In the case of the DLD series of alloys (Fig. 2B), both DLD-B and DLD-C exhibited clear passive regions, as evidenced by constant current densities of $\sim$6 μA/cm^{-2} over the applied potential range. Conversely, DLD-A maintained a steady passive current density ($\sim$6 μA/cm²) until the polarisation potential reached $\sim$0.7 V following which a gradual increase in current density growth could be observed. However, as with the SLM Ti-6Al-4V, there was no evidence of a classical breakdown for DLD-A, and current densities remained below those expected for active dissolution. Compared to the polarisation curve of cp-Ti, the polarisation curves of the DLD alloys displayed some electrochemical noise with increasing potential – perhaps suggestive of metastable pitting [31]. This is interesting to note, as the electrochemical stability of DLD produced Ti alloys is an active area of investigation. In the context of permanent implants, the electrochemical response in the vicinity of the corrosion potential (E$_{corr}$) is of greatest significance.

The E$_{corr}$ and estimated corrosion current densities (i$_{corr}$) were assessed from polarisation curves, and the mean values with standard deviation are listed in Table 2. It does merit comment that the determination of i$_{corr}$ values is not considered definitive in the case of metals displaying a passive region. This is because i$_{corr}$ determination is an approximate assessment from curve fitting dominated from a linear fit in the region of E$_{corr}$ (as assessed by EC-lab software, see Experimental). The authors acknowledge this limitation, however given the E$_{corr}$ values are tabulated, we also felt it was important to tabulate i$_{corr}$ on the basis that (i) this is done in other studies and also allows the reader to observe what would be a negligible difference on the basis of the i$_{corr}$ parameter alone, and (ii) we definitively show what i$_{corr}$ should be using on-line ICP via the AESEC method further below, so the user determined i$_{corr}$ value provides some context in why the subsequently reported AESEC results are valuable.

From inspection of the i$_{corr}$ alone, all tested alloys reveal what would be typical features of passive metals, i.e. very low i$_{corr}$ values (<1 μA/cm²). In terms of typical E$_{corr}$ scatter in electrochemical tests, it can also be extended that alloys displayed similar corrosion potentials of around −600 mV$_{SCE}$ (+/− $\sim$100 mV), except for SLM Ti-6Al-4V which showed a significantly more noble corrosion potential of $\sim$300 mV$_{SCE}$ – which from inspection of Fig. 2A, appears to be from much higher attendant cathodic kinetics. In terms of i$_{corr}$, DLD-C showed the lowest value ($\sim$0.23 μA/cm²), while the highest i$_{corr}$ was observed on SLM Ti-6Al-4V ($\sim$0.65 μA/cm²). The other tested alloys showed comparable corrosion current densities, ranging from 0.33 to 0.43 μA/cm².

3.2. Potentiostatic measurements and in-situ scratching

The repassivation behaviour of experimental alloys was measured by a bespoke test that required an attendant measurement of current, of which the temporal evolution could be monitored

Fig. 2. Potentiodynamic polarisation curves of pure Ti and Ti alloys after 10 min OCP stabilisation in MEM at 37 °C.

Table 2
Average E$_{corr}$ and i$_{corr}$ values determined from potentiodynamic polarisation testing.

Alloys	E$_{corr}$ (mV$_{SCE}$)	i$_{corr}$ (μA.cm^{-2})
Commercially pure Ti (cp-Ti)	−630 ± 13	0.33 ± 0.06
Ti-6Al-4V (Ti64)	−562 ± 43	0.34 ± 0.05
SLM Ti-6Al-4V (SLM Ti64)	−312 ± 61	0.65 ± 0.07
Ti-29Nb-13Ta-4.5Zr (TNTZ)	−706 ± 13	0.42 ± 0.06
DLD 50Ti-35Nb-15Zr (DLD-A)	−609 ± 65	0.31 ± 0.18
DLD 67Ti-25Nb-8Zr (DLD-B)	−500 ± 97	0.43 ± 0.11
DLD pure Ti (DLD-C)	−634 ± 48	0.23 ± 0.07
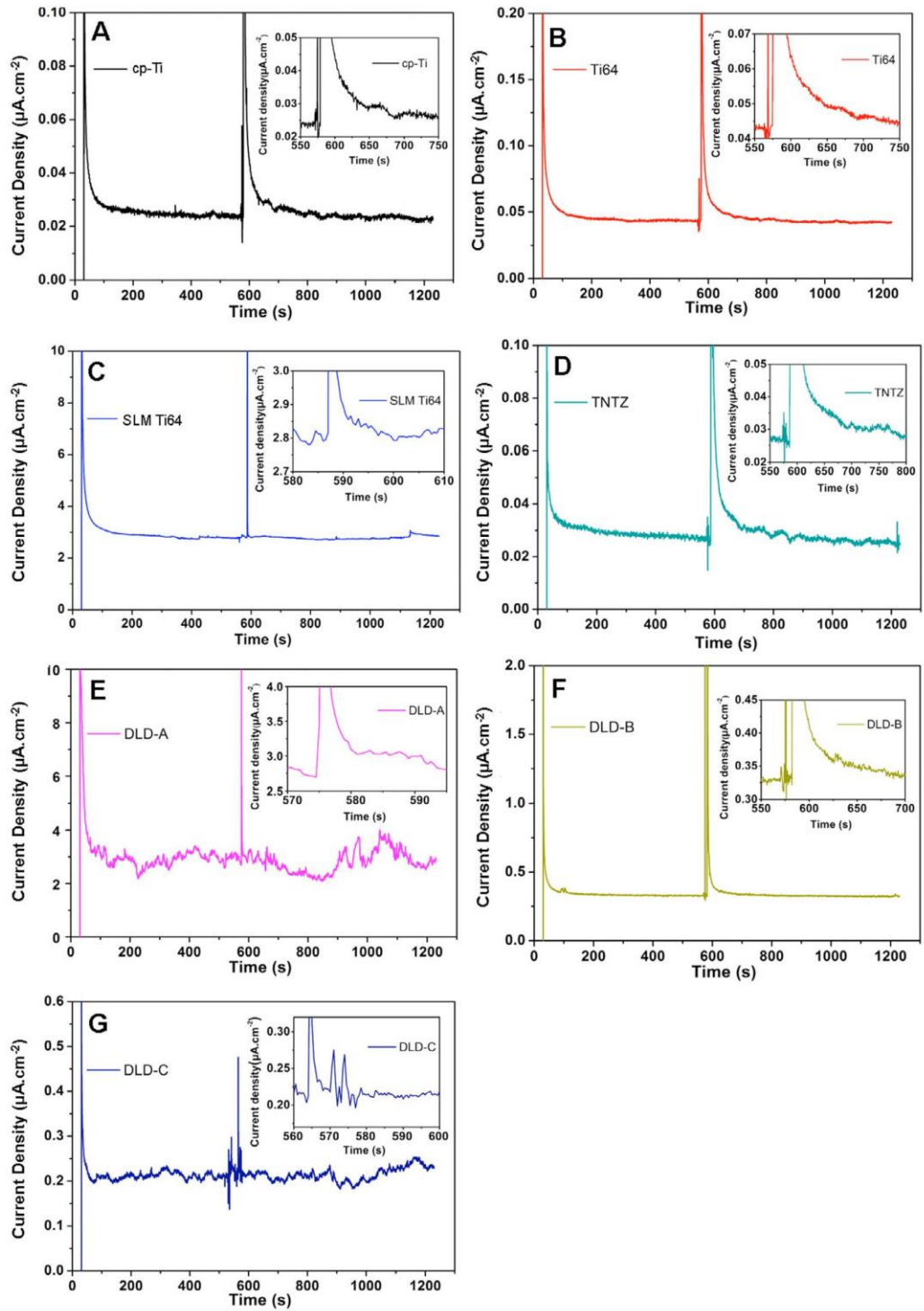
Fig. 3. The variation of the current density at the potentiostatic potential of 0.1V$_{SCE}$ in MEM at 37 °C. The inset image magnifies the current density recovery following the application of a single mechanical scratching event.

during a manual disruption / breakdown event. Herein, it needs to be borne in mind that the testing regime is custom and that repassivation was not measured in the absence of polarisation, with specimens potentiostatically held at +0.1 V_{SCE} before, during, and after physical scratching under physiological conditions, the results of which are shown in Fig. 3.

A magnified inset is included in the chronoamperometry plots shown in Fig. 3, to reveal the detailed changes in current density as a result of scratching. Two peaks can be seen in each chronoamperometry plot; the first peak indicates current density stabilisation (associated with the charging of the electrochemical double layer) at the commencement of the recording period, while the second peak shows the current transient associated with manual scratching, where the bare Ti surface is exposed, leading to a dramatic rise in current density. To highlight the mechanical scratching event, the inset images in Fig. 3 magnify the current density recovery following the single mechanical scratching event What is interesting to note, is that for all specimens studied, the current densities following scratching were able to return to the baseline current density (i_{base}) – which is defined as the current density immediately prior to scratching. What is immediately obvious is that differences in alloy composition or fabrication method revealed notably different values of i_{base}, ranging from 0.028 μA/cm^2 to 3.5 μA/cm^2. Furthermore, the time required to restore i_{base} following film scratching, defined as re-establishment time, varied dramatically, from ~14 s to ~167 s.

Both i_{base} and re-establishment time as obtained from chronoamperometric curves, presented as average values and corresponding range, are summarised in Table 3.

It was observed that cp-Ti and TNTZ alloys exhibited the lowest i_{base} values of ~0.028 μA/cm^2, whilst SLM Ti-6Al-4V and DLD-A alloys showed the highest i_{base} values of ~3.3 μA/cm^2. Notably, all of the cast/wrought Ti alloys tested, including cp-Ti, TNTZ and Ti-6Al-4V, displayed a much lower i_{base} than those produced through SLM or DLD. This finding was further generalised by comparing SLM Ti-6Al-4V with cast Ti-6Al-4V, where the i_{base} of SLM Ti-6Al-4V was about 70 times higher than that of cast Ti-6Al-4V (for the same surface preparation, thus excluding surface finish from fabrication). Similarly, the i_{base} of DLD-C (pure-Ti) was ~7 times higher than that of cp-Ti. In addition, when comparing the i_{base} values of a range of Ti alloys fabricated using the same method, different i_{base} values were also found. For instance, DLD-A exhibited a significantly higher i_{base} relative to those of both DLD-B and DLD-C, while the i_{base} of cast Ti-6Al-4V was twice as high as that of cast cp-Ti.

In the case of re-establishment time, SLM Ti-6Al-4V and DLD-A alloys were able to recover their passive current density following scratching of their surface oxide films within a small number of seconds, i.e. ~14 s and ~22 s, respectively. However, cp-Ti, Ti-6Al-4V and TNTZ required more than 2 min to restore their damaged surface films. DLD-B and DLD-C took ~40 s to restore their surface films. Given there are therefore interesting subtleties in

the collected data, the repassivation behaviour of the alloys as tested herein can be said to be associated with both the i_{base} and re-establishment time, and so these two factors were considered together and shown in Fig. 4.

A closer inspection of the collected data permits for the plotting of i_{base} versus the re-establishment time, revealing an interesting trend wherein a low i_{base} (i.e. cp-Ti, Ti-6Al-4V and TNTZ) corresponded to a longer time taken for film restoration, as compared to alloys with high i_{base} values (i.e. SLM Ti-6Al-4V and DLD TNZ-A), as shown in Fig. 5.

In fact, Fig. 5 bears log axes, such that the relationship is indeed extendable over nearly 3 orders of magnitude in each parameter. This effectively simple relationship actually tends to indicate that the repassivation time constant may be (in a first order sense) proportional to the parameter $R_P C_{dl}$. This is because a low i_{base} would correspond to a high R_P (resistance to polarisation), and where C_{dl} refers to the double layer capacitance [32]. Such a simple time constant (that is proportional to $R_P C_{dl}$) has been previously shown to be an index to the electrochemical response of metal-electrolyte interfaces in other fields of corrosion [33], however repassivation in the context of Ti in MEM would require more/further analysis to relate results to surface oxide variations and electronic properties, allowing the establishment of a more formal, mechanism based, evaluation of the repassivation time constant.
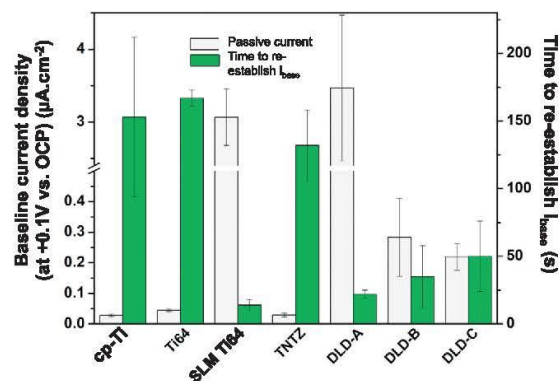

Fig. 4. Baseline current density at +0.1V_{SCE} (i_{base}) and time required to re-establish i_{base} following scratching in MEM at 37 °C
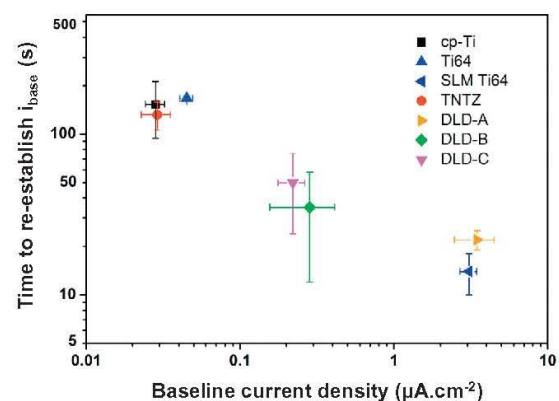

Fig. 5. Relationship between baseline current density at 0.1V_{SCE} (i_{base}) and re-establishment time following a single mechanical scratching event in MEM at 37 °C.

Table 3
Baseline current density from potentiostatic hold at 0.1V_{SCE} (i_{base}) and time required to return to i_{base}.

Alloy	i_{base} (μA.cm^{-2}) before scratching	Time required to reach i_{base} after scratching (s)
Commercially pure Ti (cp-Ti)	0.028 ± 0.004	153 ± 59
Ti-6Al-4V (Ti64)	0.045 ± 0.004	167 ± 6
SLM Ti-6Al-4V (SLM Ti64)	3.1 ± 0.4	14 ± 4
Ti-29Nb-13Ta-4.5Zr (TNTZ)	0.029 ± 0.06	132 ± 26
DLD 50Ti-35Nb-15Zr (DLD-A)	3.5 ± 1.0	22 ± 3
DLD 67Ti-25Nb-8Zr (DLD-B)	0.28 ± 0.13	35 ± 23
DLD pure Ti (DLD-C)	0.22 ± 0.04	50 ± 26

3.3. Electrochemical testing of cp-Ti in the presence of hydrogen peroxide and albumin

The typical potentiodynamic polarisation curves collected for cp-Ti specimens tested in MEM and MEM +0.1% H_2O_2 +0.1% albumin, respectively, at 37 °C are shown in Fig. 6.

In the presence of hydrogen peroxide and albumin, a comparable curve with a "passive window" over a wide range of potentials was observed. It should be noted that the corrosion potential (E_{corr}) value was approximately 0.2 V higher in the presence of hydrogen peroxide and albumin – which was attributed to the more rapid cathodic kinetics measured in the presence of H_2O_2. From the potentiodynamic polarisation testing alone, the form of the polarisation curves exhibit comparable behaviour with/without hydrogen peroxide and albumin, with passive-like region with a steady current density of ∼5–6 µA/cm², respectively.

The variation in the measured current density from potentiostatic polarisation at +0.1 V_{SCE} in MEM and MEM +0.1% H_2O_2 +0.1% albumin, is presented in Fig. 7.

It is seen in Fig. 7 that there is little apparent difference in the repassivation behaviour and time for cp-Ti as tested in MEM with/without 0.1% hydrogen peroxide and 0.1% albumin. There was (on average) a comparable baseline current density (i_{base} ∼0.028 µA/cm²) and re-establishment time (2 min); however visual inspection of the chronoamperometry record does reveal a unique response not previously seen (from the data in Fig. 3). It is apparent that current fluctuations (i.e. noise/spikes) are evident in the chronoamperometry record of cp-Ti tested in MEM with hydrogen peroxide and albumin. This noise was reproducible, and indicative of electrochemical instability which was posited to be attributed to the occurrence of metastable pitting (defined as small microscopic pitting events that initiate and repassivate at potentials below the breakdown potential) [31]. Such metastable pitting analysis was not the basis of the present work, but is be deemed to be important future work.
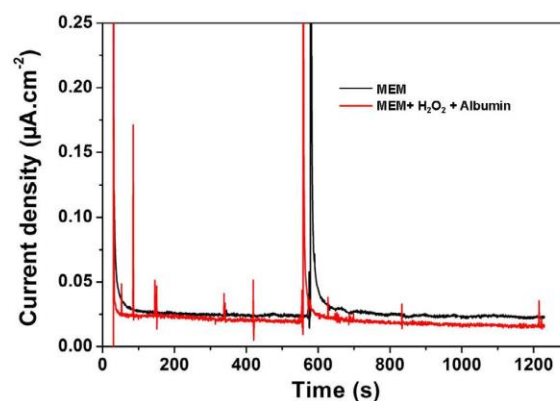
Fig. 7. The variation of the current density for cp-Ti at the fixed potential of 0.1V_{SCE} in MEM and MEM +0.1%H_2O_2 +0.1%albumin, respectively, at 37 °C. The large current transient just prior to 600 s represents the response to a single mechanical scratching event.

3.4. Atomic emission spectroelectrochemistry (AESEC)

The results of potentiodynamic polarisation testing of pure Ti in MEM and MEM +0.1% H_2O_2 +0.1% albumin at 37 °C using an electrochemical flow cell, along with the online AESEC analysis are presented in Fig. 8.

Fig. 8A displays similar data to that shown in Fig. 6, however the plots are presented uniquely on the basis that the geometry (surface area), configuration, and dynamics in the flow cell are different to those of the static cell; and in order to provide the reader with the raw data. The actual Ti dissolution current as a function of time (as determined from the downstream electrolyte exiting the flow
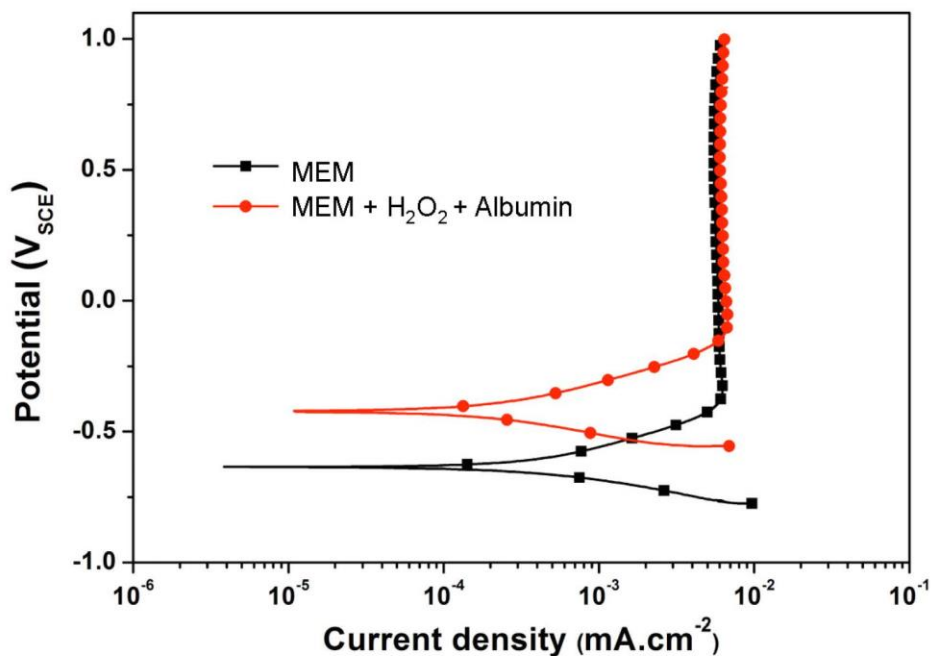
Fig. 6. Potentiodynamic polarisation curves of cp-Ti after 10 min OCP stabilisation in MEM and MEM +0.1% H_2O_2 +0.1% albumin, respectively, at 37 °C. Tests were conducted using a flat cell and non-flowing electrolyte with a working electrode area of 1 cm².

cell during polarisation [26]), is superimposed with the applied potential signals, shown in Fig. 8B.

The respective E_{corr} values of cp-Ti are $\sim$−0.5 V_{SCE} and $\sim$−0.4 V_{SCE} in MEM and MEM +0.1% H_2O_2 +0.1% albumin respectively. Polarisation commenced in an upward scan from 0.3 V below open circuit at a rate of 2 mV/s. Hence, for the initial $\sim$150 s period, the cp-Ti specimens were cathodically polarised for both electrolytes studied. The dissolution current density of pure Ti in both electrolytes was non-zero under cathodic polarisation, being in the range of $\sim$2.5 to $\sim$2 $\mu A/cm^2$ until E_{corr} was reached. Upon transition to anodic polarisation, it can be seen that the dissolution current density of cp-Ti in MEM monotonically decreased with applied anodic potential, displaying a minimum dissolution current density in the vicinity of $\sim$0.5 $\mu A/cm^2$ with maximum anodic polarisation. In contrast, in the presence of hydrogen peroxide and albumin, the dissolution current density of Ti rose substantially following anodic polarisation above E_{corr}, to a maximum value of $\sim$4.2 $\mu A/cm^2$ which was maintained as a plateau current for the wide potential range of $\sim$−0.7 to $\sim$0.6 V_{SCE}. At potentials more positive than 0.5 V_{SCE}, a decrease in dissolution current density to $\sim$1.9 $\mu A/cm^2$ was observed in the case of MEM with hydrogen peroxide and albumin.

4. Discussion

In general, Ti and its alloys display a passive window in the physiological fluids studied, owing to a surface oxide film formed upon the metal / alloy. The potentiodynamic-measured current density associated with the passive window is in the range of 5–10 $\mu A/cm^{-2}$. The utility of AESEC method indicated that within the passive window, the soluble Ti (measured downstream) represents a smaller portion of the total net anodic current than the potentiostat-measured current, revealing that a significant proportion of the measured anodic (potentiostat) current principally contributes to surface film formation. Nevertheless some dissolved Ti was measured, and the extent of measured dissolved Ti decreased with the anodic overpotential (the same was not generally true in the presence of H_2O_2 and albumin, as discussed below).

It was shown that conventional potentiodynamic polarisation testing can only characterise general electrochemical behaviour, including the realisation of the passive window; however to obtain more detailed information on repassivation, *in situ* scratching was employed to expose the bare metallic surface to the solution whilst measuring the sample current. This was shown to be capable of providing a rather high fidelity in discrimination between the electrochemical responses of the various alloys tested – depending on their composition and fabrication.

The polarisation curves presented (Fig. 2) exhibit substantial passive windows in all tested alloys, which is attributed to the formation of TiO_2 surface films on these alloys [34]. Commercial purity titanium and TNTZ displayed a slight decrease in the passive current density with anodic polarisation, suggesting the increased protective nature of the surface film as it grows. In the case of Ti-6Al-4V, SLM Ti-6Al-4V and DLD-A, the current density remained nearly constant at potentials below 0.5 V, while it gradually increased with higher anodic currents, which has also been reported in previous studies [8,9,35].

Whilst not the focus of the present work, it was noted that electrochemical fluctuations likely indicating metastable pitting were observed on the anodic polarisation curves of the DLD series of alloys. Considering the rapidly increasing interest in additively manufactured Ti implants, detailed investigation of the metastable pitting phenomena in these alloys, fabricated via additive manufacturing, is warranted. Metastable pitting of Ti alloys in physiological solutions has not been previously reported, with the exception of one study involving Ti in Ringer's solution by Burstein and co-workers [36].

4.1. Repassivation of scratched oxide films

The methodology for studying repassivation used in this study was not the classical cyclic polarisation method (which reverses the applied potential following a potential dependant surface film breakdown event). This is because no potential dependant surface film breakdown event occurs for Ti in MEM (and MEM-like electrolytes). As such, the current was measured in the passive window (from a potentiostatic hold) and the current density was monitored to assess if current densities returned to their baseline current density (i_{base}) after scratching. Results indicated that the damaged surface oxide films of all tested alloys were able to re-form. Such a finding illustrates the excellent self-healing ability of all tested Ti based alloys to unique de-passivation events. However, in the case of ongoing wear situations (not studied here), and the comparatively long repassivation times, it is conceivable that if the wear cycles are confined to times less than the repassivation times (which can be minutes), ongoing anodic dissolution can possibly result.

The difference in baseline current densities and repassivation times for the alloys tested in this study can be explained through the variations in surface films on different alloys, with respect to thickness, density, morphology, chemistry, and possibly even structure. According to Fig. 3, cast/wrought Ti alloys generally revealed lower i_{base} values than those of SLM or DLD produced Ti alloys – suggesting that fabrication method can influence surface film formation. From a microstructural perspective, cast and wrought Ti alloys usually have a uniform microstructure with fine grains and uniform grain structures, largely comprising equiaxed grains with a random texture, whilst SLM or DLD produced alloys can exhibit non-uniform microstructures inclusive of pores and a proportion of larger columnar, grains; issues which are being dealt with in the physical metallurgy community [37–40]. The present work was however firmly focused on the electrochemical and corrosion aspects of the alloys studied, and microstructural studies remain as future work.

4.2. Influence of hydrogen peroxide and albumin on the dissolution of cp-Ti

The electrochemical data herein demonstrates that the presence of hydrogen peroxide and albumin for the concentration investigated herein, accelerated the cathodic reaction rate with minimal effect on the potentiodynamically measured anodic reaction kinetics, and a minor decrease in i_{base} from potentiostatic testing. A recent report has highlighted that complexation by H_2O_2 is possible, and that adsorption of albumin may inhibit the rate of anodic reaction [17]. It was also observed that the i_{base} re-establishment time illustrated the presence of hydrogen peroxide and albumin generally have negligible influence on repassivation behaviour.

AESEC results further reveal the passive nature of Ti dissolution in MEM, and a decrease in actual Ti dissolution inferred by the potential dependent growth of the surface passive layer. In spite of these generic characteristics however, it is revealed for the first time that the ICP determined equivalent corrosion current density of pure Ti was in the vicinity 2.5 $\mu A/cm^2$ at the E_{corr}, which corresponds to a metal penetration rate of $\sim$9 μm/year. This penetration rate is not considered significant in the case of structural (engineering) materials, however the relevance of this determined penetration rate in the case of a permanent implant warrants further study – particularly in regards to clinical relevance.
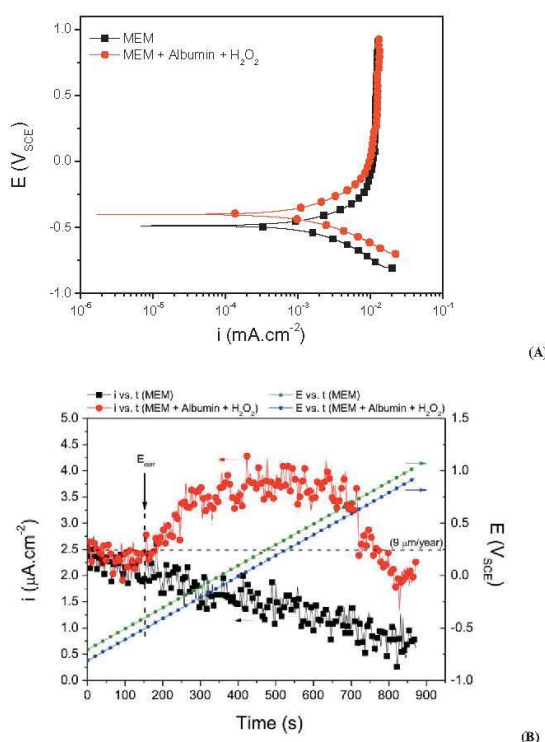
Fig. 8. (A) Potentiodynamic polarisation curves of cp-Ti in MEM and MEM +0.1% H_2O_2 +0.1% albumin. Testing was conducting using a flow cell with an exposed electrode area of 0.6 cm^2 and electrolyte flow rate of 1.5 ml/min maintained at 37 °C. (B) Online AESEC results corresponding to polarisation curve in (A). Potential provided relative to the Ag/AgCl electrode which was used with the flow cell employed.

In the presence of H_2O_2 and albumin, the AESEC data also reveals that the potential dependent passivation of Ti is disrupted, and a comparatively higher current density is sustained in the presence of H_2O_2 and albumin. In fact, at applied potentials anodic to E_{corr}, it is noted that cp-Ti sustains currents as much as 5 times greater when H_2O_2 and albumin are present in MEM. As previously mentioned, the values of the current measured by the potentiostat are larger than the values determined by AESEC, indicating that there are Ti species that are insoluble (i.e. involved in the formation of an insoluble surface layer upon the Ti surface) in addition to the possible redox reaction of H_2O_2 upon the surface of the electrode when H_2O_2 is present.

As a clearer picture emerges of the chemical make-up of physiological solutions, e.g. presence of oxidised species during inflammation [15–17], through ongoing works [41], it appears that current ASTM recommendations [42,43] for the electrochemical testing of permanent orthopaedic implants may be insufficient as they indicate simplistic test solutions such as phosphate buffered saline (PBS). Other solutions such as Ringer's solution and Hank's solution are also widely used, and go some way toward more fully mimicking the *in vivo* environment, due to the presence of additional salts and researchers also adding proteins and biological species similar to those found in physiological fluids. Recent work by Yu that examined Ti alloy corrosion with chemicals produced during inflammation (reactive oxygen species [44,45]), namely hydrogen peroxide [17], definitively indicated that addition of both H_2O_2 and albumin to physiological saline leads to a higher rate of corrosion for Ti-6Al-4V, than in the absence of H_2O_2. The present

work, as informed by the study of Yu et al. [17], also employed the methodology of examining Ti alloys in the presence of albumin and H_2O_2. A common conclusion from the work of Yu and the present work is that further studies of Ti alloy dissolution in the presence of H_2O_2 and albumin are required, to elucidate the precise effects of such an environment. From the work to date, it appears that albumin may act as a cathodic inhibitor by blocking active sites as well as oxygen diffusion to implant surfaces; while H_2O_2 was also linked to preferential attack of the β-phase in the case of the Ti-6Al-4V alloy [17], with H_2O_2 also possibly catalysing complexation reactions to produce strongly hydrated Ti(IV)-H_2O_2. Albumin was also proposed to bind and remove metal cations, with fresh albumin replacing the 'used' albumin. In the context of scratching and repassivation it may be assumed that the following could be occurring; scratching exposes the bare Ti surface, following which albumin adsorbs rapidly, possibly restricting the cathodic reaction (although, the tests herein would not reveal this as the cathode is the counter electrode) while the rate of the anodic reaction increases due to the presence of hydrogen peroxide, leading to increased ion release and dissolution. The latter was indirectly probed by the AESEC experiments, however the concept that the presence of H_2O_2 and albumin leads to a weaker (i.e. perhaps thinner and less protective) film upon Ti was also implied by the electrochemical fluctuations readily observed (metastable pitting transients) during potentiostatic testing.

5. Conclusions

Unique electrochemical tests were applied to Ti and Ti alloys produced by different means, in this study. The work has provided a number of new insights based on the experiments herein, which may be summarised as follows.

- The potentiodynamic polarisation response of various Ti alloys (of diverse compositions and fabrication routes) reveals minimal variation between alloys - with no potential dependant breakdown evident over a wide range of polarisation. As such, given that potential dependant breakdown was not observed, any potential dependant repassivation could also not be studied. Consequently, the *in vitro* repassivation characteristics of various Ti alloys were successfully studied using a physical scratch method, which required the monitoring of current during a potentiostatic hold, revealing the baseline current density and repassivation rate.
- The repassivation behaviour of Ti alloys were found to be affected by both alloy composition and fabrication method. Cast (wrought) Ti alloys revealed a lower baseline current density and slower repassivation than DLD or SLM produced alloys. Pure Ti and TNTZ alloys generally exhibited low baseline current densities and slower repassivation rates relative to the other tested Ti alloys, especially those containing high levels of alloying elements. However, all of the alloys studied returned to their baseline current density following physical scratching.
- Alloys with a low baseline current density during potentiostatic holding (i.e. cp-Ti, Ti-6Al-4V and TNTZ) tended to reveal slower repassivation kinetics in comparison to alloys showing high current densities, i.e. SLM Ti-6Al-4V and DLD-A; suggesting that the repassivation time constant is dictated by capacitive effects.
- The presence of albumin + H_2O_2 in MEM led to an increase in the cathodic kinetics measured from potentiodynamic polarisation (as H_2O_2 is an oxidiser). It was noted that the 'repassivation' behaviour of cp-Ti was also observed in the presence of albumin + H_2O_2, however the corresponding current transient revealed increased electrochemical instability posited to be associated with metastable pitting.

- The AESEC method was able to indicate several important findings; (i) the corrosion rate of cp-Ti in the vicinity of the corrosion potential is $\sim$9 μm/yr (corresponding to $\sim$2 μA/cm^2), (ii) Ti dissolution was not suppressed with cathodic polarisation of up to $\sim$−300 mV, (iii) increased anodic potentials increases the passivation of Ti, which was determined herein from reduced Ti dissolution as measured by AESEC, (iv) the presence of albumin + H$_2$O$_2$ in MEM causes increased Ti dissolution over a large range of anodic potentials (i.e. over $\sim$900 mV).

Acknowledgements

References

[1] J.A. Pura, J.D. Bobyn, M. Tanzer, Implant-delivered alendronate causes a dose-dependent response on net bone formation around porous titanium implants in canines, Clin. Orthop. Relat. Res. 474 (2016) 1224–1233.
[2] M. Geetha, A.K. Singh, R. Asokamani, A.K. Gogia, Ti based biomaterials, the ultimate choice for orthopaedic implants – A review, Prog. Mater. Sci. 54 (2009) 397–425.
[3] M. Niinomi, M. Nakai, J. Hieda, Development of new metallic alloys for biomedical applications, Acta Biomater. 8 (2012) 3888–3903.
[4] M. Geetha, A. Singh, R. Asokamani, A. Gogia, Ti based biomaterials, the ultimate choice for orthopaedic implants–a review, Prog. Mater. Sci. 54 (2009) 397–425.
[5] M. Niinomi, Mechanical properties of biomedical titanium alloys, Mater. Sci. Eng. 243 (1998) 231–236.
[6] K.I. Yokoyama, T. Ichikawa, H. Murakami, Y. Miyamoto, K. Asaoka, Fracture mechanisms of retrieved titanium screw thread in dental implant, Biomaterials 23 (2002) 2459–2465.
[7] J.J. Jacobs, J.L. Gilbert, R.M. Urban, Current concepts review-corrosion of metal orthopaedic implants, J. Bone Joint Surg. Am. 80 (1998) 268–282.
[8] M. Karthega, V. Raman, N. Rajendran, Influence of potential on the electrochemical behaviour of β titanium alloys in Hank's solution, Acta Biomater. 3 (2007) 1019–1023.
[9] S.L. de Assis, S. Wolynec, I. Costa, Corrosion characterization of titanium alloys by electrochemical techniques, Electrochim. Acta 51 (2006) 1815–1819.
[10] N. Oliveira, A.C. Guastaldi, Electrochemical stability and corrosion resistance of Ti–Mo alloys for biomedical applications, Acta Biomater. 5 (2009) 399–405.
[11] V.A. Ravi, A. Schissler, W. Chantrjaroen, C. Beecher, A. Razzak, R. Urak, S. Alas, Corrosion behaviour and biocompatibility of boron containing titanium alloys in simulated physiological environments, Corros. Eng. Sci. Technol. 47 (5) (2012) 383–387.
[12] V.A. Ravi, S. Rogers, S. Malek, D. Surmenian, I. Priddy, B. Harrison, A. Schissler, S.C. Divi, S. Tamirisakandala, D. Miracle, The environmental stability of boron-containing titanium alloys for biomedical applications, J. Miner. Metals Mater. Soc. 63 (6) (2011) 42–47.
[13] S. Samuel, S. Nag, S. Nasrazadani, V. Ukirde, M.E. Bouanani, A. Mohandas, K. Nguyen, R. Banerjee, Corrosion resistance and in vitro response of laser-deposited Ti-Nb-Zr-Ta alloys for orthopedic implant applications, J. Biomed. Mater. Res. 94 (2010) 1251–1256.
[14] S. Takemoto, M. Hattori, M. Yoshinari, E. Kawada, Y. Oda, Corrosion behavior and surface characterization of titanium in solution containing fluoride and albumin, Biomaterials 26 (2005) 829–837.
[15] S.T. Test, S.J. Weiss, Quantitative and temporal characterization of the extracellular H$_2$O$_2$ pool generated by human neutrophils, J. Biol. Chem. 259 (1984) 399–405.
[16] P.A. Hyslop, D.B. Hinshaw, I.U. Scraufstatter, C.G. Cochrane, S. Kunz, K. Vosbeck, Hydrogen peroxide as a potent bacteriostatic antibiotic: implications for host defense, Free Radical Biol. Med. 19 (1) (1995) 31–37.
[17] F. Yu, O. Addison, A.J. Davenport, A synergistic effect of albumin and H$_2$O$_2$ accelerates corrosion of Ti6Al4V, Acta Biomater. 26 (2015) 355–365.
[18] F. Contu, B. Elsener, H. Böhni, A study of the potentials achieved during mechanical abrasion and the repassivation rate of titanium and Ti6Al4V in inorganic buffer solutions and bovine serum, Electrochim. Acta 50 (2004) 33–41.
[19] J.L. Gilbert, C.A. Buckley, E.P. Lautenschlager, Titanium oxide film fracture and repassivation: the effect of potential, pH and aeration, in: Medical applications of titanium and its alloys: The material and biological issues, ASTM International, 1996
[20] M. Sakairi, M. Kinjyo, T. Kikuchi, Repassivation behavior of titanium in artificial saliva investigated with a photon rupture method, Electrochim. Acta 56 (2011) 1786–1791.
[21] Y.F. Ding, R.W. Li, M. Nakai, T. Majumdar, D.H. Zhang, M. Niinomi, N. Birbilis, P. N. Smith, X.B. Chen, Osteoanabolic implant materials for orthopedic treatment, Adv. Healthcare Mater. 5 (2016) 1740–1752.
[22] T. Borkar, S. Nag, J. Tiley, R. Banerjee, Titanium based metal-matrix composites via in-situ nitridation, in: Proceedings of the 13th World Conference on Titanium, John Wiley & Sons, Inc, 2016, pp. 1311–1316.
[23] S. Nag, R. Banerjee, Laser deposition and deformation behavior of Ti-Nb-Zr-Ta alloys for orthopedic implants, J. Mech. Behav. Biomed. Mater. 16 (2012) 21–28.
[24] S. Lebouil, O. Gharbi, P. Volovitch, K. Ogle, Mg dissolution in phosphate and chloride electrolytes: Insight into the mechanism of the negative difference effect, Corrosion 71 (2015) 234–241.
[25] S. Lebouil, A. Duboin, F. Monti, P. Tabeling, P. Volovitch, K. Ogle, A novel approach to on-line measurement of gas evolution kinetics: Application to the negative difference effect of Mg in chloride solution, Electrochim. Acta 124 (2014) 176–182.
[26] K. Ogle, Atomic emission spectroelectrochemistry: A new look at the corrosion, dissolution and passivation of complex materials, Corros. Mater. 37 (2012) 58–65.
[27] K. Ogle, M. Serdechnova, M. Mokaddem, P. Volovitch, The cathodic dissolution of Al, Al2Cu, and Al alloys, Electrochim. Acta 56 (2011) 1711–1718.
[28] J. Światowska, P. Volovitch, K. Ogle, The anodic dissolution of Mg in NaCl and Na2SO4 electrolytes by atomic emission spectroelectrochemistry, Corros. Sci. 52 (2010) 2372–2378.
[29] K. Ogle, J. Baeyens, J. Swiatowska, P. Volovitch, Atomic emission spectroelectrochemistry applied to dealloying phenomena: I. The formation and dissolution of residual copper films on stainless steel, Electrochim. Acta 54 (2009) 5163–5170.
[30] L.F. Hou, L. Raveggi, X.-B. Chen, W. Xu, K.J. Laws, Y. Wei, M. Ferry, N. Birbilis, Investigating the Passivity and Dissolution of a Corrosion Resistant Mg-33at. % Li Alloy in Aqueous Chloride Using Online ICP-MS, J. Electrochem. Soc. 163 (2016) C324–C329.
[31] D.E. Williams, C. Westcott, M. Fleischmann, Stochastic models of pitting corrosion of stainless steels I. Modeling of the initiation and growth of pits at constant potential, J. Electrochem. Soc. 132 (1985) 1796.
[32] E. Barsoukov, J.R. Macdonald, Impedance spectroscopy: theory, experiment, and applications, 2nd ed., John Wiley & Sons, Hoboken, New Jersey, USA, 2005.
[33] N. Birbilis, L.J. Holloway, Use of the time constant to detect corrosion speed in reinforced concrete structures, Cem. Concr. Compos. 29 (2007) 330.
[34] C. Kuphasuk, Y. Oshida, C.J. Andres, S.T. Hovijitra, M.T. Barco, D.T. Brown, Electrochemical corrosion of titanium and titanium-based alloys, J. Prosthetic Dent. 85 (2001) 195–202.
[35] S. Yu, J. Scully, Corrosion and passivity of Ti-13% Nb-13% Zr in comparison to other biomedical implant alloys, Corrosion 53 (1997) 965–976.
[36] G.T. Burstein, C. Liu, R.M. Souto, The effect of temperature on the nucleation of corrosion pits on titanium in Ringer's physiological solution, Biomaterials 26 (2005) 245–256.
[37] L. Thijs, F. Verhaeghe, T. Craeghs, J. Van Humbeeck, J.-P. Kruth, A study of the microstructural evolution during selective laser melting of Ti–6Al–4V, Acta Mater. 58 (2010) 3303–3312.
[38] R. Banerjee, P. Collins, A. Genc, H. Fraser, Direct laser deposition of in situ Ti–6Al–4V–TiB composites, Mater. Sci. Eng. 358 (2003) 343–349.
[39] H.J. Rack, J. Qazi, Titanium alloys for biomedical applications, Mater. Sci. Eng. 26 (2006) 1269–1277.
[40] R. Banerjee, P. Collins, D. Bhattacharyya, S. Banerjee, H. Fraser, Microstructural evolution in laser deposited compositionally graded α/β titanium-vanadium alloys, Acta Mater. 51 (2003) 3277–3292.
[41] M. Aziz-Kerrzo, K.G. Conroy, A.M. Fenelon, S.T. Farrell, C.B. Breslin, Electrochemical studies on the stability and corrosion resistance of titanium-based implant materials, Biomaterials 22 (2001) 1531–1539.
[42] ASTM F3044-14 Test Method for Standard Test Method for Evaluating the Potential for Galvanic Corrosion for Medical Implants, ASTM International, West Conshohocken, United States, 2014.
[43] ASTM F2129-15 Standard Test Method for Conducting Cyclic Potentiodynamic Polarization Measurements to Determine the Corrosion Susceptibility of Small Implant Devices, ASTM International, West Conshohocken, United States, 2015.
[44] G. Mabilleau, S. Bourdon, M.L. Joly-Guillou, R. Filmon, M.F. Basle, D. Chappard, Influence of fluoride, hydrogen peroxide and lactic acid on the corrosion resistance of commercially pure titanium, Acta Biomater. 2 (2006) 121–129.
[45] J. Pan, D. Thierry, C. Leygraf, Hydrogen peroxide toward enhanced oxide growth on titanium in PBS solution: blue coloration and clinical relevance, J. Biomed. Mater. Res. 30 (1996) 393–402.

Chapter 6: The joint replacement/bone interface; the deposition of SrP coatings for enhanced osseointegration

A major factor in orthopaedic implant efficacy is the strength of fixation between the implant and host bone. Strategies for improving implant fixation can be applied during the implant fabrication process, as discussed in chapters 2, 3 and 4. Implant fixation can also be influenced through post-fabrication surface modification techniques.

A common method for the improvement of first instance communication and subsequent osseointegration between the host bone and implant surface is the application of hydroxyapatite. Hydroxyapatite (HA) is a bone mineral which, when applied to implant surfaces, has been shown to improve osteoblast activity. Moreover, the incorporation of certain bioactive elements into this multi-substituted mineral has the potential to further improve osteoblast activity. However, the application of reliable HA coatings is difficult. Thus, a two-step deposition method is investigated in this study, and applied to various Ti-based alloys.

The two step deposition method involves the application of an alkaline hydrothermal treatment to the Ti alloy surface followed by a hydrothermal treatment to result in the formation of a strongly bonded complete layer of $SrPO_4$. The $SrPO_4$ coating, mimicking and building on the properties of HA, has been shown to modulate the activity of osteoblast (OB) and osteoclast (OC) cells during bone formation. Owing to the release of Sr ions from the $SrPO_4$ coating and its unique surface topography, OB cells demonstrate increased proliferation and differentiation, while the cellular responses of OC are suppressed. This $SrPO_4$ coating was also applied to a new alloy Ti-29Nb-13Ta-4.6Zr (wt.%), demonstrating the versatility of the coating technique.

This chapter was prepared as a paper, and published in *Advanced Healthcare Materials.* The paper appears here as published.

FULL PAPER

Osteoanabolic Implant Materials for Orthopedic Treatment

Yun-Fei Ding, Rachel W. Li, Masaaki Nakai, Trina Majumdar, Dong-Hai Zhang, Mitsuo Niinomi, Nick Birbilis, Paul N. Smith, and Xiao-Bo Chen*

Osteoporosis is becoming more prevalent due to the aging demographics of many populations. Osteoporotic bone is more prone to fracture than normal bone, and current orthopedic implant materials are not ideal for the osteoporotic cases. A newly developed strontium phosphate ($SrPO_4$) coating is reported herein, and applied to Ti-29Nb-13Ta-4.6Zr (wt%), TNTZ, an implant material with a comparative Young's modulus to that of natural bone. The $SrPO_4$ coating is anticipated to modulate the activity of osteoblast (OB) and osteoclast (OC) cells, in order to promote bone formation. TNTZ, a material with excellent biocompatibility and high bioinertness is pretreated in a concentrated alkaline solution under hydrothermal conditions, followed by a hydrothermal coating growth process to achieve complete $SrPO_4$ surface coverage with high bonding strength. Owing to the release of Sr ions from the $SrPO_4$ coating and its unique surface topography, OB cells demonstrate increased proliferation and differentiation, while the cellular responses of OC are suppressed, compared to the control case, i.e., bare TNTZ. This TNTZ implant with a near physiologic Young's modulus and a functional $SrPO_4$ coating provides a new direction in the design and manufacture of implantable devices used in the management of orthopedic conditions in osteoporotic individuals.

1. Introduction

Osteoporosis is a major clinical issue, closely associated with the global ageing population.[1] Osteoporotic bone is less robust than normal bone, and at a much greater risk of fracture. Elderly patients with osteoporosis are also the population at risk of arthritis, and orthopedic surgical implants are required to

Dr. Y.-F. Ding, T. Majumdar, Prof. N. Birbilis,
Dr. X.-B. Chen
Department of Materials Science and Engineering
Monash University
20 Research Way, Clayton, VIC 3800, Australia
E-mail: xiaobo.chen@monash.edu
Dr. R. W. Li, Dr. D.-H. Zhang, Prof. P. N. Smith
The Medical School
The Australian National University
Acton, ACT 0200, Australia
Dr. R. W. Li, Prof. P. N. Smith
The John Curtin School of Medical Research
The Australian National University
Acton, ACT 0200, Australia
Prof. M. Nakai, Prof. M. Niinomi
Department of Biomaterials Science
Institute for Materials Research
Tohoku University
Aoba-ku, Sendai 980-8577, Japan

manage these issues.[2] The ideal requirements for implantable orthopedic devices include: i) comparable mechanical properties, in particular elastic modulus (the index of stiffness), to that of natural bone in order to avoid stress shielding;[3] ii) a biocompatible surface of the to-be-implanted device to minimize any detrimental effect on the host tissue(s); and iii) a bioactive surface which may enhance bone-implant integration and bone formation. In addition, such an ideal bioactive surface would also minimize bone resorption. Research associated with such functionalized implant materials, however, remains in its infancy.

Of the existing commercial metallic biomaterials used for orthopedic implant manufacture, titanium (Ti) and its alloys greatly outperform other conventional biomaterials, i.e., stainless steel 316L and cobalt-chromium (CoCr) alloys, owing to their high mechanical strength, low density, immunity to corrosion, and superior biocompatibility.[4,5] Such properties have given rise to a widespread implementation of Ti alloys in the clinical setting, however, there is now an awareness of disadvantages associated with commercial Ti alloys as implantable materials—for instance the inclusion of inorganic elements of no biological function such as aluminum (Al)[6] and vanadium (V),[7] and a mismatched stiffness (higher Young's modulus) with that of bone.[3,8]

A recent breakthrough in the development of Ti alloys for orthopedic implementation was made by the group led by Niinomi, leading to a single β-phase Ti alloy termed "TNTZ" (Ti-29Nb-13Ta-4.6Zr, wt%).[9,10] This material consists of biocompatible alloying elements of niobium (Nb), tantalum (Ta) and zirconium (Zr), and Young's modulus (approximate 60 GPa and 35 GPa in polycrystalline and single crystalline alloys, respectively) significantly closer to that of human bone (≈10–30 GPa).[11] A further unique feature of this alloying composition is a highly bioinert surface. To activate the surface of TNTZ for higher cellular affinity and bone formation, a number of pretreatment and coating techniques have been investigated to deposit bioactive hydroxyapatite (HA) based substances, including alkaline-heat treatment,[12] anodic oxidation,[13] hydrogen peroxide treatment,[14] direct laser deposition,[15] and metal organic chemical vapor deposition.[16] Although such HA/apatite coated surface is able to promote new bone formation to some degree compared to that of the uncoated TNTZ, there is a pressing need to further enhance bone formation, in particular for the patients with low quality (osteoporotic) bones.

Strontium (Sr), a bone seeking trace element chemically similar to calcium, has been employed clinically for treatment of osteoporosis.[17] Sr^{2+} ions have been shown to improve osteoblast (OB) proliferation and differentiation, while simultaneously inhibit the proliferation and differentiation of osteoclasts (OCs).[1] This occurs largely through the activation of signaling pathways in OBs and OCs.[18] The efficacy of therapeutically administered Sr is dependent on dose, calcium availability and kidney function.[18] Thus, systemic approaches like oral administration are less favorable than the methods that minimize systemic toxicity by providing localized administration of Sr to the target regions of bone-implant contact.[19] Current research efforts are focused on tunable Sr releasing systems such as bioactive coatings[20,21] that enhance OB proliferation,[22] increase alkaline phosphatase activity (ALP) and mineral density,[23] and promote osteointegration and bone regeneration.[21,24] In addition to their positive role in terms of bone formation, strontium phosphate (SrPO$_4$) based coatings are able to modulate the degradation process of a magnesium substrate in physiological environments.[20]

Here we report the development of SrPO$_4$ coated TNTZ (SrPO$_4$-TNTZ) with superior biomechanical properties suitable for the management of orthopedic conditions associated with osteoporosis. A hydrothermal approach, normally seen in clinical sterilization, was adopted to create a favorable surface condition of TNTZ in 2.5 M sodium hydroxide (NaOH) solution at 200 °C for 24 h, and followed by a coating growth procedure conducted in SrPO$_4$ solution at 200 °C for 24 h to obtain full SrPO$_4$ coverage on TNTZ. The coating exhibits high crystallinity, closely packed spatial arrangement, excellent bonding strength, a slow and sustainable degradation profile in vitro, superior biocompatibility, and remarkable modulation of cellular performances of OBs and OCs in opposite ways. These promising properties illustrate a significant potential for the SrPO$_4$-TNTZ biomaterial to clinically address bone fracture, in particular to satisfy the urgent and exclusive requirements for the patients suffering fractures with involvement of low quality (osteoporotic) bone.

2. Results

2.1. Preparation and Surface Topography of the SrPO$_4$ Coatings

The fabrication of a highly crystalline SrPO$_4$ coating on TNTZ was realized using a hydrothermal alkaline pretreatment followed by a hydrothermal in situ assembly approach. A complete surface coverage of the implant with a bioactive coating is preferable for satisfactory bone-implant fixation.[25] Briefly, the naturally formed TiO$_2$ film on Ti and its alloys possesses a high inertness and compact morphology that declines any positive cellular responses or natural formation of any functional surface condition. However, by proper hydrothermal alkaline pretreatment, it is possible to convert such inert TiO$_2$ into chemically active compounds with a porous configuration, such as sodium titanate (Na$_2$Ti$_5$O$_{11}$) gel[4,26] or titania nanowires.[27,28]

Observation (**Figure 1**a–j) by scanning electron microscopy (SEM) exhibits an activated surface of TNTZ through the hydrothermal alkaline pretreatment, which is essential for permitting the formation of a high quality SrPO$_4$ coating on TNTZ (Figure 1a–g in comparison with h). Both particle size and thickness of the resulting SrPO$_4$ coating on non-pretreated TNTZ are inferior compared to the coatings on well-pretreated surfaces (Figure 1–g). As such, the optimized processing parameters provided in Figure 1c (i.e., pretreated in 2.5 M NaOH at 200 °C for 24 h and subsequently coated in a SrPO$_4$ bath at 200 °C for 24 h) were determined to give rise to SrPO$_4$ deposits with a full surface coverage on both commercially pure Ti (c.p. Ti) control and TNTZ alloy, indicating the growth rate and quality (i.e., less defects, high compactness, narrow particle size distribution, and high thickness) of SrPO$_4$ is a function of processing time and temperature (Figure S1, Supporting Information).

2.2. SrPO$_4$ Coating Characterization

X-ray diffraction patterns (XRD, Figure S2, Supporting Information) display the characteristic crystalline structure of the SrPO$_4$ coating on TNTZ substrate, including β-type Ti, Nb$_2$O$_5$, TiO$_2$ and SrPO$_4$. It is evident that the quantity of SrPO$_4$ deposits on TNTZ is a function of the processing temperature involved with the pretreatment and coating duration, as illustrated from the intensity of the XRD peaks assigned to the SrPO$_4$ phase. Energy dispersive X-ray spectroscopy (EDS) mapping of the elemental distribution over SrPO$_4$-TNTZ (Figure S3, Supporting Information) reveals that the signals of underlying Ti and Nb were surpassed by those of Sr, P and O, key components constituting the top SrPO$_4$ coating, in agreement with XRD analysis and validating the processing temperature of alkaline pretreatment and coating duration are critical factors determining the growth rate and quality of the resulting SrPO$_4$ coatings. The high-resolution TEM image (Figure S4a, Supporting Information) displays resolved lattice fringes of (222) planes with a spacing of 0.202 nm, which is in agreement with the XRD patterns of Figure S2 in the Supporting Information. Selected area electron diffraction (SAED, Figure S4b, Supporting Information) pattern reveals diffraction rings, indicating a polycrystalline nature of the SrPO$_4$ deposits, which are composed of many crystallites of varying size and orientation. The hydrothermal treatment was able to promote the effective growth and self-assembly of the minute individual particles, leading to the growth of a compact SrPO$_4$ coating on the surface of TNTZ. Tensile bonding strength analysis (Figure 1j) was carried out on TNTZ with full SrPO$_4$ coating coverage (i.e., the samples alkaline pretreated at 200 °C and followed by coating at 200 °C for 12, 24, and 48 h respectively). The results reveal that the adhesion between coating and TNTZ substrate is time dependent and a ≈24 h coating duration is a key requirement to achieve a bonding strength of approximate 21.5 MPa, which exceeds that of most HA coatings chemically or physically fabricated on Ti alloys.[29] Vickers hardness (Figure 1k,l) was evaluated through identifying hardness on two isolated regions with a distance interval of 150 µm (5 sites in a line, 10 lines in total) on the surface of SrPO$_4$-TNTZ. Analogous to bonding strength, hardness is also a function of the processing time in respect to coating growth, indicated by the increase in hardness value from 155–190 HV (12 h, Figure 1k) to 220–245 HV (24 h, Figure 1l), depending on the location of measurement.

126

FULL PAPER
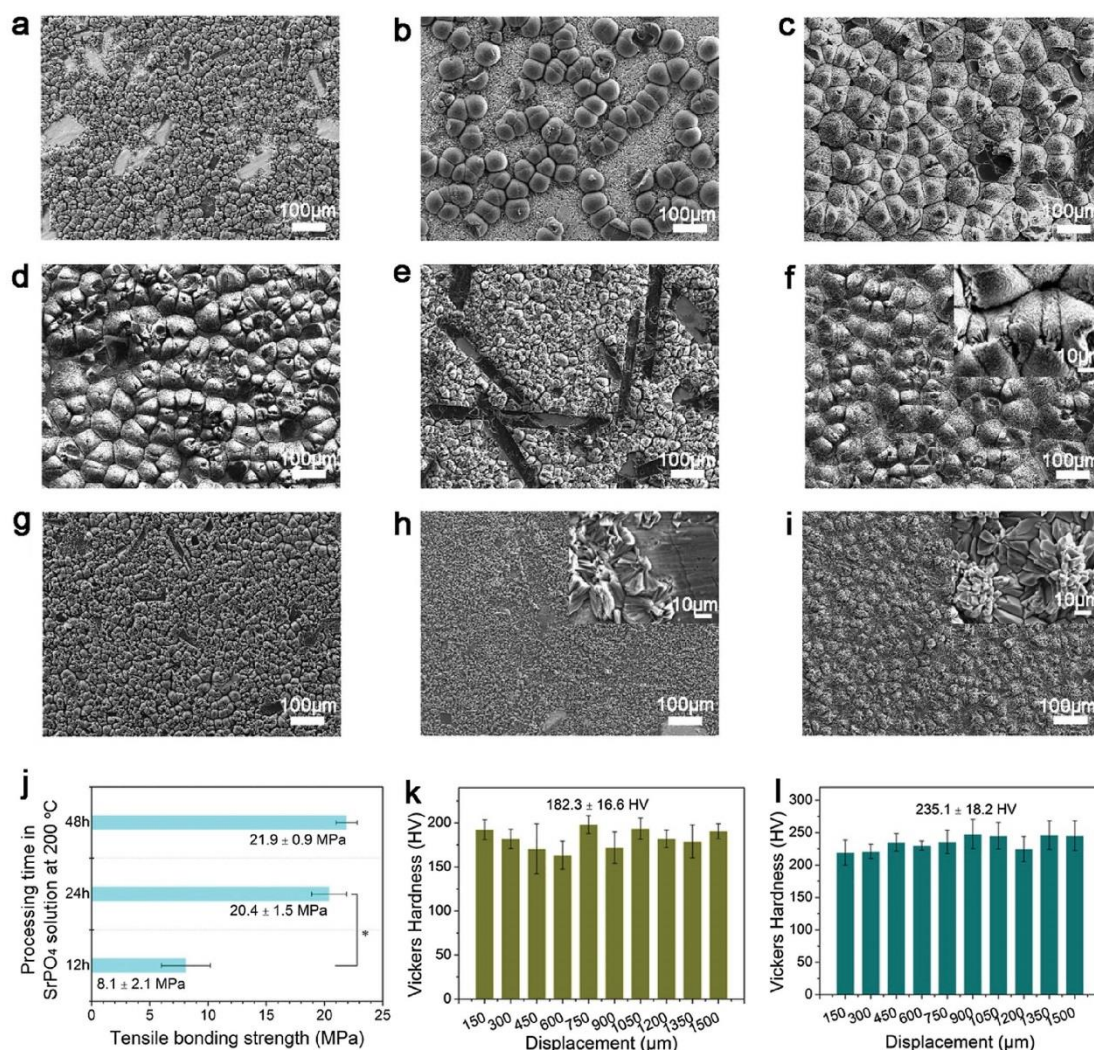
Figure 1. SrPO$_4$ coating characterization. a–h) Surface morphology of the TNTZ discs processed with alkaline pretreatment and followed by SrPO$_4$ coating growth, illustrating the critical influence of processing conditions on the SrPO$_4$ coating formation a) alkaline pretreatment at 190 °C, 24 h and SrPO$_4$ growth at 200 °C, 24 h; b) alkaline pretreatment 200 °C, 24 h and SrPO$_4$ growth 190 °C, 24 h; c) alkaline pretreatment 200 °C, 24 h and SrPO$_4$ growth 200 °C, 24 h; d) alkaline pretreatment 200 °C, 24 h and SrPO$_4$ growth 200 °C, 12 h; e) alkaline pretreatment 200 °C, 12 h and SrPO$_4$ growth 200 °C, 24 h; f) alkaline pretreatment 200 °C, 24 h and SrPO$_4$ growth 200 °C, 48 h; g) alkaline pretreatment 190 °C, 24 h and SrPO$_4$ growth 200 °C, 48 h; and h) no alkaline pretreatment and SrPO$_4$ growth 200 °C, 24 h. i) Surface morphology of the SrPO$_4$ coating on c.p. Ti control group processed with alkaline pretreatment (200 °C, 24 h) and subsequent SrPO$_4$ growth (200 °C, 24 h). j) Tensile bonding strength of the SrPO$_4$ coatings on the TNTZ alloys with alkaline pretreatment (200 °C, 24 h) and SrPO$_4$ growth (200 °C, 12/24/48 h). k) Microhardness of SrPO$_4$ coating from two isolated regions on TNTZ with alkaline pretreatment (200 °C, 24 h) and SrPO$_4$ growth (200 °C, 12 h). l) Microhardness of SrPO$_4$ coating from two isolated regions on TNTZ with alkaline pretreatment (200 °C, 24 h) and SrPO$_4$ growth (200 °C, 24 h).

2.3. Correlation between Surface Chemistry and Coating Growth

Identical pretreatment and coating processes were conducted on commercially pure Ti, Nb, Ta and Zr discs to study the influential mechanisms of the surface chemistry on the coating formation on TNTZ. SEM micrographs and EDS mapping demonstrate that different surfaces exhibit discrete abilities to facilitate SrPO$_4$ growth. In detail, it can readily obtain full SrPO$_4$ coverage on c.p. Ti (Figure S5a, Supporting Information), while no detectable trace of SrPO$_4$ on Nb with a roughened surface after both alkaline and coating treatments, indicating general dissolution of Nb occurred (Figure S5b, Supporting Information). In comparison, Ta presented a pitting corroded surface morphology, which is attributed to the alkaline pretreatment,

Materials
Views
www.MaterialsViews.com

ADVANCED
HEALTHCARE
MATERIALS
www.advhealthmat.de

FULL PAPER

and being covered by a number of scattered SrPO$_4$ deposits (Figure S5c, Supporting Information). Zr displayed the highest immunity to the alkaline pretreatment and coating growth process, manifested by the persistence of surface asperities generated by the initial surface preparation and grinding process (Figure S5d, Supporting Information). There were no detectable phases of SrPO$_4$ revealed by XRD upon Zr following the alkaline pretreatment and coating treatment, which is ascribed to the low quantity of Sr-containing deposits, however peaks belonging to oxides were intensified by alkaline pretreatment and coating process for the cases of Ta and Nb (Figure S6, Supporting Information). Satisfactory SrPO$_4$ growth on c.p. Ti was validated by XRD, as anticipated.

2.4. Influence of the SrPO$_4$ Surface on OB Cell Morphology, Proliferation, and Differentiation

After seeding and 3 d of culture, OB cells exhibited full spreading with spindle shaped morphology on the surfaces of all tested materials, i.e., SrPO$_4$-TNTZ, pristine TNTZ, SrPO$_4$-c.p. Ti and pristine c.p. Ti, as illustrated by SEM (**Figure 2**). SrPO$_4$ coating promoted desirable morphology, attachment and spreading of the cultured OBs as indicated by well-developed filopodia that, more specifically, contained widely extended microspikes firmly attaching on the region consisting of numerous individual needle shaped SrPO$_4$ crystals on TNTZ (Figure 2b). Similarly, well developed cytoplasmic extensions were observed to project to the surface of SrPO$_4$-c.p. Ti (Figure 2e,f). It was confirmed that the control surfaces without presence of SrPO$_4$, i.e., pristine TNTZ (Figure 2c) and c.p. Ti (Figure 2g) hosted OB attachment over the same culture time frame, i.e., 3 d. However, the cells seemed growing longitudinally along the parallel grooves of the surfaces, created during grinding process. More remarkably,

these cells displayed either excessively longer or shorter microspikes (Figure 2d) than the cells spread on the SrPO$_4$ modified surfaces. Analysis based on the cell numbers acquired from 3 isolated visual regions per sample reveals an explicit increase in OB cell density on the surfaces covered with SrPO$_4$, while a marginal difference was identified between either coated substrates or non-coated counterparts (Figure 2h). Since the cells, cultured on the pristine metal surfaces, did not display widely extended microspikes as those on the SrPO$_4$ modified ones, this is indicative of the SrPO$_4$ coating promoting OB cell proliferation. It was hypothesized that subsequent OB cell differentiation could be promoted by SrPO$_4$ over longer period culture, such as 7 d time frame, as the cells were well attached to the surface with the unique stratification features (Figure 2b,f). To elucidate this hypothesis, we further investigated bioactivity of SrPO$_4$ coatings in day 7 cultures with OBs.

2.5. Osteoanabolic Function of the SrPO$_4$ Coating

Osteocalcin, known as bone gamma carboxyglutamic acid-containing protein (BGLAP), is a primary non-collagenous protein produced by OB cells, which signals terminal osteogenic differentiation. To address the possibility that SrPO$_4$ modified surface is favorable for OB differentiation, we further immunostained the day 7 cultures with osteocalcin primary antibody, followed by FITC conjugated IgG secondary antibody. Osteocalcin was stained positively from the day 7 OB cultures on all tested surfaces, however, it was noticed that the brightest staining was present on the SrPO$_4$ coated specimens (**Figure 3**a–d). The number of viable OB cells counted on the SrPO$_4$ coated surface in the day 7 culture, as anticipated, was significantly higher than that on the controls (Figure 3e). The degree of osteocalcin protein expression detected using Western blot depicts an
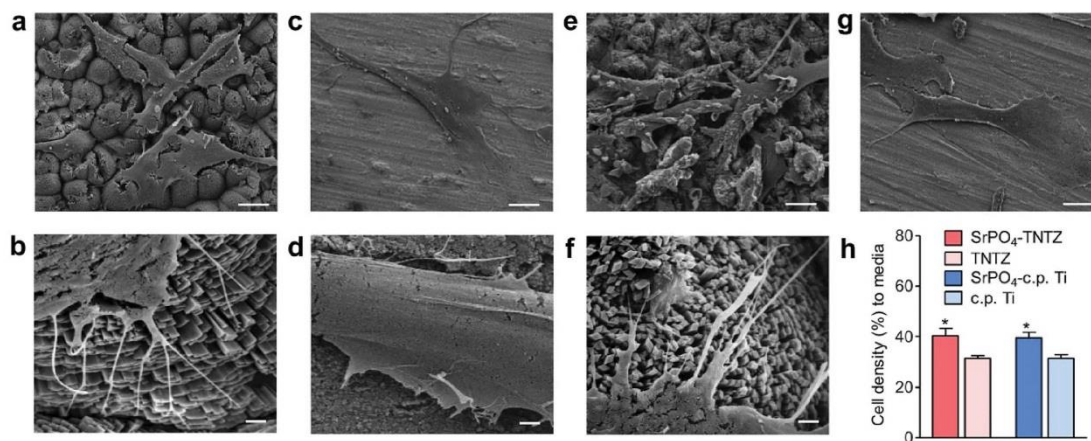
Figure 2. SEM images showing OB cell morphology and proliferation on four different surfaces cultured for 3 d. a) OBs on SrPO$_4$-TNTZ. b) OBs on SrPO$_4$-TNTZ observed at high magnification. c) OBs on pristine TNTZ, which served as control in respect to the surface modified counterpart. d) OBs on pristine TNTZ observed at high magnification. e) OBs on SrPO$_4$-c.p. Ti, which served as control of substrate material. f) OBs on SrPO$_4$-c.p. Ti observed at high magnification. g) OBs on c.p. Ti, served as control in respect to the surface modified counterpart. h) Percentage of cell proliferation, data are representative of six visual fields ($n = 6$). Error bars indicate standard deviation (SD). *$p < 0.01$ versus control. Scale bar is 2 μm in (b,f) and 20 μm in the remaining micrographs.
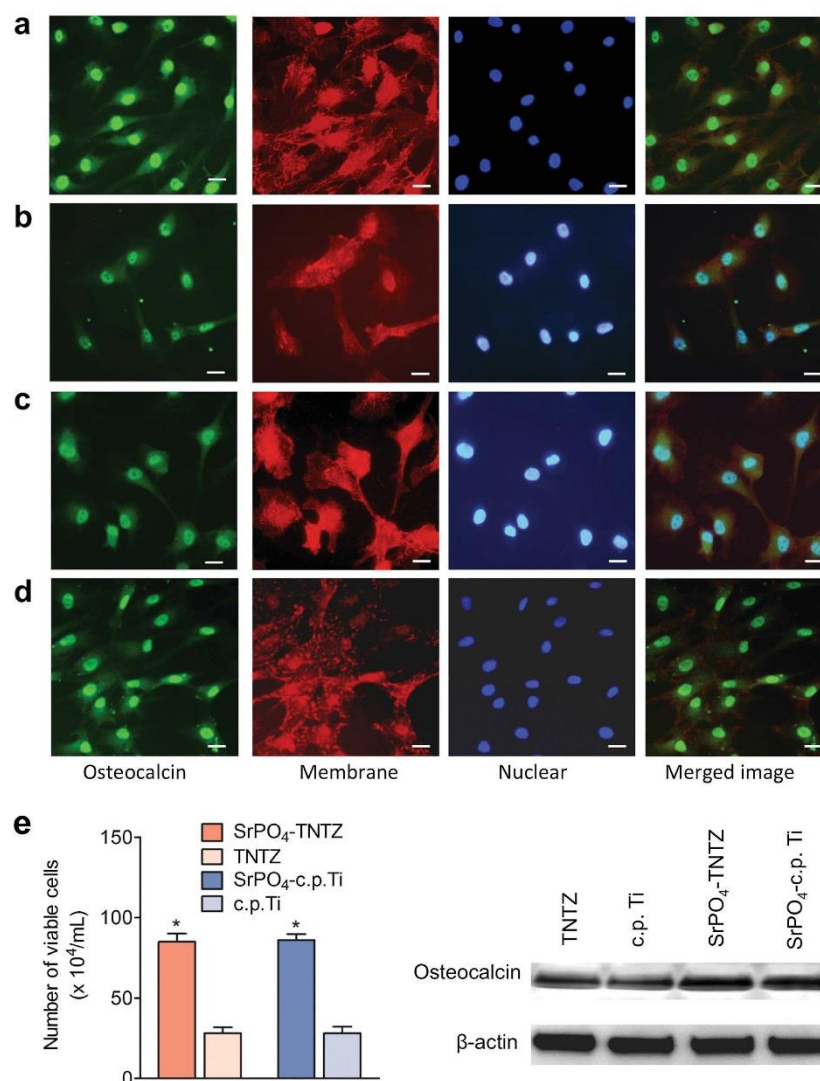
Figure 3. SrPO$_4$-TNTZ promoted OB cell differentiation and osteoclacin expression. a–d) OBs were cultured on the surface of SrPO$_4$-TNTZ, pristine TNTZ, pristine c.p. Ti, and SrPO$_4$-c.p. Ti specimens for 7 d respectively, and stained with an anti-human osteocalcin mAb and a FITC-conjugated secondary antibody (green). An anti-β1 integrin human mAb and a secondary antibody Cy3-conjugated donkey anti-rabbit IgG were used in membrane staining (red). DAPI (4',6-diamidino-2-phenylindole) was used to stain nuclei (blue). Merged images of osteocalcin, membrane, and nuclear staining are shown in the far right column. e) Number of viable OB cells (left) and osteocalcin protein expression (right) in the day 7 culture ($n = 6$). Error bars indicate SD. $^*p < 0.001$ versus control. Scale bar is 10 µm.

agreement with the viable cell counting analysis. Taken together, these results suggest that the SrPO$_4$ coating induced an osteoanabolic function to both TNTZ and c.p. Ti.

2.6. Two-Way Regulation of SrPO$_4$ Coating on OBs and OCs in Co-Cultures

As described in the Experimental section, the morphology of OC cells cultured on the material surfaces was examined and it

was perceived that the conditioned medium of OC progenitor cells failed to engender the cells to mature OCs on the SrPO$_4$-TNTZ surface (**Figure 4**a). In contrast to the cell debris on the SrPO$_4$-TNTZ, it is discerned that many giant cells grown on the control discs of pristine TNTZ and c.p. Ti. To confirm our assumption in terms of the role of SrPO$_4$ modified surface in the communication between OBs and OCs, a primary co-culture protocol was established for the first time, in which contained OBs from human trabecular bone in the presence

129

Materials
Views
www.MaterialsViews.com

ADVANCED
HEALTHCARE
MATERIALS
www.advhealthmat.de

FULL PAPER
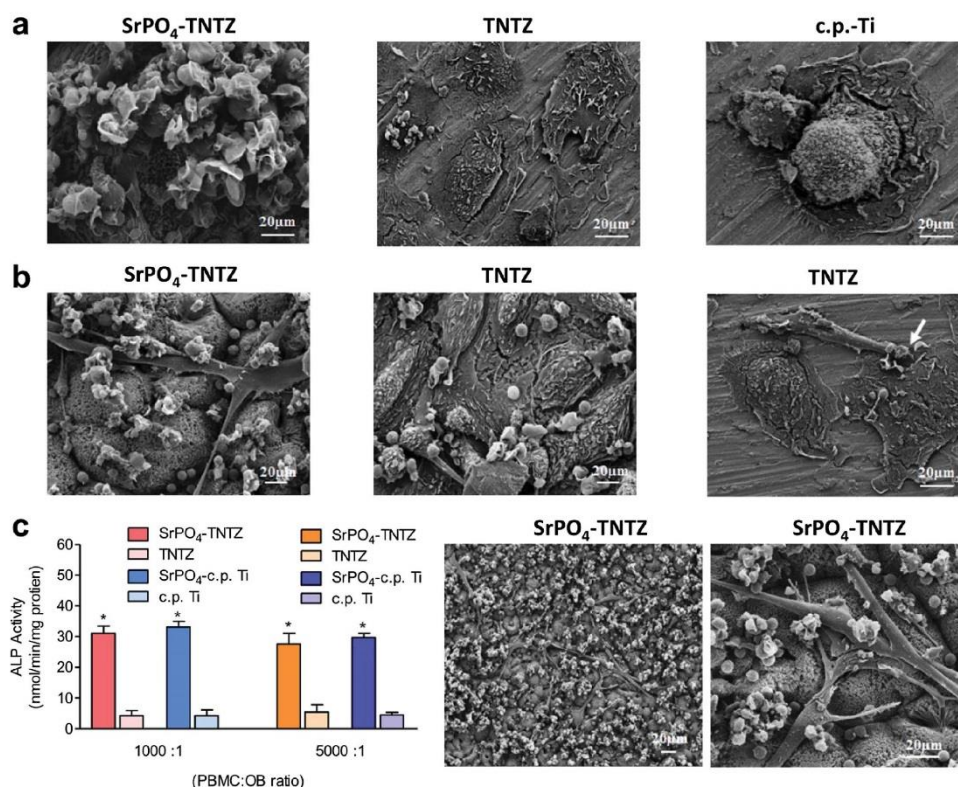
Figure 4. Morphology of OCs, co-cultured OBs and OCs on the surfaces of various tested materials, and alkaline phosphatase activity. OC progenitor cells (PBMCs) were seeded on the surfaces of tested materials and cultured in conditioned medium for 7 d before being co-cultured with OBs. The cell morphology was observed under SEM at day 11. Quantitative measurement of ALP activity was performed on the 13 d co-cultures from a separate set of specimens. Scale bar represents 20 μm. a) OC progenitor cells on the tested discs. b) Co-cultured OCs and OBs (seeding ratio, 1000:1). b the far right) Co-cultures, white arrow indicating an osteoclast in the process of engulfing and destroying an OB. c) Co-cultured OCs and OBs with two PBMCs seeding densities (1000:1 and 5000:1) on the surface of SrPO$_4$-TNTZ. c left) ALP activity measured from co-cultured OCs and OBs ($n = 3$ cultures) on SrPO$_4$-TNTZ. c right) SEM micrographs of co-cultured OCs and OBs (seeding ratio, 5000:1). Error bars indicate SD ($n = 6$). $^{*}p < 0.001$ versus control.

of OCs derived from OC progenitors (PBMCs) cultured in the conditioned medium on the surfaces of tested discs. In this particular co-culture protocol, a sequential seeding of OCs and OBs was conducted, i.e., OB seeding initiated on the day 7 cultures of OC in the medium. Likewise, SrPO$_4$-TNTZ significantly inhibited OC progenitor cells progressing to OCs, but not in OB's growth (Figure 4b left). In addition to cell debris that were generated by cell apoptosis, a number of PBMCs in their initial stage with round shape and small size were observed on the SrPO$_4$ modified surface. In contrast, OC progenitor cells on the bare TNTZ surface were provoked to regular OCs (Figure 4b middle). An interesting view as indicated by white arrows in Figure 4b right, exhibited two OC cells with their filopodia acting as osteoclastic tentacles and pulling bound an OB cell towards them for resorption. While it remains challenging to observe this interaction in situ when the cells were alive, engulfing and destroying OBs by these OC cells are anticipated.

ALP activity, an indicator of OBs differentiation, signals a difference among the co-cultured cells growing on the different surfaces of the specimens (Figure 4c left). It was determined

ALP activity of the day 13 co-cultures (i.e., day 7 cultures with respect to OB) was significantly higher in the cells cultured on the discs with SrPO$_4$ modified surface than those on the control discs. When re-investigating the co-cultured cells using an increased ratio of OC progenitors and OBs by elevating PBMCs seeding density, it was found that an increase in the seeding density of PBMCs did not seem to raise the numbers of matured OCs. An overview of co-cultured OCs and OBs and magnified images from high PMMCs seeding density (Figure 4c, middle and right) confirms a two-way regulation of SrPO$_4$-TNTZ on growth of OCs (negative) and OBs (positive).

2.7. Negative Regulation of SrPO$_4$ Coatings on Cathepsin K from OCs

Cathepsin K (CTSK) is a lysosomal cysteine protease with strong collagenolytic activity that mediates bone resorption in OCs. It has been extensively used as marker for OCs. To determine whether the decreased number and size of OCs or OC

130

**ADVANCED
HEALTHCARE
MATERIALS**

www.advhealthmat.de

FULL PAPER

Materials Views

www.MaterialsViews.com
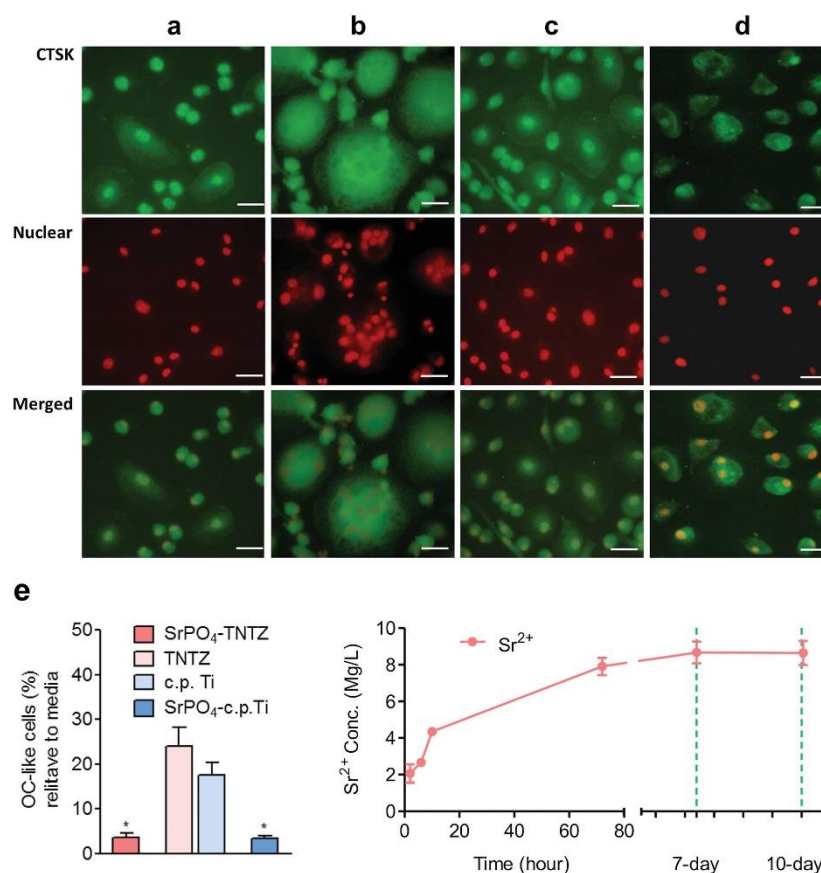
Figure 5. SrPO$_4$ surface decreased OC cell differentiation. OCs were induced by culturing PBMCs on the alloy discs with conditional culture medium consisting of dexamethasone, Vitamin D3, m-csf and RANKL up to 13 d. Fluorescence micrographs of OC showing Cathepsin K (green) was detected with a rabbit anti-human CTSK antibody polyclonal and a FITC-conjugated secondary antibody. The nuclei were stained using PI. Merged images of CTSK and nuclear staining are shown in the left column. a) Induced OC progenitor cells on SrPO$_4$-TNTZ. b) Mature OC cells with multiple nuclei and positive Cathepsin K stain on the surface of pristine TNTZ. c) OC progenitor cells on pristine c.p. Ti. d) OC progenitor cells on SrPO$_4$-c.p. Ti. e) left: percentage of OC-like cells (with over three nuclei in a cell) relative to the number of OCs present in medium control, is presented as a mean value of five isolated fields of each sample ± SD ($n = 6$). e) right: released Sr^{2+} ion concentrations (mg L^{-1}) from SrPO$_4$-TNTZ after immersing in α-MEM solution at 37 °C for various time durations, determined by ICP–MS analysis of α-MEM extracts ($n = 3$). Error bars indicate SD. $^*p < 0.001$ versus control. Scale bar is 20 μm.

progenitor cells on SrPO$_4$ coatings have an inhibitory effect on maturation of OCs, cell differentiation was analyzed. PBMCs with a conditioned culture medium were introduced on the surface of SrPO$_4$-TNTZ, SrPO$_4$-c.p. Ti, and control discs and maturation of OCs was evaluated. After 13 d culture, OC-like cell formation was evident over the surface of all tested samples with osteoclastic markers, such as multiple nuclei and CTSK expression. The OC-like cells on the SrPO$_4$-discs illustrate a significant lower number of mature OCs, i.e., containing more than three nuclei in a cell (**Figure 5**e) and less bright CTSK expression (Figure 5a,d) than on the control samples, pristine TNTZ and c.p. Ti (Figure 5b,c). Although a higher number of OC-like cells was found on c.p. Ti control (Figure 5c), CTSK detected in those cells was not as bright as that on the TNTZ disc. ICP–MS analysis was conducted to

monitor Sr^{2+} ion concentrations released from SrPO$_4$-TNTZ after immersing in α-MEM solution over different scheduled time intervals (Figure 5e right). It was evident that Sr^{2+} ion dissolution sharply increased in the first 12 h of immersion in α-MEM medium, and then slowly approached to a plateau level of around 8 mg L^{-1} when immersion was beyond 7 d.

2.8. SrPO$_4$ Coating Regulates Major Target Molecules Coupling Bone Formation and Bone Resorption

One of the major issues associated with the use of currently available anti-resorption drugs for the treatment of osteoporosis and osteoporotic fractures is that while they are efficient in reducing OC cell numbers and actively leading to

131

Materials
Views
www.MaterialsViews.com

ADVANCED
HEALTHCARE
MATERIALS
www.advhealthmat.de

FULL PAPER
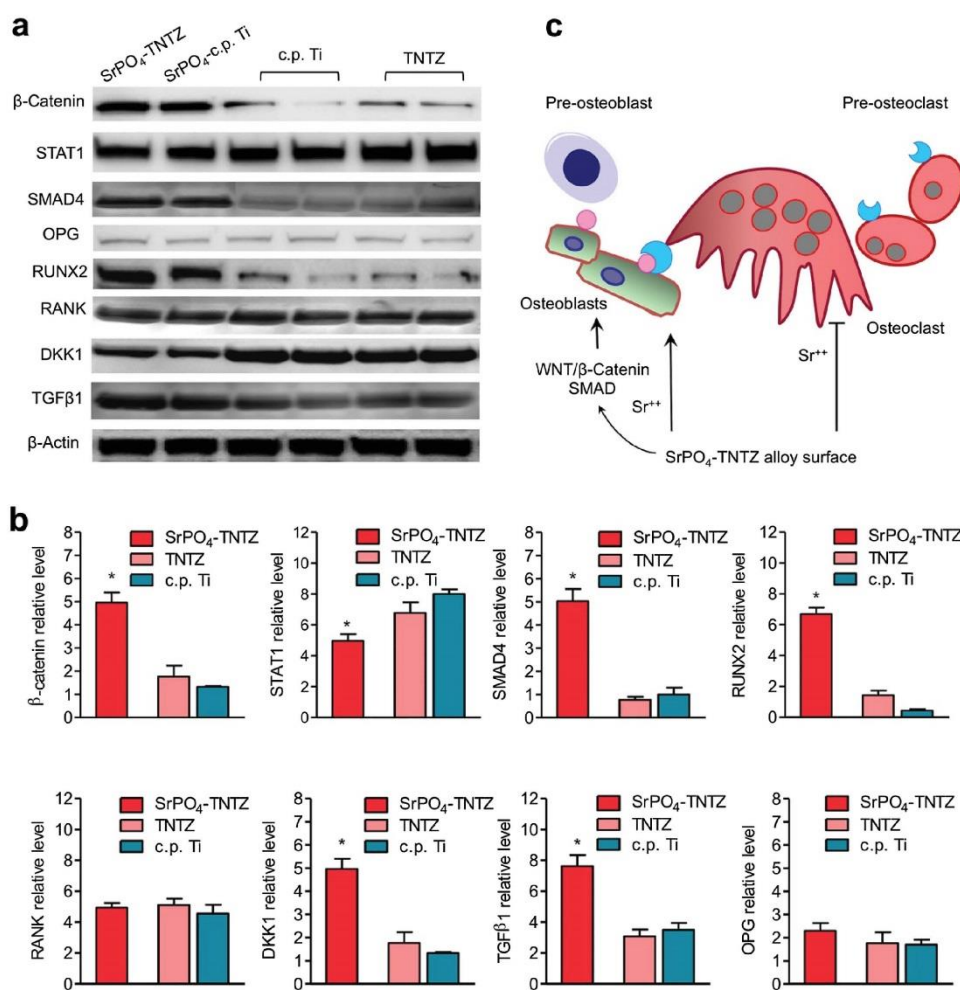
Figure 6. SrPO$_4$ coating on TNTZ regulated protein expression of target molecules in co-cultured OBs and OCs. a) Protein expression was detected using rabbit-anti-human primary antibodies followed by conjugated goat-anti-rabbit IgG secondary antibodies which were detected by enhanced chemiluminescence. Representative expression profiles of molecules involved in OB differentiation and OB–OC cell communication namely TGFβ1, STAT1, DKK1, SMAD4, RUNX2, β-catenin, and RANK on the material surfaces of SrPO$_4$-TNTZ and its control discs. The samples were from day 13 cultures. β-actin was used as protein loading control. b) Mean relative expression of proteins ($n = 6$). c) Schematic representation of the proposed function of SrPO$_4$ structural surface and chemical component in bone formation. Error bars indicate SD. $^*p < 0.05$ versus control.

markedly alleviated bone resorption, they also profoundly suppress bone formation.[30] Given the SrPO$_4$ coating has exhibited a two-way regulation on (promoting) OBs and (inhibiting) OCs regardless of the substrates, we attempted to address a critical issue of what are the major molecules in either WNT/β-catenin or BMP2/SMAD pathway were targeted by our architecturally and chemically modified surface of TNTZ through SrPO$_4$ deposition. Western blot analysis was carried out from the extracts of the cells co-cultured on surfaces of the specimens (**Figure 6**a). Overexpressed TGFβ1, RUNX2, SMAD4 and β-catenin were identified on SrPO$_4$-TNTZ in comparison with controls (Figure 6b), while STAT1 and DKK1 were downregulated. Although theses downstream

molecules in either WNT or SMAD signaling pathways have been reported as molecular event influenced by Sr containing surface modification, we herein, for the first time, report SrPO$_4$ coated surface possessing such a promising two-way regulatory role in OB and OC co-culture model. RANK and OPG expression of the cells on SrPO$_4$ modified surfaces, however, remained marginally different from those of the controls (Figure 6b). In summary, our findings provide a molecular explanation for the role of SrPO$_4$ coating on TNTZ in regulating the interactions of OBs and OCs and identify that a suitable concentration of Sr^{2+} ions in culture medium is critical for osteoanabolic implant function (Figure 6c) from a chemical perspective.

132

FULL PAPER

3. Discussion

3.1. Physical and Chemical Characterization of SrPO₄ Coating

SEM, EDS (Figure S5, Supporting Information), and XRD (Figure S6, Supporting Information) analyses manifest that biocompatible Nb, Ta and Zr are reluctant to dissolve (corrode) in the aggressive aqueous solutions used for respective pretreatment and coating growth. The dissolution of these noble metals in aqueous solution can elevate pH at the interface of metal and liquid, which is critical to trigger heterogeneous nucleation of SrPO₄ deposits over metal surface and subsequent coating growth through continuing consumption of Sr^{2+} and PO_4^{3-} ions from the coating solution.[20] The coating quality, including morphology, chemical composition, spatial architecture, adhesion, durability, toughness and stability, contributes significantly to their desirable in vivo performance, in particular for satisfactory bone-implant integration. An optimized set of processing parameters associated with pretreatment and coating manipulation to overcome the high inertness of TNTZ to yield a functional SrPO₄ coating with complete coverage were described herein. The quality of SrPO₄ coating was promoted via the elevated temperature involved in alkaline treatment and coating process, and the time length of the latter, which can be attributed to the endothermic nature of the formation of phosphate based coatings.[20] According to the results presented, supplemented by previous findings, it is possible to propose a mechanism in terms of formation of SrPO₄ coatings, which is applicable for metal implants as following Equations (1), (2), (3)

$$M \rightarrow M^{n-} + ne^- \tag{1}$$

$$2H_2O + 2e^- \rightarrow 2OH^- + H_2 \uparrow \tag{2}$$

$$5Sr^{2+} + 3PO_4^{3-} + OH^- \rightarrow Sr_5(PO_4)_3(OH)\downarrow \tag{3}$$
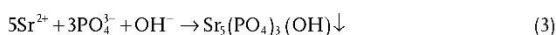
Where M presents the metallic elements of substrate, and n is the number of electrons discharged from the ionized metal atom. Equations (1)–(3) reveal that a metal having a strong tendency to dissolve in water and release OH^- ions, will elicit a high formation rate of SrPO₄ coating on its surface, which was confirmed by SEM micrographs and EDS mapping (Figure S5, Supporting Information) of pure Ti, Nb, Ta, and Zr. Regarding to TNTZ alloy, the surface chemistry determining SrPO₄ growth is dominated by Ti component (53.4 wt%), which requires more aggressive processing conditions than those for pure Ti, i.e., 200 °C and 24 h for pretreatment, and pH 2.0, 200 °C and 24 h for coating process, but nicer than those for pure Nb, Ta, and Zr. Different explanations for SrPO₄ based coating formation exist, such as initially formed $Ca_{0.5}Sr_{0.5}TiO_3$ nuclei to induce Sr-HA coating on anodized Ti[31] and the "feeding ground" provided by a medium containing with a large number of Sr^{2+} and PO_4^{3-} stimulating Sr-apatite nucleation,[32] suggesting this particular topic remains not fully understood.

An ideal coating is expected to be dense and have good mechanical properties such as bonding strength and hardness, to minimize the mismatch between the coatings and

substrate.[33] In addition, bonding strength attributes greatly to the longevity of coated Ti implants[4] and has been improved for the case of SrPO₄-TNTZ through prolonged processing time scale in SrPO₄ solution (Figure 1l). In general, the failure load of coatings was recorded and calculated by the following equation:[34]

$$\sigma = kF \tag{4}$$

Where F is the maximum force applied on the coatings before fracture (failure load), and k is a constant depending on the thickness and the Young's modulus of the tested materials. The complete coverage and increased thickness of SrPO₄ coating on TNTZ as a result of increased processing time in SrPO₄ solution (Figure 1a–j), gave rise to the accretion of the bonding strength. In fact, the bonding strength to the substrate, is defined as the reversible work created in the interface between two bonded substances, and it also can be defined as follows:[35]

$$W_{ab} = \gamma_a + \gamma_b - \gamma_{ab} \tag{5}$$

Where W_{ab} is the reversible work in the interface; γ_{ab} is the interfacial specific free energy; γ_a and γ_b is the specific surface energy of substances a and b, respectively. With processing time rising from 12 to 24 h, more SrPO₄ particles were deposited and distributed over TNTZ surface, which represents an accumulated interface and dramatic changes of surface energy of the coating. Albeit the parameters in Equation (5) were unknown, it is ascertained that the increased surface energy was superior to that of the interfacial specific free energy, which is attributed to the enhancement of the bonding strength with the increasing coating time. When the processing time approached 24 and 48 h, growth of SrPO₄ coating in terms of coverage and thickness, remained stable and resulted in a slight increase in bonding strength. Average micro-hardness of the SrPO₄ coatings on TNTZ processed by alkaline pretreatment and coating growth at 200 °C for 24 h was approximate 235.0 HV. It is well comparative to that of bulk TNTZ (230–330 HV),[36] implying enhanced wear resistance and lubrication of the SrPO₄-TNTZ implant in practical use, though lower than that of dense HA (≈663 HV).[33]

3.2. In Vitro Biological Functions of SrPO₄ Coating

Our results demonstrate a number of important findings regarding material surface interaction with OC and OB cells. First, it demonstrated that the SrPO₄ conversion coating on TNTZ surface plays a structural and chemical role in regulating critical osteoblastic and osteoclastic behaviors. Second, evidence was provided to support that the surface of SrPO₄ coatings, other than molecules secreted from cells or extracellular matrix, also can be a factor coupling OBs to OCs, i.e., bone formation to bone resorption. Third, new insight into the two-way regulating property of Sr^{2+} ions was delivered. Furthermore, a novel experimental protocol using co-cultured human primary OCs and OBs on the surface of SrPO₄ coating was established, which provides a further perspective to evaluate the (in vitro)

Materials
Views
www.MaterialsViews.com

ADVANCED
HEALTHCARE
MATERIALS
www.advhealthmat.de

FULL PAPER

cytotoxicity, functions and performance for the vast amount of emerging biomaterials prior to costly and time-consuming in vivo trials.

Bone homeostasis is dynamic with reciprocal OC and OB communication and the corresponding coordinated bone resorption and formation events highly regulated processes. The interactions among bone cells, and between host tissues and guest implants, are even more complex. Our in vitro model in terms of co-cultured OCs and OBs on metal specimens is a novel protocol to assess the complicated influence of implant materials on bone cells. On the basis of quantitative and qualitative results, an important discovery of the present study is that $SrPO_4$ surface performs an uncommon two-way regulatory function on OBs and OCs. It is generally recognized that topographical, chemical and mechanical properties of material surface contribute greatly to the cellular behavior of OBs.[28,37] Our results have identified the $SrPO_4$ coating provides essential contribution to substantially promote OBs in early adhesion and later proliferation periods.[38] The pristine surface of either TNTZ or c.p. Ti, by contrast, exhibits a negative effect on PBMC's propensity to settle and subsequent osteoclastic differentiation.

A number of mechanisms were proposed to underlie the osteogenesis derived from $SrPO_4$ coating. Sista et al. have reported that the differentiation of OBs is a surface sensitive phenomenon, which is influenced by the topography, roughness, and the composition of the materials surface.[39] In the present study, the physical feature of $SrPO_4$ coating contains a certain degree of characteristic texture and roughness, which provides OBs favorable sites for firm attachment to the surface. Those well attached OBs on such a desirable surface morphology rapidly develop numerous long needle shaped filopodia. Our results demonstrate and confirm the coated surfaces facilitate a great OB proliferation. The strong cellular attachment enhances the cell differentiation, which is confirmed by a higher ALP activity in $SrPO_4$-TNTZ than that in the pristine TNTZ discs. Gene and protein expression analyses of BGLAP, a specific marker of OB differentiation, also provide solid evidence that the $SrPO_4$ coating has an anabolic function.

In contrast, $SrPO_4$ coating significantly inhibits PBMCs, i.e., OC progenitor cells, in their progression to mature OCs. OCs are highly differentiated cells of hematopoietic origin. During OC induction under the presence of a combination of dexamethasone from the beginning of the culture to the addition of the well-known osteoclastogenic factors of M-CSF and RANKL, the cell size increases from 2–8 µm up to over 100 µm, and from mononuclear to multiple nuclei. The physical feature of the $SrPO_4$ coating, in particular the crystallographic properties, might limit and stress the cells, eventually incur cell death. Although the cellular behavior of OCs in such a physically modified micro-environment deserves further investigation, our result hints a novel approach to effectively evaluate in vitro functions of implantable biomaterials.

The chemical components of the $SrPO_4$ play a key regulatory role in the OB–OC coupling process. Osteoporosis is the result of excessive bone resorption over the bone formation during the modelling process and the existing approach for the treatment is administration of antiresorptive drugs. As a consequence of the coupling process, inhibition of bone resorption

generally elicits to a parallel reduction in terms of bone formation.[30] From a therapeutic perspective, our findings that the $SrPO_4$ conversion coated surface causes an osteoanabolic effect are of particular interest and significance. As one of the elements commonly found in soil and water, Sr is a trace mineral in diet. The average total body storage (primarily in bone) for Sr in humans is estimated to be 300–400 mg. There is supporting evidence suggesting that Sr^{2+} ions participate in the regulation of OB formation and function,[10] while its function in osteoclastogenesis remains unclear. Our results, for the first time, provide evidence that Sr^{2+} ions at a premium concentration, i.e., 8 mg L^{-1}, could be related to the inhibition of OC differentiation and maturation. Although this result does not directly translate into clinical applicability at the moment, it provides an important proof-of-principle for the potential bioactivity of $SrPO_4$ coating for TNTZ, c.p. Ti or other implant materials. The CTSK, a lysosomal cysteine protease mediating bone resorption in OCs, has been extensively employed as a marker of OCs.[40] In recent years, CTSK has emerged as a promising target for the treatment of osteoporosis. Our observations from immunofluorescence staining of CTSK illustrate that less accumulation of this OC marker on the $SrPO_4$-TNTZ and $SrPO_4$-c.p. Ti in comparison to their pristine controls.

4. Conclusion

In summary, compact and crystalline $SrPO_4$ coating prepared on the surface of TNTZ and c.p. Ti acheived by a controlled pretreatment and coating process was reported. The reported $SrPO_4$ coating contains numerous crystalline particles as building blocks to construct a unique 3D architecture—demonstrating an uncommon two-way regulatory mechanism in terms of growth of osteoblasts (positive) and osteoclast (negative), attributed to the unique topography and chemistry of the $SrPO_4$ coating. Such a promising osteoanabolic effect of $SrPO_4$ coating provides significant clinical relevance, revealing a suitability for a large range of applications in orthopedic implantation, in particular for patients who suffer from low quality bone organism and slow fracture recovery.

5. Experimental Section

Materials Preparation: TNTZ bar (Φ 8 mm) containing single β-phase was prepared as previously reported[14,16] produced at the Department of Biomaterials Science, Institute for Materials Research, Tohoku University. Discs of TNTZ (8 mm in diameter and 3 mm thick) and commercially pure Ti (c.p. Ti, Atlantic Equipment Engineers, Inc., USA), and in-house made pure Ta, Nb, and Zr were prepared through electrical discharge machining (EDM). Prior to surface pretreatment, samples were ground using 600 grit silicon carbide paper under running distilled water and sequentially washed in acetone, absolute ethanol, Mili-Q water in an ultrasonic bath for 15 min, and then oven dried at 40 °C for 2 h.

Surface pretreatment was conducted hydrothermally onto metal samples using 2.5 M NaOH solution in stainless steel autoclaves at a temperature ranging from 190 to 200 °C for 24 h with a constant ratio between surface area of the samples and volume of NaOH of 1.8 cm^2:18.0 mL, followed by cleaning in absolute ethanol and Mili-Q water for 10 min, and finally oven dried at 40 °C for 2 h. $SrPO_4$ coating was produced on the surface pretreated samples through an one-step hydrothermal process, which was performed in a clear aqueous

134

**ADVANCED
HEALTHCARE
MATERIALS**
www.advhealthmat.de

**Materials
Views**
www.MaterialsViews.com

FULL PAPER

Table 1. Processing conditions of the alkaline pretreatment and $SrPO_4$ coating growth.

Groups	Materials	Alkaline pretreatment		$SrPO_4$ conversion	
		Temperature [°C]	Processing time [h]	Temperature [°C]	Processing time [h]
1	TNTZ	190	24	200	24
2	TNTZ	190	24	200	48
3	TNTZ	200	24	200	12
4	TNTZ	200	24	200	24
5	TNTZ	200	24	200	48
6	TNTZ	N/A	N/A	200	24
7	c.p. Ti	200	24	200	24
8	Nb	200	24	200	24
9	Ta	200	24	200	24
10	Zr	200	24	200	24

solution containing 1 M strontium nitrate $(Sr(NO_3)_2)$ and 0.6 M ammonium dihydrogen phosphate $(NH_4H_2PO_4)$, with pH value of 2.0, adjusted by HNO_3 and the identical ratio between surface area of the metal specimens and volume of the coating solution to that used in pretreatment. The coating process was undertaken at a temperature varying slightly between 190 and 200 °C over a minimum of 12 h to yield a coating with full surface coverage.

To investigate the optimal coating conditions, TNTZ along with c.p. Ti, Ta, Zr and Nb discs with an uncoated surface were also used for comparison (refer to **Table** 1 for the chosen immersion time duration and the temperature for surface pretreatment and $SrPO_4$ coating growth). $SrPO_4$-TNTZ and control group specimens were ultrasonically cleaned in Mili-Q water at room temperature for minimum 2 h to remove any loose deposits from the sample surface, and finally dried in air and stored in desiccator. All chemicals used herein were analytical grade supplied by Sigma-Aldrich, Australia.

Surface Morphological and Crystallographic Characterization: Microstructure of $SrPO_4$ coated samples was observed using SEM (Supra 55 VP, Zeiss, Germany), and elemental analysis was performed using energy dispersive X-ray spectrometry (EDX, Oxford, UK). A conductive carbon coating was deposited on the samples prior to microscopy observation. XRD (X'pert, Philips, The Netherlands) employing Cu Kα radiation at an accelerating voltage of 40 kv and a current of 40 mA, was recorded to identify the phase constituents of the coatings. Transmission electron microscopy (TEM) images were obtained using a JEM-2100 electron microscope (JEOL, Tokyo, Japan) operating at an accelerating voltage of 200 kV. $SrPO_4$ powder was scraped off from the surface of $SrPO_4$-TNTZ specimens with a sharp blade. Raw $SrPO_4$ powder was ground and followed with ultrasonic dispersal in 5 mL ethanol. The suspension of $SrPO_4$ powder was then dropped onto a copper TEM grid with carbon film for TEM characterization.

Measurements of Bonding Strength and Hardness: Bonding strength of $SrPO_4$ coating to substrate was measured using a modified ASTM C-633 method.[41] Cylindrical stainless steel jigs with a diameter of 8 mm and length of 40 mm were used and further machined into a rectangular solid shape (5 × 5 × 30 mm) in order to fit the size of the instrument. Both sides of the samples including the surface with $SrPO_4$ coating were attached to the jigs by using Super Strength Araldite glue (Selleys, Australia, Figure S7, Supporting Information). Bonding strength of the $SrPO_4$ coatings was evaluated by the tensile loading at a cross-head speed of 1 mm min^{-1} until fracture occurred using an Instron universal tester with a video extensometer (Instron 5967, USA) at room temperature. A nano-based indentation system (Ultra Micro-Indentation System, UMIS-2000, CSIRO, Australia) was employed to determine the hardness of the coatings with a Berkovich indenter based on a continuous stiffness measurement mode. Peak force of 5 mN was applied with a constant loading rate of 5 μN s^{-1}. 50 indentations with a

separating distance of 150 μm were carried out on the coatings in the matrix of 5 × 5 located in two isolated regions in the randomly selected area within the coatings. The mean hardness value of each selected site was determined using experimental raw data from five replicate measurements.

Human OB Cell Culture: The normal trabecular bone specimens were collected from three healthy males (aged 40–50 years) undergoing orthopedic operations due to causes unrelated to arthritis and osteoporosis, such as ligament reconstruction and trauma,[42] with the permission of the Human Research Ethics Committees of Australian National University (ref. 2014/250) and Australian Capital Territory Health (ref. ETH9.07.865) and informed patient consent. The exclusion criteria for recruiting donors included (i) taking immune suppressant/ stimulating drugs, cytokine, or IFN therapy in the 3 month prior to surgery; (ii) treatment with anabolic agents; and (iii) any other conditions that, in the opinion of the investigators, could compromise the study. Briefly, the bone fragments were rinsed with phosphate-buffered saline (PBS) and cultured in minimal essential medium-alpha (α-MEM, Invitrogen, Australia) supplemented with fetal bovine serum 10% (Life Technologies, Australia), 2×10^{-3} M L-glutamine (Gibco, Life Technologies), 100×10^{-6} M ascorbic acid, 20×10^{-3} M HEPES buffer (Merck Millipore, Australia), 1% antibiotic solution at 37 °C with 5% CO_2 in an incubator. After culture for 2 weeks, outgrowing cells surrounding bone fragments were subcultured and designated as "Passage 1". OBs were subcultured to confluence prior to use for cell proliferation and differentiation studies and osteoblast/osteoclast co-culture.

OB Cellular Assays: To assess whether OB proliferation and ALP activity would be influenced by the different material discs, OBs were seeded in 24-well plate containing metallic specimens at a density of 5×10^3 cells per well in 1 mL of cell culture medium and cultured for respective 3 and 7 d. Because the OB cells reached saturation, and their differentiation and mineralization were initiated at day 7 as indicated in Figure S8 in the Supporting Information and under the selected experimental conditions, the best proliferation time (log phase) was between 3–5 d after seeding, OB cell proliferation assay was performed at these particular time points (Figure 2h). The cells were trypsinized, washed, and resuspended in cold PBS. The cells were counted using cell viability analyzer (Vi-Cell XR, Beckman Coulter). Cell viability numbers represented the quantity of surviving cells on each disc. ALP activity was assessed by measurement of the release of *p*-nitrophenol from *p*-nitrophenol phosphate (*p*NPP using a SensoLyteTM *p*NPP ALP assay kit, Ana Spec Inc., CA, USA) following the manufacturer's instructions. ALP activity was normalized to the total cellular protein and presented as ng mg^{-1} protein.

Immunofluorescent Staining: Osteocalcin expression was determined by immunofluorescent staining. The OBs cultured on the tested discs were fixed in freshly prepared 2% paraformaldehyde at room temperature

Materials
Views
www.MaterialsViews.com

ADVANCED
HEALTHCARE
MATERIALS
www.advhealthmat.de

FULL PAPER

for 10 min. Regarding the permeabilization, cells were incubated in 0.4% Triton-X100/PBS at room temperature for 15 min. Blocking was performed with PBS containing 1% bovine serum albumin (BSA, Sigma-Aldrich) and 0.1% Tween-20 for 45 min at room temperature. The staining was performed with rabbit anti-human osteocalcin primary antibody at 1:200 dilution (Merck Millipore) for 1 h incubation at room temperature. Goat anti-rabbit IgG (H+L) antibody conjugated with fluorescein isothiocyanate (FITC, Invitrogen) was used as secondary antibody. An anti-β1 integrin rabbit mAb and a secondary antibody Cy3-conjugated donkey anti-rabbit IgG were exploited in membrane staining, followed by DAPI (4′,6-diamidino-2-phenylindole) staining for nuclei location (Sigma-Aldrich). The specimens were visualized using confocal microscopy (LSM 510 and LSM 5 Exciter, Carl Zeiss MicroImaging, North Ryde, Australia).

Human OC Cell Induction and Co-Culture with OBs: Human OCs were generated from "buffy coat" cell preparation from approximate 400 mL whole blood (a 40-year-old male volunteer) provided by the Australian Red Cross Blood Service with approval from Human Research Ethics Committee of Australian National University (ref. 2014/253). PBMCs were isolated using the Ficoll–Paque method as described previously[43] with slight modifications. 15 mL buffy coat was diluted with warm dilution buffer, i.e., PBS free of Ca^{2+} and Mg^{2+} ions. 10 mL of the diluted mixture was added into 7 mL of Ficoll–Paque solution (Sigma-Aldrich, Australia), and centrifuged at $500 \times g$ at 20 °C for 30 min. The mononuclear cells at interface was collected and resuspended in 10 mL warm dilution buffer. The diluted cell suspension was further rinsed with PBS (containing 5% FCS and free of Ca^{2+} and Mg^{2+}) at pH 7.2, then centrifuged at $500 \times g$ for 5 min at 4 °C to remove supernatants. After repeating this washing step twice, the PBMCs were immediately used for the induction of OCs. The PBMCs were resuspended in α-MEM and cell viability was determined before plating in 12-well plates containing metallic specimens at 2.5×10^5 cells per well in 1 mL of OC conditioned culture medium, α-MEM containing 10% FCS and antibiotics, 10×10^{-9} M dexamethasone (Sigma-Aldrich, Australia), 10×10^{-9} M 1,25(OH)$_2$D$_3$ (Sigma-Aldrich, Australia), and 25 ng mL^{-1} human M-CSF (Merck Millipore, Australia). Half of the cell culture medium was refreshed twice a week. The OC inductive medium supplemented with recombinant human RANKL (Merck Millipore) at 50 ng mL^{-1} was used at the day 6 of culture. To monitor OC formation, the PBMCs were also seeded to the wells containing glass coverslips 6 mm in diameter (Thermo Scientific, Australia) and cultured under the identical conditions. After trypsinization, the primary cultured OBs (2×10^4 per well) were added to the OC culture in 12-well plates at day 7 of culture. The co-cultured OB and OC cells were maintained in the inductive culture medium for 3–4 d (i.e., at the OC culture day 10 or day 11). The co-culture was terminated either for OC formation assay observation with SEM (Zeiss Ultra Plus, Germany) or biological and mechanistic studies.

Immunofluorescent Staining with Antibodies to Cathepsin K in OCs: OC cells express CTSK, a lytic enzyme initiating bone resorption. CTSK protein expression was detected by immunofluorescent staining as described above, with the addition of the primary antibody. OC cells were incubated with a rabbit polyclonal anti-human CTSK antibody (1:100 dilution, Life Sciences, Australia), at room temperature for 50 min, and then incubated with a secondary goat anti-rabbit antibody conjugated with FITC for 50 min, followed by propidium iodide (PI) staining (Sigma-Aldrich, Australia).

OB and OC Cell Morphology and Adhesion: The cells of OB, OC, co-cultured OB, and OC were washed with warm PBS and immediately fixed with the primary fixation solution, 2% Glutaldehyde in 0.1 M sodium cacodylate buffer, for 2 h at room temperature. The primary fixation was rinsed with 0.1 M sodium cacodylate buffer for three times (30 min for each run). Secondary fixation was performed using 1% osmium tetroxide at room temperature for 60 min. Samples were then washed with distilled water three times (30 min for each run) before progressive dehydration in ethanol with a series of concentrations, i.e., 10, 50, 70, 90, and 100%. The samples were critical point dried and coated with gold and examined using SEM (Zeiss Ultra Plus, Germany).

Statistical Analyses: All statistical analyses were performed using the computer program Graphpad Prism 6.0 (GraphPad Software, Inc. CA, USA) through a one-way analysis of variance (ANOVA) followed by Tukey's test. All data were assessed for Gaussian distribution using the D'Agostino-Pearson normality test before analysis with these parametric tests. The level of statistical significance was fixed at $p \leq 0.05$. The *n* numbers of each individual in vitro test ($n = 6$) were provided in the caption legends.

Supporting Information

Supporting Information is available from the Wiley Online Library or from the author.

Acknowledgements

[1] http://www.who.int/mediacentre/news/releases/2014/lancet-ageing-series/en

[2] D. M. Brunette, P. Tengvall, M. Textor, P. Thomsen, *Titanium in Medicine*, Springer, Berlin Heidelberg **2001**.

[3] M. Niinomi, M. Nakai, J. Hieda, *Acta Biomater.* **2012**, *8*, 3888.

[4] X. Liu, P. K. Chu, C. Ding, *Mater. Sci. Eng. R* **2004**, *47*, 49.

[5] D. Duraccio, F. Mussano, M. Faga, *J. Mater. Sci.* **2015**, *50*, 4779.

[6] D. Krewski, R. A. Yokel, E. Nieboer, D. Borchelt, J. Cohen, J. Harry, S. Kacew, J. Lindsay, A. M. Mahfouz, V. Rondeau, *J. Toxicol. Environ. Health B* **2007**, *10*, 1.

[7] D. Kuroda, M. Niinomi, M. Morinaga, Y. Kato, T. Yashiro, *Mater. Sci. Eng. A* **1998**, *243*, 244.

[8] a) H. Liu, M. Niinomi, M. Nakai, K. Cho, *Acta Biomater.* **2015**, *24*, 361; b) S.-C. Kim, H.-J. Lee, S.-G. Son, H.-K. Seok, K.-S. Lee, S.-Y. Shin, J.-C. Lee, *Acta Biomater.* **2015**, *12*, 322.

[9] a) M. Niinomi, *Mater. Sci. Eng. A* **1998**, *243*, 231; b) M. Niinomi, *Biomater.* **2003**, *24*, 2673.

[10] M. Tane, S. Akita, T. Nakano, K. Hagihara, Y. Umakoshi, M. Niinomi, H. Nakajima, *Acta Mater.* **2008**, *56*, 2856.

[11] J.-Y. Rho, T. Y. Tsui, G. M. Pharr, *Biomaterials* **1997**, *18*, 1325.

[12] A. Fukuda, M. Takemoto, T. Saito, S. Fujibayashi, M. Neo, S. Yamaguchi, T. Kizuki, T. Matsushita, M. Niinomi, T. Kokubo, T. Nakamura, *Acta Biomater.* **2011**, *7*, 1379.

[13] J. Hieda, M. Niinomi, M. Nakai, K. Cho, T. Mohri, T. Hanawa, *Mater. Sci. Forum* **2014**, *783-786*, 1261.

[14] J. Hieda, M. Niinomi, M. Nakai, H. Kamura, H. Tsutsumi, T. Hanawa, *J. Biomed. Mater. Res. B* **2013**, *101*, 776.

[15] M. Tlotleng, E. Akinlabi, M. Shukla, S. Pityana, *Mater. Sci. Eng. C* **2014**, *43*, 189.

[16] J. Hieda, M. Niinomi, M. Nakai, K. Cho, T. Gozawa, H. Katsui, R. Tu, T. Goto, *J. Mechan. Behav. Biomed. Mater.* **2013**, *18*, 232.

136

[17] S. Pors Nielsen, *Bone* **2004**, *35*, 583.

[18] E. Bonnelye, A. Chabadel, F. Saltel, P. Jurdic, *Bone* **2008**, *42*, 129.

[19] Z. Saidak, P. J. Marie, *Pharmacol. Therapeut.* **2012**, *136*, 216.

[20] a) B. Zhang, D. Myers, G. Wallace, M. Brandt, P. Choong, *Int. J. Mol. Sci.* **2014**, *15*, 11878; b) Y. Xin, J. Jiang, K. Huo, T. Hu, P. K. Chu, *ACS Nano* **2013**, *3*, 3228.

[21] X. B. Chen, D. R. Nisbet, R. W. Li, P. N. Smith, T. B. Abbott, M. A. Easton, D. H. Zhang, N. Birbilis, *Acta Biomater.* **2014**, *10*, 1463.

[22] C. Capuccini, P. Torricelli, F. Sima, E. Boanini, C. Ristoscu, B. Bracci, G. Socol, M. Fini, I. N. Mihailescu, A. Bigi, *Acta Biomater.* **2008**, *4*, 1885.

[23] W. Zhang, Y. Shen, H. Pan, K. Lin, X. Liu, B. W. Darvell, W. W. Lu, J. Chang, L. Deng, D. Wang, W. Huang, *Acta Biomater.* **2011**, *7*, 800.

[24] X. N. Gu, X. H. Xie, N. Li, Y. F. Zheng, L. Qin, *Acta Biomater.* **2012**, *8*, 2360.

[25] P. Habibovic, F. Barrère, C. A. Van Blitterswijk, K. de Groot, P. Layrolle, *J. Am. Ceram. Soc.* **2002**, *85*, 517.

[26] a) X.-B. Chen, A. Nouri, Y. Li, J. Lin, P. D. Hodgson, C. E. Wen, *Biotech. Bioeng.* **2008**, *101*, 378; b) X.-B. Chen, Y.-C. Li, J. D. Plessis, P. D. Hodgson, C. E. Wen, *Acta Biomater.* **2009**, *5*, 1808.

[27] M. Takemoto, S. Fujibayashi, M. Neo, J. Suzuki, T. Matsushita, T. Kokubo, T. Nakamura, *Biomaterials* **2006**, *27*, 2682.

[28] W.-J. Dong, T.-R. Zhang, J. Epstein, L. Cooney, H. Wang, Y.-B. Li, Y.-B. Jiang, A. Cogbill, V. Varadan, Z. R. Tian, *Chem. Mater.* **2009**, *19*, 4454.

[29] H. Zhao, W. Dong, Y. Zheng, A. Liu, J. Yao, C. Li, W. Tang, B. Chen, G. Wang, Z. Shi, *Biomaterials* **2011**, *32*, 5837.

[30] X.-B. Chen, Y. Li, P. D. Hodgson, C. E. Wen, *Mater. Sci. Eng. C* **2009**, *29*, 165.

[31] S. Lotinun, R. Kiviranta, T. Matsubara, J. A. Alzate, L. Neff, A. Luth, I. Koskivirta, B. Kleuser, J. Vacher, E. Vuorio, W. C. Horne, R. Baron, *J. Clin. Invest.* **2013**, *123*, 666.

[32] J. Zhou, Y. Han, *Appl. Surf. Sci.* **2013**, *286*, 384.

[33] a) K. Zhu, K. Yanagisawa, R. Shimanouchi, A. Onda, K. Kajiyoshi, *J. Eur. Ceram. Soc.* **2006**, *26*, 509; b) S.-H. Tan, X.-G. Chen, Y. Ye, J. Sun, L.-Q. Dai, Q. Ding, *J. Hazard. Mater.* **2010**, *179*, 559.

[34] T. Nieh, A. Jankowski, J. Koike, *J. Mater. Res.* **2001**, *16*, 3238.

[35] J. Wu, J. Zhou, W. Zhao, B. Gao, *Mater. Sci. Eng. C* **2013**, *33*, 140.

[36] K. Mittal, *Active Passive Electron. Comp.* **1976**, *3*, 21.

[37] T. Akahori, M. Niinomi, Y. Koyanagi, T. Kasuga, H. Toda, H. Fukui, M. Ogawa, *Mater. Trans.* **2005**, *46*, 1564.

[38] a) D. J. T. Kyle, A. Oikonomou, E. Hill, A. Bayat, *Biomaterials* **2015**, *52*, 88; b) A. Bachhuka, J. Hayball, L. E. Smith, K. Vasilev, *ACS Appl. Mater. Interfaces* **2015**, *7*, 23767.

[39] A. J. Engler, S. Sen, H. L. Sweeney, D. E. Discher, *Cell* **2006**, *126*, 677.

[40] S. Sista, C. Wen, P. D. Hodgson, G. Pande, *J. Biomed. Mater. Res. A* **2011**, *97*, 27.

[41] M. Novinec, B. Lenarcic, *Biol. Chem.* **2013**, *394*, 1163.

[42] *Standard Test Method for Adhesion or Cohesion Strenght of Thermal Spray Coatings, ASTM Standards C633-13*, ASTM International, West Conshohocken, PA, **2013**.

[43] P. N. Smith, C. Freeman, D. Yu, M. Chen, P. A. Gatenby, C. R. Parish, R. W. Li, *J. Orthop. Res.* **2010**, *28*, 1315.

[44] M. Susa, N. H. Luong-Nguyen, D. Cappellen, N. Zamurovic, R. Gamse, *J. Transl. Med.* **2004**, *2*, 6.

137

**ADVANCED
HEALTHCARE
MATERIALS**

Supporting Information

Osteoanabolic Implant Materials for Orthopedic Treatment

*Yun-Fei Ding, Rachel W. Li, Masaaki Nakai, Trina Majumdar,
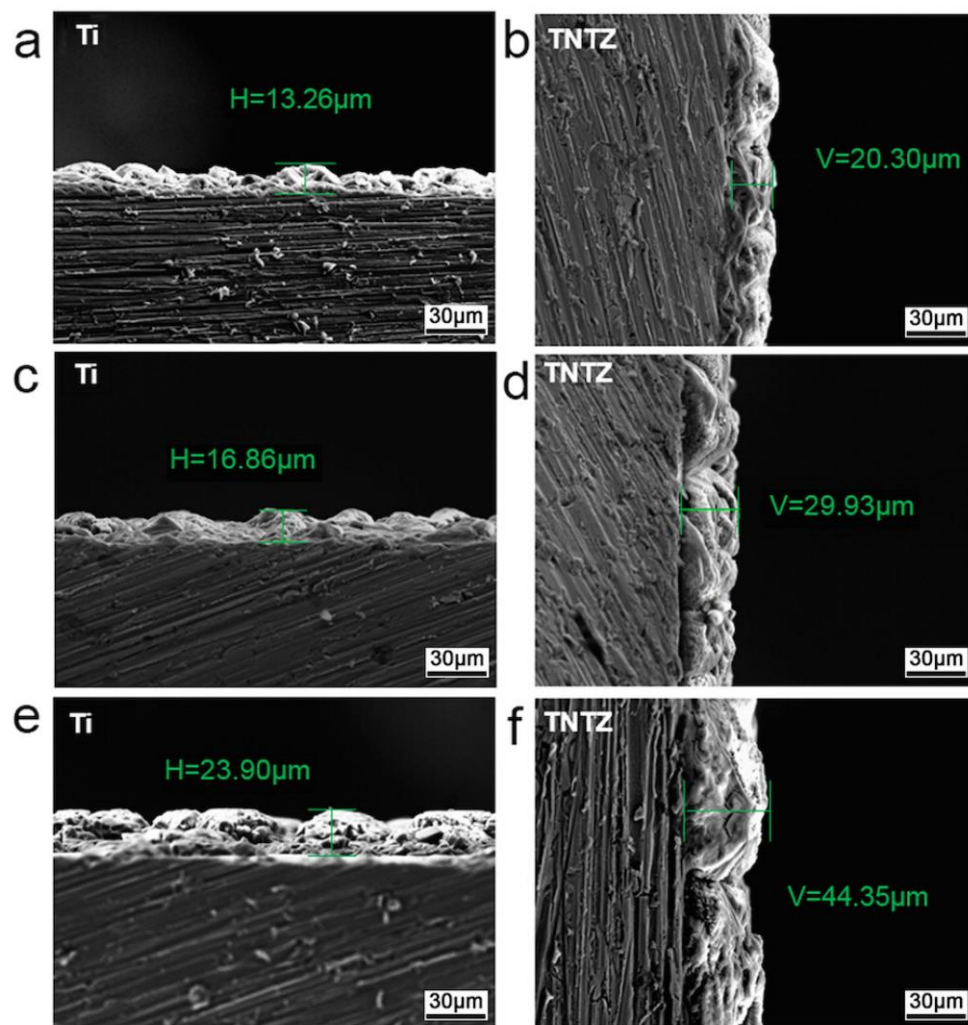Dong-Hai Zhang, Mitsuo Niinomi, Nick Birbilis, Paul N.
Smith, and Xiao-Bo Chen**

Supporting Information

Osteoanabolic Implant Materials for Orthopaedic Treatment

Yun-Fei Ding[a, #], Rachel W. Li[b, c, #], Masaaki Nakai[d], Trina Majumdar[a], Dong-Hai Zhang[b], Mitsuo Niinomi[d], Nick Birbilis[a], Paul N. Smith[b, c] and Xiao-Bo Chen[a],*

([#]These authors contributed equally)

Supplementary Figure S1

SEM micrographs of interface of SrPO₄ coated c.p. Ti and TNTZ processed with a pre-treatment in alkaline solution at 200 °C for 24 h, and SrPO₄ coating growth at 200 °C for **various temperatures** (**a, b**) 12 h; (**c, d**) 24 h; (**e, f**) 48 h. It is evident that the thickness of the SrPO₄ coating on either c.p. Ti or TNTZ is a funciton of processing time in the SrPO₄ coating bath.
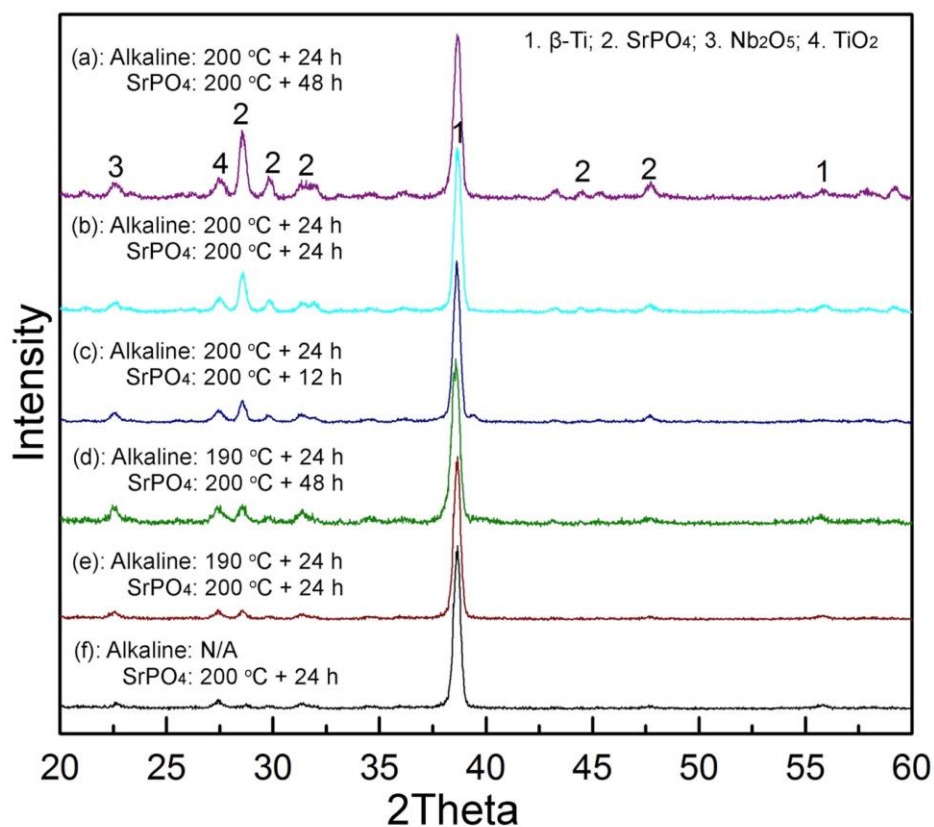
Supplementary Figure S2

XRD patterns of TNTZ discs. (**a-e**) TNTZs with alkaline treatment and the $SrPO_4$ bath, and (**f**) TNTZs without alkaline treatment.
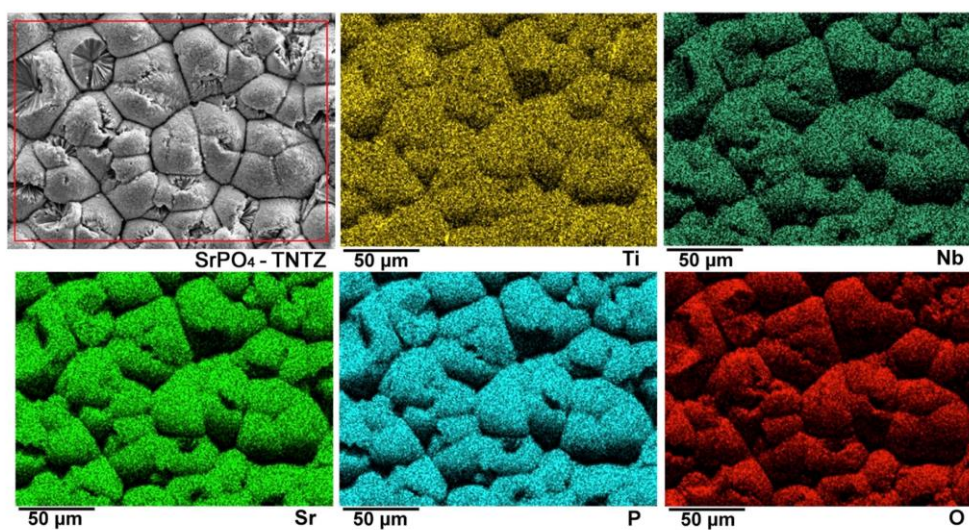
Supplementary Figure S3

EDS with elements distributions of TNTZ discs with full coverage of SrPO$_4$ coating (alkaline at 200 °C for 24 h; SrPO$_4$: at 200 °C for 24 h).

0.202nm

2 nm

5 1/nm
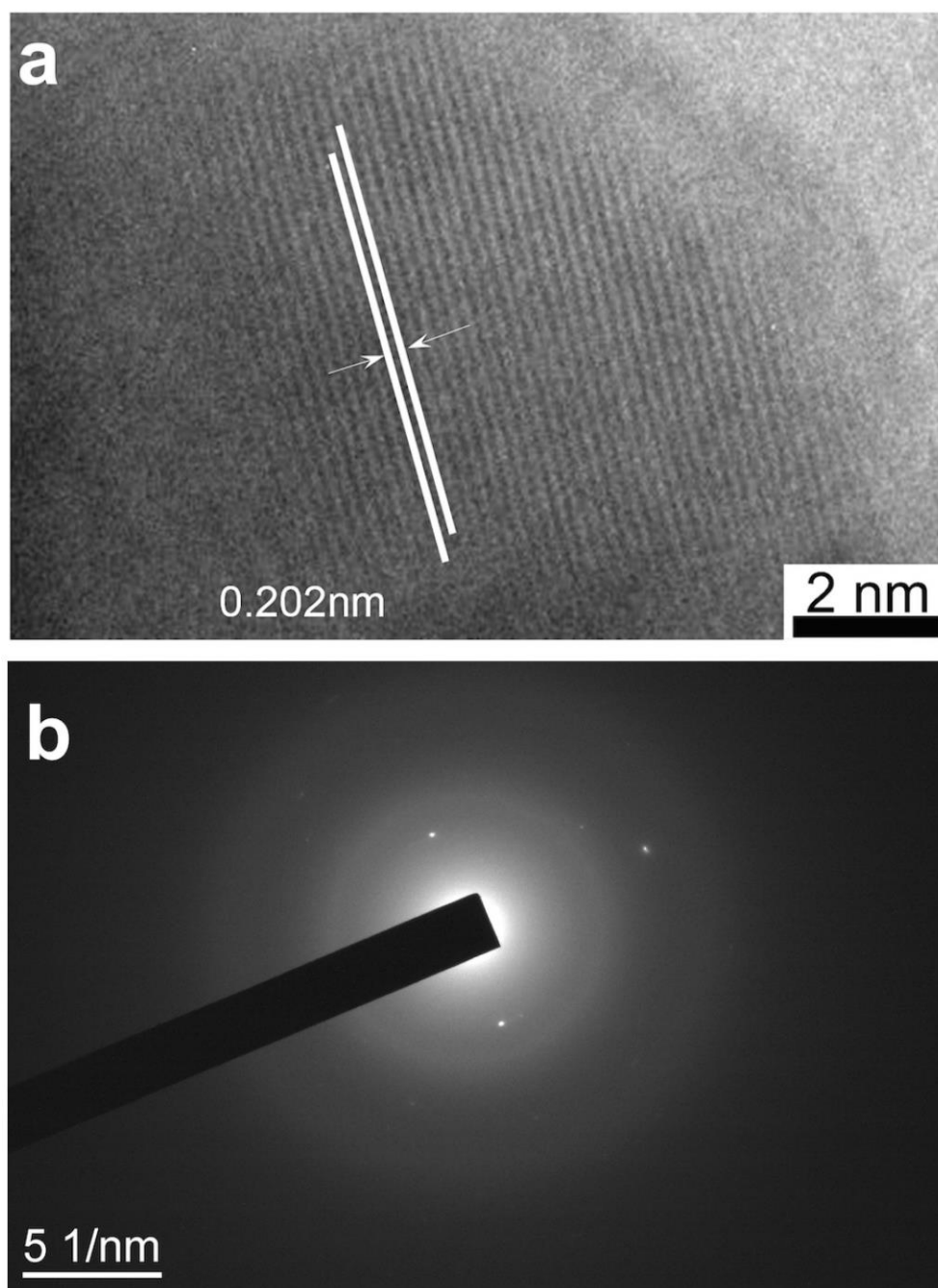
Supplementary Figure S4
(a) The high-resolution TEM image and (b) SAED pattern of $SrPO_4$.
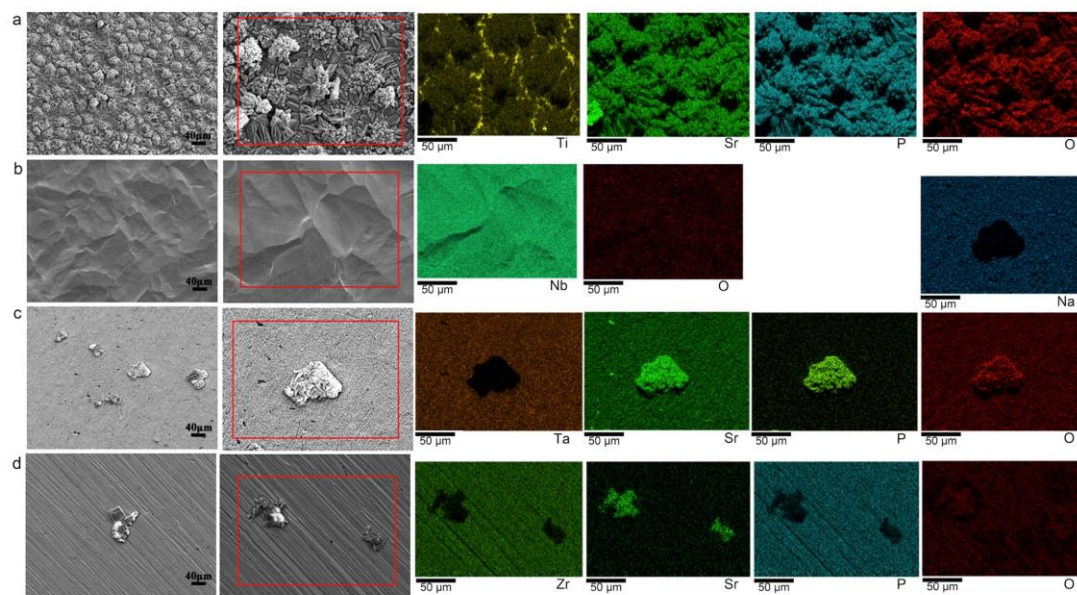
Supplementary Figure S5
SEM morphologies and elements distribution for (a) c.p. Ti, (b) Nb, (c) Ta and (d) Zr after alkaline treatment at 200 °C for 24h and SrPO$_4$ converstion at 200 °C for 24 h.
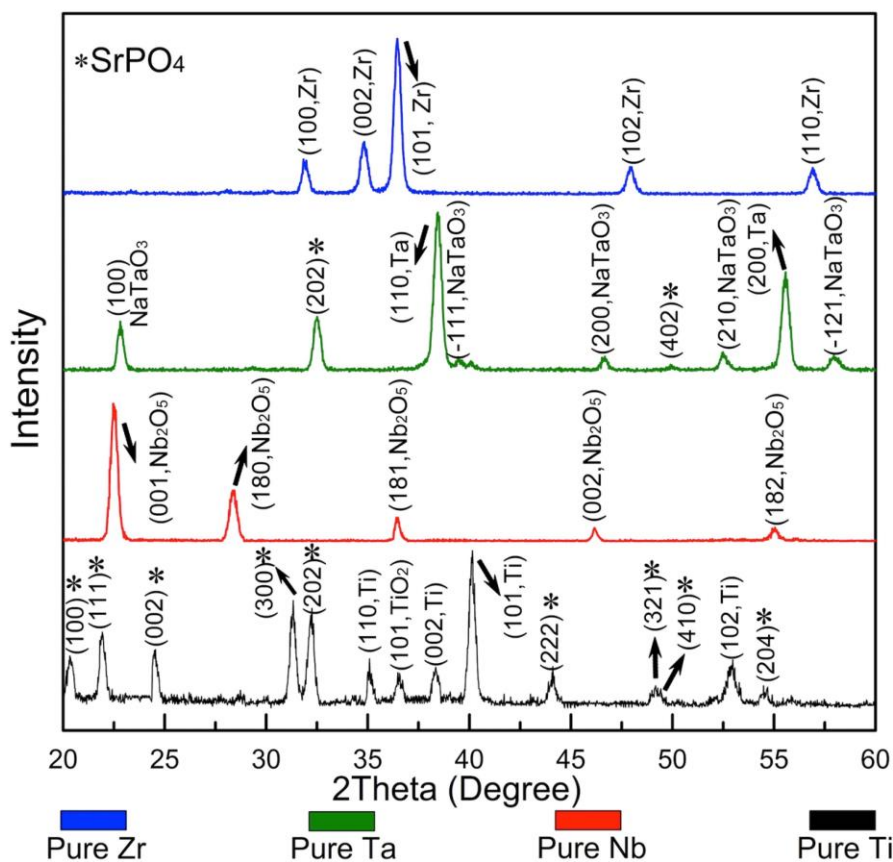
Supplementary Figure S6
XRD patterns of pure metallic discs (control group) after alkaline treatment at 200 °C for 24 h and $SrPO_4$ bath at 200 °C for 24 h.

7
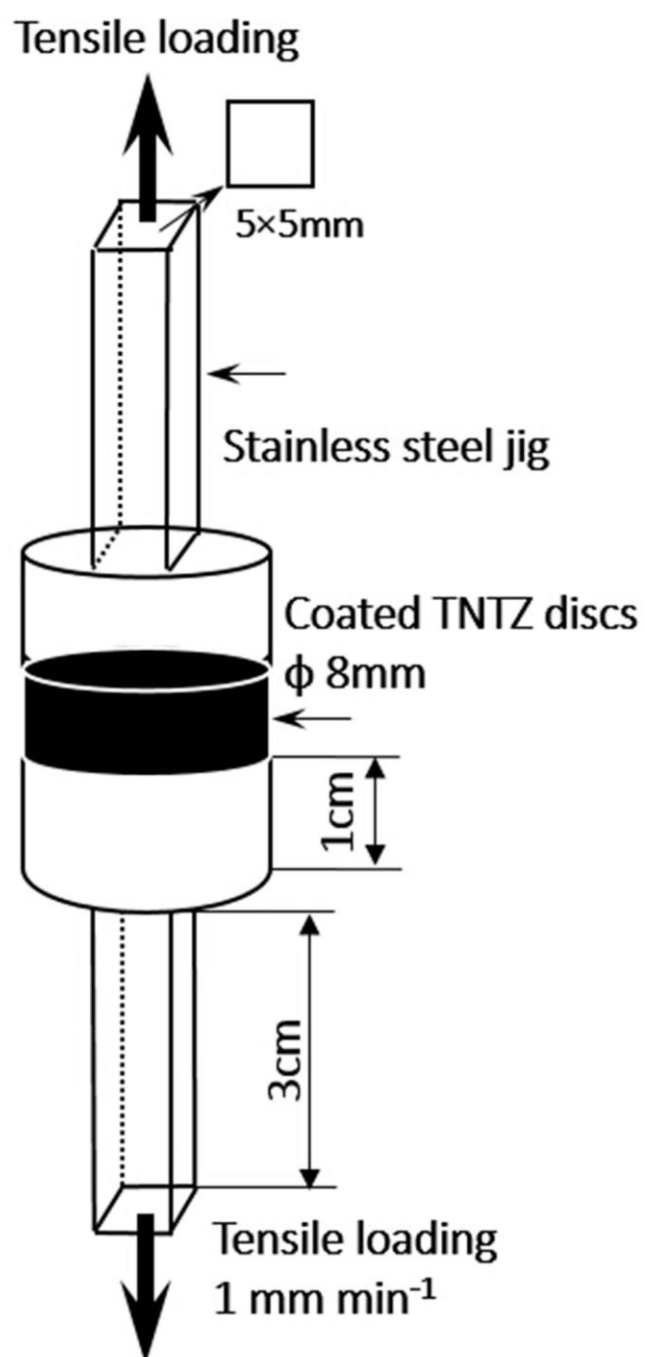
Supplementary Figure S7
Schematic drawing of tensile bonding strength testing set.

8

Osteoblast Cell Growth Curve
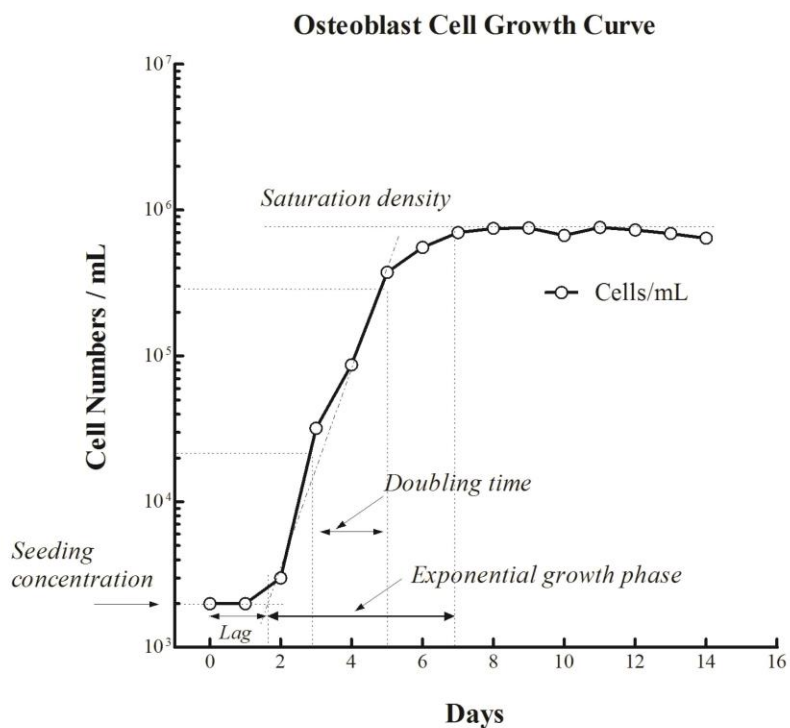
Supplementary Figure S8

Cell growth curve as a function of culture time. Because of space limits in our designed Figure 2, we did not present the complete suite of results in the application. Under our laboratory conditions, the best proliferation time (log phase) is between 3-5 days after seeding, which is the reason we presented data at that specified time point in Figure 2h.

9

Chapter 7: The cartilage/bone interface; tuning the viscoelastic behaviour of mineralised interfacial regeneration hydrogels

---

Musculoskeletal conditions such as osteoarthritis are becoming more common worldwide, and among those suffering from musculoskeletal conditions, a large portion have damaged joints which may require either complete joint replacements and/or other therapies to restore function. Thus, reducing the disability burden of musculoskeletal conditions requires not only an understanding of how best to design orthopaedic implants for optimal osseointegration, but an understanding of how to heal damaged joints, or the bone-cartilage interface. This region is composed of both hard and soft components, and thus approaches toward healing this region require the incorporation of both hard (metallic) and soft (hydrogels) biomaterials.

The healing of osteoarthritic joints through the regeneration of the region between articular cartilage and bone is complex, due to varying viscoelastic properties across this region. Articular cartilage is a viscoelastic tissue whose structural integrity is important in maintaining joint health. Understanding the dynamic viscoelastic behaviour (in both healing and healed joints) across this region is needed for the successful design of regenerative scaffolds for this area. The use of natural origin hydrogels as well as bioactive components such as bone minerals are especially promising in this regard.

Here, a rotating simplex model was used to optimise the composition of natural origin agarose and gellan hydrogel composites with hydroxyapatite (HA), to approximate the viscoelastic behaviour of human cartilage. Adding HA particles reinforced both agarose and gellan matrices up to a critical concentration (< 3 w/v %). Beyond this, larger agglomerates were formed 7as evidenced by micro computed tomography data), which acted as stress risers and reduced the ability of these composites

to dissipate energy. A maximum compressive modulus of 450.7±24.9 kPa was achieved with a composition of 5.8 w/v% agarose and 0.5 w/v% HA. Interestingly, when loaded dynamically (1–20 Hz), this optimised formulation did not exhibit the highest complex modulus; instead, a sample with a higher concentration of mineral was identified (5.8 w/v% agarose and 25 w/v% HA). This demonstrates the importance of examining the mechanical behaviour of biomaterials under conditions representative of physiological environments. While the complex moduli of the optimised gellan (1.0 ±0.2 MPa at 1 Hz) and agarose (1.7±0.2 MPa at 1 Hz) constructs did not match the complex moduli of healthy human cartilage samples (26.3±6.5 MPa at 1 Hz), similar tan δ values were observed between 1 and 5 Hz. This is promising since these frequencies represent the typical heel strike time of the general population. In summary, this study demonstrates the importance of considering more than just the strength of biomaterials.

In summary, this study demonstrates the importance of considering more than just the strength of biomaterials since tissues like cartilage play a more complex role.

The bulk of the experimental data for this section was gathered during a research stay at the University of Birmingham (United Kingdom), under the supervision of Dr Sophie Cox. This chapter was prepared as a paper, and published in the *Journal of the Mechanical Behavior of Biomedical Materials*. The paper appears here as published.
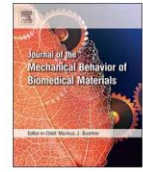
Formulation and viscoelasticity of mineralised hydrogels for use in bone-cartilage interfacial reconstruction

Trina Majumdar[a,1], Megan E. Cooke[b,c,1], Bernard M. Lawless[d,1], Francis Bellier[e], Erik A.B. Hughes[c], Liam M. Grover[c], Simon W. Jones[b], Sophie C. Cox[c,*]

[a] Materials Science and Engineering Department, Monash University, Australia
[b] Institute of Inflammation and Ageing, MRC-ARUK Centre for Musculoskeletal Ageing Research, Queen Elizabeth Hospital, University of Birmingham, Birmingham B15 2WB, United Kingdom
[c] School of Chemical Engineering, University of Birmingham, United Kingdom
[d] Department of Mechanical Engineering, University of Birmingham, United Kingdom
[e] Materials Engineering, Toulouse National Polytechnic Institute, France

ARTICLE INFO

ABSTRACT

Articular cartilage is a viscoelastic tissue whose structural integrity is important in maintaining joint health. To restore the functionality of osteoarthritic joints it is vital that regenerative strategies mimic the dynamic loading response of cartilage and bone. Here, a rotating simplex model was employed to optimise the composition of agarose and gellan hydrogel constructs structured with hydroxyapatite (HA) with the aim of obtaining composites mechanically comparable to human cartilage in terms of their ability to dissipate energy. Addition of ceramic particles was found to reinforce both matrices up to a critical concentration (< 3 w/v%). Beyond this, larger agglomerates were formed, as evidenced by micro computed tomography data, which acted as stress risers and reduced the ability of composites to dissipate energy demonstrated by a reduction in tan δ values. A maximum compressive modulus of 450.7 ± 24.9 kPa was achieved with a composition of 5.8 w/v% agarose and 0.5 w/v% HA. Interestingly, when loaded dynamically (1–20 Hz) this optimised formulation did not exhibit the highest complex modulus instead a sample with a higher concentration of mineral was identified (5.8 w/v% agarose and 25 w/v% HA). Thus, demonstrating the importance of examining the mechanical behaviour of biomaterials under conditions representative of physiological environments. While the complex moduli of the optimised gellan (1.0 ± 0.2 MPa at 1 Hz) and agarose (1.7 ± 0.2 MPa at 1 Hz) constructs did not match the complex moduli of healthy human cartilage samples (26.3 ± 6.5 MPa at 1 Hz), similar tan δ values were observed between 1 and 5 Hz. This is promising since these frequencies represent the typical heel strike time of the general population. In summary, this study demonstrates the importance of considering more than just the strength of biomaterials since tissues like cartilage play a more complex role.

1. Introduction

Articular cartilage covers the ends of bones to provide a low-friction joint surface and transfers load to the subchondral bone. The complex organisation of articular cartilage varies through its depth. Within joint spaces four distinct sub-zones are distinguishable: hyaline cartilage, calcified cartilage, sub-chondral bone, and cancellous bone (Costa and Mano, 2015; Liu et al., 2011). Variation in the structure of the extracellular matrix occurs between different layers, specifically glycosaminoglycan (GAG) concentration and the ratio of collagen type II to X. The hyaline cartilage layer has the lowest concentration of GAGs and

compressive modulus, and highest ratio of collagen II to collagen X, while the opposite is true for the cancellous bone region (Nguyen et al., 2011). This hierarchical structure is responsible for the viscoelastic response of articular cartilage under deformation. To restore the functionality of osteoarthritic joints it is vital that candidate biomaterials mimic the dynamic loading response of cartilage and bone.

Since the Young's modulus of biological tissues may depend on strain rate, i.e. they are viscoelastic (Hukins et al., 1999), it is important to understand the mechanical behaviour of biomaterials in relation to strain rates. The compressive modulus of cartilage has been shown to be strain rate dependent (Shepherd and Seedhom, 1997). Methods, such as

creep and stress relaxation testing, have been used to characterise the viscoelastic response of cartilage and biomaterials, such as hydrogels (Fick and Espino, 2011; Moxon et al., 2017). However, unlike these methods, Dynamic Mechanical Analysis (DMA) is a dynamic testing approach to determine the viscoelastic properties of a material (Barnes et al., 2016; Burton et al., 2017) or multiple component structures (Lawless et al., 2017a, 2016). For DMA, an oscillating force is applied to a specimen and the out-of-phase displacement response is analysed (Menard, 2008). Viscoelastic properties of the material can then be characterised in terms of its storage modulus (ability to store energy for elastic recoil) and loss modulus (ability to dissipate energy); these are the real and imaginary parts of the complex modulus. The storage (E') and loss (E'') moduli are related to the complex modulus (E*) and the phase lag (δ), of the viscoelastic material (Hukins et al., 1999):

$$|E^*| = \sqrt{E'^2 + E''^2} \qquad (1)$$

$$\delta = tan^{-1}\left(\frac{E''}{E'}\right) \qquad (2)$$

Studies have used DMA to quantify the frequency dependent viscoelastic properties of cartilage (Fulcher et al., 2009; Temple et al., 2016) and to understand factors that affect the viscoelastic properties, including resistivity of bone (Lawless et al., 2017b), hydration (Pearson and Espino, 2013), its thickness (Espino et al., 2014) and the induced stress (Lawless et al., 2017b). Also, frequency, independent of load, has been shown to be an important factor in relation to how cartilage damages (Sadeghi et al., 2015) while crack propagation, of articular cartilage, has been shown to be frequency dependent (Sadeghi et al., 2018). Thus, materials intended to replace this tissue should not only exhibit similar mechanical strength but also have comparable frequency response.

Since cartilage is avascular, it is critical that regenerative strategies have the ability to support cellular ingrowth. Generally, hydrogels are the material of choice for the formulation of tissue engineered scaffolds to regenerate cartilage due to the possibility to incorporate cells (Almeida et al., 2016; Balakrishnan et al., 2014; Parmar et al., 2015). However, the frequency dependent viscoelastic response of hydrogels is often overlooked (Cameron et al., 2011). There is also typically a trade-off between the mechanical suitability of hydrogels and cytocompatibility (Bartnikowski et al., 2015; Mironi-Harpaz et al., 2012). The incorporation of a secondary phase to the hydrogel matrix presents the possibility to add complementary properties (Osmałek et al., 2014), such as mechanical response or enhanced cell adhesion. Addition of a mineral phase is an attractive strategy to reinforce the hydrogel matrix and induce osseous tissue growth (D'Este and Eglin, 2013; Hu et al., 2016). This may be particularly useful in hydrogels that display low cell adhesion, such as agarose and gellan gum (Zhang et al., 2012). Many synthetic bone mineral analogues have been explored, including calcium phosphates such as hydroxyapatite ($Ca_{10}(PO_4)_6(OH)_2$; HA) (Danoux et al., 2016; Tamaddon and Czernuszka, 2013). While the advantages for such an approach are clear, the influence of incorporating these secondary phases on the viscoelasticity of hydrogels is currently limited, that is despite the frequency response of these materials being recognised as critical for the intended application (Bartnikowski et al., 2015; Wands et al., 2008).

In this study, we selected two natural origin hydrogels, gellan gum and agarose, that may be thermally gelled so that suitable specimens for DMA experiments could be produced with relative ease compared with other materials that require more complex gelation mechanisms. This enabled the work to explore the possibility of structuring gellan gum and agarose, with hydroxyapatite to create cytocompatible constructs with comparable viscoelastic properties to native cartilage. To achieve this, a Doehlert type rotating simplex model was used to systematically formulate mineralised composites. Optimisation of the constructs was performed iteratively by varying hydrogel and mineral concentration.

DMA was employed to characterise the viscoelastic response of the hydrogel/mineral composites as well as human cartilage samples. Use of micro-computed tomography allowed for visualisation of mineral distribution and size, which was used to further elucidate the influence of hydroxyapatite on the observed mechanical response. To complement this mechanical analysis, the effect of incorporating HA into agarose and gellan constructs on cell adhesion was also studied in-vitro.

2. Materials and methods

2.1. Development of experimental plan

A model to relate the effects of varying the concentration of polymer and mineral on composite mechanical behaviour was developed according to Doehlert's theory of experimental design (Jethara and Patel, 2015; Mennini et al., 2012). This allowed for the resolution of a second degree system to find optimal compositions, whilst allowing for refinement through shifts in experimental field based on initial results (Gabrielsson et al., 2002; Jethara and Patel, 2015; Mennini et al., 2012). While the concentration of gel and mineral were optimised all other processing parameters, including temperature and shear rate, were kept constant. An initial experimental domain for testing hydrogel composite properties was specified: 2.75–6.75 w/v% agarose to 0–25 w/v% hydroxyapatite (HA), and 1.5–6 w/v% gellan to 0–15 w/v% HA. Details of all compositions tested can be found in Supplementary Information 1. At least 5 repeats were conducted for model validation. Coefficients and optimal compositions were obtained through polynomial regression and optimisation was completed for rupture stress. The model was validated by Fisher tests and any significance of coefficients were determined using student t-tests. A p value less than 0.05 was deemed significant.

2.2. Preparations of gels and composites

Agarose and gellan gum were selected for this study since both may be set via thermal gelation hence samples suitable for the proposed mechanical testing (Section 2.3) could be produced with relative ease and high batch reproducibility. To prepare the gels, agarose (genetic analysis grade, Fisher Scientific, UK) and gellan (food grade, Kelcogel, CP Kelco, UK) powders were dissolved in deionised water (pre-heated to 100 °C for gellan) while stirring on a magnetic hot plate at 200 rpm and 100 °C resulting in transparent solutions. HA (≥ 90%, Sigma-Aldrich, UK) was added if necessary, and the solution stirred for a further 10 min at 200 rpm. Gels were cast into sealed cylindrical moulds (diameter 6 cm and height 10 cm), and allowed to cool at room temperature overnight prior to testing. Following testing, optimal compositions were chosen as determined, on the basis of rupture stress, through the model and used for all following tests. A full list of all compositions tested can be viewed in Supplementary information 1. Notably, incorporation of HA particles within the two matrices exhibited different behaviour and hence the concentrations investigated for each material group were not the same.

2.3. Mechanical testing

All hydrogel/mineral specimens (diameter = 14 ± 1 mm; height = 6 ± 1 mm; n = 4) were mechanically tested by using a Bose ElectroForce 5500 controlled by WinTest 7 software (TA Instruments, New Castle, DE USA). Quasi-static mechanical testing was performed at a rate of 0.1 mm/min until specimen failure. The loads were applied using a flat compression platen with a diameter of 25 mm. For each group, the Young's modulus and rupture stress were calculated and reported as mean ± standard deviation (SD) (n = 6). Viscoelastic testing was performed, with the WinTest 7 DMA software, on the optimal and boundary conditions for both matrices. DMA was performed with a sinusoidal compressive strain between 15% and 20% of the specimen

height. Following pre-conditioning cycles at 0.2 and 0.5 Hz, each specimen was tested at 1, 5, 10 and 20 Hz. For each frequency, the complex (E*) and the dissipation factor (tan δ), also known as loss factor, were quantified. Further information on the calculation of these properties can be found elsewhere (Barnes et al., 2016; Fulcher et al., 2009; Lawless et al., 2016). For each composition, four repeats were completed.

All cartilage explants were taken from human femoral condyles. The study was approved by the United Kingdom National Research Ethics Service (Nottingham Research Ethics Committee 1 (05/Q2403/24) and Derby Research Ethics Committee 1 (11/H0405/2)). Informed consent was provided patients next of kin. The cartilage explants (diameter = 5.2 mm; height = 1.47 ± 0.36 mm; n = 3 healthy) were tested using a Bose ElectroForce 3200 controlled by 4.1 WinTest software (TA Instruments, New Castle, DE, USA). In accordance with previous studies, the cartilage explants were saturated with Ringer's solution prior to the frequency sweep (Temple et al., 2016). Following pre-conditioning cycles at 25 and 50 Hz (Espino et al., 2014; Temple et al., 2016), compressive load was applied between 16 and 36 N at 1, 8, 10, 12, 29 Hz to fully hydrated healthy (post-mortem cartilage from individuals with no history of joint pain) cartilage explants. All mechanical tests of the hydrogel/mineral specimens and cartilage explants were performed under unconfined conditions, in air at room temperature.

2.4. Visualisation of hydroxyapatite distribution in selected composites

Optimal hydrogel and mineral compositions for both agarose and gellan with HA were determined using Doehlert's model. For these two selected formulations the distribution of HA particles within the matrix was visualised in 3-dimensions (3D) using a Skyscan1172 micro-computed tomography (micro-CT) system (Bruker, Belgium). Composite cylinders (n = 1) were scanned with a 64 kV maximum X-ray energy, 6.4 W beam power, 1150 ms exposure per projection, 0.5 mm aluminium filter, and 9.87 μm pixel size. Data was reconstructed using *NRecon* (1.6.10.2, Bruker), binarised by applying a global threshold using *CTAn* (version 1.15.4.0, Bruker) and grey scale data was visualised in 3D using *CTVox* (version 3.0, Bruker).

2.5. In vitro adhesion and viability of MC3T3 pre-osteoblast cells

Since both agarose and gellan gum hydrogels are known to be non-cell adhesive an initial assessment of the effect of HA incorporation on the ability of native cells to adhere and survive on the composite samples was warranted. Given the focus of this study is the whole osteochondral unit pre-osteoblasts were selected as a native cell population for this initial in-vitro work due to their relatively rapid growth rate and robustness. Alpha Minimum Essential Media (α-MEM) with

sodium bicarbonate, ribonucleosides and deoxyribonucleosides (M426, Sigma, UK) was used as a base medium. Complete growth media was made by supplementing α-MEM media with a final concentration of 10% fetal bovine serum (F7524, Sigma, UK), 2.4% L-glutamine (G7513, Sigma, UK) and 1% penicillin-streptomycin (F4333, Sigma, UK). MC3T3-E1 preosteoblast cells (Subclone 4, CRL-2593, ATCC, USA) were cultured in complete growth media as per supplier instructions. Prior to in vitro experiments, hydrogel samples (5.8 w/v% agarose with and without 0.5 w/v% HA, gellan 5.3 w/v% with and without 3.0 w/v% HA) prepared as described in Section 2.2, were washed with 100% ethanol, and sterilised for 24 h under ultra-violet light immersed in complete growth media. Following, aliquots of MC3T3-E1 cells (2 × 10^4 cells/cm^2) were seeded on to the surface of hydrogel samples and tissue culture plastic as a control. Cells were allowed to adhere for 2 h and after this time complete growth media was added to each well to cover the sample surface. Cultures were incubated in 5% CO_2 atmosphere maintained at 37 °C. The viability of cells after culturing for 1, 3, and 7 days were analysed by staining with calcein-AM (1 mg/mL, Molecular Probes, UK) and propidium iodide (1 mg/mL, Invitrogen, UK), respectively in the dark. Stained cultures were visualised (n = 3) using a scanning confocal microscope (Olympus FV1000, Multiple Ar laser, Germany).

2.6. Statistical analysis

All data was analysed and figures generated using Prism software (version 6 for Windows, GraphPad Software, USA). All figures are presented as mean ± SD of n ≥ 5. One-way analysis of variance (ANOVA) was used for single factor testing, while two-way ANOVA was used for analyses with two variables. Both tests were followed by post-hoc Tukey's (when comparing to a control group) or Dunnett's tests (when comparing multiple groups). P values < 0.05 were considered significant.

3. Results

3.1. Optimising hydrogel and HA composite ratios

For both matrices, the concentration of gel was shown to affect both compressive modulus and maximum stress (Fig. 1). Increasing the gellan concentration for composites containing 12.8 w/v% HA, from 1.5 to 4 w/v% showed a three-fold increase in the maximum stress from 10.4 kPa (1.5GG 12.8HA) to 37.2 kPa (4GG 12.8HA). Similarly for agarose samples containing 0.5 w/v% HA, an increase in the concentration of matrix from 2.8 to 5.8 w/v% caused a 3-fold increase in both rupture stress (p < 0.0001) and compressive modulus (p < 0.0001).

Increasing the amount of HA in 5.8 w/v% agarose from 0 to 0.5 w/v
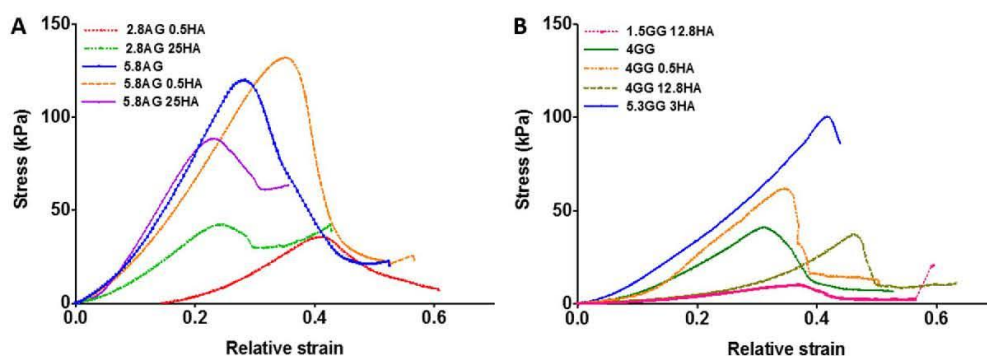

Fig. 1. The effect of changing hydrogel and HA composition on Young's modulus and rupture stress, representative curves of boundary compositions for both mineralised (A) agarose (AG) and (B) gellan (GG) constructs.
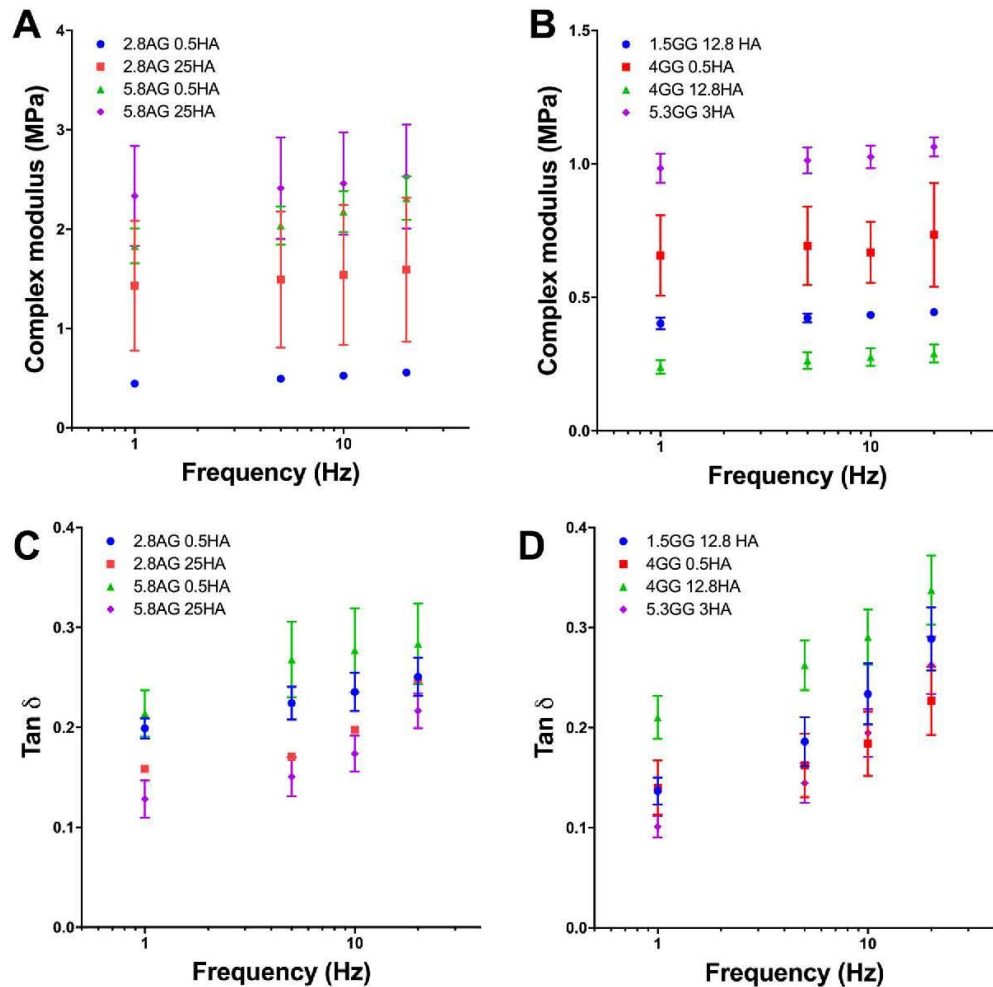
Fig. 2. The effect of changing hydrogel and HA composition on complex modulus (MPa) and loss factor (tan δ) with a) agarose and HA composition stiffness, b) gellan and HA composition complex modulus, c) agarose and HA loss factor and d) gellan and HA loss factor. Data represented as mean ± standard deviation (n = 5).

% caused an increase in average rupture stress from 120.2 ± 6.7 to 156.3 ± 16.5 kPa. Further increases in HA concentration for this matrix reduced rupture stress; 25 w/v% HA resulted in a rupture stress of 92.1 ± 3.5 kPa. For mineralised gellan composites both rupture stress and compression modulus increased up to a critical point of HA incorporation (4GG 0.5HA) and beyond this deterioration occurred (4GG 12.8HA). Using the Doehlert model, 5.8AG 0.5HA and 5.3GG 3.0HA were determined to be the optimal concentrations with respect to maximum stress. Boundary conditions for agarose were found to be: 2.8AG 0.5HA, 2.8AG 25HA, and 5.8AG 25HA. For gellan boundary conditions were 1.5GG 12.8HA, 4GG 0.5HA, and 4GG 12.8HA.

Analysis of viscoelastic behaviour up to 20 Hz revealed that hydrogel composites exhibited a tunable frequency response (Fig. 2). Similar to the quasi-static testing, the viscoelastic behaviour of the boundary compositions determined from the model demonstrated that agarose/HA constructs generally exhibited a higher complex modulus than the gellan/HA composites (Fig. 2a and b). The complex modulus, of the AG optimal and boundary conditions, gradually increased within the examined range of 1–20 Hz ($R^2 > 0.90$, $p < 0.05$). In comparison, for the gellan gum composites similar trends were observed ($R^2 > 0.73$, $p < 0.05$). For both matrices, the highest complex modulus across all

frequencies for the model boundary conditions was 5.8AG 25HA (2.3 ± 0.5 MPa at 1 Hz) and 5.3GG 3HA (1.0 ± 0.1 MPa at 1 Hz). Notably, for the agarose samples this result did not agree with the optimal formulation determined from quasi-static testing (5.8AG 0.5HA).

The dissipation factor (tan δ), also known as loss factor, of composites was quantified (Fig. 2c and d). Between 1 and 20 Hz, a gradual increase in loss tangent was observed, which revealed that more energy was stored by constructs than dissipated. The lowest loss tangent values were observed for 4GG 12.8HA (tan δ = 0.21 ± 0.02 at 1 Hz) and 5.8 AG 25HA (tan δ = 0.12 ± 0.03 at 1 Hz). For agarose samples, tan δ values were lower at all frequencies for constructs containing more HA.

3.2. Comparison of the dynamic mechanical behaviour of human cartilage and mineralised hydrogel composites

The complex moduli of the mineralised hydrogel samples were clearly shown to be lower than human cartilage isolated from healthy patients at all tested frequencies ($p < 0.05$) (Fig. 3a). The optimised agarose (5.8AG 0.5HA) and gellan (5.3GG 3.0HA) formulations exhibited complex moduli of 1.7 ± 0.1 and 1.0 ± 0.2 MPa, respectively, at 1 Hz while healthy cartilage (HC) was 26.3 ± 6.5 MPa. Cartilage was
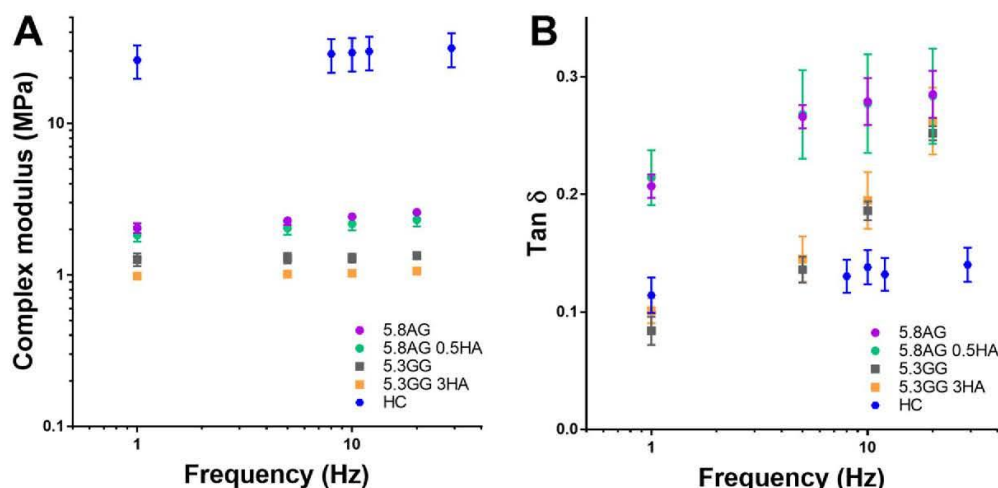
Fig. 3. A comparison of healthy human cartilage (HC) behaviour with synthetic analogues over a frequency range approximating normal human movement, with regards to A) complex modulus (E*) and B) loss factor (tan δ). Data represented as mean ± standard deviation (n = 5).

shown to be substantially higher than these hydrogel composites (26.3 ± 6.5 MPa at 1 Hz). The complex modulus of human cartilage and agarose samples with, as well as without, mineral was shown to increase logarithmically with increasing frequency ($R^2 > 0.9$). When gellan was used as the composite matrix this relationship was found to fit a second order polynomial.

The dissipation factor of gellan samples up to 5 Hz were found to have comparable tan δ values to HC (Fig. 3b). Above this frequency the gellan samples exhibited an increase in the ability to store energy as evidenced by a significant increase in tan δ values (y = 0.008, $R^2 > 0.98$, p < 0.01). At 1 Hz, the loss factor of the 5.8AG 0.5HA was found to be almost double the value for HC; 0.19 ± 0.00 compared with 0.11 ± 0.02 (Fig. 3b).

Micro-CT was employed to visualise the agglomeration behaviour of HA particles within optimised AG and GG composites to identify any differences in particle size and homogeneity, which may have influenced mechanical response (Fig. 4). HA particles (white) were distinguishable from both matrices (grey) through differences in X-Ray attenuation (Fig. 4a). A sample of human articular cartilage isolated from femoral condyles allowed for visualisation of the bone to cartilage interface, however, it was not possible to resolve any variation between sub-zones of the cartilage structure (Fig. 4b). Agglomeration of individual HA particles was identified in both AG and GG structures and 3D visualisation revealed that the calcium phosphate was not entirely homogeneous throughout the matrices. The majority of HA clusters were found to be less than 110 μm for both hydrogels, however notably a higher proportion > 150 μm was observed in 5.8AG 0.5HA compared with 5.3GG 3.0HA (Fig. 4c).

3.3. Cytotoxicity studies

In addition to assessing the mechanical suitable of the mineralised hydrogel constructs it is important to also consider the ability of native cells to survive and proliferate at the biomaterial/tissue interface, in particular for an avascular tissue such as cartilage. The viability and adherence of MC3T3 pre-osteoblasts on optimised formulations with and without HA was visualised (Fig. 5). As expected, very few cells were found to be viable on AG and GG constructs without HA after 1 day of culture. The addition of HA to both matrices was shown to facilitate attachment of MC3T3 pre-osteoblast cells. After 3 days of culture, the distribution of cells across mineralised hydrogel surfaces was generally less dense compared with the control (tissue culture

plastic). Notably, cells appeared to preferentially adhere in localised regions on 5.8AG 0.5HA and 5.3GG 3.0HA samples at days 3 and 7. The number of MC3T3s on the mineralised composites appears to increase over 7 days and cells were observed to spread across the surface, however compared with the control there was clearly fewer adherent cells.

4. Discussion

The use of a simplified Doehlert model to optimise the composition of mineralised hydrogel constructs allowed for the determination of a domain and predicted composite behaviour on the basis of experimental data. A limitation of the Doehlert model is that it does not represent physical or chemical phenomena and therefore, predictions may not fit all circumstances. Thus, experimental quasi-static testing was performed to validate the model. The compositions determined by the model to be optimal (5.8AG 0.5HA and 5.3GG 3.0HA) were confirmed to be consistent with the quasi-static mechanical testing results (Fig. 1). The composition which had the highest average compressive modulus was 5.8AG 0.5HA (450.7 ± 24.9 kPa). In relation to the viscoelastic properties quantified by DMA, the 5.3GG 3.0 HA composition had the highest complex modulus of the GG hydrogels (Fig. 2b). However, for the optimal agarose sample (5.8AG 0.5HA) this was the second stiffest for every frequency tested (Fig. 2a). This may highlight a potential limitation of the optimisation technique as the prediction may not fit all circumstances of mechanical loading.

Here a reduction in temperature was the only mechanism used to induce gellan gelation, which is known to cause a random coil-helix transition to occur and further aggregation of helices leads to the formation of junction zones (Miyoshi et al., 1996). However, since the sol-gel transition of gellan is ionotropic the presence of cations is necessary for the formation of a more stable hydrogel, which may explain why gellan samples were generally less stiff compared with agarose constructs (Fig. 1). Coutinho et al. demonstrated that it is possible to formulate both physically and chemically crosslinked gellan hydrogels by incorporating methacrylate groups into the polymer chain (Coutinho et al., 2010). These methacrylated gellan hydrogels exhibited highly tunable quasi-static properties, for example ultimate stress varied from 11.7 to 889.5 kPa and ultimate strain 34.2–96.1%, however Coutinho et al. did not consider viscoelastic response. In this study, gellan samples exhibited maximum stress values below 100 kPa and ultimate strain of up to 40% (Fig. 1b).
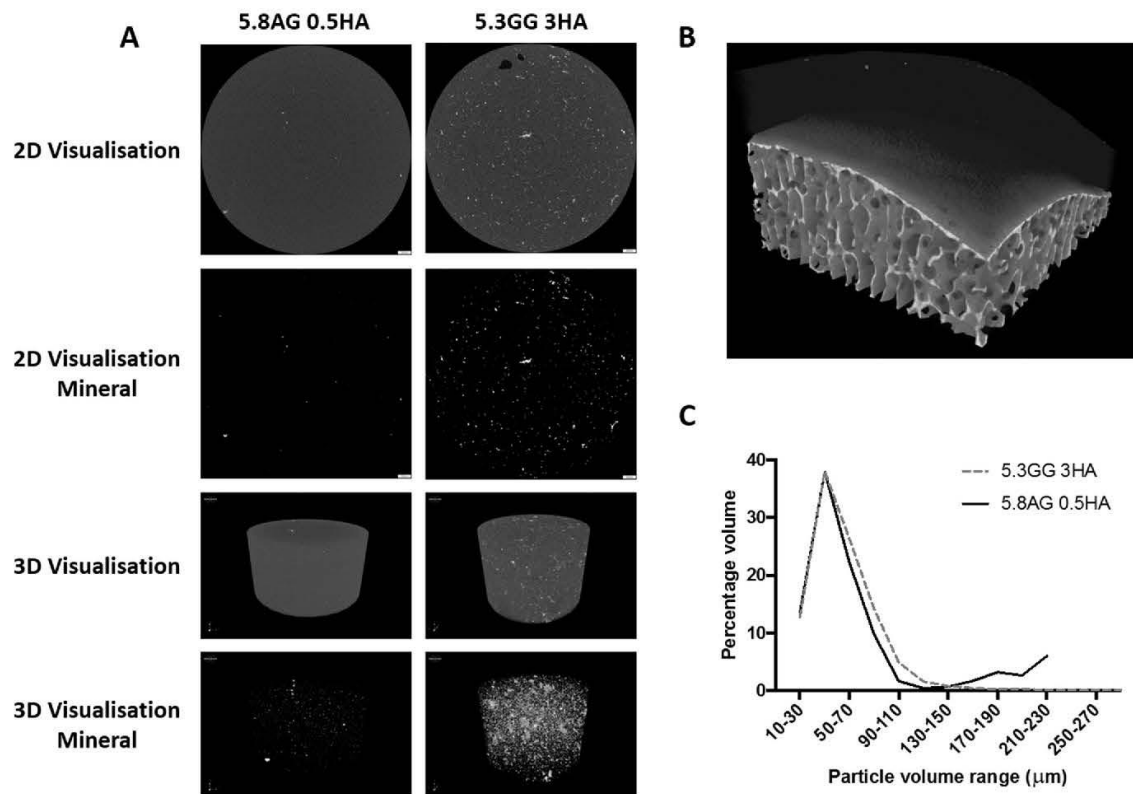
37

Fig. 4. Micro-CT scans of mineralised hydrogels and human tissue, showing a) optimised agarose and gellan compositions b) the cartilage/bone interface and c) mineral particle sizing. Scale bars = 300 µm.

Matrix and HA concentration were both found to have an effect on the quasi-static mechanical properties of gellan and agarose composites (Fig. 1). For both hydrogel matrices a critical concentration at which reinforcement with ceramic particles led to a reduction in rupture stress and compressive modulus was observed. Jamshidi et al. noted a similar phenomenon when incorporating HA into gellan, however, notably this critical concentration was found to be substantially higher for nano-sized HA sol compared with microcrystalline HA (Jamshidi et al., 2012). A maximum compressive strength of 162.5 ± 9.3 kPa was achieved for a 2.5 w/v% gellan hydrogel reinforced with 50 w/v% nano-sized HA (Jamshidi et al., 2012). Here a significantly lower critical concentration of HA (3 w/v%) was found to have a similar effect. This may be attributed to the method of particle incorporation; following mixing some sedimentation was observed, which lead to agglomeration as demonstrated in micro-CT images (Fig. 4). Particle size has been demonstrated to impact rupture stress and compressive modulus (D'Este and Eglin, 2013). If the ceramic is not incorporated into the matrix homogeneously the particles may behave as sites of stress concentration. While small amounts of HA may act as brittle networks, allowing for the dissipation of stress through the breaking of bonds locally around the particles, which explains the initial increase in quasi-static properties, as the amount of HA is increased these sites begin to overlap leading to earlier failure. The stress rising effect of the HA particles was particularly evident for agarose samples, which exhibited lower tan δ values at all frequencies for composites containing increased concentrations of ceramic powder (Fig. 2c). This may be linked with the higher proportion of HA particles > 150 µm in agarose samples as determined by particle size analysis conducted on micro-CT data (Fig. 4c). However, to confirm this further scanning would need to

be conducted and statistical significance demonstrated. The greater propensity for HA to agglomerate in AG compared with GG may be due to difference in gelation kinetics and gel chemistry. The gelation mechanism of both AG and GG proceeds through a thermal transition, occurring when heated gel solutions are cooled (Section 2.2). Unlike agarose, the molecular structure of gellan gum is known to possess acyl groups that facilitate crosslinking in the presence of cations (e.g. Mg^{2+}, Ca^{2+}, etc.). If such cations are present during cooling, GG can undergo a more efficient gelation. Therefore, it is postulated that Ca^{2+} associated with HA particulate surfaces becomes liberated during composite processing, in turn enhancing gelation efficiency. Ultimately, this stabilises the distribution of HA particulates in the gelling GG matrix. Agarose does not have an affinity for Ca^{2+}, thus particulates of HA in AG/HA formulations may not be stabilised as gelling proceeds, potentially allowing for the greater extent of agglomeration as demonstrated by microCT analysis (Fig. 4).

As cartilage is a frequency-dependent viscoelastic material (Fulcher et al., 2009; Temple et al., 2016), comparing the compressive modulus, obtained through quasi-static testing, does not provide all the information required to compare synthetic and natural cartilage viscoelastic behaviour. In this present study, a general understanding of the composites compression moduli were obtained through quasi-static mechanical testing, but it should be noted that as hydrogels are viscoelastic, their behaviour is significantly affected by the frequency of loading (Vincent, 2012). Similarly to other studies (Espino et al., 2014; Lawless et al., 2017b; Temple et al., 2016), the viscoelastic properties of both synthetic and natural cartilage was observed to be frequency-dependent. Mineralised agarose compositions displayed higher complex moduli than the mineralised gellan compositions between 5 and 20 Hz
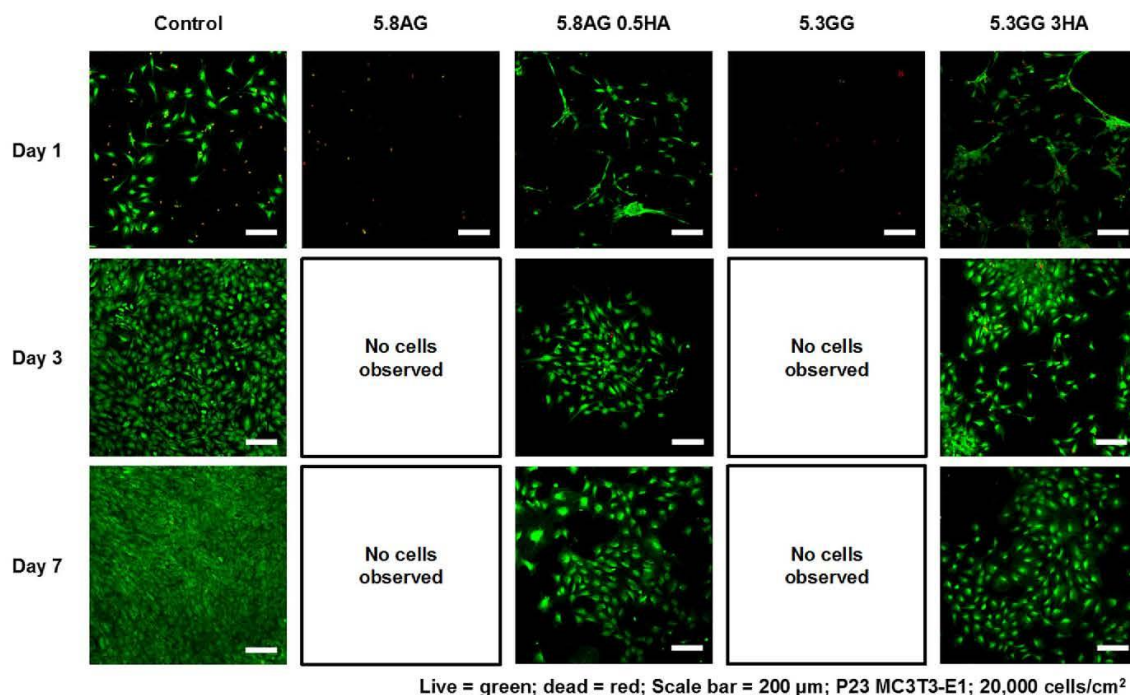
Fig. 5. Typical fluorescence micrographs illustrating the viability of MC3T3 osteoblast precursor cells after 1, 3, and 7 days of culture on optimised mineralised hydrogel compositions.

(p < 0.05), but were lower compared to native cartilage explants for all tested frequencies (p < 0.05) (Fig. 3). At 1 Hz the complex moduli of the optimised gellan (5.3GG 3.0HA) and agarose (5.8AG 0.5HA) constructs were 1.0 ± 0.2 MPa and 1.7 ± 0.2 MPa, respectively, compared with 26.3 ± 6.5 MPa for healthy human cartilage.

The specific organisation and morphological arrangement of collagen fibrils throughout the superficial, transitional and deep zones of articular cartilage structure enables the tissue to resist forces imposed upon it during articulation. Tensile, shear and compressive forces can be countered effectively by collagen fibrils of the superficial zone due to being highly aligned parallel to the surface in contact with synovial fluid. In contrast, AG and GG are absent of such specific alignment, therefore requiring the addition of a mineral phase to reinforce physical properties. In healthy tissue, HA and the extracellular matrix (ECM) interact in calcified regions of articular cartilage, contributing to an interface between cartilage and bone. Natural ECM structure facilitates strong binding interactions with hydroxyapatite, with collagen providing sites for mineral deposition, and non-collagenous proteins possessing a high affinity for hydroxyapatite mineral. Mineral formation is tightly regulated in such tissues in terms of mineral distribution, as well as the size and shape of crystallites. The mineral component of the composites analysed in this study is formed in the absence of the matrix component, such that interactions between HA with AG and GG phases are reliant on the development of mechanical interlocking between hydrogel chains and mineral particulates. Taken together, differences in the viscoelastic behaviour between the mineralised composites and natural cartilage are likely due to a combination of differences in composition, molecular organisation and mineral/hydrogel interactions. However, between 1 and 5 Hz, the gellan compositions displayed a comparable dissipation factor to healthy human cartilage. In general, the rise time of the heel strike force is approximately 100–150 ms (Shepherd and Seedhom, 1997). At 5 Hz, the rise time of the heel strike is 100 ms, thus the optimised gellan composition (5.3GG 3.0HA) formulated in the present study, has a similar loss-rate of energy to human healthy cartilage at a heel strike rise time of the general population. Therefore, further mechanical evaluation of this hydrogel will be conducted at physiological temperatures, and under different cyclical loading conditions.

The axial frequency dependent viscoelasticity of calcium alginate with HA have been previously quantified up to 20 Hz (Bouropoulos et al., 2010; Wands et al., 2008); this maximum frequency is comparable to the present study, Similar to Bouropoulos et al. (2010) and Wands et al. (2008), the present study demonstrates that the alginate hydrogels can be stiffen by HA and that the viscoelastic properties are frequency dependent (up to 20 Hz). Unlike the previous studies (Bouropoulos et al., 2010; Wands et al., 2008), the present study compared the results of the hydrogels to healthy cartilage and discovered that the agarose composition (5.8 AG 0.5 HA) dissipation factor was up to two times greater than healthy cartilage. Furthermore, the frequency dependent viscoelastic properties of gelatin methacrylamide (GelMA), Gellan Gum (GG), gellan gum methacrylate (GGMA) and combinations of GelMA/GG and combinations of GelMA/GGMA were quantified 0.01–5.12 Hz (Bartnikowski et al., 2015). Similar to the present study, Bartnikowski et al. (2015) found that the fabrication of the hydrogels resulted in frequency-dependent viscoelastic properties and discovered that the tan δ values of 1.0GG was most comparable to human donor cartilage. However, in the present study it was identified that the optimum gellan composition (5.3GG 3.0HA) displayed a similar dissipation factor to healthy human cartilage between 1–5 Hz. Extrapolatory to the frequency range used by Bartnikowski et al. (2015), this present study demonstrates that at frequencies greater that 5 Hz, the dissipation factor of the GG hydrogels were larger than the dissipation factor of healthy human cartilage. Further investigations of hydrogel frequency-dependency viscoelastic properties should evaluate the material at frequencies greater than 20 Hz as Radin et al. (1991) identified a subset of the population to have a heel-strike rise time of around 5–25 ms.

The final part of this study examined the effect of HA particle

inclusions in gellan and agarose composites on cell adhesion and viability. While agarose and gellan can support cell encapsulation these hydrogels do not facilitate cell adhesion due to a lack of ligands as seen here in confocal live/dead images (Fig. 5). It has been hypothesised that the addition of HA and/or other bioceramics may provide building blocks or signposts for cell migration and attachment (D'Este and Eglin, 2013; Suzawa et al., 2015). Here incorporation of 0.5 and 3.0 w/v% HA into agarose and gellan composites, respectively was shown to facilitate adherence of pre-osteoblast cells up to 7 days of culture. While there was some degree of cell spreading observed, generally live cells on these samples were seen in clusters (Fig. 5). This behaviour may be because cells were only able to adhere where HA agglomerations were near the surface and acted as anchors for initial attachment. To confirm this suggestion further work could be conducted to analyse the co-localisation efficiency between cells and HA, which could be labelled with Alizarin red (Moriguchi et al., 2003). Furthermore, it would be of interest to assess the ability of all native osteochondral cell types, including chondrocytes, seeded on the surface to infiltrate the composites. Overall, this initial cytotoxicity assessment demonstrates that potentially there is a trade-off between the mechanical influence of HA particles and the positive effect inclusions may have on controlling cellular responses.

5. Conclusion

The frequency-dependent viscoelastic properties of gellan and agarose hydrogels were found to be significantly affected by the addition of HA. While small amounts of HA reinforced the composite matrix, concentrations over a critical amount resulted in higher degrees of agglomeration and acted as stress risers, which was evidenced by micro-CT analysis and tan δ values. A Doehlert model was used in combination with quasi-static mechanical testing to iteratively optimise formulations; 5.8 AG 0.5HA and 5.3GG 3.0HA were found to exhibit the highest maximum stresses. Interestingly, the agarose sample which was the most promising based on quasi-static tests did not exhibit the highest complex modulus between 1 and 20 Hz, instead a sample with increased mineral (5.3 AG 25HA) was found to be more comparable to human cartilage.

Generally the complex moduli of the optimised gellan (1.0 ± 0.2 MPa at 1 Hz) and agarose (1.7 ± 0.2 MPa at 1 Hz) constructs did not match the complex moduli of healthy human cartilage samples (26.3 ± 6.5 MPa at 1 Hz). However, the dissipation factors of this gellan composition were found to be comparable to human cartilage between 1 and 5 Hz. Since 5 Hz is representative of the heel strike rise time for the general population, further mechanical evaluation of this formulation is suggested.

In summary, this study demonstrates the advantages of using a model to systematically optimise hydrogel composites as well as the importance of examining the mechanical behaviour of biomaterials under conditions representative of the native environment. Furthermore, this approach needs to be balanced with a biological assessment of the material being developed.

Appendix A. Supporting information

Supplementary data associated with this article can be found in the online version at http://dx.doi.org/10.1016/j.jmbbm.2018.01.016.

References

Almeida, H.V., Eswaramoorthy, R., Cunniffe, G.M., Buckley, C.T., O'Brien, F.J., Kelly, D.J., 2016. Fibrin hydrogels functionalized with cartilage extracellular matrix and incorporating freshly isolated stromal cells as an injectable for cartilage regeneration. Acta Biomater. 36, 55–62. http://dx.doi.org/10.1016/j.actbio.2016.03.008.

Balakrishnan, B., Joshi, N., Jayakrishnan, A., Banerjee, R., 2014. Self-crosslinked oxidized alginate/gelatin hydrogel as injectable, adhesive biomimetic scaffolds for cartilage regeneration. Acta Biomater. 10, 3650–3663. http://dx.doi.org/10.1016/j.actbio.2014.04.031.

Barnes, S.C., Lawless, B.M., Shepherd, D.E.T., Espino, D.M., Bicknell, G.R., Bryan, R.T., 2016. Viscoelastic properties of human bladder tumours. J. Mech. Behav. Biomed. Mater. 61, 250–257. http://dx.doi.org/10.1016/j.jmbbm.2016.03.012.

Bartnikowski, M., Wellard, R.M., Woodruff, M., Klein, T., 2015. Tailoring hydrogel viscoelasticity with physical and chemical crosslinking. Polymers (Basel) 7, 2650–2669. http://dx.doi.org/10.3390/polym7121539.

Bouropoulos, N., Stampolakis, A., Mouzakis, D.E., 2010. Dynamic mechanical properties of calcium alginate-hydroxyapatite nanocomposite hydrogels. Sci. Adv. Mater. 2, 239–242. http://dx.doi.org/10.1166/sam.2010.1092.

Burton, H.E., Freij, J.M., Espino, D.M., 2017. Dynamic viscoelasticity and surface properties of porcine left anterior descending coronary arteries. Cardiovasc. Eng. Technol. 8, 41–56. http://dx.doi.org/10.1007/s13239-016-0288-4.

Cameron, A.R., Frith, J.E., Cooper-White, J.J., 2011. The influence of substrate creep on mesenchymal stem cell behaviour and phenotype. Biomaterials. http://dx.doi.org/10.1016/j.biomaterials.2011.04.003.

Costa, A.M.S.S., Mano, J.F., 2015. Extremely strong and tough hydrogels as prospective candidates for tissue repair – a review. Eur. Polym. J. 72, 344–364. http://dx.doi.org/10.1016/j.eurpolymj.2015.07.053.

Coutinho, D.F., Sant, S.V., Shin, H., Oliveira, J.T., Gomes, M.E., Neves, N.M., Khademhosseini, A., Reis, R.L., 2010. Modified Gellan Gum hydrogels with tunable physical and mechanical properties. Biomaterials 31, 7494–7502. http://dx.doi.org/10.1016/j.biomaterials.2010.06.035.

D'Este, M., Eglin, D., 2013. Hydrogels in calcium phosphate moldable and injectable bone substitutes: sticky excipients or advanced 3-D carriers? Acta Biomater. 9, 5421–5430. http://dx.doi.org/10.1016/j.actbio.2012.11.022.

Danoux, C., Pereira, D., Döbelin, N., Stähli, C., Barralet, J., van Blitterswijk, C., Habibovic, P., 2016. The effects of crystal phase and particle morphology of calcium phosphates on proliferation and differentiation of human mesenchymal stromal cells. Adv. Healthc. Mater. 5, 1775–1785. http://dx.doi.org/10.1002/adhm.201600184.

Espino, D.M., Shepherd, D.E.T., Hukins, D.W.L., 2014. Viscoelastic properties of bovine knee joint articular cartilage: dependency on thickness and loading frequency. BMC Musculoskelet. Disord. 15, 205. http://dx.doi.org/10.1186/1471-2474-15-205.

Fick, J.M., Espino, D.M., 2011. Articular cartilage surface rupture during compression: investigating the effects of tissue hydration in relation to matrix health. J. Mech. Behav. Biomed. Mater. 4, 1311–1317. http://dx.doi.org/10.1016/j.jmbbm.2011.04.018.

Fulcher, G.R., Hukins, D.W.L., Shepherd, D.E.T., 2009. Viscoelastic properties of bovine articular cartilage attached to subchondral bone at high frequencies. BMC Musculoskelet. Disord. 10, 61. http://dx.doi.org/10.1016/j.jmbbm.2011.04.018.

Gabrielsson, J., Lindberg, N.-O., Lundstedt, T., 2002. Multivariate methods in pharmaceutical applications. J. Chemom. 16, 141–160. http://dx.doi.org/10.1002/cem.697.

Hu, J., Zhu, Y., Tong, H., Shen, X., Chen, L., Ran, J., 2016. A detailed study of homogeneous agarose/hydroxyapatite nanocomposites for load-bearing bone tissue. Int. J. Biol. Macromol. 82, 134–143. http://dx.doi.org/10.1016/j.ijbiomac.2015.09.077.

Hukins, D.W.L., Leahy, J.C., Mathias, K.J., 1999. Biomaterials: defining the mechanical properties of natural tissues and selection of replacement materials. J. Mater. Chem. 9, 629–636. http://dx.doi.org/10.1039/A807411I.

Jamshidi, P., Ma, P., Khosrowyar, K., Smith, A.M., Grover, L.M., 2012. Tailoring gel modulus using dispersed nanocrystalline hydroxyapatite. J. Exp. Nanosci. 7, 652–661. http://dx.doi.org/10.1080/17458080.2012.724182.

Jethara, S.I., Patel, M.R., 2015. Optimizing oral controlled release drug delivery systems using experimental designs. Intellect. Prop. Rights Open Access 3, 1–6. http://dx.doi.org/10.4172/2375-4516.1000142.

Lawless, B.M., Barnes, S.C., Espino, D.M., Shepherd, D.E.T., 2016. Viscoelastic properties of a spinal posterior dynamic stabilisation device. J. Mech. Behav. Biomed. Mater. 59, 519–526. http://dx.doi.org/10.1016/j.jmbbm.2016.03.011.

Lawless, B.M., Espino, D.M., Shepherd, D.E.T., 2017a. In vitro oxidative degradation of a spinal posterior dynamic stabilisation device. J. Biomed. Mater. Res. Part B Appl. Biomater. 1–8. http://dx.doi.org/10.1002/jbm.b.33913.

Lawless, B.M., Sadeghi, H., Temple, D.K., Dhaliwal, H., Espino, D.M., Hukins, D.W.L., 2017b. Viscoelasticity of articular cartilage: analysing the effect of induced stress and the restraint of bone in a dynamic environment. J. Mech. Behav. Biomed. Mater. 75, 293–301. http://dx.doi.org/10.1016/j.jmbbm.2017.07.040.

Liu, Y., Lian, Q., He, J., Zhao, J., Jin, Z., Li, D., 2011. Study on the Microstructure of Human Articular Cartilage/Bone Interface. J. Bionic Eng. 8, 251–262. http://dx.doi.org/10.1016/S1672-6529(11)60037-1.

Menard, K.P., 2008. Dynamic Mechanical Analysis: A Practical Introduction, 2nd ed. CRC press, Taylor & Francis Group, Boca Raton, Florida.

Mennini, N., Furlanetto, S., Cirri, M., Mura, P., 2012. Quality by design approach for

developing chitosan-Ca-alginate microspheres for colon delivery of celecoxib-hydroxypropyl-β-cyclodextrin-PVP complex. Eur. J. Pharm. Biopharm. 80, 67–75. http://dx.doi.org/10.1016/j.ejpb.2011.08.002.

Mironi-Harpaz, I., Wang, D.Y., Venkatraman, S., Seliktar, D., 2012. Photopolymerization of cell-encapsulating hydrogels: crosslinking efficiency versus cytotoxicity. Acta Biomater. 8, 1838–1848. http://dx.doi.org/10.1016/j.actbio.2011.12.034.

Miyoshi, E., Takaya, T., Nishinari, K., 1996. Rheological and thermal studies of gel-sol transition in gellan gum aqueous solutions. Carbohydr. Polym. 30, 109–119. http://dx.doi.org/10.1016/S0144-8617(96)00093-8.

Moriguchi, T., Yano, K., Nakagawa, S., Kaji, F., 2003. Elucidation of adsorption mechanism of bone-staining agent alizarin red S on hydroxyapatite by FT-IR microspectroscopy. J. Colloid Interface Sci. 260, 19–25. http://dx.doi.org/10.1016/S0021-9797(02)00157-1.

Moxon, S.R., Cooke, M.E., Cox, S.C., Snow, M., Jeys, L., Jones, S.W., Smith, A.M., Grover, L.M., 2017. Suspended manufacture of biological structures. Adv. Mater. 29. http://dx.doi.org/10.1002/adma.201605594.

Nguyen, L.H., Kudva, A.K., Saxena, N.S., Roy, K., 2011. Engineering articular cartilage with spatially-varying matrix composition and mechanical properties from a single stem cell population using a multi-layered hydrogel. Biomaterials 32, 6946–6952. http://dx.doi.org/10.1016/j.biomaterials.2011.06.014.

Osmałek, T., Froelich, A., Tasarek, S., 2014. Application of gellan gum in pharmacy and medicine. Int. J. Pharm. 466, 328–340. http://dx.doi.org/10.1016/j.ijpharm.2014.03.038.

Parmar, P.A., Chow, L.W., St-Pierre, J.-P., Horejs, C.-M., Peng, Y.Y., Werkmeister, J.A., Ramshaw, J.A.M., Stevens, M.M., 2015. Collagen-mimetic peptide-modifiable hydrogels for articular cartilage regeneration. Biomaterials 54, 213–225. http://dx.doi.org/10.1016/j.biomaterials.2015.02.079.

Pearson, B., Espino, D.M., 2013. Effect of hydration on the frequency-dependent viscoelastic properties of articular cartilage. Proc. Inst. Mech. Eng. H 227, 1246–1252. http://dx.doi.org/10.1177/0954411913501294.

Radin, E., Yang, K., Riegger, C., Kish, V., O'Connor, J., 1991. Relationship between lower limb dynamics and knee joint pain. J. Orthop. Res. 9, 398–405.

Sadeghi, H., Lawless, B.M., Espino, D.M., Shepherd, D.E.T., 2018. Effect of frequency on crack growth in articular cartilage. J. Mech. Behav. Biomed. Mater. 77, 40–46.

Sadeghi, H., Shepherd, D.E.T., Espino, D.M., 2015. Effect of the variation of loading frequency on surface failure of bovine articular cartilage. Osteoarthr. Cartil. 23, 2252–2258. http://dx.doi.org/10.1016/j.joca.2015.06.002.

Shepherd, D.E.T., Seedhom, B.B., 1997. A technique for measuring the compressive modulus of articular cartilage under physiological loading rates with preliminary results. Proc. Inst. Mech. Eng. H 211, 155–165. http://dx.doi.org/10.1243/0954411971534278.

Suzawa, Y., Kubo, N., Iwai, S., Yura, Y., Ohgushi, H., Akashi, M., 2015. Biomineral/agarose composite gels enhance proliferation of mesenchymal stem cells with osteogenic capability. Int. J. Mol. Sci. 16, 14245–14258. http://dx.doi.org/10.3390/ijms160614245.

Tamaddon, M., Czernuszka, J.T., 2013. Critical review. The need for hierarchical scaffolds in bone tissue engineering 2, pp. 1–8.

Temple, D.K., Cederlund, A.A., Lawless, B.M., Aspden, R.M., Espino, D.M., 2016. Viscoelastic properties of human and bovine articular cartilage: a comparison of frequency-dependent trends. BMC Musculoskelet. Disord. 17, 419. http://dx.doi.org/10.1186/s12891-016-1279-1.

Vincent, J.F.V., 2012. Structural biomaterials. Appl. Biophys. http://dx.doi.org/10.1002/9780470513156.ch15.

Wands, I., Shepherd, D.E.T., Hukins, D.W.L., 2008. Viscoelastic properties of composites of calcium alginate and hydroxyapatite. J. Mater. Sci. Mater. Med. 19, 2417–2421. http://dx.doi.org/10.1007/s10856-007-3364-3.

Zhang, L.-M., Wu, C.-X., Huang, J.-Y., Peng, X.-H., Chen, P., Tang, S.-Q., 2012. Synthesis and characterization of a degradable composite agarose/HA hydrogel. Carbohydr. Polym. 88, 1445–1452. http://dx.doi.org/10.1016/j.carbpol.2012.02.050.

158

Supplementary Information

Table 1. Summary of agarose/HA compositions tested

% w/v agarose	% w/v HA			
	0	0.5	12.75	25
2	x		x	
2.8		x	x	x
3.5	x		x	
4.3		x	x	x
5		x	x	x
5.8	x	x	x	x
6.5	x		x	

Table 2. Summary of gellan/HA compositions tested

% w/v gellan	% w/v HA				
	0	0.5	6	12.75	15*
1.5		x		x	
2.1		x	x	x	
2.8				x	
3			x		x
3.4		x	x	x	
4	x	x		x	
6	x				

* %w/v HA greater than 15% were not investigated as 15% was found to be the upper limit for successful homogeneous HA particle incorporation. Above 15%, composite homogeneity could not be maintained.

Chapter 8: Summary and future work

8.1 Summary

A holistic view of permanent Ti-based orthopaedic implant design was used to guide this project. The life-cycle of orthopaedic implant design occurs generally as follows; patient data is collected and used to choose or modify the implant design, the implant material is selected, a fabrication method and post-processing requirements are determined, an initial prototype is created and refined based on predictions regarding performance in the body, an optimised implant is produced, sterilised, perhaps post-processed and implanted, and further, expected to last for >20 years. There are many stages in this process where a biomaterials engineer can intervene, most importantly, in the fabrication, post-processing and performance prediction stages.

The following aspects of Ti-6Al-4V orthopaedic implant design and performance were investigated in detail:

- The interplay of laser scan speed and laser power during the SLM fabrication of Ti-6Al-4V, and the contribution thereof to SLM Ti-6Al-4V properties. A large process window was examined, with laser scan speeds from 200-1200 mm/s and laser powers from 80-280 W used to produce Ti-6Al-4V samples for analysis. The hardness, roughness, porosity and corrosion resistance of SLM Ti-6Al-4V was found to vary according to the process parameter combinations used, due to the effects of changing laser scan speed and/or laser power on melt pool cooling rates, and thus overall microstructure. This data was used to create process maps indicating the likely Ti-6Al-4V properties based on SLM process parameters. Key findings demonstrate that, although different combinations of laser scan speeds and laser intensities may result in the same volumetric energy density (thermal energy per unit area) supplied to

the material, volumetric energy density is a poor predictor for part properties, and should not be used as a design variable in determining the optimal process parameters to use for the SLM fabrication of Ti-6Al-4V products with particular requirements. Matching SLM laser scan speed and laser intensity (e.g. slow scan speed and lower laser intensity) results in more stable melting and cooling, and was shown to produce Ti-6Al-4V with more uniform properties. Low stochastic porosity (0–5%) was produced through the use of intermediate laser powers and scan speeds (120-180 W and 400-600 mm/s respectively).

- Differences in the bioactivity of SLM Ti-6Al-4V produced with differing laser scan speed/laser power combinations. The process parameters chosen for the SLM fabrication of Ti-6Al-4V have an enormous effect on the layer-wise cooling rates and fusion, and thus affect microstructure and surface properties. Four combinations of laser scan speed and laser power were used to produce SLM Ti-6Al-4V samples for in vitro testing, and examined in order to determine whether alternate combinations of SLM process parameters can facilitate improved Ti-6Al-4V bioactivity in comparison to the most commonly used process parameters (280 W, 1200 mm/s). The combined effects of altering laser scan speed and laser power on SLM Ti-6Al-4V were examined in relation to their effects on cell (human osteoblast) viability, morphology and mineralisation as compared to wrought Ti-6Al-4V samples. Key findings indicate that SLM Ti-6Al-4V produced with a laser power of 120 W and a laser scan speed of 500 mm/s (lower power and lower speed than commonly used) can facilitate increased biological activity as compared to both wrought Ti-6Al-4V and SLM Ti-6Al-4V produced with the most commonly used process parameters (280 W, 1200 mm/s). This indicates that SLM machines with reduced technical capabilities (i.e. maximum achievable laser power <130W) may be used to produce orthopaedic implants with improved bioactivity, as compared to high-end machines and conventional means.

- Lab bench (*ex vivo*) methods for accurately predicting and understanding the *in vivo* re-passivation of Ti-based alloys. As Ti-based alloys display such high corrosion resistance, it is near impossible to disrupt their passive layers through standard electrochemical techniques. Thus, a novel experimental technique was developed, combining manual passive layer disruption with high resolution chronoamperometry and atomic emission spectroelectrochemistry (AESEC) to produce high precision data regarding the re-establishment of the passive layer for various Ti-based alloy compositions. Results revealed that both fabrication method and alloying elements influence 're-passivation' behaviour, and AESEC as applied to cp-Ti revealed actual dissolution currents of ~2–3 μA/cm^{-2} (i.e. ~9 μm/yr).

- Methods for the deposition of uniform, strongly bonded strontium phosphate (compound behaving similarly to HA) containing coatings on Ti-based implants to enhance bone formation processes. Incorporating strontium phosphate onto orthopaedic implant surfaces has been shown to improve osseointegration, however, most common coating methods require extremely high sintering temperatures or voltages, and result in the deposition of line-of-sight weakly bonded, crack-prone HA coatings. A biomimetic two-step hydrothermal method was adapted here and used to successfully apply uniform, strongly bonded, strontium phosphate coatings on various Ti-based alloys. Further, the release of strontium ions from the coating was found to increase osteoblastic cell proliferation and differentiation, while suppressing the activity of osteoclasts.

- Post-fabrication approaches for improving the healing of the implant/bone/cartilage interface. The viscoelastic behaviour of the bone/implant/cartilage interface is seldom taken into consideration in the development of regenerative scaffolds. The static and dynamic viscoelastic behaviour of the implant/bone/cartilage interface was investigated in detail, and the resulting data was used to guide the development of a biomimetic mineralised hydrogel

composite as a candidate scaffold for supporting the healing of this interface. Composites were formed using synthetic HA and natural origin agarose or gellan. The addition of HA particles was found to reinforce both agarose and gellan matrices up to a critical concentration (< 3 w/v %). Beyond this, larger agglomerates were formed, as evidenced by micro computed tomography data, which acted as stress risers and reduced the ability of composites to dissipate energy demonstrated by a reduction in tan δ values. The optimised composites did not replicate the complex moduli of health human cartilage, however, the energy dissipation factor of the optimised gellan composite (5.3 w.v. % gellan with 3.0 w.v. % HA) was found to be comparable to that of healthy human cartilage between 1 and 5 Hz. While agarose and gellan do not normally facilitate cell attachment, the incorporation of HA facilitated the attachment of osteoblasts (mouse calvaria derived), indicating that combining two commonly used approaches (i.e. hydrogel scaffolds and bone-like mineral signposting) can lead to more than the sum of their parts.

8.2 Future work

This project sought to develop various strategies in the improvement of osseointegration of Ti-6Al-4V implants. A variety of approaches were used, encompassing improvements in implant fabrication, the accurate analysis of Ti-based alloy re-passivation behaviour, the application of bioactive coatings and the development of mineralised hydrogels for interfacial regeneration.

The preliminary investigation of the interplay of SLM process parameters on Ti-6Al-4V properties showed that parameters must be chosen in concert to ensure the stability of the melt pool during building. The work contained herein focuses on the interplay of two processing parameters, namely laser scan speed and laser power. Future work should examine the effects of other important process parameters such as layer height, as well as the interplay of multiple parameters.

The characterisation and performance testing completed on the SLM Ti-6Al-4V samples did not include any examination of fatigue and wear. This is an important factor to consider in orthopaedic implant performance, and requires the development of careful experimental protocols to accurately determine the relationship between surface properties (and build orientation vs. implanted surface orientation) and wear. Difficulties remain in predicting the wear and fatigue behaviour of SLM Ti-6Al-4V implants without the use of geometries similar to those implants.

The investigation of changes in osteoblast behaviour on SLM Ti-6Al-4V *in vitro,* with respect to changes in processing parameters, was completed over a relatively short time period of 7 days. Future work should extend this time period and examine the behaviour of osteoblasts on the various surfaces over periods of up to 3 months. Future work should also examine the various implant improvement strategies through the use of *in vivo* models. Future work should also focus on further biocompatibility testing, namely long-term analysis of the growth of osteoblasts on various surfaces, such as LENS

deposited TNZ alloys and SLM fabricated Ti-6Al-4V. The successful pre-treatment and bioactive SrP coating treatment will be investigated in terms of its efficacy on SLM fabricated Ti-6Al-4V. There is potential for the application of the developed mineralised hydrogel composites to be used as regenerative scaffolds for the implant/bone interface.

References

1. Zhang BGX, Myers DE, Wallace GG, Brandt M, Choong PFM. Bioactive coatings for orthopaedic implants-recent trends in development of implant coatings. Int J Mol Sci. 2014;15(7):11878–921.

2. Liu X, Chu PK, Ding C. Surface modification of titanium, titanium alloys, and related materials for biomedical applications. Mater Sci Eng R Reports. 2004;47(3–4):49–121.

3. Browne M, Gregson PJ. Surface modification of titanium alloy implants. Biomaterials. 1994 Sep;15(11):894–8.

4. Matsuno H, Yokoyama A, Watari F, Uo M, Kawasaki T. Biocompatibility and osteogenesis of refractory metal implants, titanium, hafnium, niobium, tantalum and rhenium. Biomaterials. 2001 Jun 1;22(11):1253–62.

5. Sidambe A. Biocompatibility of advanced manufactured titanium implants - a review. Materials (Basel). 2014 Dec 19;7(12):8168–88.

6. Basalah A, Shanjani Y, Esmaeili S, Toyserkani E. Characterizations of additive manufactured porous titanium implants. J Biomed Mater Res - Part B Appl Biomater. 2012 Oct;100 B(7):1970–9.

7. Marcu T, Todea M, Maines L, Leordean D, Berce P, Popa C. Metallurgical and mechanical characterization of titanium based materials for endosseous applications obtained by selective laser melting. Powder Metall. 2012;55(4):309–14.

8. El-Hajje A, Kolos EC, Wang JK, Maleksaeedi S, He Z, Wiria FE, et al. Physical and mechanical characterisation of 3D-printed porous titanium for biomedical applications. J Mater Sci Mater Med. 2014;25:2471–80.

9. Wohlers T. Wohlers Report 2013: Additive Manufacturing and 3D Printing State of the Industry–Annual Worldwide Progress Report, Wohlers Associates. Inc., Fort Collins. Colorado: Wohlers Associates; 2013.